12-15-2014

Low Reynolds Number Turbulence: Mechanisms and Applications

Wei Zhao
University of South Carolina - Columbia

LOW REYNOLDS NUMBER TURBULENCE: MECHANISMS AND APPLICATIONS

by

Wei Zhao

Bachelor of Science
Dalian University of Technology, 2003

Master of Science
Huazhong University of Science and Technology, 2006

Submitted in Partial Fulfillment of the Requirements

For the Degree of Doctor of Philosophy in

Mechanical Engineering

College of Engineering and Computing

University of South Carolina

2014

Guiren Wang, Major Professor

Jamil Khan, Committee Member

Tanvir Farouk, Committee Member

Juan Caicedo, Committee Member

Lacy Ford, Vice Provost and Dean of Graduate Studies

DEDICATION

I dedicate my dissertation work to my parents, ancestors, friends and colleagues. First, to my loving parents, Dahua Zhao and Bo Liu, who encouraged me to perform an excellent Ph.D research.

Then, to my ancestors, although I don't know who you were, I will do my best to contribute to this family with glories.

I also want to dedicate this dissertation to my friends and colleagues who give me help and support throughout the long and tough progress. I really enjoy the time work with your guys.

At last, I want to dedicate my works to my loving country, China, and my second hometown, USA.

ACKNOWLEDGEMENT

I wish to thank my committee members who were more than generous with their expertise and precious time. A special thanks to Dr. Guiren Wang, my supervisor for his help and support throughout the entire process. I also appreciate for the help of Dr. Sarah Baxter and helpful discussions with Dr. Juan Caicedo and Dr. Paul Huray on my researches. Thank you Dr. Jamil Khan, Dr. Juan Caicedo, Dr. Farouk for agreeing to serve on my committee.

I would like to acknowledge and thank all the staff in our department for their patience and assistance in the last 6 and a half years.

Also, I want to give special thanks to North America Mixing Forum for their financial support in my first two years.

Finally, I would like to thank all my previous supervisors and teachers.

ABSTRACT

Turbulence, as one of "the most important unsolved classical problem in physics" (R. Feynman, 1932), has been investigated for more than 130 years. Conventionally, turbulence is believed to be a phenomenon of high Reynolds numbers (Re). However, we find that turbulence can also be achieved at low Re by proper external forcing, either in macroflows or in microflows.

In macroflows, the characteristics of high Re turbulence can be achieved in confined flows, when the bulk flow Re is around 400, by external forcing at its optimal frequency (Wang 2003; Wang 2006). Interestingly, the optimal narrow band of frequency is fixed (5-6 Hz) independent of the bulk flow Re in either mixing layers or plane wakes. At the optimal frequency, an extremely fast mixing between initial two streams can be achieved. However, the mixing enhancement mechanism is still unknown. Therefore, we focus on both the dynamical process of the flow and the corresponding mechanism of the optimal frequency which significantly affects the dynamics of the fast mixing mechanism. The detailed dynamical process of the flows, especially the velocity and vorticity fields are investigated first. Then, the kinetic energy and the effect of each term in turbulent energy equation are studied in details. We found that, the strongly three-dimensional (3-D) nonlinear flow caused by streamwise vortex structures is the main reason of the fast mixing. It has two major roles: (1) enhances significantly the mean flow in vertical direction and increases the spreading rate of the mixing layer; (2) accelerate the evolution of flow from

two-dimensional (2-D) to 3-D that again enhance the transport of turbulent energy, and thus the scalar and mixing as well. The existence of corner vortex is validated and its relation with streamwise vortex is also analyzed.

Meanwhile, in order to explain the cause of the optimal frequency, both parametric study and numerical simulation are carried out. Several important phenomena are discovered to help understand this mysterious optimal frequency: (1) the frequency is not due to any known flow instability mechanism; (2) the frequency is insensitive to the changing of dimensions of all the downstream parts of the settling chamber, indicating the optimal frequency is not simply attributed to one-dimensional (1-D) acoustic resonance; (3) by numerical simulations, we find there do exist a low-frequency acoustic eigenmode around 6 Hz. The eigenfrequency qualitatively increases with the decreasing of lengths of all the parts, except the settling chamber; (4) the mixing enhancement is tightly related to the local geometry of splitter plate at the trailing edge and acoustically induced shedding vortices. A large curvature diameter of trailing edge inhibits the generation of the acoustically induced shedding vortex and significantly decrease the mixing enhancement. Hence, acoustic resonance could be related to the mechanism related to the optimal frequency.

In microflows, turbulence in a low Re flow field in microchannel is recently realized for the first time when an electrokinetic (EK) force is applied to a pressure driven flow with two initial streams of different conductivities. The so-called micro EK turbulence is systematically investigated and many features of high Re turbulence, such as Kolmogorov -5/3 slope, Obukhov-Corrsin -5/3 spectrum, scaling law and exponential tail of probability density function (PDF) etc., have been amazingly found in microfluidics at the low Re

microflow. The corresponding theory of the EK turbulence is proposed to help understand why there can be micro EK turbulence and the correspondingly observed phenomena. A new scaling law of the EK turbulence is theoretically suggested by direct derivation from Navier-Stokes equation and dimensional analysis, which is also verified experimentally.

To successfully measure micro EK turbulence, a novel velocity measurement method — Laser Induced Fluorescence Photobleaching Anemometer (LIFPA) which has simultaneously ultrahigh spatial and temporal resolution, is developed, since so far no available velocimeters can measure the micro EK turbulence. The temporal resolution of LIFPA is theoretically investigated and experimentally compared to the standard micro Particle Imaging Velocimetry (μPIV) method. The results demonstrate the unbeatable temporal resolution and accuracy of LIFPA. Then, the error in LIFPA measurement is analyzed. Proper correction methods on the statistics of velocity measurement by LIFPA are introduced.

We believe, the present work should have important impact on turbulence research, not only on phenomena, but also on the physical mechanisms, and as well as the relevant measuring technique. The present investigations have important practical applications in the fields where fast mixing is highly desired, such as the design of heat exchanger and chemical reactor in process industry, and Lab-on-a-chip.

TABLE OF CONTENTS

LIST OF TABLES

LIST OF FIGURES

Chapter 1

LOW REYNOLDS NUMBER TURBULENCE IN CONFINED MIXING LAYER IN MACROFLOW

1.1 Introduction

Mixing enhancement by forcing in free mixing layer and jet has been investigated for several decades. No matter in incompressible (Ho and Huang ; Ho and Huerre ; Dziomba and Fiedler ; Fiedler and Mensing ; Roberts ; Browand and Ho ; Wang ; Wang ; Wiltse and Glezer 2011) or compressible fluids (Ho and Nosseir 1981; Oster and Wygnanski 1982; Weisbrot and Wygnanski 1988; Wiltse and Glezer 1998; Wiltse and Glezer 2004; Wang 2006; Li et al. 2009), reactive flows (Koochesfahani and Dimotakis 1986; Dimotakis 2005; Wędołowski et al. 2011) etc., many interesting phenomena have been found and studied in details.

In plane free mixing layers, based on the Kelvin-Helmholtz (KH) instability and vortex merging, subharmonic mode is believed to be the most effective mechanism for mixing enhancement (Ho and Huang 1982; Ho and Huerre 1984). However, the enhancement is limited. Fiedler et al. (Fiedler and Mensing 1985) reported when the forcing intensity exceeds 6.5%, the spreading rate (Cantwell 1981; Dimotakis 1986) of mixing layer stops increasing due to the nonlinear saturation. At the same velocity ratio, compared to the neutral case, the spreading rate of mixing layer is only at most two times

larger under the subharmonic actuating (Weisbrot and Wygnanski 1988). Recently, Wiltse et al (Wiltse and Glezer 2004; Wiltse and Glezer 2011) investigated the possibility of using an spanwise array of heater as actuators at the upstream of trailing edge to enhance the mixing effect. By increasing the streamwise vorticity and the strength of the vortices, triple mixing enhancement has been achieved.

In 1999, Wang (Wang 1999; Wang 2003) reported a very attractive mixing phenomenon in confined mixing layer under forcing at a specific narrow frequency band. The mixing is so fast that even at Re=400 (defined by the diameter of mixing chamber and bulk flow velocity), the turbulent spectrum of scalar — Obukhov–Corrsin spectrum (-5/3 law) is achieved adjacent to the inlet of the mixing chamber. A drastic mixing happens immediately at the inlet of mixing chamber. As the Reynolds number increases to moderate value, the mixing becomes even faster with larger spreading rate. Increasing the forcing intensity, the spreading rate of the mixing layer continues increasing until the spreading angle reaches almost 180 degrees. The aforementioned nonlinear saturation in free mixing layer doesn't happen in this process. The most unusual phenomenon is that, the optimal actuating frequency corresponding to the highest spreading rate happens to be in a narrow frequency band (near 6 Hz, abbr. *f*-band) which is independent with Reynolds number and velocity ratio. This is a great advantage for practical application, since the control process can be apparently simplified.

Recently, there are two major topics on this fast mixing process. First is the dynamical process of the fast mixing. Second is the cause of the unchanged optimal frequency.

In this manuscript. we first introduce the flow dynamics in confined mixing layer. Compared to the free mixing layer, the mixing layer in confined flow field has stronger 3-D and nonlinearity. The 3-dimensionality of free mixing layer was first reported by Miksad (Miksad 1972; Miksad 1973) in free mixing layer. Then Bernal (Bernal 1981) gave a detailed experimental investigation and provided clear morphology of the streamwise vortex. In 1982, Pierrehumbert & Widnall (Pierrehumbert and Widnall 1982) found that the streamwise vortices in free mixing layer were attributed to elliptical secondary instability (also named Widnall instabiltiy) in spanwise direction and their numerical simulations were in good agreement with Bernal's (Bernal and Roshko 1986) experiments. Their result showed the secondary instability was generated on the basis of finite-amplitude flow of shear layer. The maximum temporal growth rate can be achieved when spanwise wavy number decreases to 0, i.e. degraded to 2-dimensional problem. Thereby, it can't be a strong instability mechanism.

In 1985, Roberts (Roberts 1985) first found a symmetric streamwise vortices in confined wake flow. Then in 1997, in confined wake flow with square cross-section, Mackinnon & Koochesfahani (MacKinnon and Koochesfahani 1997) found similar flow structures as in our experiments, i.e. the counter-rotation mushroom-like vortex structures. Furthermore, they reported the streamwise vortex could be affected by outer excitation. However, recently, to our knowledge, there is no detailed investigations on flow dynamics in confined mixing layer, and also no comparison with conventional free mixing layer. Here, we investigate the dynamic process of flow in the following steps:

First, compare the unforced confined mixing layer with the conventional free mixing layer, and check if the basic flow has different instability or universal character.

Then, the receptivity of flow in nozzle section under forcing at different frequencies and forcing intensities are investigated. The characteristic flow structures under forcing due to the receptivity are investigated later, such as mean and fluctuating velocity, vorticity.

The evolution of kinetic energy distribution in mixing chamber is finally compared with the receptivity to explain the complicated dynamic process.

From the above steps, we can understand why the mixing is so fast and what flow structures dominate the fast mixing process. However, this cannot directly explain the cause of the fixed optimal frequency. From visualization, we can see the drastic mixing is always accompanied and dominated by the intensive flow fluctuations which can be induced by many mechanisms, such as absolute instability, acoustic resonance and so on. Wang (Wang 2006) postulated the fast mixing may be due to the influence of corner vortex and its instability. However, the researches on corner flow (Zamir and Young 1970; Gessner 1973; Zamir 1981; Goldstein et al. 1992; Dhanak 1993; Balachhandar and Malik 1995; Dhanak and Duck 1997; Duck and Owen 2004) indicate the corner flow instability is tightly related to the bulk flow velocity and pressure gradient. This is conflict to the fact that the optimal frequency doesn't vary with Re. Hence, it's doubtable that the corner flow instability is the dominant mechanism which results in the fast mixing and the unchanged optimal frequency. Meanwhile, from the receptivity of flow in nozzle section, if the highest receptivity in nozzle is found at the optimal frequency (this is also the truth), the optimal frequency should not be caused by the special downstream flow instability. But some other mechanism pre-exist upstream or caused by the whole water tunnel system. Since the narrow f-band is independent of Re, intuition attributes the phenomenon of the fast mixing and high receptivity to the resonance. As the resonance has been widely studied in mixing

enhancement in nozzle of combustors and closed cavity (Parikh and Moffat 1982; Matta et al. 1996; Dimotakis 2005). It becomes one of the most probable mechanisms that cause the fast mixing. Hence, parametric researches are taken to find out the dominant of optimal frequency.

1.2 Experimental techniques and setup

In this section, the facilities and instruments are introduced in details.

1.2.1 Water tunnel system

The experimental setup is designed to be consistent to Wang's work (Wang 1999; Wang 2003) to ensure that the previous work is repeatable, as shown in Figure 1.1(*a*). In order to avoid external disturbance, gravity driven flow is adopted by using two 416 Liter water tanks, which are 2.5 m over the test section. One is filled with pure water and the other is filled with aqueous fluorescent dye solution for flow visualization. The waste solution is drained to another water tank (568 L). Two sets of rotameters are used to control the bulk flow velocity of the two initial streams of the mixing layer. Each set is constituted with one 7510 series (2-20 Gallon per Minute, or GPM) and one 7511 series (0.2-2 GPM) rotameters from King Instrument. Control valves are placed at the downstream of rotameters to avoid potential influence on the accuracy of rotameters.

External vibrations, especially low frequency components, could seriously disturb the flow and contaminate the experimental results. Therefore, several ways are applied to eliminate the potential vibration influence. A heavy experimental table is constructed of welded frames of 3-inches square steel and 38mm thick wood as top. Vibration absorbing

feet are placed underneath the table to depress vibration. The settling chamber, mixing chamber and the drain pipes are fixed on the table with vibration absorbing clamps. As the purpose for flexible adjustment, rubber pipes with 51mm inner diameter and 5mm wall thickness are adopted as the water supply pipes which connect the control valves and the settling chamber. They are clamped on aluminum frames which are fixed on the experimental table. The actuating device (speaker box) is also fixed on the table with independent vibration absorber under it to avoid interaction with other parts. All the measurement instruments are located on another optical breadboard with individual vibration absorber. They are kept away from the water tunnel and actuating device to minimize the negative influence of vibration.

The experimental setup is diagramed in Figure 1.1(*a*). In the settling chamber, the inner diameter (ID) of the straight section is 130 mm, and its length is 396 mm. Followed that is a contraction section which is 98 mm long and has 41.3 mm diameter at the nozzle to reach 10:1 contraction ratio. The profile of the contraction section is designed in light of Börger's theory (Börger 1975) to avoid flow separation. In the contraction section, the splitter plate contracts at small slope (less than 5°) and forms a sharp tip at the trailing edge. To improve the quality of inlet flow, four pairs of screens are placed equidistantly in the straight section with a pair of honeycomb between the 3rd and 4th pair of the screens. The mixing chamber (an acrylic pipe with ID of 41.3 mm) is connected to the settling chamber at the nozzle with a flange. At the end of mixing chamber, an optical vessel is mounted for flow visualization.

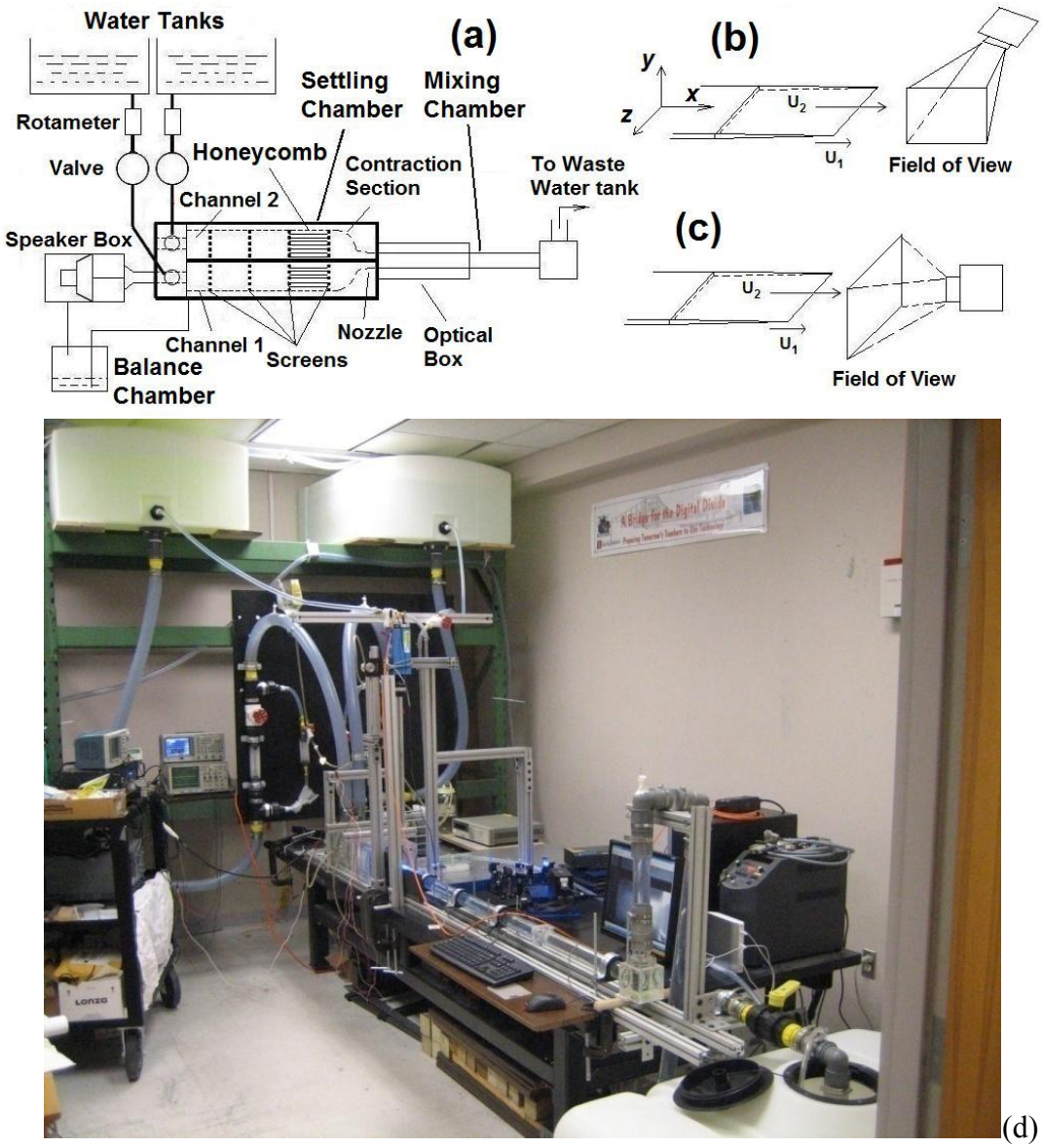

(d)

Figure 1.1 (a) Experimental setup, coordinates of field of (b) side view, (c) cross view and (d) overview of the system

The forcing system is constituted of a subwoofer (a kind of speaker which is designed for low frequency application), rigid plastic plate with rubber membrane, laser displacement sensor (Keyence LB-12/LB-72), power amplifier (Pyle Pro PTA1000) and function generator (Tektronix AFG3102). The former three parts are sealed into a speaker box which is connected directly to the low-speed side of the settling chamber. The round

rigid plastic plate is driven directly by the subwoofer, sealed by the rubber membrane and works as a piston. To reduce the drag due to the pressure difference between speaker box and settling chamber, a balance vessel is applied. The inherent frequency of driven unit is about 45 Hz. It is far from the optimal frequency in our research and won't affect the experimental results.

1.2.2 Visualization by Laser Induced Fluorescence (LIF)

Flow visualization is carried out by laser induced fluorescence. The fluorescent dye is Fluorescein Sodium Salt. It absorbs 473 nm blue light (from 75mW laser) and emits green light around 520 nm. The images are recorded by Cooke's SensiCam QE high performance camera. For wider field of view, Nikon Micro Nikkor 35 mm lens is adopted. A green light band-pass filter is mounted between the camera and lens to improve the signal-noise ratio (SNR) of images. The coordinate system and the field of view (FOV) for flow visualization are plotted in Figure 1.1(b).

1.2.3 Velocity measurement by Particle Imaging Velocimetry

A 2-dimensional PIV system is utilized in this research, which is constituted with a PCO Cooke Sensicam QE camera, NewWave Solo III laser and Davis 7 software. To reduce the image distortion from side view, one optical box is attached on the mixing chamber and filled with water. And another box is mounted directly at the end of mixing chamber for the image correction in cross section. Before carrying on the measurement,

standard calibration procedure of Davis 7 is adopted to further lower the error of velocity calculation.

1.2.4 Notes on experimental procedures

Before starting experiments, the water in the two tanks are fully stirred to eliminate any possible influence of temperature difference between the two flow streams. This process can also reduce the possibility of generation of air bubbles dissolved in water.

While doing the experiments, the flow rate will be adjusted every several minutes to correct any possible error due to the change of the water level within the tanks.

1.2.5 Generally used definitions of parameters

Table 1.1 The definitions of physical quantities in chapter 1.

local temporally averaged velocity	*U: x* direction *V: y* direction *W: z* direction
temporal velocity fluctuations	*u′: x* direction *v′: y* direction *w′: z* direction
Instant velocity	u=U+u': x direction v=V+v': y direction w=W+w': z direction
local temporally averaged vorticity	Ω_x*: x* direction Ω_y*: y* direction
temporal vorticity fluctuations	ω_x*′: x* direction ω_y ': y direction
Instant vorticity	$\omega_x = \Omega_x + \omega_x$': x direction $\omega_y = \Omega_y + \omega_y$': y direction
Bulk flow velocity in mixing chamber	<U>, $\sim (U_L + U_H)/2$

Bulk flow velocity in nozzle section	U_L U_H For subscript: *L:* low speed side, i.e. stream 1 in this research. *H:* high speed side, i.e. stream 2 in this research.
Velocity ratio	$\lambda=(U_H-U_L)/(U_H+U_L)$
Diameter of pipe	D
Kinetic viscosity	ν
Reynolds number	Re=<U>D/ν
Absolute forcing intensity	$A_f = A_p f_f$
Amplitude of the vibration plate	A_p
Forcing frequency	f_f
Relative forcing intensity	$A_{fL} = \frac{\sqrt{\widetilde{u'^2}}}{U_L} = \frac{\sqrt{2}A_f}{U_L}\frac{S_p}{S_L}$ $A_{fH} = \frac{\sqrt{\widetilde{u'^2}}}{U_H} = \frac{\sqrt{2}A_f}{U_H}\frac{S_p}{S_H}$ $A_{fm} = \frac{\sqrt{\widetilde{u'^2}}}{\langle U\rangle} = \frac{\sqrt{2}A_f}{\langle U\rangle}\frac{S_p}{S_m}$
Local area	SL: the area of nozzle on low speed side SH: the area of nozzle on high speed side Sm: the area of mixing chamber Sp: the area of vibration plate

For example, if the flow rate of low speed size is 0.5 GPM (gallons per minute) and that of high speed size is 1 GPM, the Re is about 2939, approximately 3000. And the velocity ratio is 1/3. If both of the streams have flow rate of 0.75 GPM, Re is still 2939, but λ is 0.

1.3 Basic flow dynamics and universal law of natural frequency

1.3.1 Basic flow visualization and velocity fields

The flow visualization of unforced mixing layer is plotted in Figure 1.2. It can be seen, the typical Kelvin-Helmholtz (K-H) instability induced vortex structures are easily found.

So, intuitively, in this confined mixing layer, the instability mechanism has no apparently difference from conventional free mixing layer.

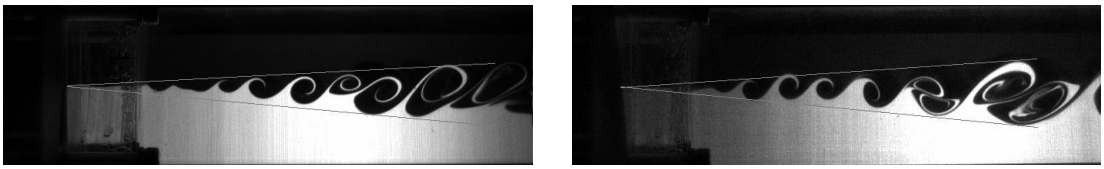

(a) (b)

Figure 1.2 Visualization of unforced flow at Re=2939, λ=1/3. (a) The length of mixing chamber is L=0.25 m and (b) L=1.753 m.

The mean velocity distributions (normalized by U) at *Re*=2939 and λ=1/3 are plotted in Figure 1.3.

According to the development of wall boundary layer on splitter plate, the influence of its wake spread to almost x^*=0.85 (in this paper, $x^*=x/D$, $y^*=y/D$, $z^*=z/D$). After that, as shown in Figure 1.3(a), the streamwise velocity U in the central plane exhibits a typical "tanh-shaped" profile similar as in free shear layer. To compare with conventional free mixing layer, the momentum thickness of mixing layer is investigated, which is:

$$\theta_m = \int_{y_0}^{y_1} \frac{U-U_L}{U_H-U_L}\left(1-\frac{U-U_L}{U_H-U_L}\right) dy \tag{1.1}$$

where $y_\alpha = y[U = U_L + \alpha(U_H - U_L)]$, hence, $y_0 = y(U = U_L)$ and $y_1 = y(U = U_H)$. The variation of θ_m along x direction is plotted in Figure 1.3(c). In the field of interest (FOI, marked by the window with gray dashed line in Figure 1.6 and Figure 1.8), the local momentum thickness Reynolds number $Re_\theta = (U_H - U_L)\theta_m/\nu$ varies with streamwise positions from 21 to 81. If in free mixing layer, this belongs to the laminar and transition region (Winant and Browand 1974; Ho and Huerre 1984). However, in confined mixing

layer, the flow seems more "stable". Through a power fitting, the scaling exponent is found to be about 0.5 (θ_m~$x^{0.5}$), which is consistent with the researches by Winant and Browand and Ho and Huerre in laminar (or pre-transition) region of unforced free mixing layer. Flow visualization in Figure 1.6(a) also verifies the laminar character in the FOI even at Re_θ = 81.

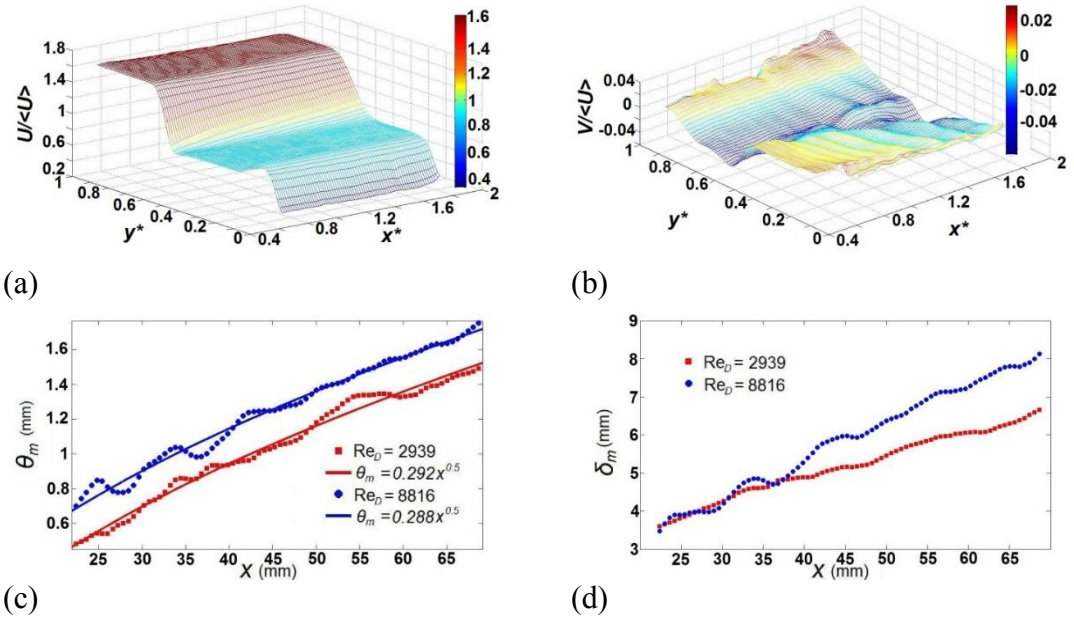

(a) (b)

(c) (d)

Figure 1.3. (a) The distribution of U in unforced mixing layer, Re=2939, λ=1/3, (*b*) The distribution of V in unforced mixing layer, Re=2939, λ=1/3, (*c*) Momentum thickness of unforced mixing layer vs *x*, fitted by power-distribution curves, where λ=1/3. (*d*) The width of mixing layer vs *x*, where λ=1/3.

Similar conclusions are also found when increasing Re to 8816 and keeping λ=1/3 Figure 1.3(c). In the FOI, Re_θ varies from 97 to 251 which apparently set down into the turbulent region. However, from Figure 1.3(c), the scaling behavior of momentum thickness (θ_m~$x^{0.5}$) indicates the flow is still laminar, only except at the downstream end of FOI where transition begins as shown in Figure 1.8(a). Thus, the transient is obviously postponed compared with free mixing layer.

In the FOI, the averaged $d\theta_m/dx$ in this region is 0.022 for Re=2939 and 0.023 for Re=8816 respectively. Both of them are two times larger than that in free mixing layer investigated by Winant et al (1974) and even comparable with the value in forced free mixing layer (Ho and Huang 1982; Oster and Wygnanski 1982; Roberts 1985; Weisbrot and Wygnanski 1988). As the slope of spreading momentum thickness is proportional to velocity ratio, at the equivalent Re, a higher $d\theta_m/dx$ is achieved even under a smaller velocity ratio compared to Winant et al's work (1974). This is really surprising. The higher $d\theta_m/dx$ means a higher rate of momentum loss. It may be attributed to the relatively high area-to-volume ratio of the channel. As known, in laminar pipe flow with same bulk velocity, due to the viscosity, the rate of momentum loss in unit length can be estimated as:

$$dM/dt = -8\upsilon\pi\langle U\rangle \tag{1.2}$$

which is of the order $O(D^0)$. But the total momentum of flow is $M = \pi D^2\langle U\rangle/4$ which is at the order of $O(D^2)$. Hence the relative rate of momentum loss, Π, defined as:

$$\Pi = \frac{1}{M}\frac{dM}{dt} \tag{1.3}$$

should be proportional to D^{-2}. This indicates, under the same bulk flow velocity, the smaller the scale of cross section, the faster the momentum loss is. That's maybe why in confined mixing layer, the momentum thickness has larger value. The rapid loss of momentum is also the result of secondary flow and its vortex structures near side wall. This will be detailed discussed later. The width of mixing layer δ_m ($=y_{0.95}-y_{0.1}$, by Liepmann & Laufer (Liepmánn, 1947 #168)) under both Reynolds numbers is plotted in Figure 1.3(*d*). As the width of mixng layer is not an universal quantity, it is just for reference here.

1.3.2 Natural frequency

As in free mixing layer, the natural frequency (estimated by vortex passage frequency) of K-H instability is proportional to $<U>^{3/2}$. Here, the vortex passage frequency (λ=1/3) at Re~1200, 3000, 6000 and 9000 are investigated and compared with $<U>^{3/2}$ law, as shown in Figure 1.4. It can be seen, in confined mixing layer, the experimental natural frequency approximately fits the 3/2 law. This means in this confined shear layer with circular transverse mixing chamber, K-H instability is still the most important instability mechanism for mean flow. Besides, with different length of mixing chamber, the difference of frequency is neglectable, as shown in Figure 1.4(a) and (b). The shortened mixing chamber will not affect the character of basic flow by introducing more disturbances from downstream. This is consistent with K-H instability which is convective instability, not absolute instability.

All these founds mean that there is no other instability mechanism which may introduce un-expected self-sustain frequency in this flow field. The parametric investigations in section 1.5 on the effect of 1-D acoustic resonance have the same basic flow.

1.3.3 Short discussion

From above investigations, we can see, the instability of flow in free mixing layer and confined mixing layer has no intrinsic difference. The fast mixing in confined mixing layer

is unique which indicates the specialty of velocity field in forced confined mixing layer. This will be investigated in details in the following sections.

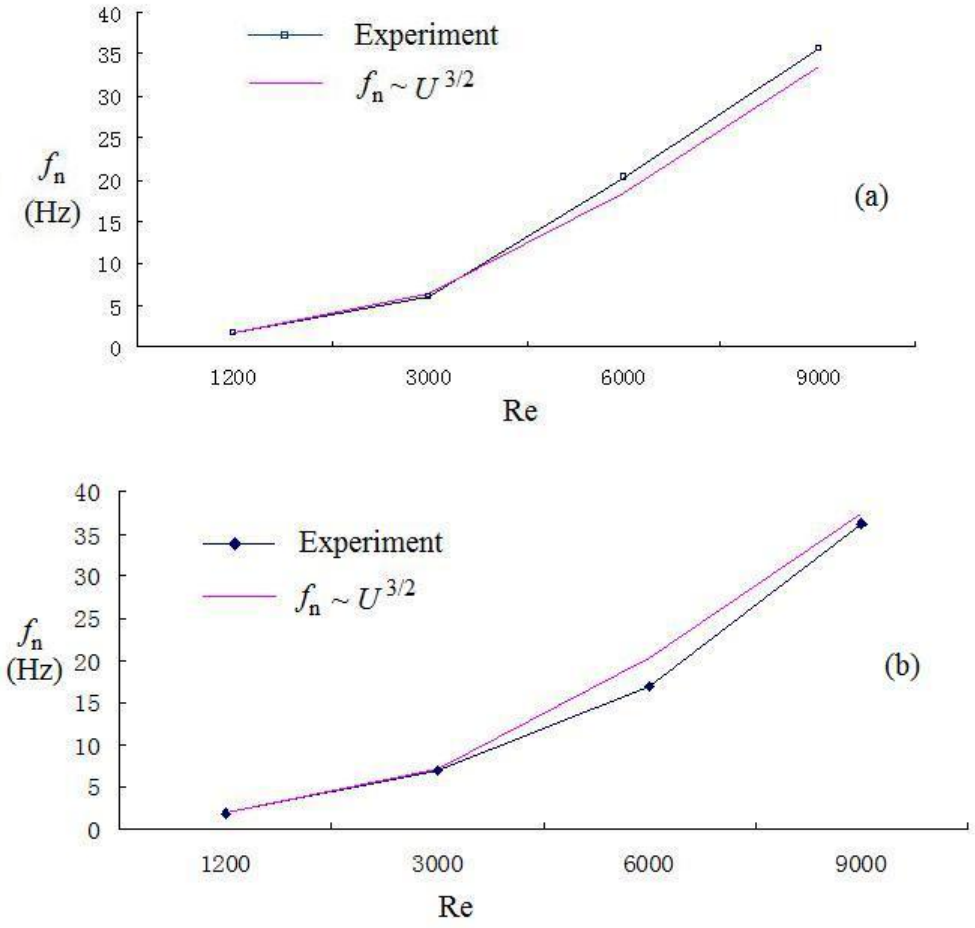

Figure 1.4 The experimental natural frequency (λ=1/3) vs 3/2 law in free shear layer. (a) mixing chamber of 0.25 m long. (b) mixing chamber of 1.753 m long.

1.4 Mixing enhancement mechanisms

In this research, there are two important questions: (1) Why the mixing can be so fast? Or what is the character of flow that causes the fast mixing? (2) Why is optimal frequency is around 5-6 Hz without changing with Reynolds number and shear ratio? What mechanism causes the fixed optimal frequency. In this section, we will try to give a clear

explanation on the first question, by elucidating the velocity and vorticity fields, and the evolution of kinetic energy.

1.4.1 Visualization of phenomenon

The flow structures under different forcing frequencies and intensities are investigated. When the forcing intensity is low and A_{fm}=5.6%, as shown in Figure 1.5, the enhancement is almost the same as in free mixing layer. When Re=2939, the vortex passage frequency is around 7 Hz. At 3.5 Hz, as shown in Figure 1.5(b), the flow indicates a typical subharmonic mode with vortex pairing interaction (Ho and Huang 1982; Ho and Huerre 1984). The vortex passage frequency at this forcing frequency is approximately half of the unforced cases. The spreading rate at 3.5 Hz is apparently larger than at other frequencies, including 5.3 Hz (Figure 1.5(c)). Hence, at low forcing frequency, the subharmonic mechanism which is dominant on mixing enhancement in free mixing layer is still important in the confined mixing layer.

However, while the forcing intensity A_{fm} keeps increasing to 21.9% (A_f=2.37 mmHz), the mixing under similar frequencies exhibit totally different effects, as shown in Figure 1.6. At 3.5 Hz (Figure 1.6(b)), the familiar subharmonic mode and vortex pairing interaction disappears. Instead is the large clockwise rotating vortices with large spreading rate initially. After fast developing after the trailing edge, kinder of nonlinear saturation emerges and the sustained downstream vortex exhibits neglectable spreading rate, as marked by the gray lines. The mixing enhancement at this frequency is limited. Forcing at 7.8 Hz, which is close to the natural frequency of basic flow, indicates similar evolution of

spreading rate as 3.5 Hz, i.e. a large initial value with small sustained value, as shown in Figure 1.6(d). The only difference is the structure of vortices. At 7.8 Hz, a more complicated vortex structure is generated right after the trailing edge. From the visualization, two frequencies can be estimated. One is still the natural frequency close to 7.8 Hz, for the clockwise rotating vortices. Another one is about 15 Hz, which is nearly double of the natural frequency and shown as the small but counter-rotation vortices (CRV). At 20 Hz (Figure 1.6(e)), there is no apparent difference from the unforced flow and mixing enhancement is negligible.

While at 5.3 Hz and A_{fm}=21.9%, we can see a big difference from visualization at other frequencies. As plotted by Figure 1.6(c), at this frequency, a large initial spreading rate due to the fast development of initially shedding vortex is formed adjacent to trailing edge. Later, different compared to at 3.5 Hz and 7.8 Hz, there is still a relatively larger sustained spreading rate at 5.3 Hz. The shedding vortex is also counter-rotation and more unstable compared to at other frequencies. The vortex structures become broken up and form small-scale structures much earlier than other cases. A much better mixing effect can be achieved at this frequency.

When Re=2939, the natural frequency of vortex passage is about 7 Hz. Both 3.5 Hz and 5.3 Hz are located in the frequency range that subharmonic exciting mechanism works. To make sure the mixing enhancement at 5.3 Hz is not due to the subharmonic exciting mechanism, flow visualization at Re =8816 and λ=0.33 is conducted as shown in Figure 1.8. In this case, the natural frequency of vortex passage is about 36.8Hz. The absolute forcing intensity A_f is also 2.37 mm Hz. It can be easily found no matter under the fourth-subharmonic (Fig. 5(*c*)), second subharmonic (Fig. 5(*d*)) or the harmonic mode (Fig. 5(*e*)),

the mixing is much weaker than that at 5.3 Hz (Fig. 5(*b*)). 5.3 Hz is still the optimal frequency and doesn't vary with Reynolds number. The subharmonic exciting mechanism can be ignored. This is consistent with Wang's works (which is 6 Hz in his works) (Wang 2003; Wang 2006).

Keep increasing the forcing intensity to around 100%, an extremely fast mixing can be found at 5.3 Hz, as shown in Figure 1.7(a). A uniform mixing is almost immediately achieved at the entrance of mixing chamber. The spreading rate is 180º. This is really astonishing. At the same forcing intensity, at 7 Hz (Figure 1.7(b)), the mixing effect is much weaker than that at 5.3 Hz. And at 10 Hz (Figure 1.7(c)), the mixing enhancement is also negligible. The weak mixing could be due to two reasons: one is the weak receptivity; the other is due to some unknown dynamic process downstream. This will be discussed in details in next two sections.

Compared to the weakly forced flow when A_{fm}=5.6%, where at 7 Hz and 10 Hz, the vortex passage frequency is same as natural frequency of basic flow, at this strong forcing intensity, the vortex passage frequencies are same as the forcing frequencies, not the natural frequency any more. At this case, the frequencies that are smaller than 5.3 Hz, such as 3.5 Hz, cannot achieve this high forcing intensity, due to the travel distance of forcing plate. But, this will not affect our judgment that 5.3 Hz is the optimal frequency.

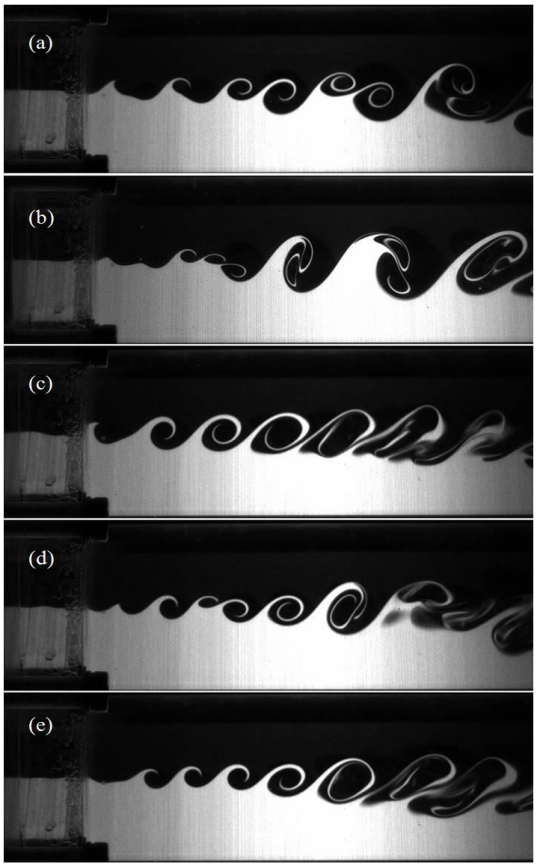

Figure 1.5. Re=2939, λ=1/3, A_{fm}=5.6% (a) unforced, (b) 3.5 Hz, (c) 5.3 Hz, (d) 8 Hz, (e) 20 Hz.

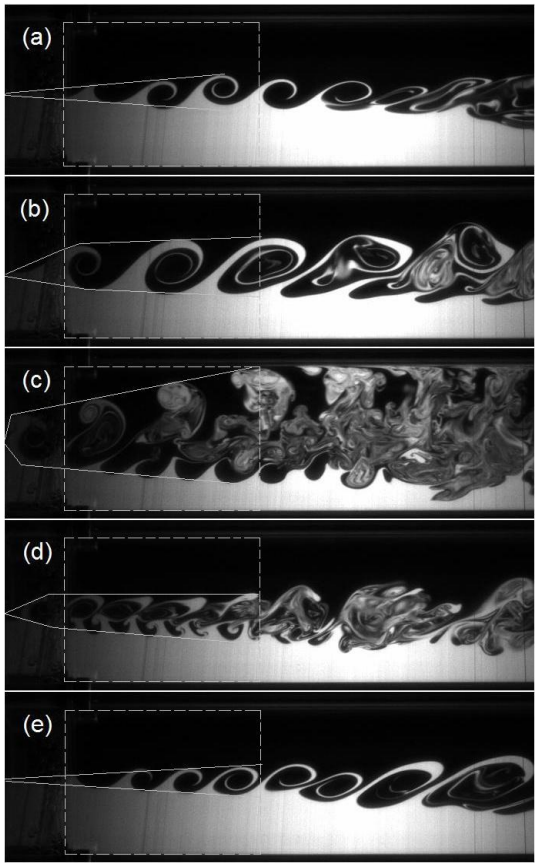

Figure 1.6. Re=2939, λ=1/3, A_{fm}=21.9% (a) unforced, (b) 3.5 Hz, (c) 5.3 Hz, (d) 7.8 Hz, (e) 20 Hz.

Hence, the mixing enhancement can be separated into two stages, depends on the forcing intensity. For small forcing intensity, the mixing enhancement can be effectively achieved by subharmonic modes, which is similar as in free mixing layer. But at large forcing intensity, the flow is attenuated by the external forcing. And the largest mixing enhancement is achieved only around 5.3 Hz.

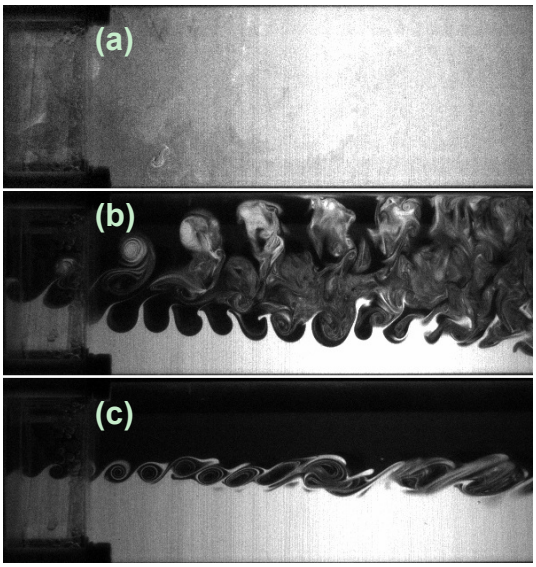

Figure 1.7. Re=2939, λ=1/3, A_{fm}~100%, (a) 5.3 Hz, (b) 7 Hz, (c) 10 Hz.

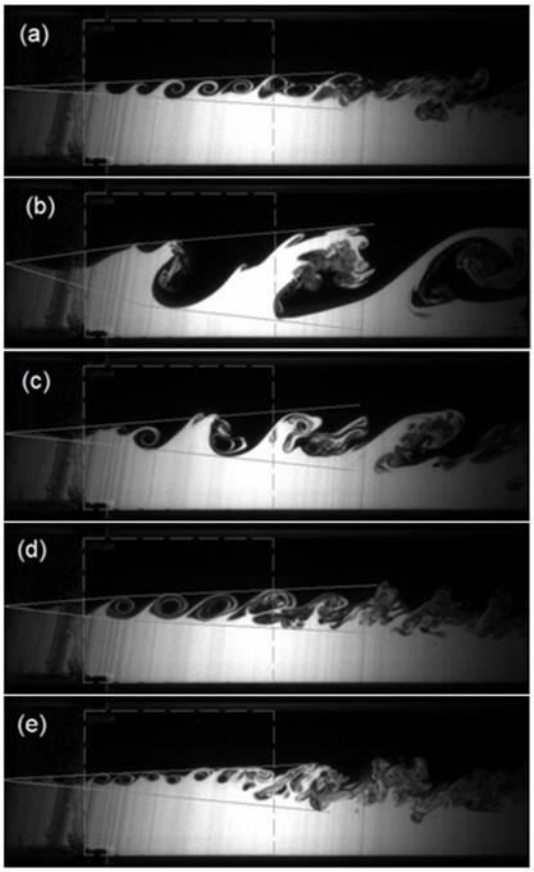

Figure 1.8 Flow visualization by LIF at Re=8813 and λ=1/3. The A_f here is same as used in Figure 1.6, i.e. A_f=2.37 mmHz. (a) no forcing, (b) 5.3 Hz, (c) 9.2 Hz, (d) 18.4 Hz, (e) 36.8 Hz.

1.4.2 Fluid dynamics and energy evolution

As our purpose in this section is finding out what is the characteristic flow structures of forced flow, especially at 5.3 Hz. At high forcing intensity, the development of flow structures is too fast to be captured. Hence, all the researches on fluid dynamic process are constrained to low or moderate forcing intensities, i.e. A_{fm}≤21.9%.

1.4.2.1 Mean velocity field

The distribution of mean velocity U and V under 5 different forcing frequencies at A_{fm}=21.9% (equivalent to A_{fL}= 65.8%) are shown in Figure 1.9 and Figure 1.10, respectively. At 3.5 Hz, the U profile is still kinder of "tanh" type as shown in Figure 1.9 (*b*). The only difference relative to the unforced case is the much wider mixing layer. However, at 5.3 Hz, (Figure 1.9 (*c*)), apparent extrusions appear in the U profile at the edge relative to the unforced mixing layer. At x^*=0.66, there is only one peaks and 2 inflexions in the region of mixing layer (i.e. regardless of the wall boundary layer). While x^* increases to 1.67, the inflexions increase to 4. The profile becomes wavier and more unstable waves with different frequency components might be generated and developed downstream due to local K-H instability. The profile of U under 7.8 Hz is similar as the case of 5.3 Hz, but recovers earlier at downstream, as shown in Figure 1.9 (*d*). When the frequency increases to 20 Hz (Figure 1.9(e)), even highly excited, no noticeable difference of U profile from the unforced flow (Figure 1.9(a)) can be found, which is consistent with the flow visualization shown in Figure 1.6(e).

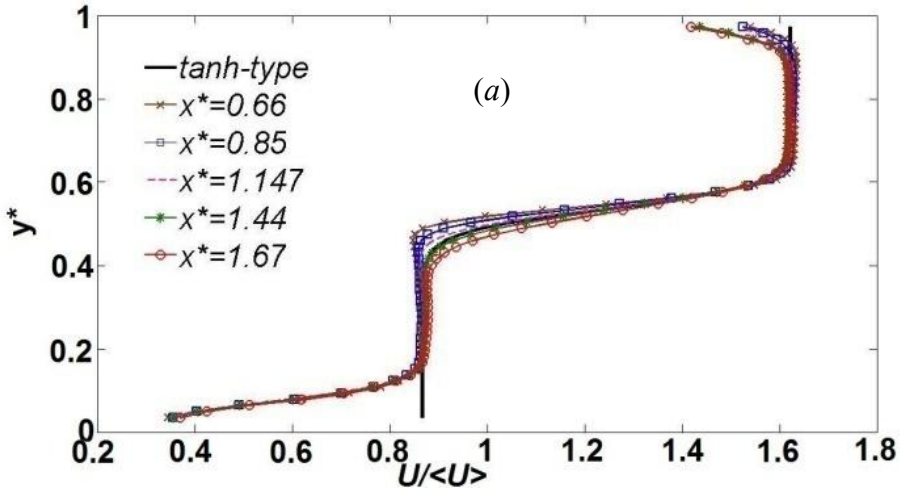

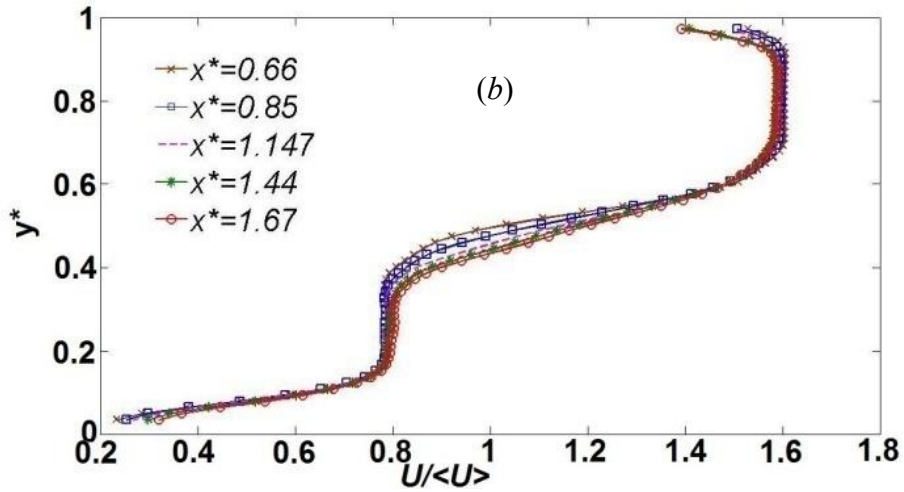
(b)
x*=0.66
x*=0.85
x*=1.147
x*=1.44
x*=1.67
y*
U/<U>

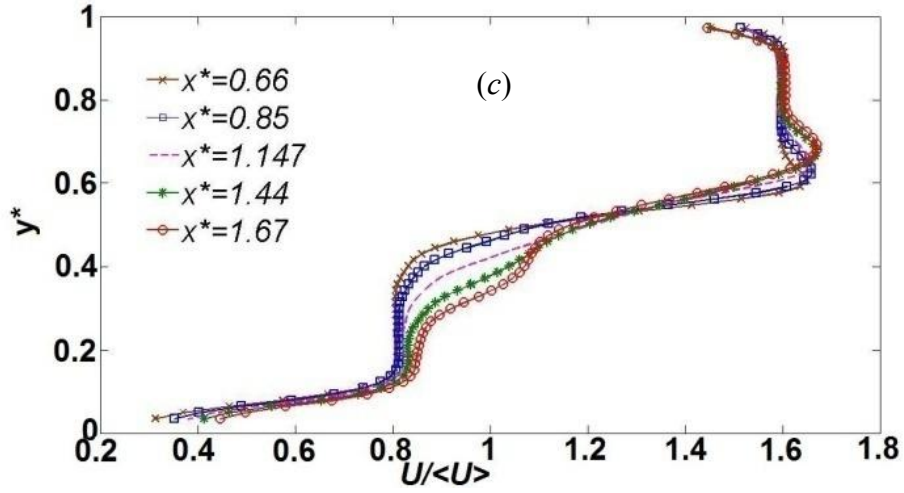
(c)
x*=0.66
x*=0.85
x*=1.147
x*=1.44
x*=1.67
y*
U/<U>

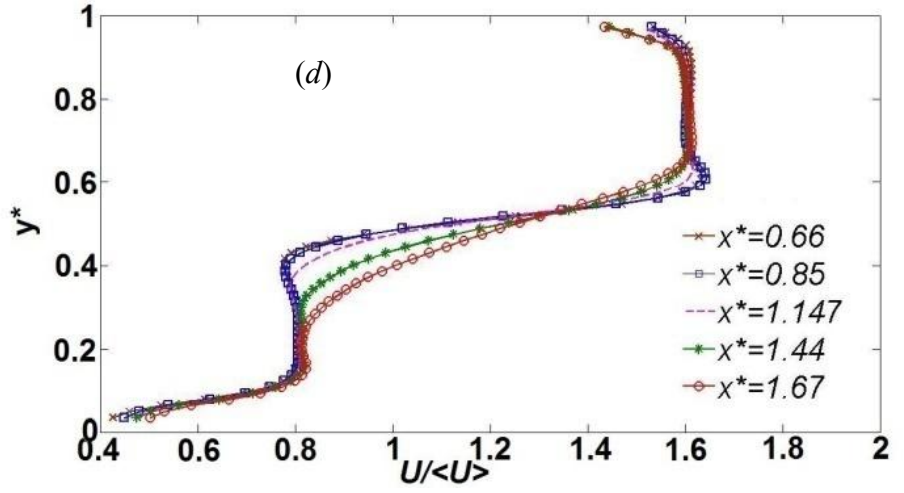
(d)
x*=0.66
x*=0.85
x*=1.147
x*=1.44
x*=1.67
y*
U/<U>

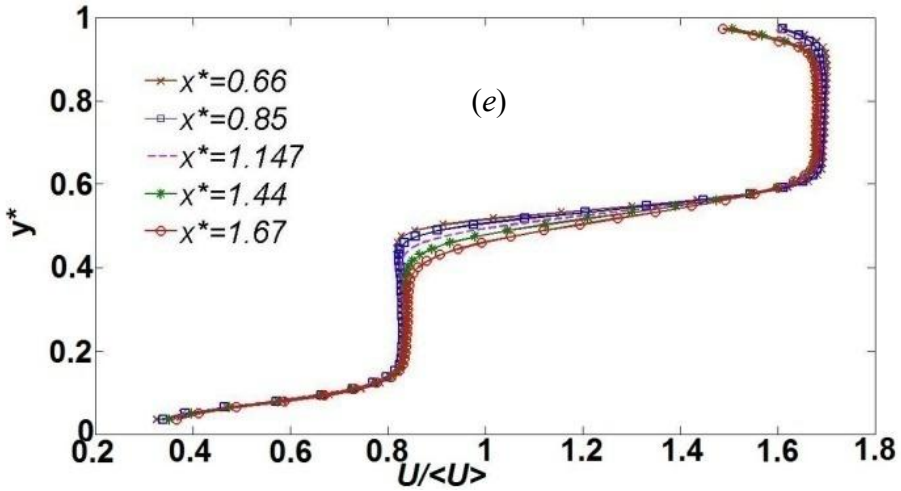

Figure 1.9 U profile at 5 streamwise positions under A_{fm}=21.9%: (a) No forcing, (b) f_f=3.5Hz, (c) f_f=5.3Hz, (d) f_f=7.8Hz, (e) f_f=20Hz.

The V profile is plotted in Figure 1.10. In the unforced case, the flow is approximately 2-dimentional due to the tiny magnitude of V (Figure 1.10 (a)). While under lower frequencies especially at 3.5, 5.3 and 7.8 Hz, the V profile exhibits apparent response and cardiogram style curves are found at the vertical center, as shown in Figure 1.10 (*b*, *c*, *d*). At 5.3 Hz, no matter the positive or negative peaks of V is the highest in the considered frequency range. As the distance from trailing edge increases, the V becomes more negative. The positions of the positive and negative peaks move upward and downward separately. The peak magnitude of V profile descends very quickly. At 20 Hz, its peak value is of the same level as the unforced flow, with similar topological structures (Figure 1.10 (*d*)).

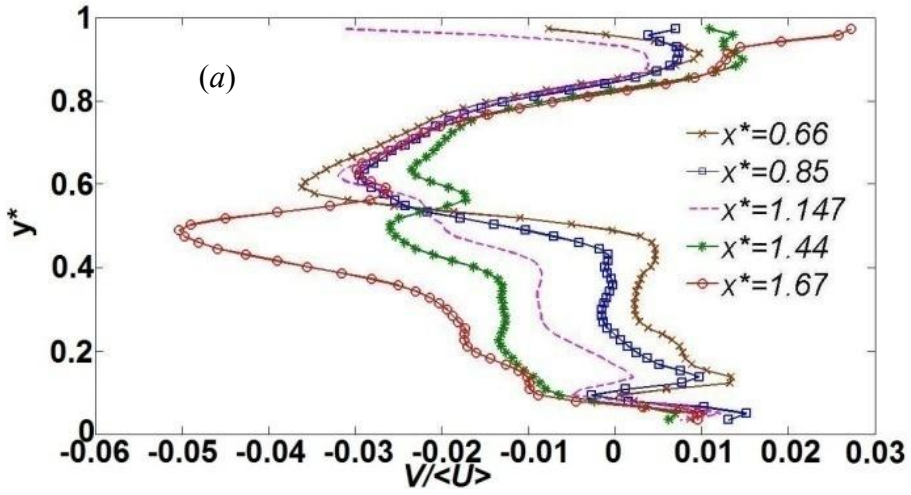
(a)
x*=0.66
x*=0.85
x*=1.147
x*=1.44
x*=1.67
y*
V/<U>

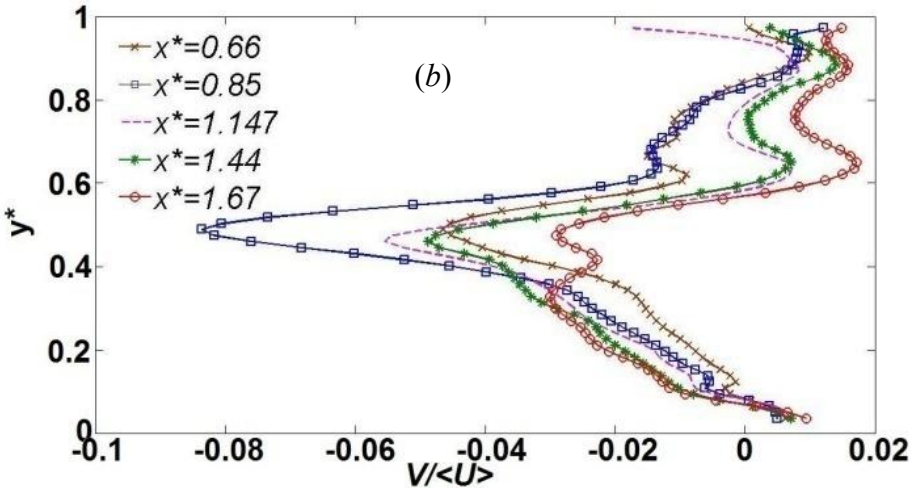
(b)
x*=0.66
x*=0.85
x*=1.147
x*=1.44
x*=1.67
y*
V/<U>

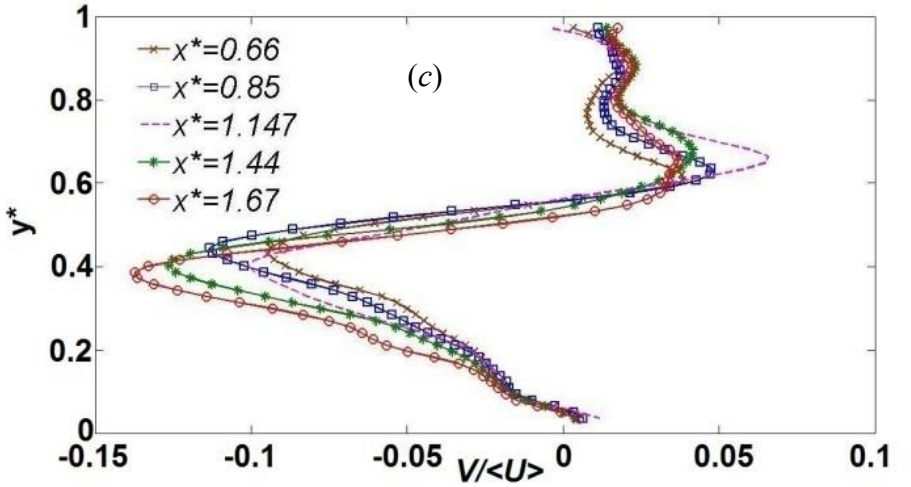
(c)
x*=0.66
x*=0.85
x*=1.147
x*=1.44
x*=1.67
y*
V/<U>

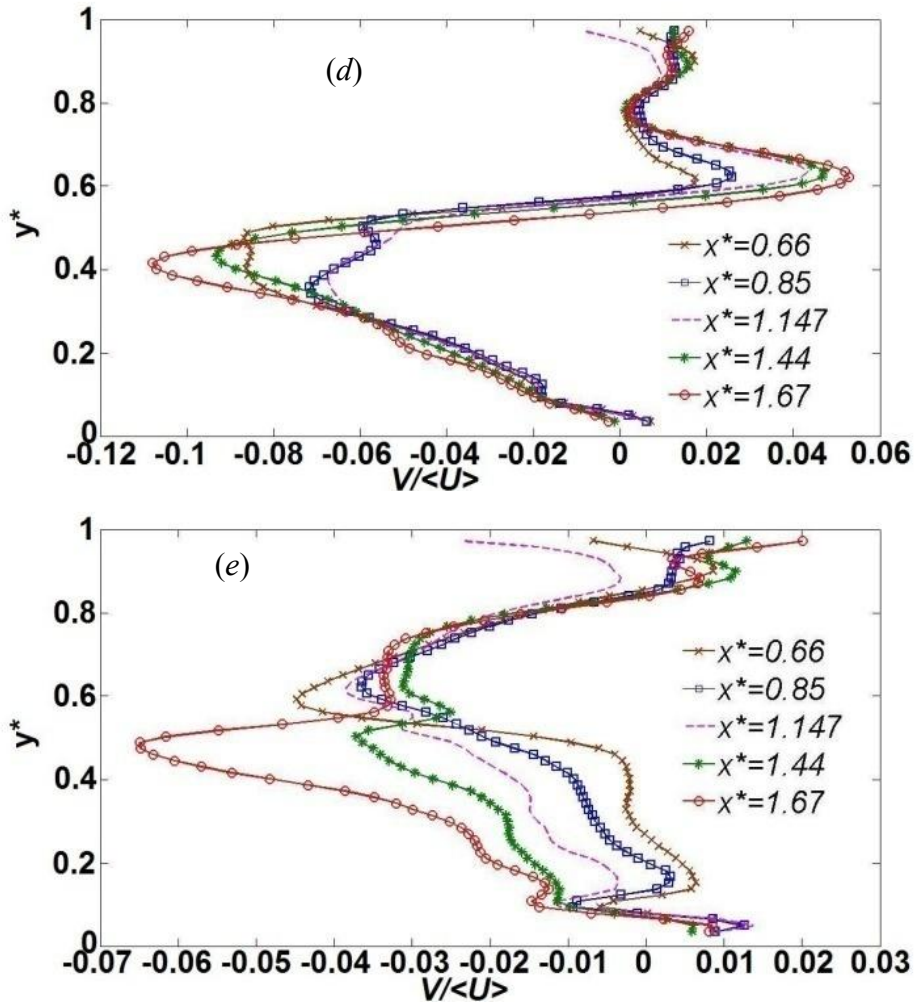

Figure 1.10 V profile at 5 streamwise positions under Afm=21.9%: (a) No forcing, (b) ff=3.5Hz, (c) ff =5.3Hz, (d) ff =7.8Hz, (e) ff =20Hz.

The highly asymmetric V distribution and its large magnitude have three major influences. First is expanding the mixing layer and accelerating the momentum transport in vertical direction. This can be clearly found from the streamlines of mean flow in Figure 1.11. At 5.3 Hz (Figure 1.11(c)), the spreading rate of streamline is much higher than any other frequencies. So does the spreading of mixing layer. Detailed discussion will be carried on in section 1.4.2.6. The second influence is the highly stretching on instant vortex structures. The stretch will cause the large scale vortex more unstable and break earlier

which can further accelerate the mixing process. The third one is on turbulent energy evolution. This will be detailed introduced in section 1.4.2.5.

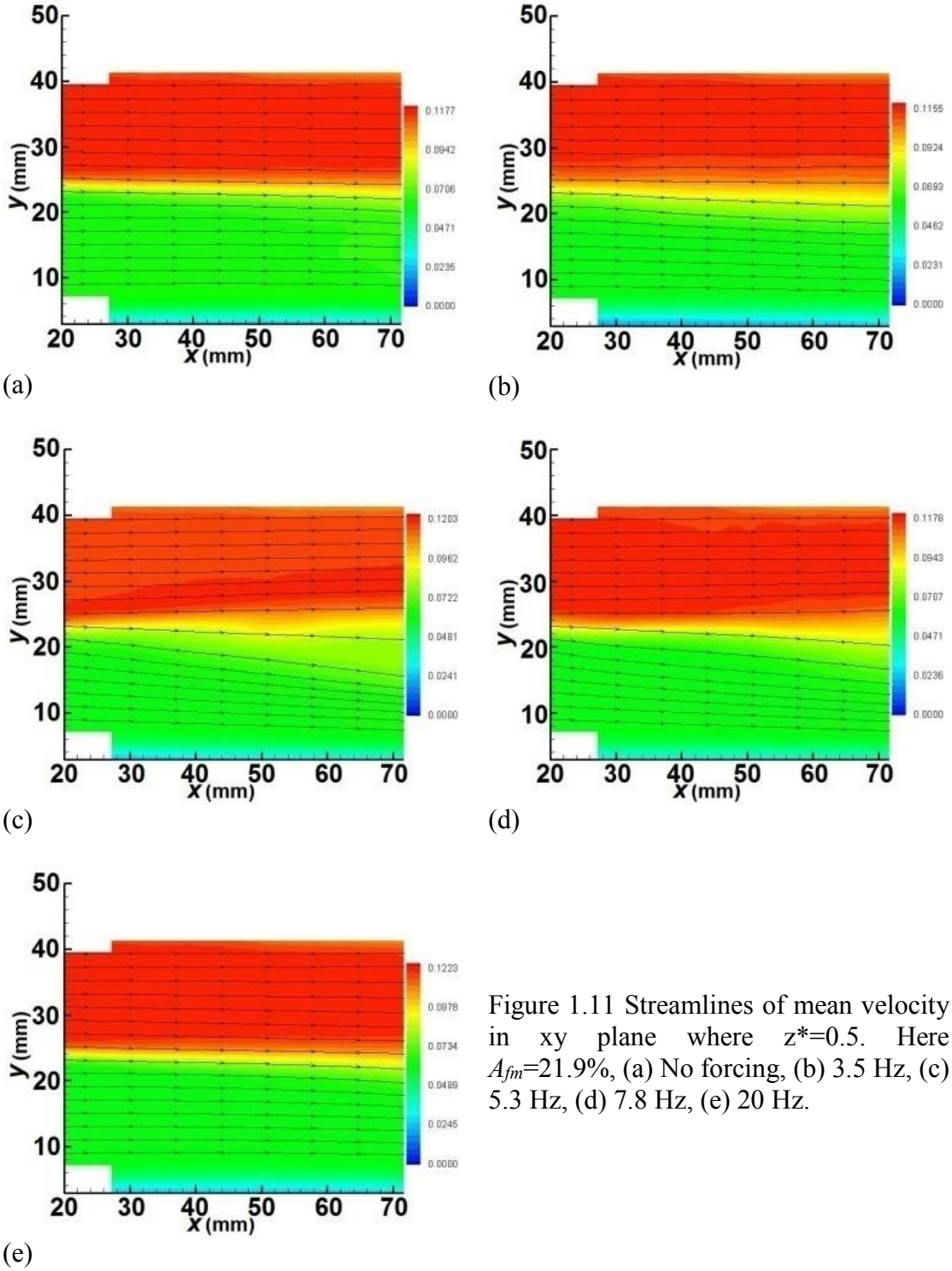

Figure 1.11 Streamlines of mean velocity in xy plane where z*=0.5. Here A_{fm}=21.9%, (a) No forcing, (b) 3.5 Hz, (c) 5.3 Hz, (d) 7.8 Hz, (e) 20 Hz.

1.4.2.2 The inflow receptivity

The receptivity of inflow is evaluated by the normalized velocity fluctuation, I_L, where:

$$I_L = (u'^2 + v'^2)/U_L \tag{1.4}$$

The experimental results of I_L measured in nozzle section on both low speed and high speed sides are plotted in Figure 1.12(*a*), where Re=2939. Several characters can be found from this figure. First, 5.3 Hz has the highest receptivity at most of the actuating intensities. Around 5.3 Hz, the bandwidth of frequency where exhibits high receptivity is very narrow. Even at 7.8 Hz, the receptivity falls apparently. At 20 Hz, the receptivity is no more than 1/4 of the value at 5.3 Hz and only 2 times larger than the neutral case (i.e. in unforced flow). Second, the receptivity in the flow of high-speed side is higher than that in low-speed side, especially at 5.3 Hz and 3.5 Hz. This is really astonishing because the forcing is directly imposed on channel 1, i.e. the low-speed side. The receptivity is not weakened by the higher convection velocity in channel 2, but enhanced. Thereafter, we kept the maximum A_f the same as used in Re=2939 and measured at Re=8816 (hence, A_{fL}=21.9%). Similar results were observed as shown in Figure 1.12 (*b*). Not only 5.3Hz has the highest receptivity, but also the higher receptivity locates at high-speed side. The comparison between the low-speed side at Re=8816 and high-speed side at Re=2939 indicates, even the former has higher convection velocity, at 5.3 Hz, the velocity fluctuation $(u'^2 + v'^2)$ of former is not distinguishably higher than the latter case. Hence, the different receptivity in the two sides is not directly related to the convection velocity, but some other mechanism.

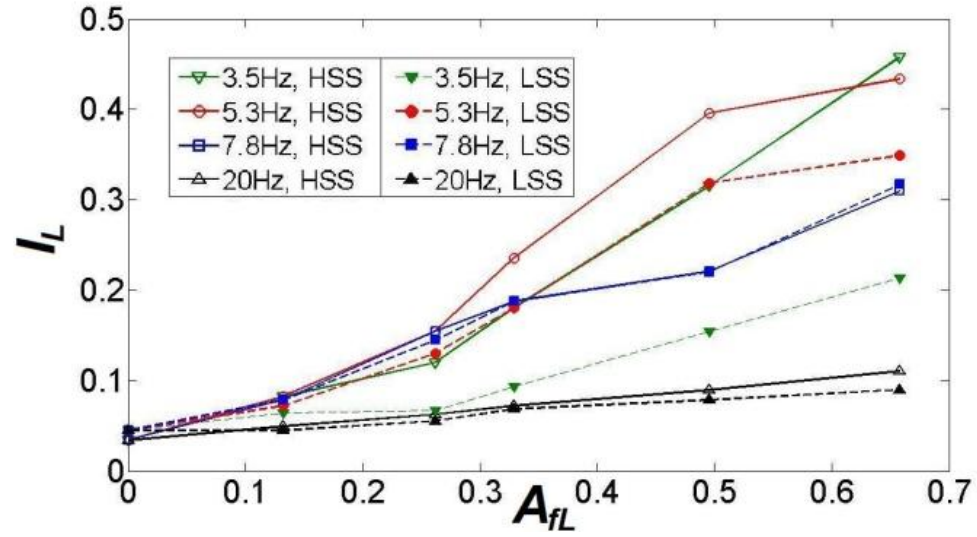

(a)

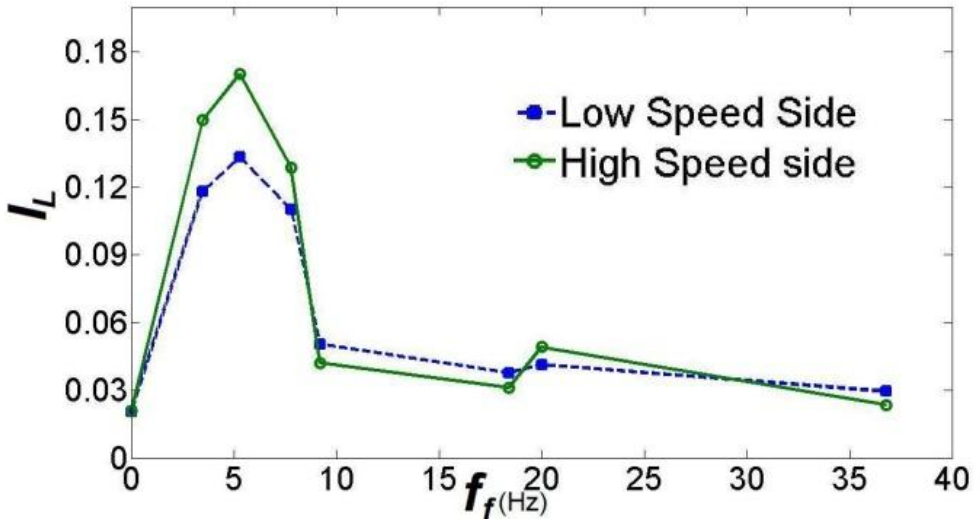

(b)

Figure 1.12 The receptivity of inflow under different actuating frequencies. Here λ=1/3. (a) Re=2939, "HSS" means high speed side flow, "LSS" means low sped side flow, (b) Re=8816, A_{fL}=21.9%.

The mixing effect under forcing at Re=2939 and λ=1/3 is shown in Figure 1.6. Consistent with the receptivity in Figure 1.12(*a*), the optimal frequency of mixing enhancement with largest spreading rate is 5.3 Hz. Under low actuating frequencies, such as 3.5, 5.3 and 7.8 Hz, the spreading of visual mixing layer can be clearly separated into two stages, as marked by the gray lines in Figure 1.6 (*b*, *c*, *d*). In the first stage, an initial

vortex structure is generated adjacent to the trailing edge. The size of the vortex is determined by the actuating frequency and intensity, and finally results in a different initial spreading angle. After the vortex structure is generated, it advects downstream and continues spreading at a smaller angle. This is the second stage. These two stages are apparently due to different mechanisms. In the section about flow dynamics, we focus on the second stage to explain the cause of large sustaining spreading at relatively farther downstream fields. And the possible cause of first stage due to shedding vortex will be introduced in acoustic induced vortex.

In next section, detailed analysis on velocity field is given to take a glance at the outlandish mixing process while forced.

1.4.2.3 The velocity fluctuations in mixing chamber

Side view

The receptivity of inflow is discussed in front. However, this doesn't necessarily mean the velocity fluctuations in mixing chamber will have the same response as in nozzle part. And the distribution of them is very important in describing both momentum and scalar transport. Hence, the downstream evolution of velocity fluctuations will be introduced.

The u' and v' distributions (evaluated by their root-mean-square value) at five different positions are plotted in Figure 1.13 and Figure 1.14 respectively.

In the unforced case (Figure 1.13 (*a*)), no noticeable difference of u'_{rms} distribution is found compared to free mixing layer (only in the region of mixing layer, regardless of boundary layer). Close to the trailing edge, due to the boundary of splitter plate, the influence of wake is apparent which exhibits two peaks in u'_{rms} distribution. After x^*=0.85,

one peak gradually dismissed and the u'_{rms} profile becomes single-peak with increasing peak value. The position of peak is a little bias to high-speed side which is same as in free mixing layer (Wygnanski and Fiedler 1970). The u'_{rms} profile forced at 20 Hz exhibits similar distribution as the unforced case, only differs in the larger peak value and shorter wake region, as shown in Figure 1.13(e). The forced flow under lower frequencies is more complicated. At 3.5 Hz (Figure 1.13 (*b*)), the peak of u'_{rms} increases to almost 22% of $<U>$. The two-peak profile exists in the whole FOI and exhibits total asymmetry. The peak value decreases with x^* first, then increases. The peak values of u'_{rms} at 5.3 Hz are similar as at 3.5 Hz (Figure 1.13 (*c*)). But the distribution is more flexuous and stronger changing of vortex structures can be inferred. When forcing frequency increases to 7.8 Hz (Figure 1.13(d)), the peak value of u'_{rms} decreases drastically with more symmetrical distribution.

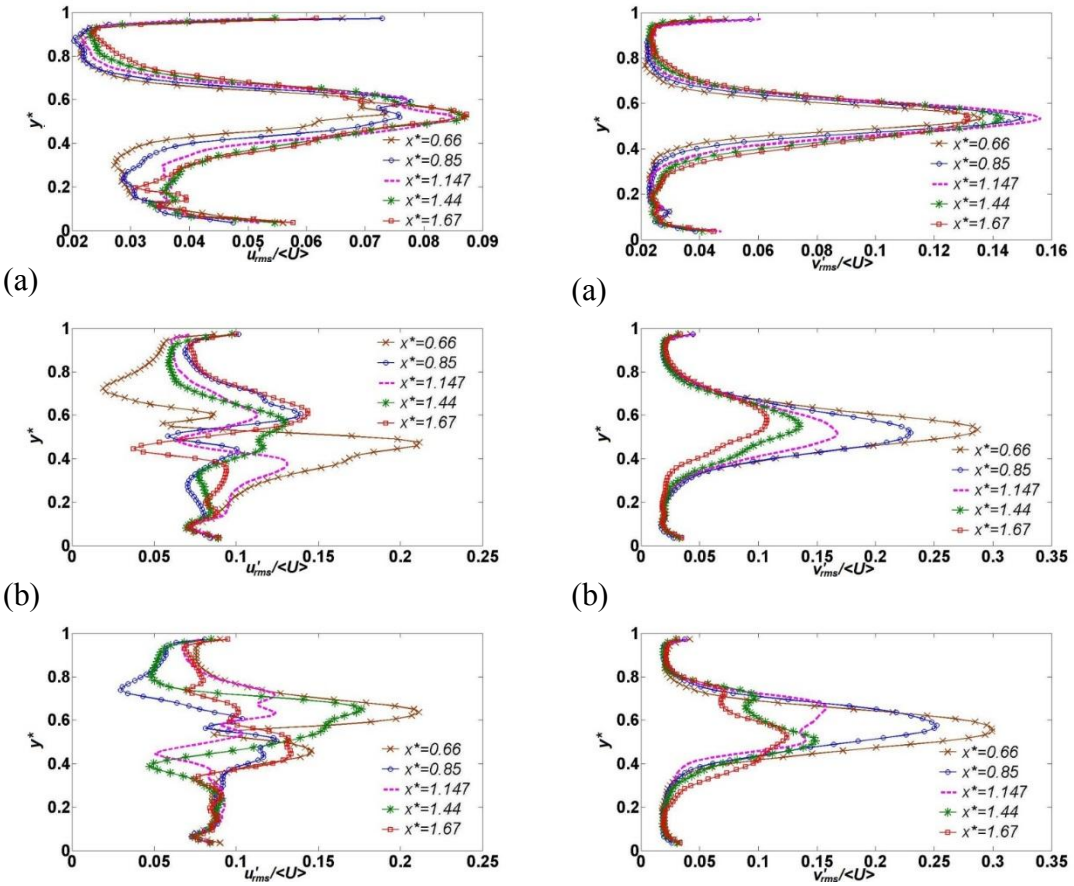

(c)

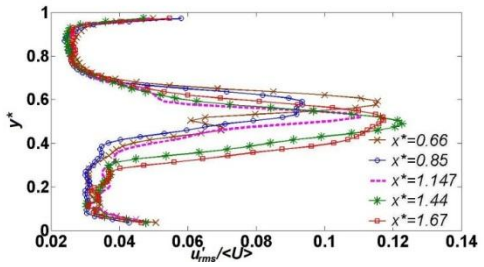

(d)

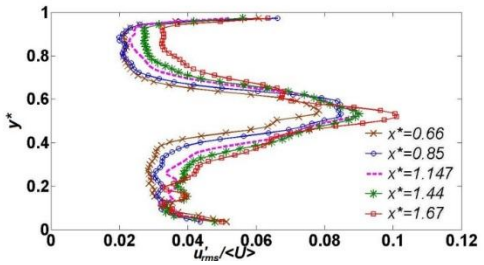

(e)

Figure 1.13 u'_{rms} profile at 5 streamwise positions under A_{fm}=21.9%: (a) No forcing, (b) f_f=3.5 Hz, (c) f_f=5.3 Hz, (d) f_f =7.8 Hz, (e) f_f=20 Hz.

(c)

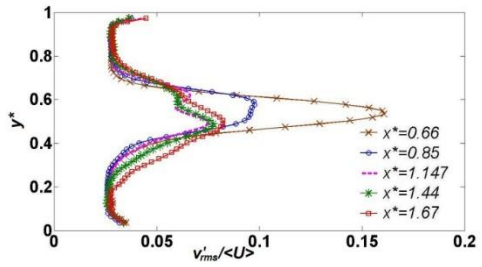

(d)

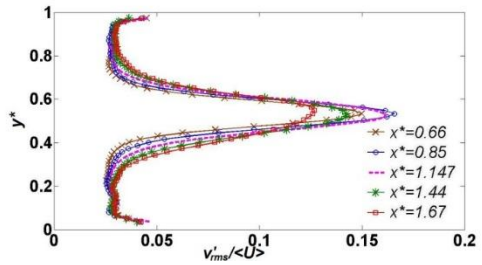

(e)

Figure 1.14 v'_{rms} profile at 5 streamwise positions under A_{fm}=21.9%: (a) No forcing, (b) f_f=3.5 Hz, (c) f_f=5.3 Hz, (d) f_f =7.8 Hz, (e) f_f=20 Hz

Compared with the u'_{rms} profile, the peaks of v'_{rms} profile are higher in each of the five cases. For the unforced flow, the v'_{rms} profile is approximately symmetric with little bias to high-speed side. Its peak value first increases with x^*, then turn over (Figure 1.14(*a*)). This can also be found in Figure 1.14 (*e*) for 20 Hz. But at 3.5, 5.3 and 7.8 Hz, the situation changed. In the FOI, the peaks of v'_{rms} profile decreases with x^* monotonically and rapidly which indicates kinder of short-range influence. At 3.5Hz, the v'_{rms}profile becomes asymmetric and bias towards high-speed flow (Figure 1.14 (*b*)). However, it's still single-peaked. While at 5.3Hz, especially at larger x^*, the profile becomes two-peaked, as shown in Figure 1.14(c). This can't be due to any single 2-dimensional vortex structures. Hence, we believe there should be either vortex separation happens or 3-dimensional

vortices exist in the region. Figure 1.14 (*d*) is for 7.8 Hz as reference. Although very weak, the similar two-peak profiles can also be found.

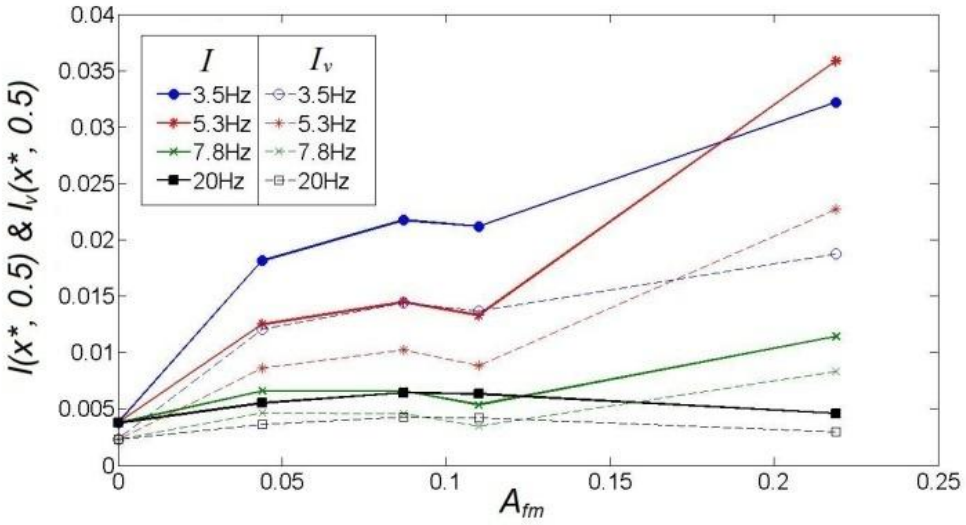

(a)

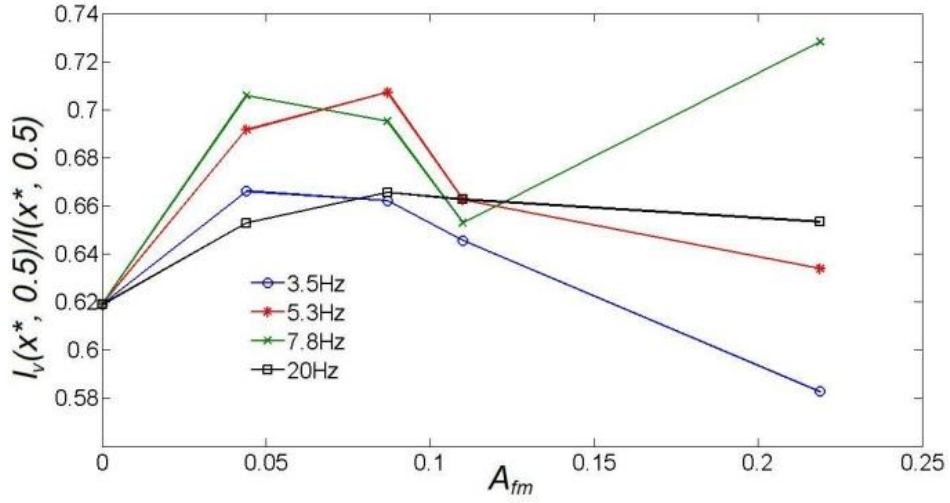

(b)

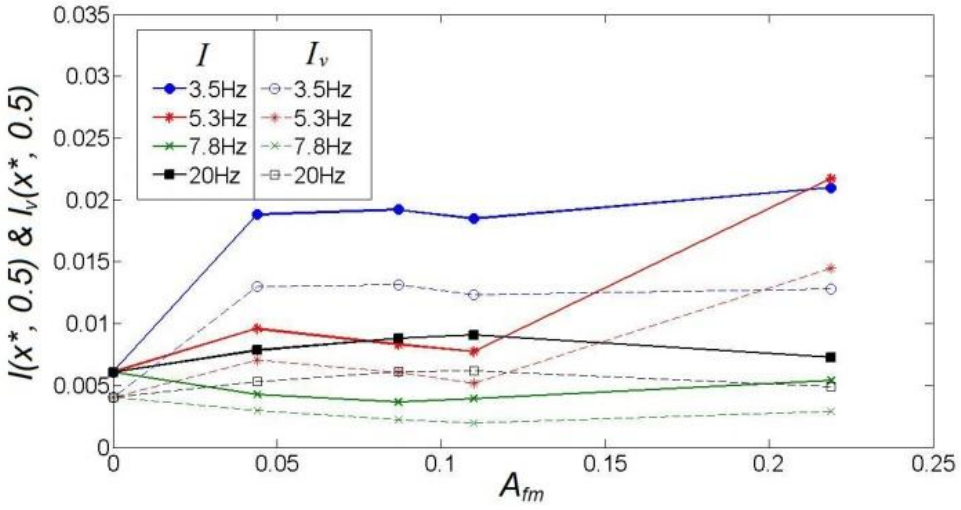

(c)

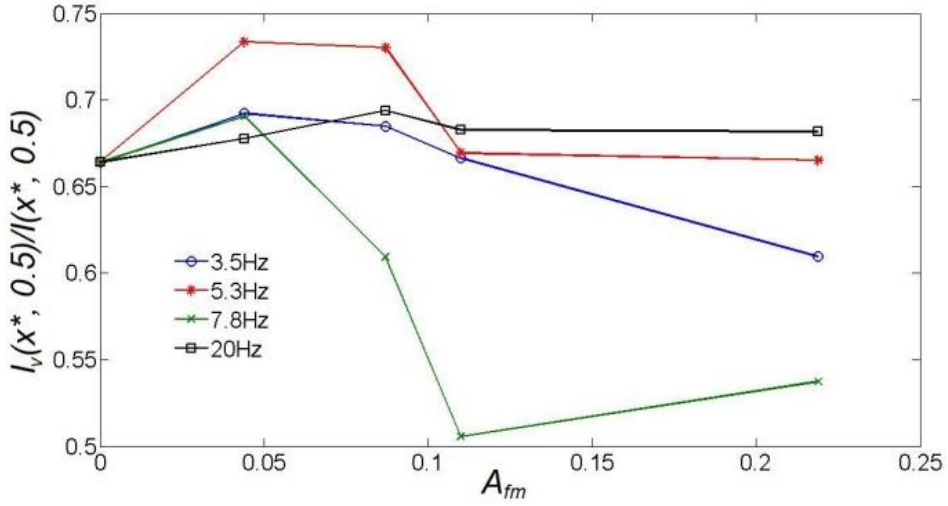

(d)

Figure 1.15 Turbulent intensity profile *vs* forcing level at different frequencies. (*a*, *b*) are at x^*=0.55 and (*c*, *d*) are at x^*=0.85. In (*a*) and (*c*) $I(x^*, 0.5)$ is plotted by straight line and solid marker and $I_v(x^*, 0.5)$ is dashed line and hollow marker. In (*b*) and (d) is $I_v(x^*,0.5)/ I(x^*,0.5)$.

The velocity fluctuations in z^*=0.5 plane is evaluated by the integral of turbulent energy, as follow:

$$I(x^*, z^* = 0.5) = I(x^*, 0.5) = \frac{1}{D_\Theta \langle U \rangle^2} \int_\Theta \left(u'^2 + v'^2 \right)(x^*, y, 0.5) dy \qquad (1.5)$$

It should be noticed that in confined mixing layer, although the wall boundary layer is also very important, it's not the protagonist. As will see most of the turbulent kinetic energy is located near the center of mixing chamber. Hence, to exclude the possible error cause by the wall boundary layer, the integration in Equation (1.5) is only conducted out of the wall boundary layer. Here, Θ means the integral region that regardless of the wall boundary layer and D_Θ is the diameter of the region.

The value of $I(x^*, 0.5)$ at x^*=0.55 under different frequencies and actuating intensities are plotted in Figure 1.15(*a*). Except the case A_{fm}=21.9%, under other lower actuating intensities, the highest fluctuation is reached at 3.5 Hz. This is opposite to the receptivity in nozzle. The fluctuations are not monotonically vary with the actuating intensity. Turning points appear for all the three lower frequencies at A_{fm}=11%. Especially at 5.3 and 7.8 Hz, the I(x*, 0.5) under A_{fm}=11% is even smaller than the case of A_{fm}=4.4%. This trend is more obvious in the distribution of *v'* constituent of turbulent energy, i.e. the dashed lines with hollow markers in Figure 1.15(*a*).

The *v'* constituent is evaluated by:

$$I_v(x^*, z^* = 0.5) = I_v(x^*, 0.5) = \frac{1}{D_\Theta <U>^2} \int_\Theta v'^2(x^*, y, 0.5)\, dy \qquad (1.6)$$

From Figure 1.15(*b*), we can find the v' constituent is always the major part of I(x*, 0.5). The turning over behavior at A_{fm}=11% is accompanied with the sudden decrease of I_v(x*, 0.5), both in magnitude and the proportion in I(x*, 0.5) (Figure 1.15 (*b*)). It may imply the possible changes of the topological structures of flow and vortex.

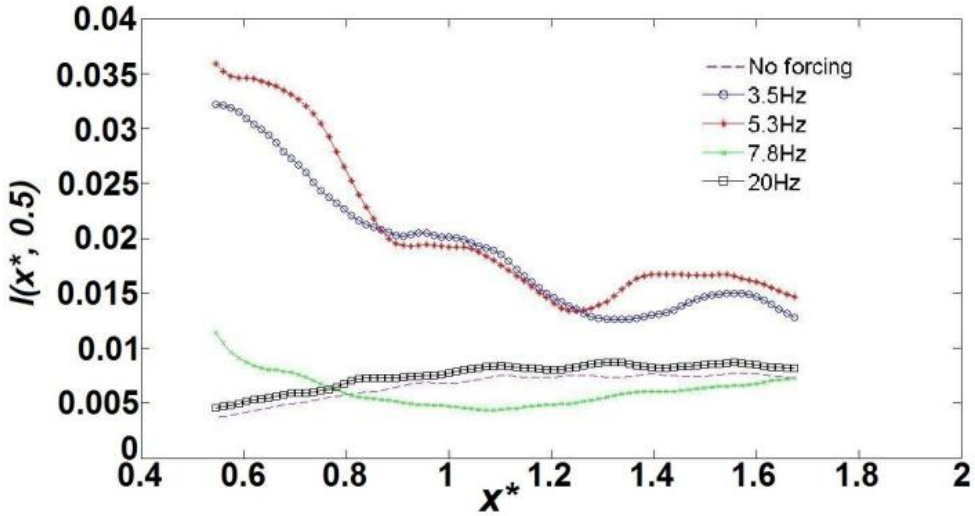

Figure 1.16 Turbulent intensity profile (A_{fm}=21.9%) vs x*

The curves at x*=0.85 are also plotted in Figure 1.15(*c*) and (*d*). Several conclusions can be found from these figures: (1) The forced flow at 3.5 Hz becomes saturated by means of the *I(x*, 0.5)*, but the varied *Iv/I* (Figure 1.15(*d*)) indicates the fluctuating structure is not the same. So does the case under 7.8 Hz. (2) Similar as at x*=0.55, the I, I_v and I/I_v at 5.3 Hz and 11% all become smaller than the case of 4.4%. But the I/I_v at 11% is the same as forcing at 21.9%, which indicates at this position and frequency, the flow structures under these two forcing intensities should belong to the same mechanism, and it is different with the dominant mechanism under smaller A_{fm}.

The streamwise evolution of *I(x*, 0.5)* when A_{fm}=21.9% is plotted in Figure 1.16. All the evolutions are consistent as what we introduced for the peaks of *u'* and *v'* profiles. At 3.5 and 5.3Hz, *I(x*, 0.5)* decreases rapidly with x*. Apparent short-range phenomenon can be found. As the velocity fluctuations are tightly related with the large scale spanwise vortex, in next section, the spanwise vortices will be introduced.

Cross view

From last section, we can see, the flow in nozzle section is most sensitive to the forcing frequency of 5.3 Hz. But the velocity fluctuations in side-view plane exhibit another response to the excitation. There is even a turn-over point of *v'* constituent when increasing the A_{fm} to 11%. Hence, the distribution of *v'* in cross section is introduced first in this section.

v' constituent at x=0.85*

The *v'* distribution (evaluated by v'_{rms}, where "*rms*" means root mean square) at x*=0.85 is listed in Figure 1.17. For the forced cases, the forcing intensity of left column is 4.4% and the right one is 11%.

The unforced flow is shown in Figure 1.17(*i*). No matter in *y* or *z* direction, the distribution is apparently symmetric with the peak value in center. The flow under 20Hz is almost the same as unforced flow as indicated in Figure 1.17(*g*, *h*) regardless of the forcing intensity which is consistent with the found of *u'* fluctuation in the side-view plane. It apparently indicates there is no receptivity at this frequency.

However, under the lower frequencies, the response of flow is totally different. At 3.5Hz, as expected, the *v'* fluctuation is much higher than the unforced case, as shown in Figure 1.17(*c*) and (*d*). The distribution of v'_{rms} is still symmetric to y-axis, but not to z-axis, especially at A_{fm}=11% (Figure 1.17(*d*)). From the Figure 1.15(*c*), it can be seen the v'_{rms} fluctuation reaches saturation at this streamwise position. This is also confirmed here. No matter distribution or intensity, there is no large difference of v'_{rms} from this cross-sectional view, except two extrudes located at the downstream of upper corner of nozzle, as graphed in Figure 1.17(*j*). Under 11%, the high fluctuation region only extends in

horizontal direction slightly compared with A_{fm}=4.4%, which exhibits limited influence of forcing on the streamwise vortex structures.

When forcing frequency increases to 5.3Hz, the flow exhibits apparently changes under the two forcing intensity. At A_{fm}=4.4%, the distribution of v'_{rms} is still asymmetric to z-axis while symmetric to y-axis. Three local peaks of v'_{rms} locate around the center of cross section, as shown in Figure 1.17(*c*). One is at the center and has the maximum v'_{rms} value. The other two locates near wall symmetrically with smaller values. While A_{fm} increases to 11%, the distribution becomes complex. The distribution becomes asymmetric to both *y* and *z* axis. There are no obvious peaks found from Figure 1.17(*d*). Instead, two high v'_{rms} streaks lay on the centerline. A valley of v'_{rms} appears at the center instead of the peak at A_{fm}=4.4%. From the color of contour here, obviously the v'_{rms} at 11% is smaller than that at 4.4%. This explains why there is a turn-over point of v'_{rms} from the side view. The flow exhibits definitely 3-dimensional character.

The *v'* constituent of turbulent energy can be evaluated by the integration of v'_{rms} in the cross-section as:

$$I_{cv}(x_c^*) = \frac{4}{\pi D^2 \langle U \rangle^2} \int\int_c v'^2_{rms}(x_c^*, y, z)\, dy\, dz \tag{1.7}$$

The subscript "*c*" means cross-section. Similar as the processing in side view, the influence of boundary layer is excluded in the integration. The variation of I_{cv} at different forcing intensity and frequencies is plotted in Figure 1.19. It can be seen from A_{fm}=4.4% to 11%, the increasing of I_{cv} at 5.3 Hz is very notable. This means the increment of v'_{rms} near the centerline is remarkable, as the v'_{rms} mainly located near the centerline. The case for 7.8Hz at A_{fm}=4.4% has very similar distribution of 5.3 Hz. Compared to latter, the *v'*

fluctuations of former is much weaker, no matter from the contour or I_{cv}. When A_{fm} increases to 11%, I_{cv} even decreases slightly due to the increasing but still weak 3-dimensionality.

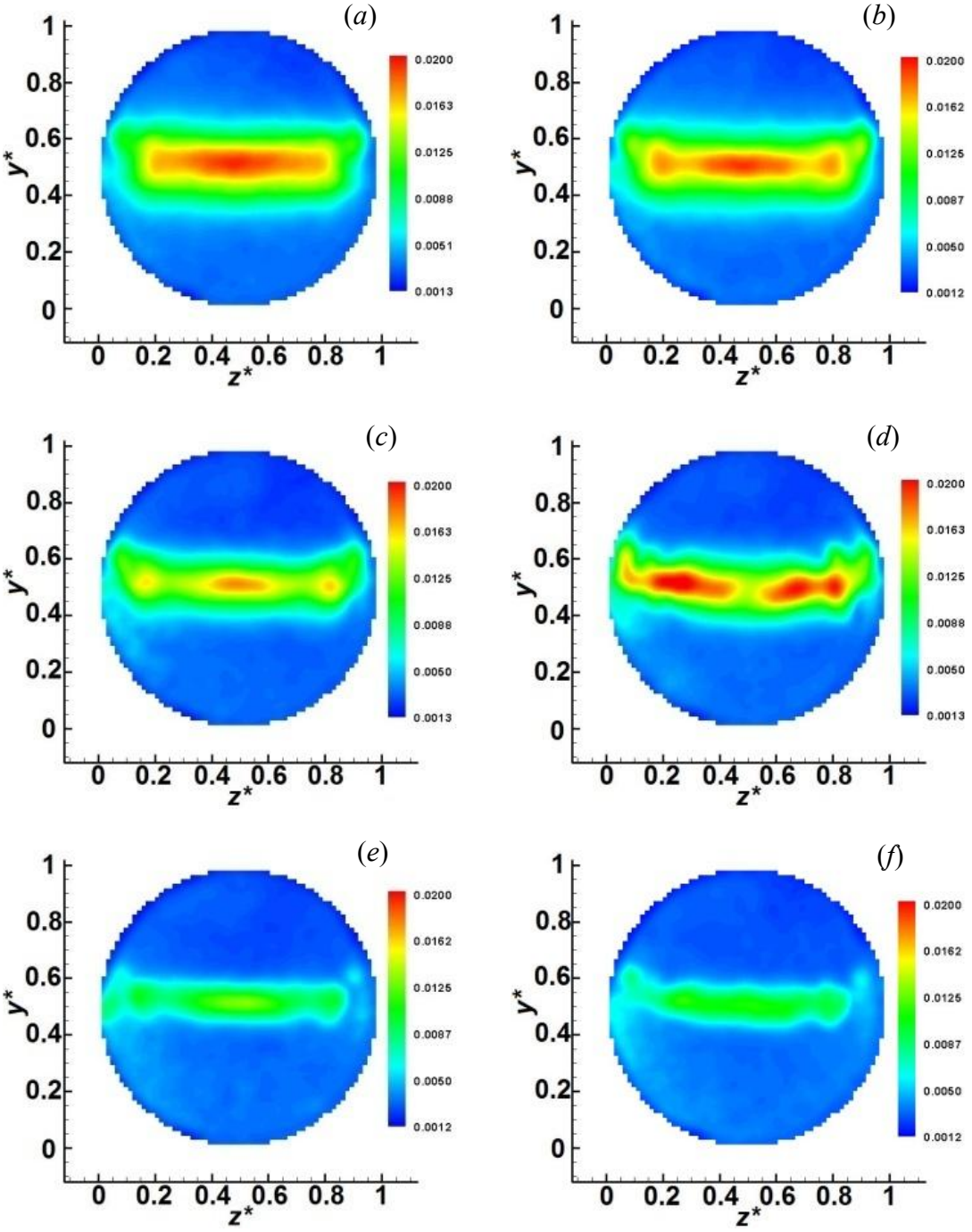

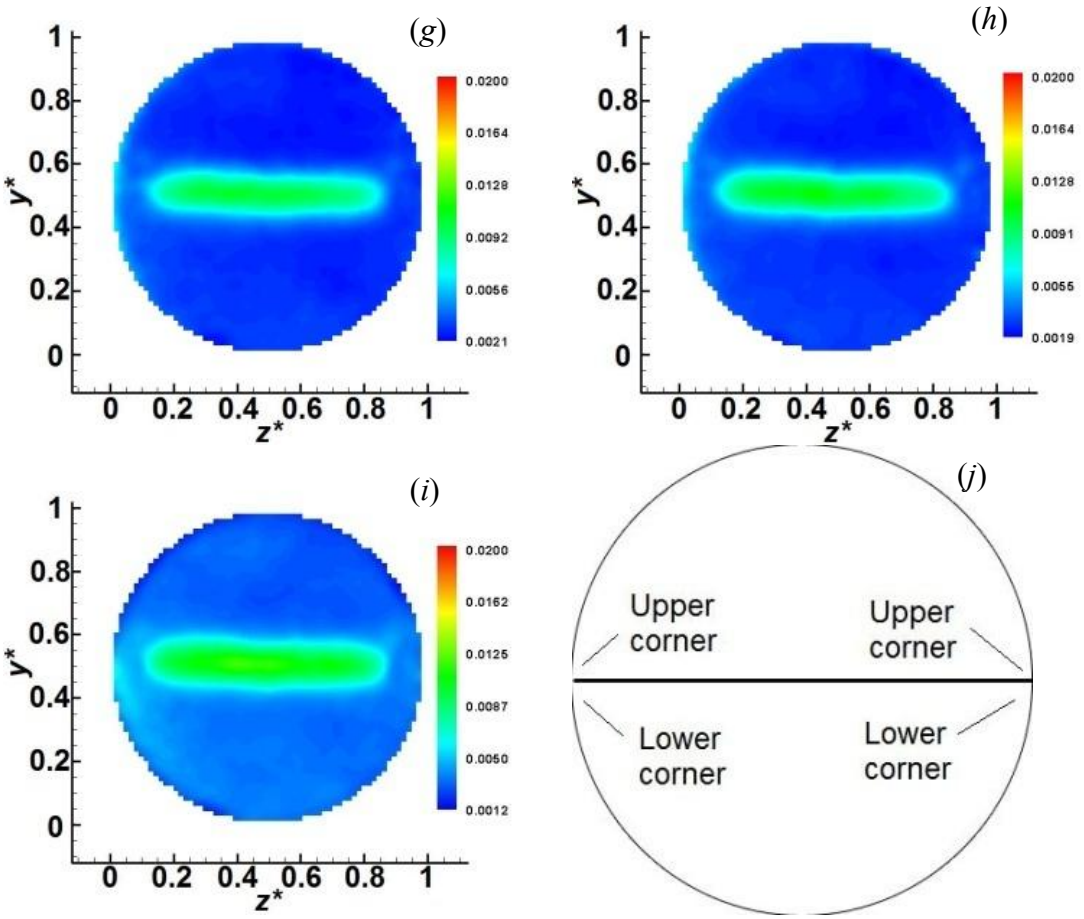

Figure 1.17. v'_{rms} in cross-section at x^*=0.85 and 4.4% (*a, c, e, g*) and 11% (*b, d, f, h*). (*i*) is unforced flow and (*j*) is the diagram of the position of nozzle corner.

w' constituent at x=0.85*

Similar as *v'*, *w'* is also evaluated by its *rms* value. The w'_{rms} distribution in unforced flow and forced at 20 Hz are given in Figure 1.18(*i*), (*g*) and (*h*), respectively. As shown, under these three cases, w'_{rms} distributions are all symmetric to both y and z axis. The intensity of w'_{rms} is not apparently affected by the forcing under 20 Hz. The w'_{rms} distribution indicates the streamwise vortex is inherently existed. (Note: The spanwise velocity fluctuations can be induced by either streamwise vortex or the vertical vortex generated due to the wall boundary layer. However, if it's due to the vertical vortex, the

high w'_{rms} region should be aligned in y-direction, not forms like a spot. Hence, the spanwise velocity fluctuation should be dominated by streamwise vortex structures.)

At 3.5 Hz, the distribution of w'_{rms} is different. The high w'_{rms} region locates a little bias to the high-speed side of the flow. Its distribution and intensity is not apparently affected by the forcing intensity, just like the v' constituent, which exhibits kinder of saturation.

But at 5.3 Hz, even the frequency difference is so small, the response is different. The w'_{rms} at this frequency is much higher than the other cases and increases drastically with the forcing intensity. The distribution is roughly symmetric to y axis, but apparently bias to the high-speed side. The main spanwise velocity fluctuations appear around the centerline. Meanwhile, another two spots of high w'_{rms} region locates just downstream of the upper corner. From the contour, the high w' fluctuations can be estimated. Compared with 5.3 Hz, the w'_{rms} at 7.8 Hz is apparently weaker, although the distribution looks similar.

From the results, it can be seen there is only a very narrow frequency band around 5.3 Hz which exhibits high receptivity. The initial energy of fluctuating velocities not only reversed transported to mean flow, but also transferred to 3-dimensional velocity fluctuations. This can be clearly explained by means of the evolution of integrated turbulent energy in cross section, which will be introduced in the energy evolution section.

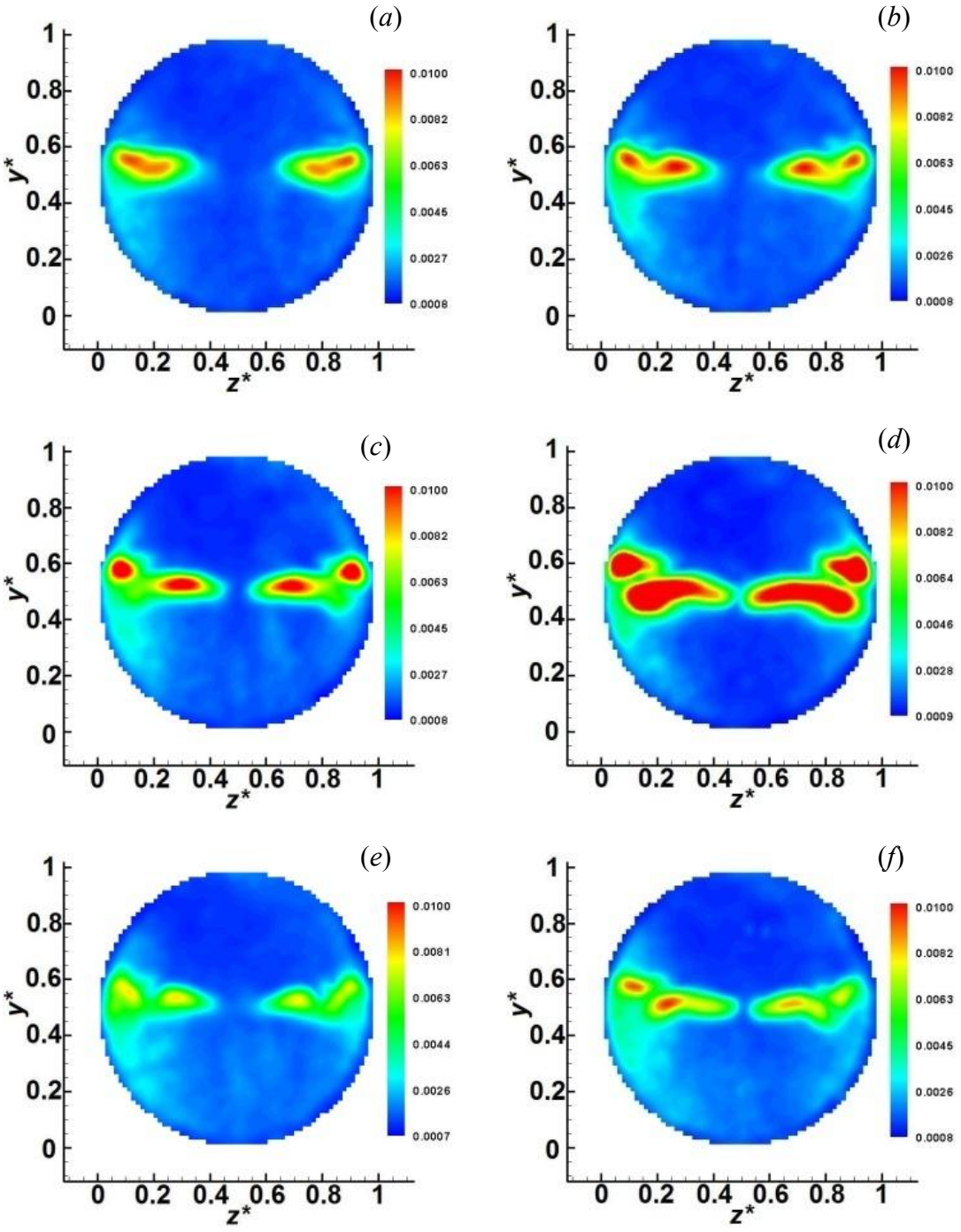
(a)
(b)
(c)
(d)
(e)
(f)
y*
z*
0
0.2
0.4
0.6
0.8
1
0.0100
0.0082
0.0063
0.0045
0.0027
0.0008
0.0026
0.0064
0.0046
0.0028
0.0009
0.0081
0.0044
0.0007

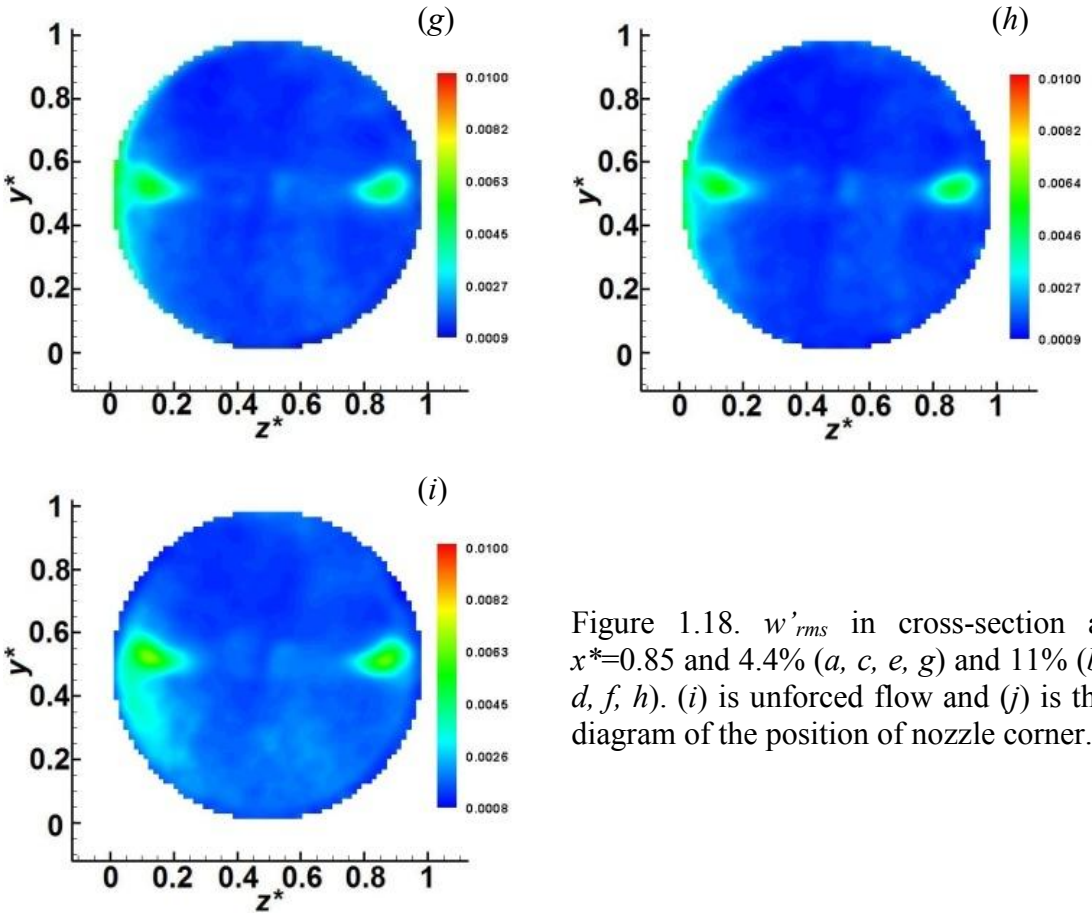

Figure 1.18. w'_{rms} in cross-section at x^*=0.85 and 4.4% (*a, c, e, g*) and 11% (*b, d, f, h*). (*i*) is unforced flow and (*j*) is the diagram of the position of nozzle corner.

The total velocity fluctuation I_c in this cross-section is estimated as below:

$$I_c(x_c^*) = \frac{4}{\pi D^2 \langle U \rangle^2} \int \int_c (v'^2_{rms} + w'^2_{rms})(x_c^*, y, z)\, dy\, dz \tag{1.8}$$

The results are also plotted in Figure 1.19.

It can be seen, due to the large contribution of I_{cv}, the I_c at 3.5 Hz is always the largest at all the three cross sections, except the case at x^*=0.85 when forced at 5.3 Hz and A_{fm}=11%. At 5.3 Hz, the I_c increases drastically from A_{fm}=4.4% to 11%. The *v'* constituent is still the majority of total turbulent energy. However, the portion of *w'* constituent in total turbulent energy increases rapidly with the forcing intensity, as shown in Figure 1.20 by

the ratio I_{cv}/I_c. This indicates the increment of v'_{rms} is not due to the simple magnification of 2-dimensional amplitude of fluctuating flow, but accompanied with the change of flow structures. The fluctuating streamwise vortex structures become more influential.

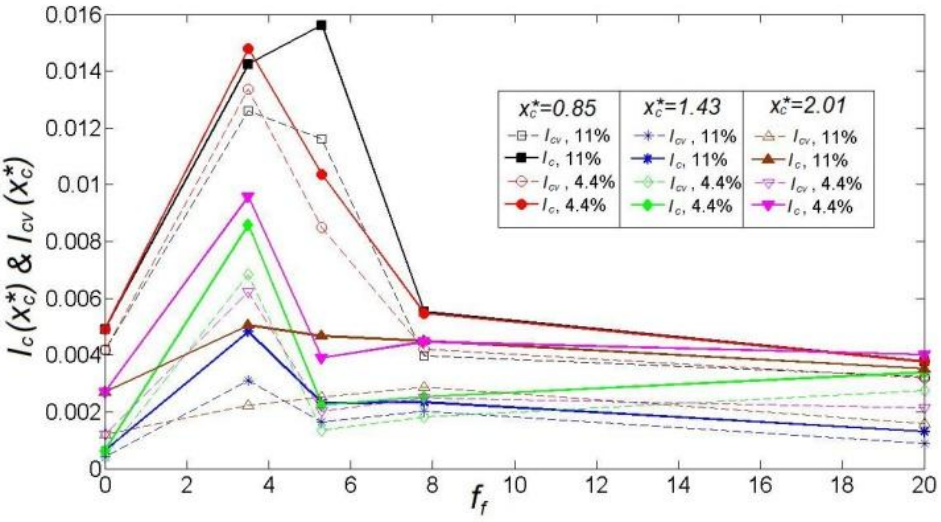

Figure 1.19. I_c at 3 cross-sections at A_{fm}=4.4% and 11.0%.

In fact, the development of streamwise vortex structures can be found in all the cases. The growing fluctuating streamwise vorticies competes with the major spanwise vortices and leads to significant near-field (or short-range) phenomenon, especially when forced at 5.3 Hz. As shown in Figure 1.19, the I_c and I_{cv} decrease with streamwise distance first, then recover at the downstream.

Actually, even without forcing, this phenomenon is also existed. In Figure 1.21(*a*) at x^*=1.43, due to the fluctuating streamwise vortices, v'_{rms} becomes much weaker in the centerline than upstream. The vertical velocity fluctuation caused by spanwise vortices is depressed by the streamwise ones. Meanwhile, two spots of v'_{rms} region and w'_{rms} intensity is definitely enhanced. Their distribution is similar as in the forced flow. All of these

indicate the growing of fluctuating streamwise vortices and their influences, which are: (1) The fluctuating streamwise vorticies can first depress the *v'* constituent caused by spanwise vortices which results in the decreasing I_c and I_{cv}. Later, as the development of fluctuating streamwise vorticies, the I_c and I_{cv} will recover and increase with x^*. (2) The forcing at low frequencies, especially 5.3 Hz, can induce earlier and faster growth of fluctuating streamwise vortices, intuitively.

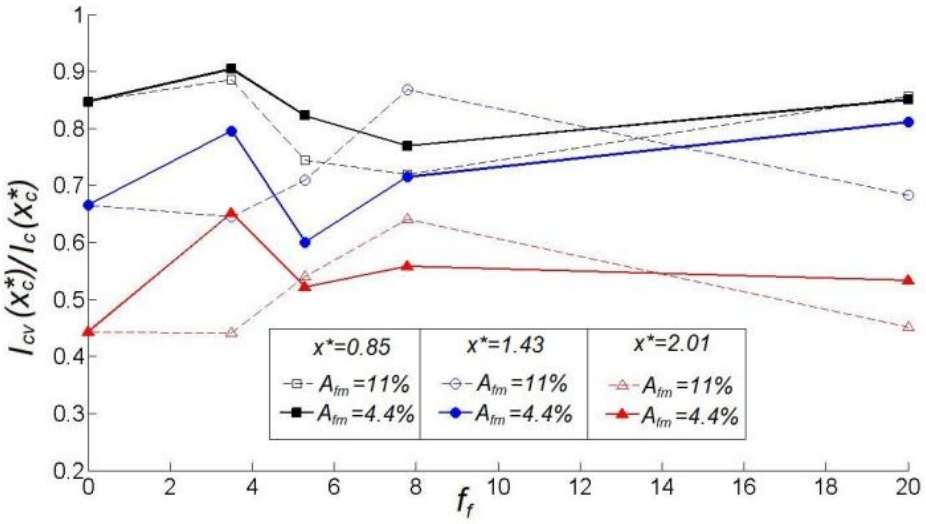

Figure 1.20. The I_{cv}/I_c at 3 cross sections at A_{fm}=4.4% and 11.0%.

The conclusions above can also be verified by I_{cv}/I_c which decreases with the streawise distance at almost all the cases. But there is still an exception which is 7.8Hz and A_{fm}=11%. As 7.8 Hz is not our focus, further discussion will not be carried on in this paper.

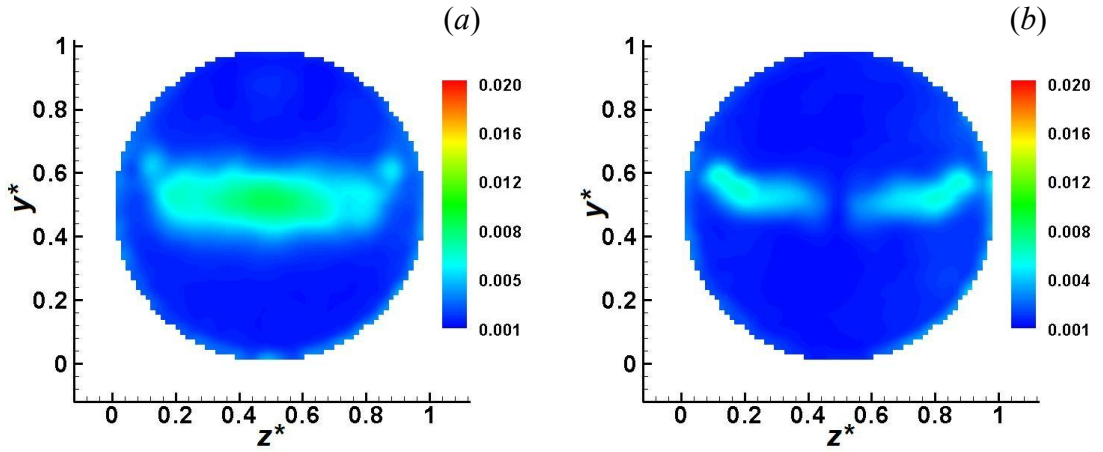

Figure 1.21. The velocity fluctuations at x*=1.43 in unforced flow, (a) v'_{rms} and (b) w'_{rms}

1.4.2.4 Vortex structures

Side view

From side-view, there is no essential difference between the types of spanwise vortex structures under 11% and 21.9% at 5.3 Hz, except the higher intensity and corresponding faster break down at higher forcing intensity. Hence, for better view of the vortex structure, the discussion is only based on lower A_{fm}.

The instant distributions of spanwise vorticity fluctuations (i.e. $\omega' = \partial v'/\partial y - \partial u'/\partial x$) at A_{fm}=11% in xy plane and z*=0.5 are graphed in Figure 1.22 by phase-averaged method. At lower forcing frequencies, i.e. 3.5 Hz, 5.3 Hz and 7.8 Hz (Figure 1.22(*b*, *c*, *d*)), the vortex structures are much stronger than that of 20 Hz (Figure 1.22(*e*)) and unforced flow (Figure 1.22(*a*)). The initial size of vortex at 3.5 Hz and 5.3 Hz are almost the same, while the intensity of former is larger. Hence, the vortex at 3.5 Hz should be more unstable and break down earlier. However, the fact is the vortex break down in advance at 5.3 Hz. From, Figure 1.22(*c*), we can find the initially generated vortex is more elliptical than that

in Figure 1.22(*b*). The vortex is apparently stretched in both x and y directions, tilted, and then break into two vortexes from the center at downstream. The evolution process is plotted in Figure 1.23 by means of the vortex at 4 phases, i.e. 0, $\pi/2$, π *and* $3\pi/2$. It can be seen, the separation actually starts at about x^*=1 and become obvious at about 1.43. The clockwise vortex spots are more unstable and easier to be break down than the counter-clockwise ones. This may due to the relatively smaller vorticity intensity.

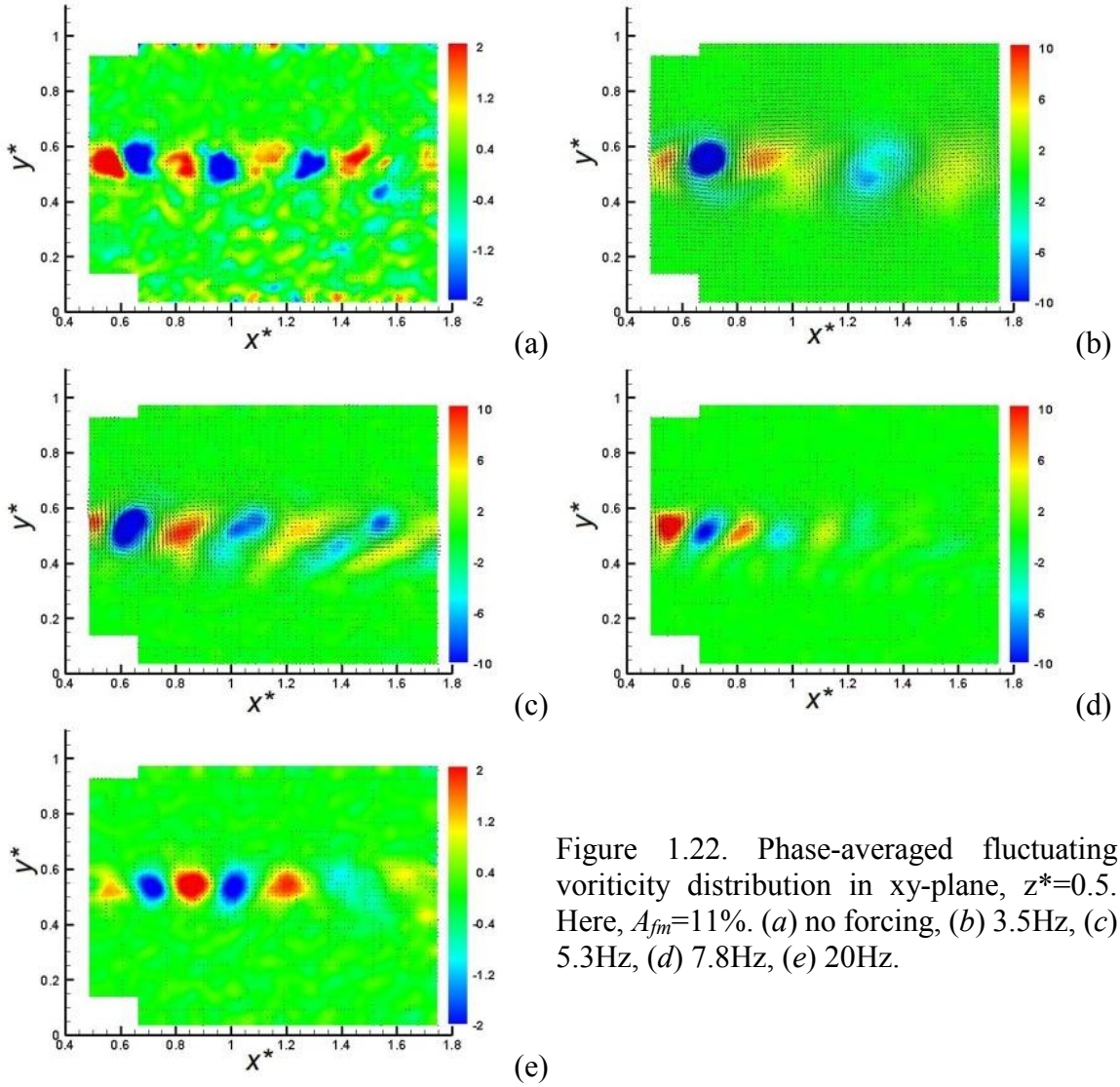

Figure 1.22. Phase-averaged fluctuating voriticity distribution in xy-plane, z*=0.5. Here, A_{fm}=11%. (*a*) no forcing, (*b*) 3.5Hz, (*c*) 5.3Hz, (*d*) 7.8Hz, (*e*) 20Hz.

We believe the stretching and breaking down process can be attributed to the high *dV/dy* around the centerline of mixing chamber, as shown in Figure 1.24. In the figure, the

mean velocity gradient is normalized by the average $(dU/dy)_{un,\ x^*=0.85}$ ($= (u_{0.95} - u_{0.1})/(y_{0.95} - y_{0.1})$) at x*=0.85 (the start position of shear-layer profile) in unforced mixing layer. It can be seen, in this FOI, the peaks of *dV/dy* are very high, no matter positive or negative. The positive one is almost 15% of $(dU/dy)_{un,\ x^*=0.85}$ and the negative can also reach 10% of that. Furthermore, their absolute values are slowly increasing in streamwise direction, which will continue the breaking down of spanwise vortices and enhancing the mixing downstream.

In fact, this phenomenon becomes more significant when the forcing intensity is higher at 5.3 Hz. The increasing of the gradient of mean vertical velocity is accompanied with the larger *V* and the corresponding kinetic energy, which is tightly related to the streamwise vortex. How this happens will be discussed later.

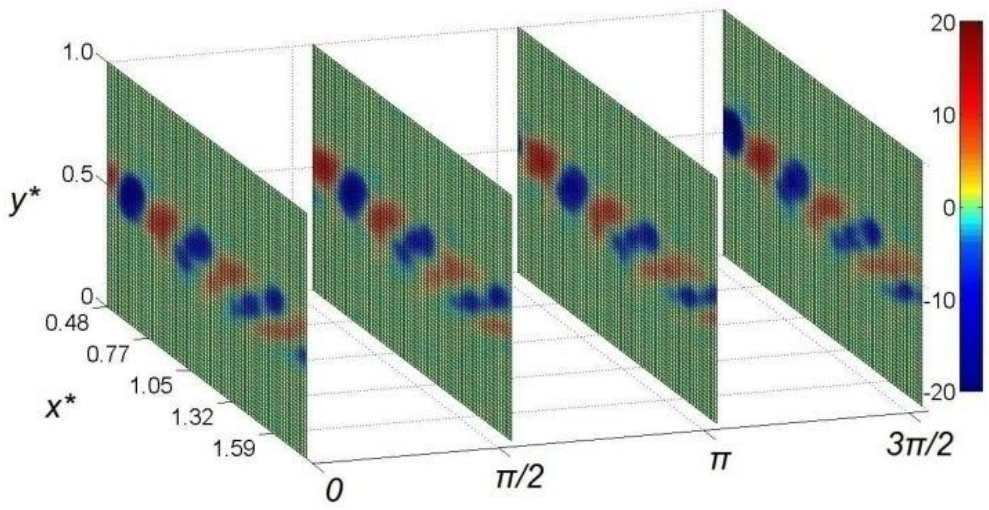

Figure 1.23. Phase evolution of vortex at 5.3 Hz and A_{fm}=11%

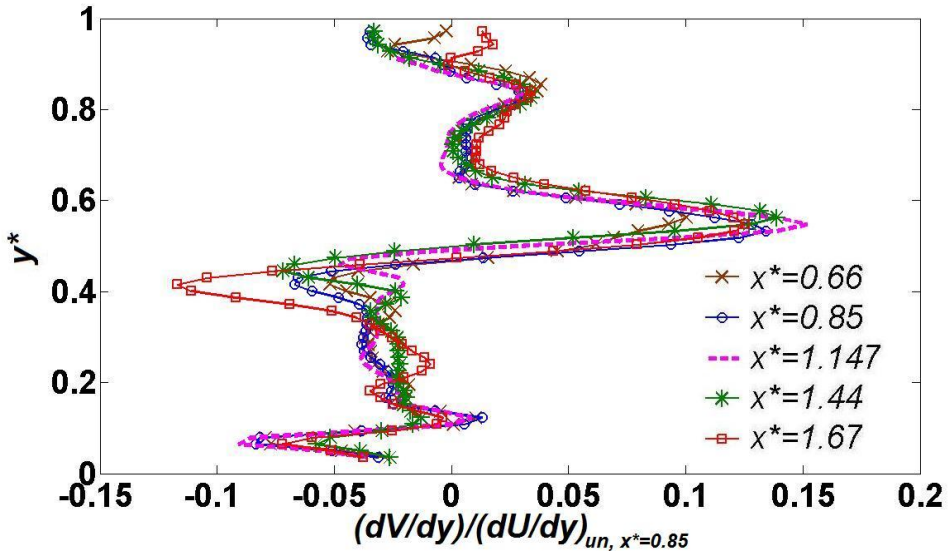

Figure 1.24. Normalized *dV/dy* at five *x**.

Cross view

In this section, the mean and fluctuating vorticity distribution of streamwise vortices will be described. Compared with the latter, the mean vorticity is even more important. As will see, the important vertical mean flow in mixing process can be attributed to the existence of mean streamwise vorticity. Hence, it will be introduced first.

The mean streamwise vorticity distribution at x=0.85*

The mean vorticity distributions at x*=0.85 while A_{fm}=4.4% and 11% are given in Figure 1.25 labeled by the same color scale.

In the unforced flow, two kinds of streamwise vortex can be found, as in Figure 1.25(*i*). One kind vortex locates far from the centerline in the format of CRV pairs as marked by the dashed box. This kind of vortex can be found in all the experiments and is not sensitive to the forcing frequency and intensities. Its vorticity only relies on the bulk flow velocity of each channel. The formation and distribution of the vortices are very similar as the

streamwise vortex caused by nonlinear traveling wave in pipe flow (Hof et al. 2006), although the symmetry is not kept due to the non-zero velocity ratio. This vortex structures have limited influence on the mixing enhancement and won't be further discussed here. A more detailed analysis will be given in another paper.

In the dash-dotted box of Figure 1.25(*i*), another kind of streamwise vortex structures is shown. This kind of vortex locates near the center, anti-symmetrically to y-axis, and in the form of vortex pairs. Different with the first type vortex, this type of vortex is very sensitive to low frequency actuating, especially at 5.3 Hz as shown in Figure 1.25(*c*) and (*d*). No matter under the lower A_{fm} or higher one, the mean vorticity intensity at 5.3 Hz is apparently higher than other cases. The streamwise vortex extends towards the center and almost covers the whole region of mixing layer. Under the influence, the mixing layer will be intensively waved and becomes extremely unstable. More important is, mean vertical velocity can be generated due to the distribution of vortex pairs as indicated by the black arrows in Figure 1.25(*d*). As a result, the scalar and momentum transport in vertical direction can be enhanced. Similar structures can also be found at 7.8 Hz as shown in Figure 1.25(*e*) and (*f*), even though apparently weaker. At 3.5 Hz, the mean streamwise vorticity is also very limited and its influence is only confined in the near wall region compared with 5.3 and 7.8 Hz, as shown in Figure 1.25(*a*) and (*b*). Hence, the mean streamwise vortices are only sensitive to the very narrow band of frequency around 5.3 Hz too, just like their fluctuating structures.

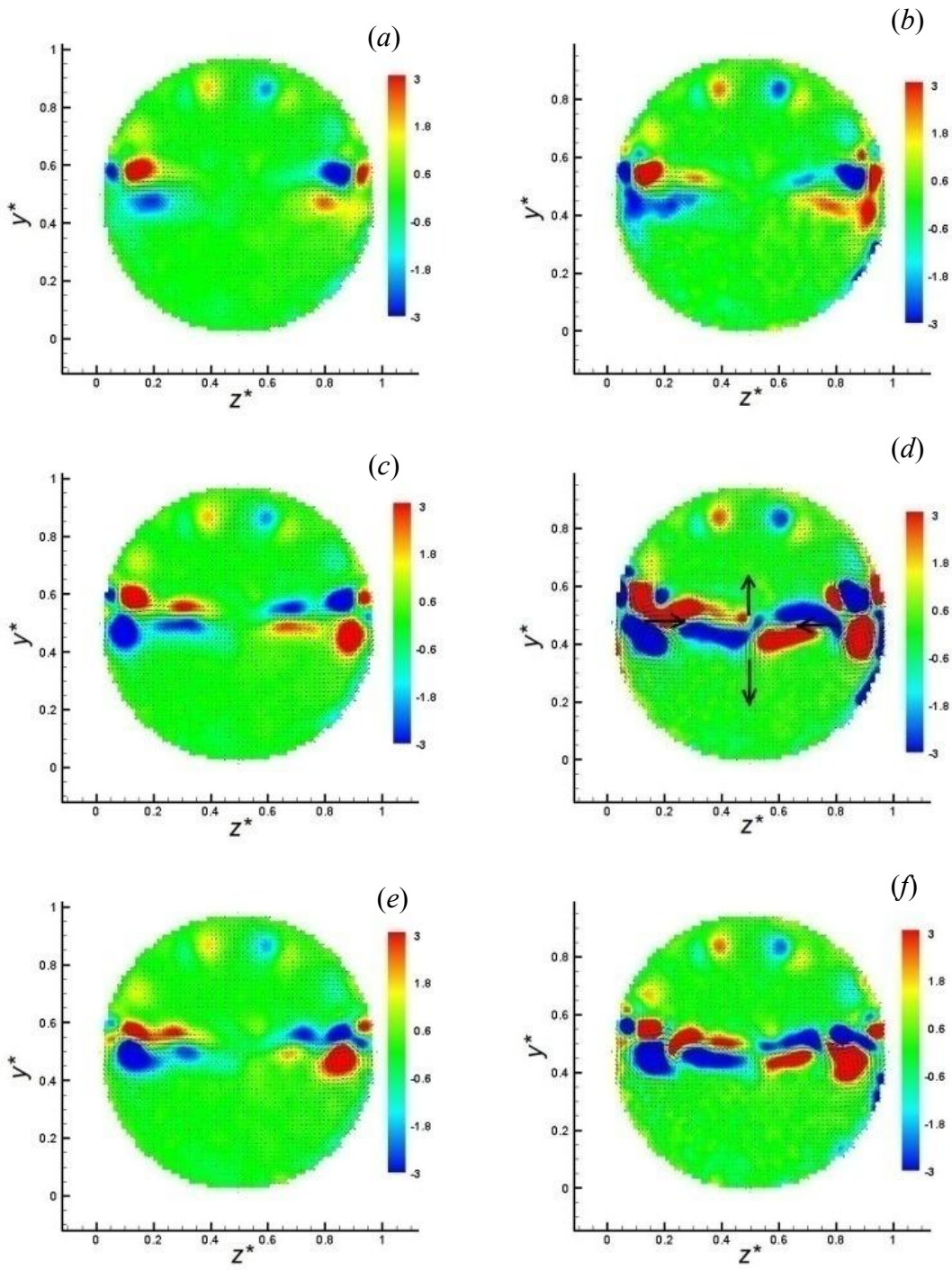
(a)
(b)
(c)
(d)
(e)
(f)
y*
z*
0
0.2
0.4
0.6
0.8
1
3
1.8
0.6
-0.6
-1.8
-3

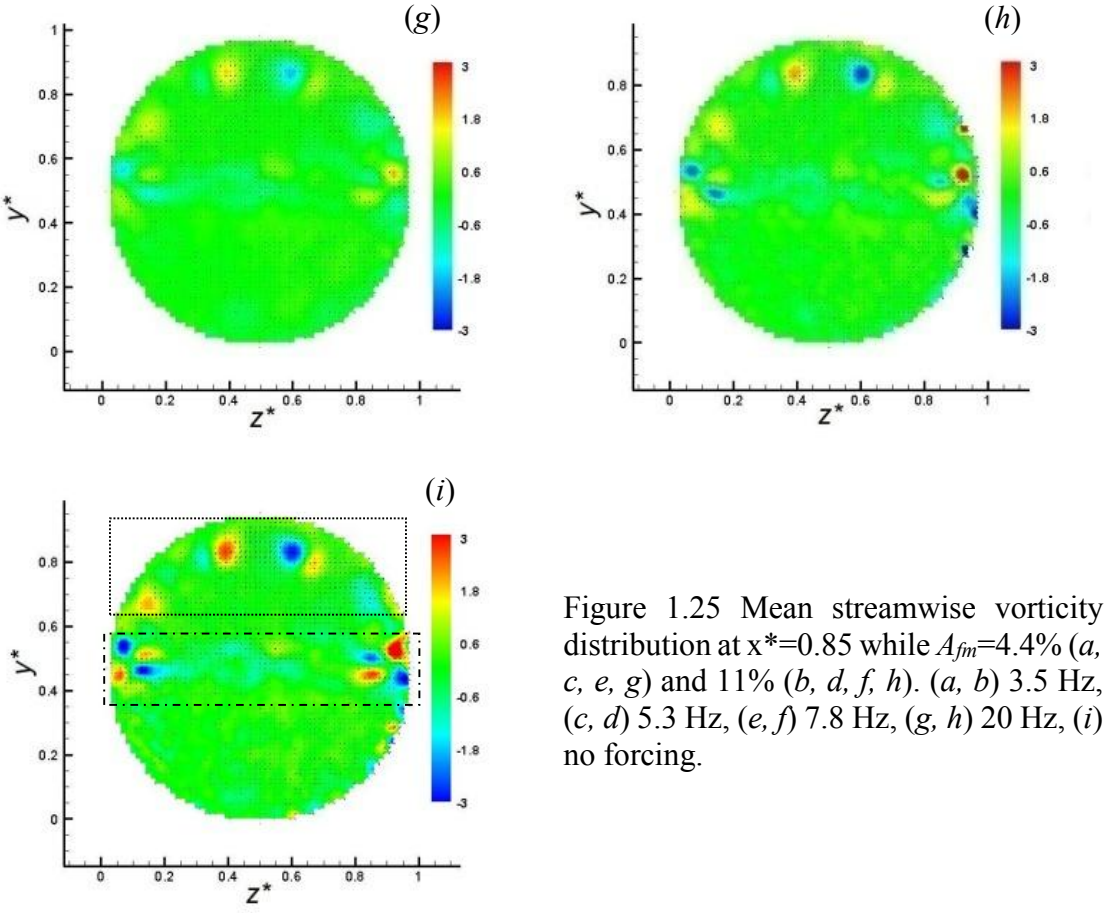

Figure 1.25 Mean streamwise vorticity distribution at x*=0.85 while A_{fm}=4.4% (*a, c, e, g*) and 11% (*b, d, f, h*). (*a, b*) 3.5 Hz, (*c, d*) 5.3 Hz, (*e, f*) 7.8 Hz, (*g, h*) 20 Hz, (*i*) no forcing.

The streamwise evolution of mean vorticity at different frequencies and A_{fm}=11% is plotted in Figure 1.26 and evaluated by the averaged and normalized enstrophy— E_x* in cross-section, which is defined as:

$$E_x^* = E_x/E_y \tag{1.9}$$

Here, $E_y = (dU_{x^*=0.85}/dy)^2/2$ is the initial enstrophy of spanwise mean vorticity in unforced mixing layer, calculated at *x**=0.85 and evaluated by Laufer's criterion (1947):

$$dU/dy = (U_{0.95,un} - U_{0.1,un})/(y_{0.95,un} - y_{0.1,un})$$

where $U_{0.95,un} = U_{1,un} + 0.95(U_{2,un} - U_{1,un})$, $U_{0.1,un} = U_{1,un} + 0.1(U_{2,un} - U_{1,un})$, $y_{0.95,un} = y(U_{un} = U_{0.95,un})$, $y_{0.1,un} = y(U_{un} = U_{0.1,un})$. The subscript "un" means unforced flow. In the research, E_y=52.5 (1/s^2). E_x is the averaged enstrophy of mean vorticity of streamwise in cross-section, defined as:

$$E_x = \frac{2}{\pi D^2} \int \int_c \Omega_x^2 (x_c, y, z) dy\, dz \tag{1.10}$$

where, $\Omega_x = \partial W/\partial y - \partial V/\partial z$. In the nozzle section, it can be seen the streamwise vortex is inherent and pre-existed before entering the mixing chamber, as shown in Figure 1.27. The enstrophy is always and roughly the highest at each forcing frequencies. At 5.3 Hz, the enstrophy is more than 4 times larger than other cases which indicates the highest receptivity of streamwise vortex to this special frequency.

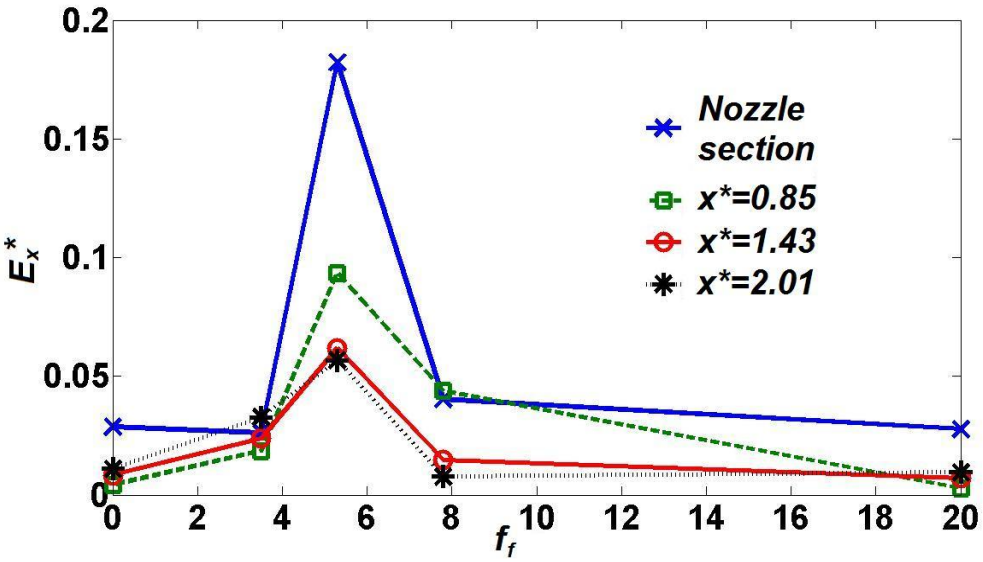

Figure 1.26 Normalized enstrophy of mean streamwise vorticity at four x* positions

In mixing chamber, at both 5.3 Hz and 7.8 Hz, as the streamwise distance increases, the enstrophy decreases rapidly which indicates the short-distance effect of the actuating.

This is consistent with what we have mentioned above and opposite with the cases of 3.5 Hz, 20 Hz and unforced flow. Except generating high *V*, much higher mean velocity in spanwise, *W*, is also developed as shown in Figure 1.27(*a*). The peak value reaches almost 20% of bulk flow velocity. Compared with the unforced mixing layer in Figure 1.27 (*b*), the spanwise transport of both momentum and mass will be more intensive which assists the rapid mixing.

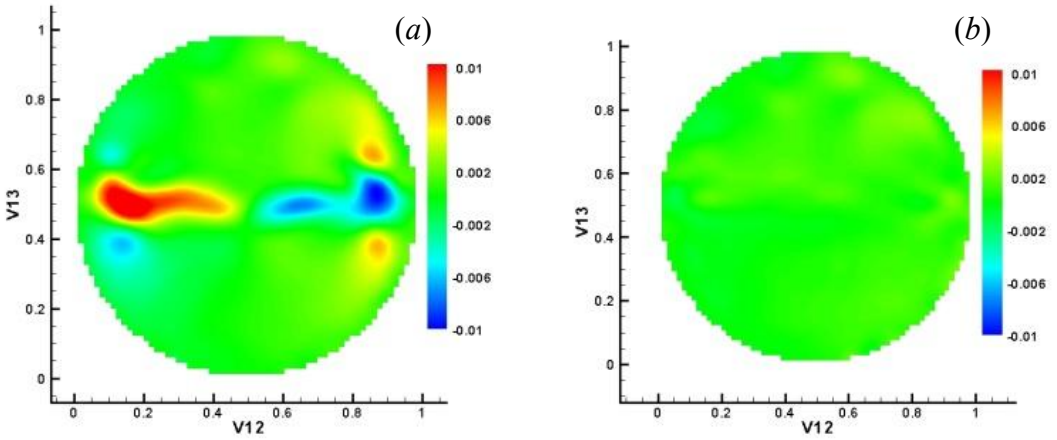

Figure 1.27 Distribution of *W* at *x**=0.85. (a) 5.3Hz, A_{fm}=11%, (b) no forcing

From the mean vorticity distribution, it can be seen the streamwise is pre-existed in nozzle section. However, due to the complexity of flow field, it doesn't mean the streamwise vortex in mixing chamber is still the same one as in nozzle. Hence, in next section, three possible models are compared and we attempt to qualitatively determine the dominant mechanism of streamwise vortex.

The fluctuating vorticity and the possible cause of streamwise vortex structures

In confined mixing layer, especially in this relatively small cross-section channel, the source of streamwise vortex is very complicated. There may be only one dominant

mechanism or several different mechanisms coexist. In this part, we summarize 3 known mechanisms to give a preliminary investigation.

The first discussed is the tilting spanwise vortices as advanced by Roberts (Roberts 1985) to explain the streamwise vortex generated in confined wake flow. This kind of vortex is also found by MacKinnon (MacKinnon and Koochesfahani 1997). In their model, they supposed the initial vortex structures are mainly oriented in spanwise, no matter forced or not. Then, in the near wall region, under the influence of wall shear layer, the spanwise vortex tube will be stretched and tilting towards streamwise as shown in Figure 1.29(*a*). This mechanism is reasonable but not applicable here. There are two reasons. First, if this mechanism is true, the vertical position of the core of fluctuating streamvise vortices should be at the centerline due to the unchanged position of fluctuating spanwise vortices (See Figure 1.6 and Figure 1.23). Apparently this is not the truth as indicated in Figure 1.30. The positive and negative cores locate on both side of the splitter plate, not the centerline. Second, at each moment, on both sides near the wall, there should be only single vortex, as sketched for the A-A and B-B cross-section in Figure 1.29(*a*). However, no matter the distribution of mean vorticity or the fluctuating vorticity, the vortex structures appear as pairs, not single. Therefore, this model can be ignored.

The second is due to the asymmetric response of mixing layer to outer actuating. As well-known, in many cases such as jet flow (Disselhorst and Van Wijngaarden 1980), while under high-intensity periodic suction or ejection, due to the difference of pressure distribution, the flow fields are not temporal symmetric which will lead to nonzero local mean velocity and vorticity, even in the geometrically symmetric scheme. This phenomenon also exists in our flow field and can be sketched as in Figure 1.29(*b*). In the

actuating circulation, the fluid in channel 1 will be pushed out of the nozzle in the first half period and then inhaled back in another half. In the half period of pushing, channel 1 works as an asymmetric jet. When the forcing intensity is high, the fluid spot will be ejected out the channel and form rolling vortex in both spanwise (along the trailing edge) and streamwise (near the wall). The cores of main streamwise vortices are located above the centerline and adjacently downstream of upper corner. Under their influence, two minus vortices are almost simultaneously induced underneath them. In another half period, the plate is pulled back. A reverse process will happen, but the location of vortex is not the same as before. Hence, the vortex structures appear as asymmetric CRV. After that, under the mutually induced velocity between the two streamwise vortex of a pair, the vortex structures will move off the wall and towards the center. As the influence of pushing and pulling process is asymmetric, mean vorticity and the related mean velocity field can be finally generated. In fact, the asymmetric CRV are commonly existed in the flow field while forced at 5.3 Hz as shown in Figure 1.28. Especially in Figure 1.28(d) where a typical asymmetric counter-rotation vortex pair is can be found. Hence, asymmetric shedding vortex is a reasonable explanation of streamwise vortex mechanism.

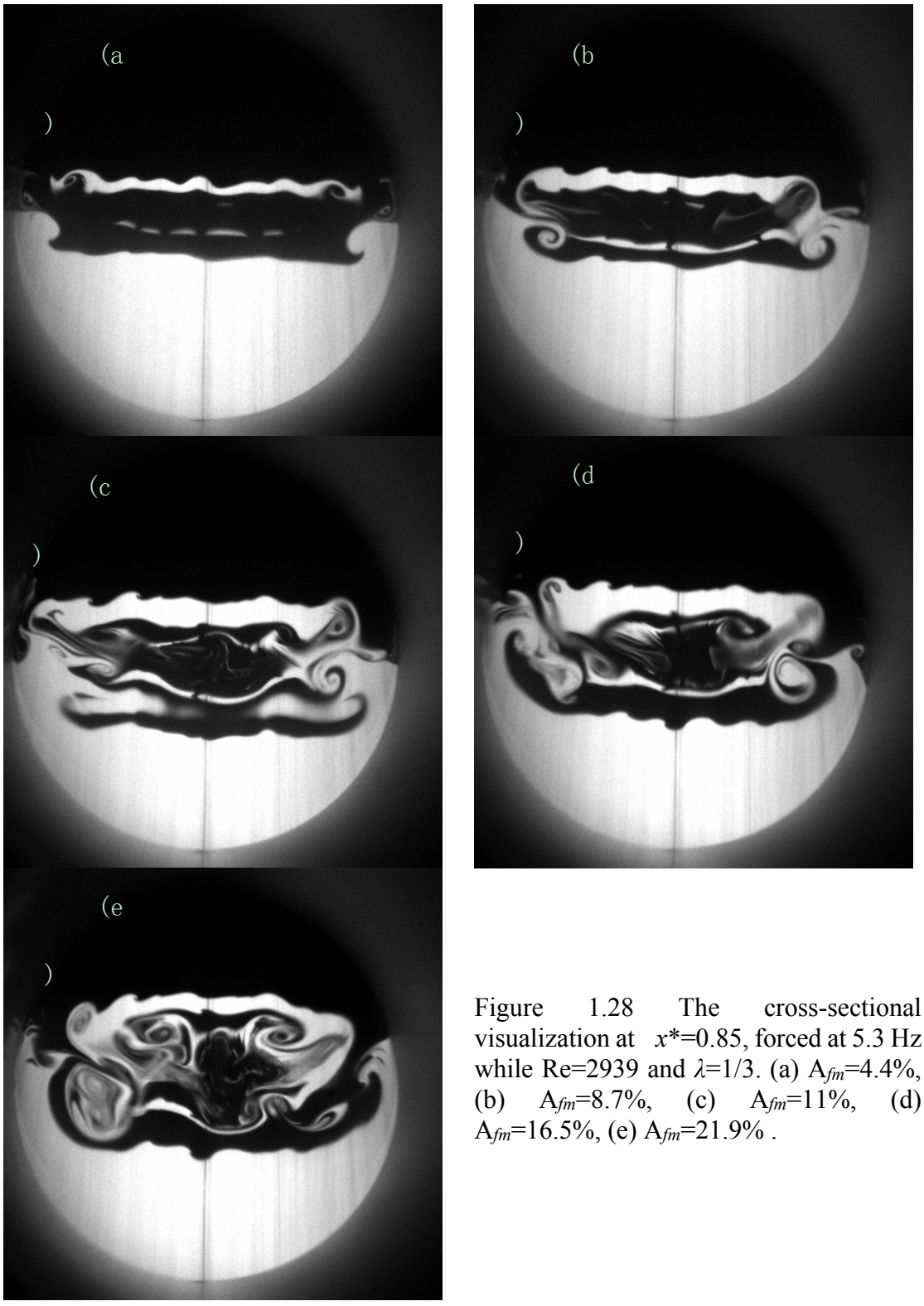

Figure 1.28 The cross-sectional visualization at x^*=0.85, forced at 5.3 Hz while Re=2939 and λ=1/3. (a) A_{fm}=4.4%, (b) A_{fm}=8.7%, (c) A_{fm}=11%, (d) A_{fm}=16.5%, (e) A_{fm}=21.9% .

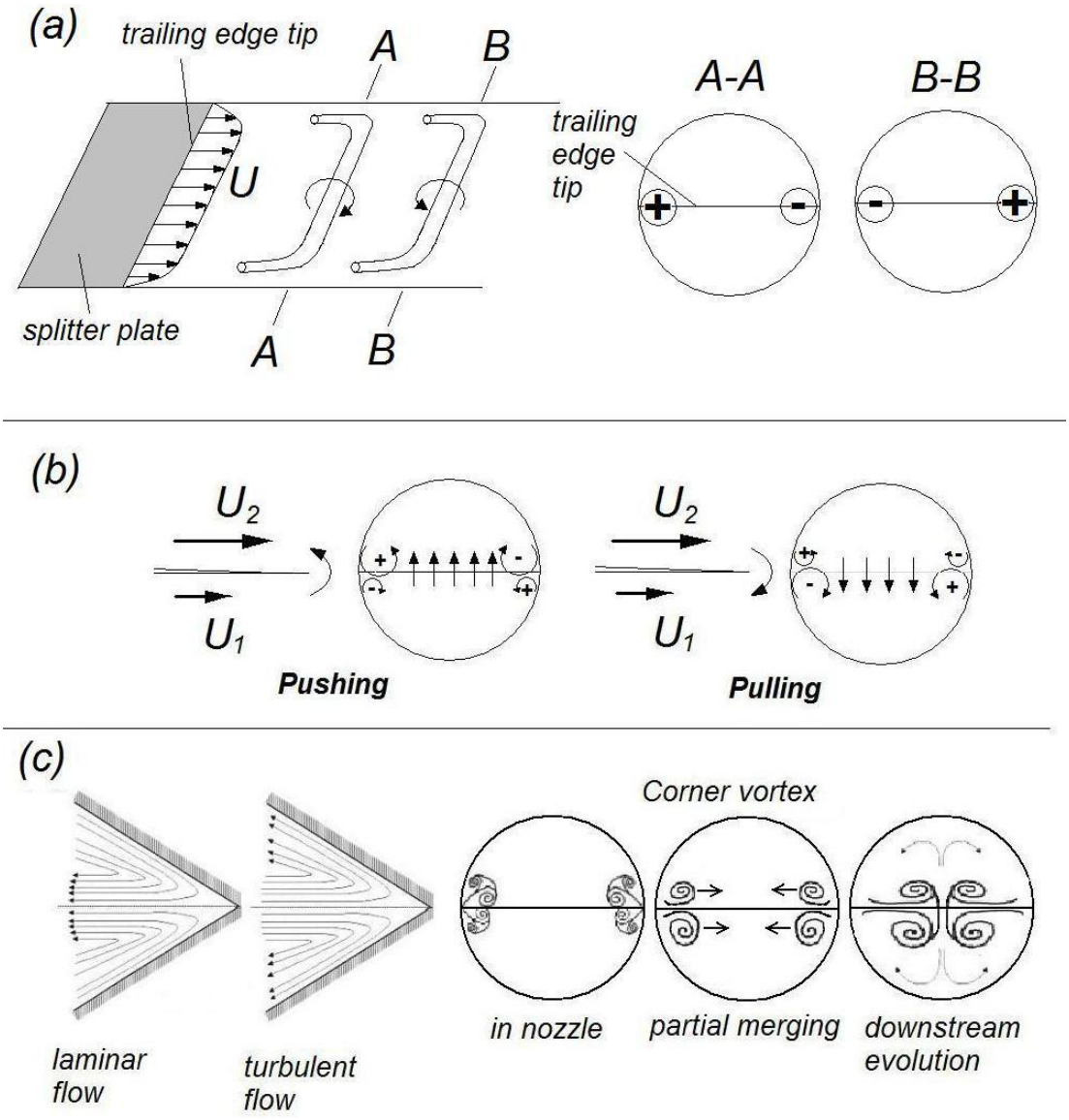

Figure 1.29 Three known mechanisms for streamwise vortex generation. (a) Tilting spanwise vortex, (b) asymmetric wake around trailing edge, (c) corner vortex.

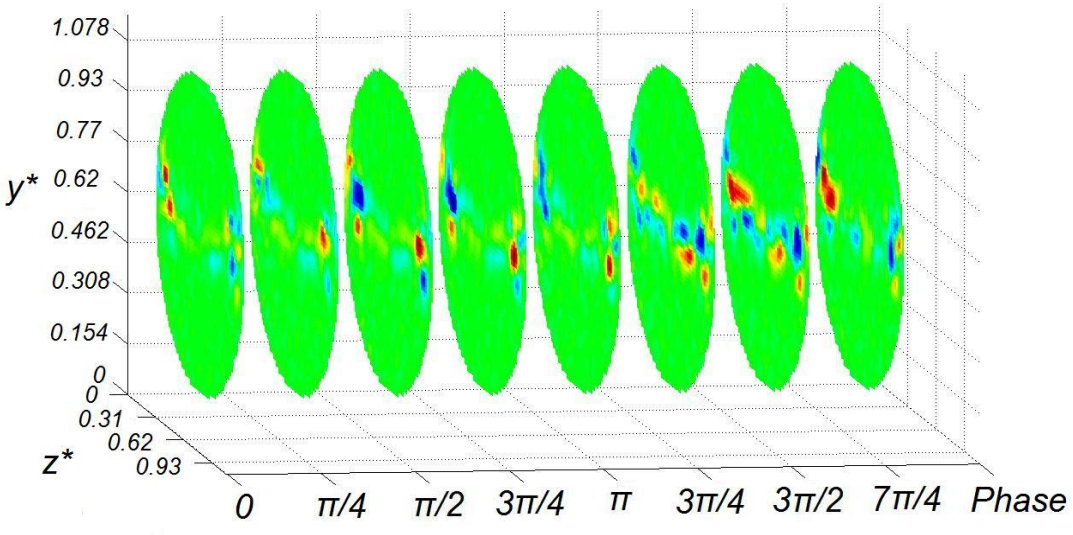

Figure 1.30 The evolution of streamwise vortices at 5.3 Hz and A_{fm}=11.6%. x*=0.85.

In this conceptional model, the vortex structures exhibit as asymmetric counter-rotation vortex pairs, i.e. shown by Figure 1.29(b). This is qualitatively consistent with Figure 1.30. This model can easily explain the generation of intensive streamwise vortex structures. The short-distance phenomenon can also be explained by the succedent vortex dissipation due to viscosity. However, because the vortices are all located at the downstream of corners, it's hard to distinguish this mechanism with the potential corner vortex mechanism as will be introduced. Hence, in next paragraph, the corner vortex model is introduced.

Corner vortex can be generated in the corner region of nozzle between wall and splitter plate as shown in Figure 1.17(*j*), due to the inflectional profile of streamwise mean velocity (Dhanak 1993; Balachhandar and Malik 1995). Related works have been pursued for more than 40 years in square duct, riblets, ridges and many other cases (Gessner and Jones 1965; Zamir and Young 1970; Gessner 1973; Zamir 1981; Goldstein et al. 1992; Dhanak 1993;

Balachhandar and Malik 1995; Dhanak and Duck 1997; Duck and Owen 2004; Moinuddin et al. 2004). In laminar flow, the cross flow in corner is shown in Figure 1.29(c)(Zamir and Young 1970). Inward flow towards the corner along the wall, merged together and then flows out along the bisector line. In turbulent flow, the process is just reversed (Gessner and Jones 1965). Outer flow moves towards the corner along the bisector line and then expelled out along the wall. Wang (Wang 2003; Wang 2006) first attribute the strong streamwise vortex structures to the corner flow instability. His conceptional model is extended for discussion in this section.

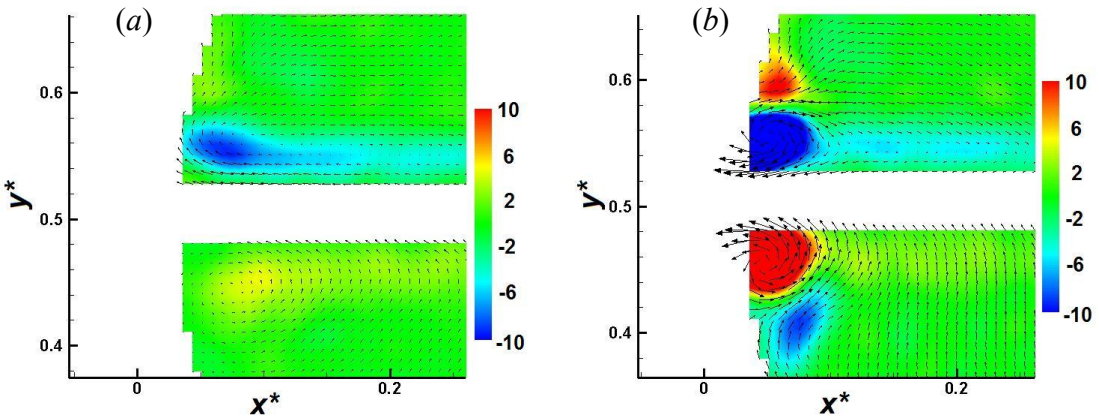

Figure 1.31 The mean streamwise vorticity in corner region of nozzle section, 3 mm upstream from the trailing edge. (a) unforced flow, (b) 5.3 Hz, A_{fm}=11%. The black arrows indicates velocity vectors.

In the considered Reynolds number (Re=2939) here, the unforced flow is apparently laminar in nozzle section. Hence, the potential corner vortex generated can be depicted as shown in Figure 1.29(*c*) right.

In nozzle section, the corner vortices are first generated in both upper and lower corners in the format of adjacent vortex pairs. As the side wall are not both flat, but one flat and one concaved, the generated vortices in each pair may be not symmetric along the

bisector line. This assumption is proved in Figure 1.31 which is captured in nozzle section and 3 mm upstream of the trailing edge. No matter forced or not, clear vortex structures can be found in the nozzle section. In Figure 1.31(a), the streamwise vortices of unforced flow are much weaker than the forced flow at 5.3 Hz and A_{fm}=11% as shown in Figure 1.31(b). However, the distribution of vorticity is roughly the. At 5.3 Hz, the vortices in corner are extremely enhanced. The mean flow in corner region is qualitatively consistent with the model of laminar corner flow in Figure 1.29(c). Hence, it can be concluded in the nozzle, the main streamwise vorticies are corner vortices.

After the nozzle section, the lower vortex of upper corner vortex pair will be completely or partially (depends on the vortex size and vorticity intensity) merged with the upper vortex of lower corner vortex pair. The residual parts of the corner vortex pairs will behave as single vortex, as sketched in Figure 1.29(*c*).

After the merging process, the vortices will continue moving towards the center under the induced velocity by each other. In this process, between them and side wall, new vortices can be induced. Meanwhile, they will be elongated, stretched and finally break into smaller vortices, as distributed in Figure 1.25.

Corner vortex mechanism is also a reasonable explanation. And from Figure 1.26, the continuous dissipation of enstrophy along streamwise direction is consistent with practical founds. However, there is still some critical questions should be answered. First, the most unstable frequency of corner flow instability is dominated by the Re number of free flow in nozzle. While, the optimal forcing frequency 5.3Hz which causes quick mixing is not varied with Re. Why? As the researches on this flow field is pretty rare, this cannot be

simply answered in this manuscript and a lot of further investigations are required. Another question, which is also the most important one, is how to distinguish the streamwise vortices generated from corner vortex mechanism from that produced after trailing edge by asymmetric shedding vortex.

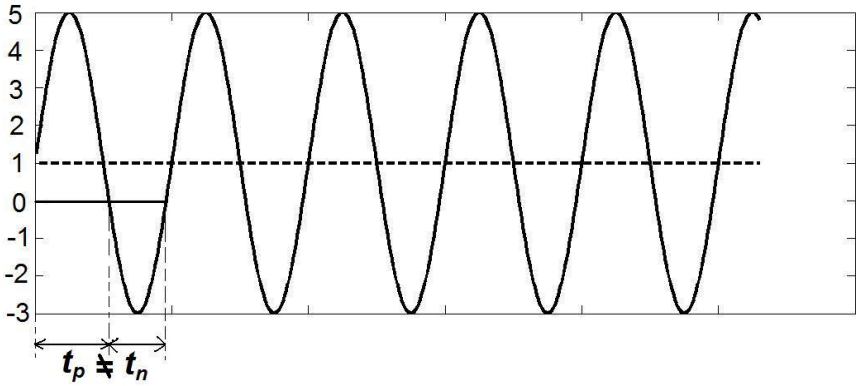

(a)

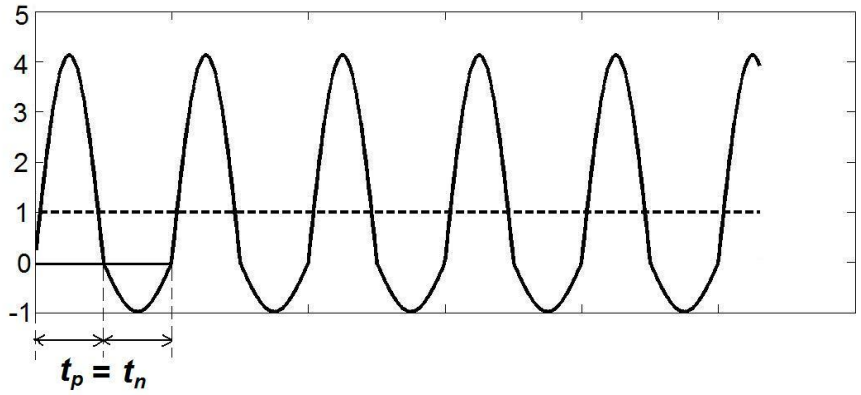

(b)

Figure 1.32 Instant vorticity of streamwise vortex structures corresponding to corner vortex model (a) and asymmetric response of flow (b).

To issue this question, two simple models are used as sketched in Figure 1.32. If corner vortex instability is the dominant mechanism, even though the forcing intensity is very high, vorticity fluctuations is still approximately periodic around their mean value as shown in Figure 1.32(*a*). Hence, the possibility that the sign of instant vorticity is same as that of mean vorticity should be more than 50%, i.e. $t_p \neq t_n$ (t_p is the time interval of

instant vorticity in positive direction, while t_n is the time interval of instant vorticity in negative direction). Contrarily, if it's caused by asymmetric process, although the mean value is the same, the process is completely different as shown in Figure 1.32(*b*). In each half period, the vorticity intensity is different as elucidated before. But the possibilities of exhibiting both positive and negative vorticity at each point should be the same, i.e. $t_p \neq t_n$. Hence, by calculating the skewness of so-called "duty circle", the difference can be distinguished. The skewness is defined as below:

$$\begin{cases} d_\omega(y,z,t) = 1, & \text{if } \omega(y,z,t) \geq 0 \\ d_\omega(y,z,t) = -1, & \text{if } \omega(y,z,t) \leq 0 \end{cases} \qquad Sk(y,z) = \overline{d_\omega^{\,3}} \Big/ \left(\overline{d_\omega^{\,2}}\right)^{3/2} \tag{1.11}$$

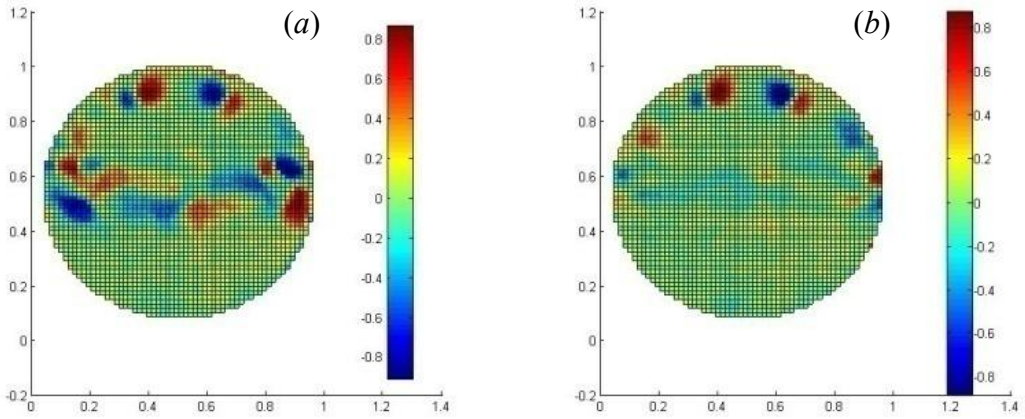

Figure 1.33 The distribution of *Sk* at *x**=0.85, (a) *ff*=5.3Hz, A_{fm}=11.0%, (b) no forcing.

The distribution of *Sk* at x*=0.85 is shown in Figure 1.33. It can be seen, no matter forced or not, for the first type streamwise vortex, the *Sk* is always very high with the same sign of the mean vorticity. This means this kind of vortices is almost pure periodic. For the second type streamwise vortices, there is a little difference. For example in the forced flow at 5.3 Hz, at the core of streamwise vortex near wall, the magnitude of *Sk* is almost 0.8 with

the same sign of the mean vorticity. This is also found in unforced flow. It indicates high correlation between the direction of instant vorticity and its mean value. Hence, the flow is nearly pure periodic with small fluctuations and the vortex here should belong to the descendent of corner vortex.

1.4.2.5 Energy evolution

(a) from side view

The energy transport and evolution is very important in explaining the momentum transport process and evolution of flow structures. From the investigations above, it can be seen there are two important and abnormal phenomena exist: (1) In the nozzle, the receptivity (evaluated by the turbulent energy) of 5.3 Hz is always the highest, compared with other forcing frequencies. However, this situation is changed in the mixing chamber where 3.5 Hz becomes the highest. (2) The *U* and *V* profiles can both be significantly affected by the forcing intensity at 5.3 Hz. Why the initial turbulent energy disappears and how the *U* and *V* energy generated is what we want to discussed in this section.

The turbulent energy equation can be shown as below:

$$U_i \frac{\partial \bar{k}}{\partial x_i} = \frac{\partial}{\partial x_i}\left(\frac{\overline{p' u_i'}}{\rho}\right) - \overline{u_i' u_j'} \frac{\partial U_i}{\partial x_j} - \frac{\partial}{\partial x_i}\left(\frac{\overline{k u_i'}}{2} - \nu \frac{\partial \bar{k}}{\partial x_i}\right) - 2\nu \overline{e_{ij} e_{ij}} \qquad (1.12)$$

Here, $i=1$, 2, 3, and $u_1'=u'$, $u_2'=v'$, $u_3'=w'$, $U_1=U$, $U_2=V$, $U_3=W$, summation convention is used for convenience, $k=u_i'u_i'$ and $e_{ij}=\frac{1}{2}\left(\frac{\partial u_i}{\partial x_j}+\frac{\partial u_j}{\partial x_i}\right)$ is the turbulent energy. Non-dimensionalized by

$$U_i^*=U_i/\langle U\rangle,\quad u_i'^*=u_i'/\langle U\rangle,\quad x_i^*=x_i/D,\quad k^*=k/\langle U\rangle^2,\quad p'^*=p'/\rho\langle U\rangle^2,$$

we have the normalized turbulent energy equation:

$$U_i^*\frac{\partial\overline{k^*}}{\partial x_i^*}=\frac{\partial}{\partial x_i^*}\left(\overline{p'^*u_i'^*}\right)-\overline{u_i'^*u_j'^*}\frac{\partial U_i^*}{\partial x_j^*}-\frac{\partial}{\partial x_i^*}\left(\frac{\overline{k^*u_i'^*}}{2}-\frac{1}{Re}\frac{\partial\overline{k^*}}{\partial x_i^*}\right)-\frac{2}{Re}\overline{\left(\frac{\partial u_i^*}{\partial x_j^*}+\frac{\partial u_j^*}{\partial x_i^*}\right)^2}$$

(a) (b) (c) (d) (e) (1.13)

In this equation, (*a*) is the convective transportation term by mean flow, (*b*) is the pressure-driven term by pressure fluctuations, (*c*) is the production term of turbulent energy, (*d*) is the diffusion term and (*e*) is the dissipation term.

In conventional free mixing layer, the mixing process is dominated by the large scale coherent structures, i.e. the spanwise vortex structures, due to the K-H instability. The velocity fluctuation is the major carrier of mass transportation. Because of the two dimensional free mixing layer, the production of velocity fluctuation can be mainly attributed to the negative Reynolds stress $\overline{u'v'}$ and positive $\partial U/\partial y$ in mixing layer (Wygnanski and Fiedler 1970), as shown in term (*a*) of Equation (1.13). And the kinetic energy is drained from mean flow to fluctuating flow which leads to the initial spreading of mixing layer.

Table 1.2 The definition of terms and their contribution to turbulent energy, from side-view measurement.

Terms	Expressions		Contribution to turbulent energy(Sign)
Convection	$C_1 = U^* \partial \overline{k^*} / \partial x^*$	$C_2 = V^* \partial \overline{k^*} / \partial y^*$	Loss(+) Gain(-)
	$k^* = \left(u'^*\right)^2 + \left(v'^*\right)^2$	$C = C_1 + C_2$	
Production	$P_1 = -\overline{u'^* v'^*} \partial U^* / \partial y^*$	$P_2 = -\overline{u'^* v'^*} \partial V^* / \partial x^*$	Gain(+) Loss(-)
	$P_3 = -\overline{\left(u'^*\right)^2} \partial U^* / \partial x^*$	$P_4 = -\overline{\left(v'^*\right)^2} \partial V^* / \partial y^*$	
	$P = P_1 + P_2 + P_3 + P_4$		
Dissipation	$D_{is1} = -\overline{\left(\partial u'^* / \partial x^*\right)^2} / \mathrm{Re}_D$	$D_{is2} = -\overline{\left(\partial u'^* / \partial y^*\right)^2} / \mathrm{Re}_D$	Loss(-)
	$D_{is3} = -\overline{\left(\partial v'^* / \partial x^*\right)^2} / \mathrm{Re}_D$	$D_{is4} = -\overline{\left(\partial v'^* / \partial y^*\right)^2} / \mathrm{Re}_D$	
Diffusion	$D_{if} = -\frac{\partial}{\partial x^*}\frac{\overline{k^* u'^*}}{2} - \frac{\partial}{\partial y^*}\frac{\overline{k^* v'^*}}{2} + \frac{1}{\mathrm{Re}_D}\left(\frac{\partial^2}{\partial x^{*2}} + \frac{\partial^2}{\partial y^{*2}}\right)\overline{k^*}$		Gain(+) Loss(-)
Pressure	$Pres = C - P - D_{is} - D_{if}$		Loss(+) Gain(-)

In Wygnanski's work (Wygnanski and Fiedler 1970), at high-Reynolds-number turbulent mixing layer, the total dissipation term can be estimated by $9\overline{(\partial u'/\partial x)^2}/Re$. However, this is not applicable in an unforced laminar mixing layer. As the axis of large scale vortex is in spanwise and the distribution of vorticity in each vortex is almost axisymmetric as shown in Figure 1.22(a), we adopt a revised asymmetric model to approximate the dissipation rate. From the work of George et al. (George and Hussein 1991), we have:

$$\varepsilon = -\frac{1}{Re}\left[-\overline{\left(\frac{\partial w'^*}{\partial z^*}\right)^2} + 2\overline{\left(\frac{\partial w'^*}{\partial x^*}\right)^2} + 2\overline{\left(\frac{\partial u'^*}{\partial z^*}\right)^2} + 8\overline{\left(\frac{\partial u'^*}{\partial x^*}\right)^2}\right]$$

Because $\overline{(\partial w'^*/\partial z^*)^2} = 3\overline{(\partial u'^*/\partial x^*)^2} - \overline{(\partial u'^*/\partial y^*)^2}$, we have:

$$\varepsilon = -\frac{1}{Re}\left[2\overline{\left(\frac{\partial w'^*}{\partial x^*}\right)^2} + 2\overline{\left(\frac{\partial u'^*}{\partial z^*}\right)^2} + \overline{\left(\frac{\partial u'^*}{\partial y^*}\right)^2} + 5\overline{\left(\frac{\partial u'^*}{\partial x^*}\right)^2}\right]$$

The first two terms can be estimated by the relevant quantities in the potential flow region, which is between the mixing layer and wall boundary layer, as below:

$$\overline{(\partial u'^*/\partial z^*)^2} \approx \overline{(\partial w'^*/\partial x^*)^2} \approx \overline{(\partial u'^*/\partial z^*)^2_{pot}} \approx \overline{(\partial w'^*/\partial x^*)^2_{pot}} \approx \overline{(\partial u'^*/\partial y^*)^2_{pot}}$$

Here, the subscript "pot" means the quantities in potential flow region. As will see, the $\overline{(\partial u'^*/\partial y^*)^2}$ term doesn't exactly equal to $\overline{(\partial v'^*/\partial x^*)^2}$. And so does the relation between $\overline{(\partial u'^*/\partial x^*)^2}$ and $\overline{(\partial v'^*/\partial y^*)^2}$. Thus, for a better estimation, the dissipation rate in mixing layer can be roughly evaluated by:

$$\varepsilon = -\frac{1}{Re}\left\{4\overline{\left(\frac{\partial u'^*}{\partial y^*}\right)^2}_{pot} + \frac{1}{2}\left[\overline{\left(\frac{\partial u'^*}{\partial y^*}\right)^2} + \overline{\left(\frac{\partial v'^*}{\partial x^*}\right)^2}\right] + \frac{5}{2}\left[\overline{\left(\frac{\partial u'^*}{\partial x^*}\right)^2} + \overline{\left(\frac{\partial v'^*}{\partial y^*}\right)^2}\right]\right\} \quad (1.14)$$

Strictly say, this is a rough estimation. But it's sufficient in unforced flow, no matter in the mixing layer or the surrounding potential flow.

Each of the convection, production, diffusion, pressure transport and dissipation terms in unforced mixing layer are spatially averaged in y-direction and plotted in Figure 1.34, respectively. The definition of the terms is listed in Table 1.2.

From Figure 1.34(*a*), it can be seen the total turbulent energy convection term *C* is dominated by its component C_1, i.e. $U^* \partial\overline{k^*}/\partial x^*$, due to the high U^*. This is the same as in traditional mixing layer where streamwise mean velocity controls the convection

transport process. The contribution of the vertical transport is very limited due to the lower C_2. The term C varies wavily with streamwise position. As U^* is always positive and has smooth distribution in FOI, the variation should be attributed to the variation of spatially averaged $\partial \overline{k^*}/\partial x^*$ due to the inhomogeneity of mixing layer.

The averaged production terms are plotted in Figure 1.34(b). It can be seen, the production term P of turbulent energy is determined by P_1, i.e. $-\overline{u'^*v'^*}\,\partial U^*/\partial y^*$. It is always positive which exhibits the kinetic energy transfer from mean flow to fluctuating flow. Hence, there is no apparent difference in momentum transfer process between unforced free and confined mixing layer.

The measureable terms of dissipation are plotted in Figure 1.34(c). As mentioned before, D_{is1} and D_{is4} are not the same. So does D_{is2} and D_{is3}. However, $2(D_{is1}+ D_{is4}) \approx D_{is2}+ D_{is3}$. That's why we use their averaged value in Equation (1.14).

In Figure 1.34(d), all the total terms are plotted and compared. The production term P is a little higher than the absolute value of D_{is}. Hence, the turbulent energy can increase with the downstream position. As the diffusion term (D_{if}) will not lead to the change of turbulent energy, but its distribution. The averaged D_{if} term is nearly 0.

The terms vs y^* at x^*=0.85 are plotted in Figure 1.35. Similar as its averaged value, the term P is dominated by P_1, as shown in Figure 1.35(b). Although P_4 term ($P_4 = -\overline{(v'^*)^2}\,\partial V^*/\partial y^*$) is also detectable, its contribution to P is minus. P majorly locates in the mixing layer while its peak bias to high-speed side. So does the high-dissipation region as shown in Figure 1.35(c).

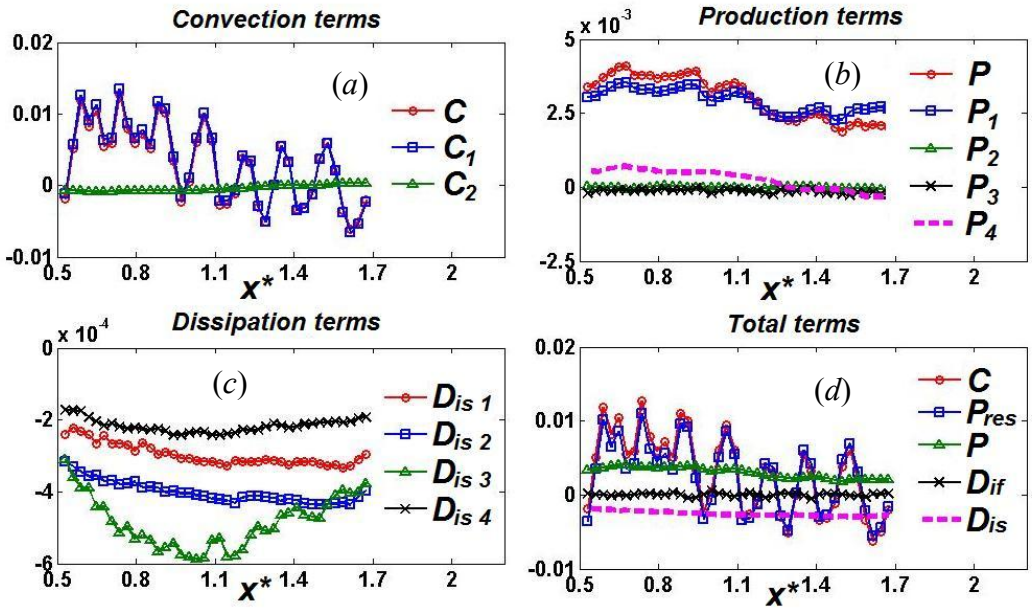

Figure 1.34. Spatial averaged terms in turbulent energy equation, unforced flow. (a) Convection terms, (b) Production terms, (c) Dissipation terms, (d) Total terms.

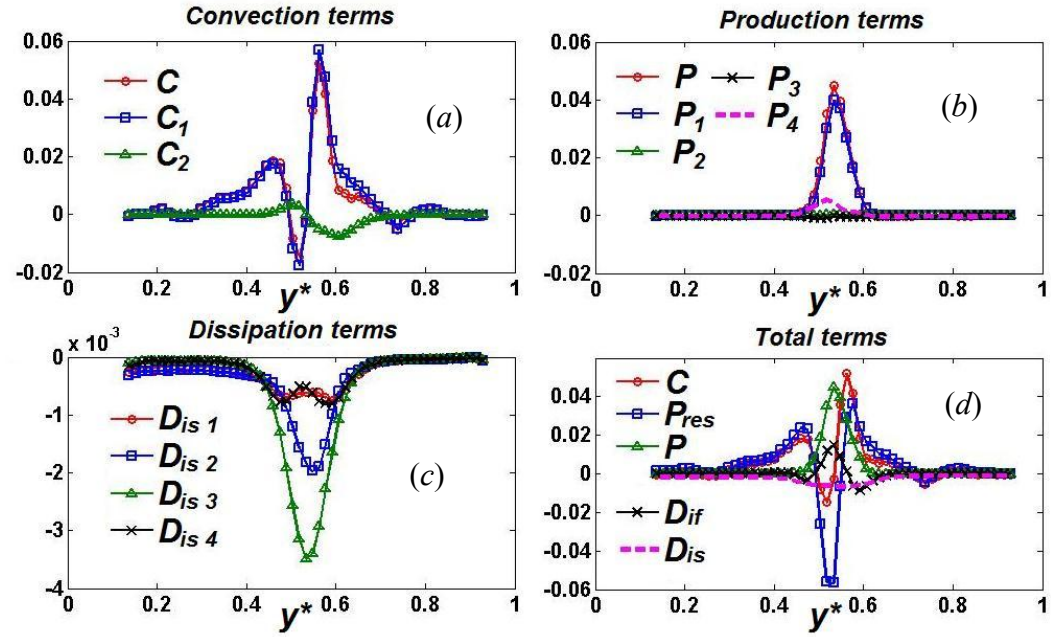

Figure 1.35 Turbulent energy terms vs y^* in unforced flow, (a) Convection terms, (b) Production terms, (c) Dissipation terms, (d) Total terms.

From the expression above, we can see in the FOI, the turbulent energy evolution of unforced flow of confined mixing layer is not apparently different from the free mixing layer. This indicates the same dominant evolution mechanism of unforced mixing layer.

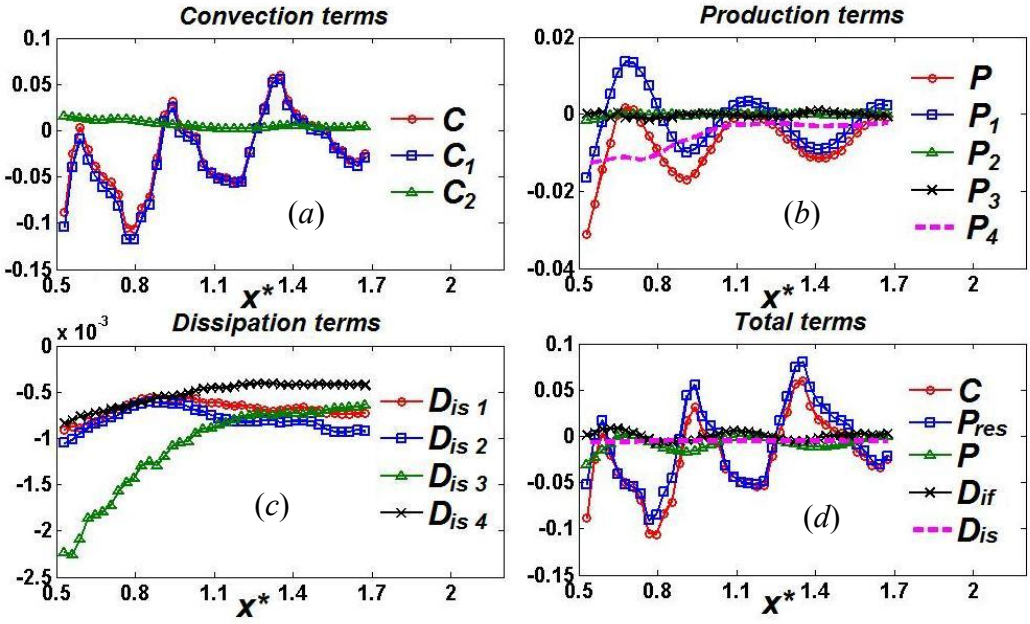

Figure 1.36 Spatial averaged terms in turbulent energy equation, 5.3 Hz, A_{fm}=21.9%. (a) Convection terms, (b) Production terms, (c) Dissipation terms, (d) Total terms.

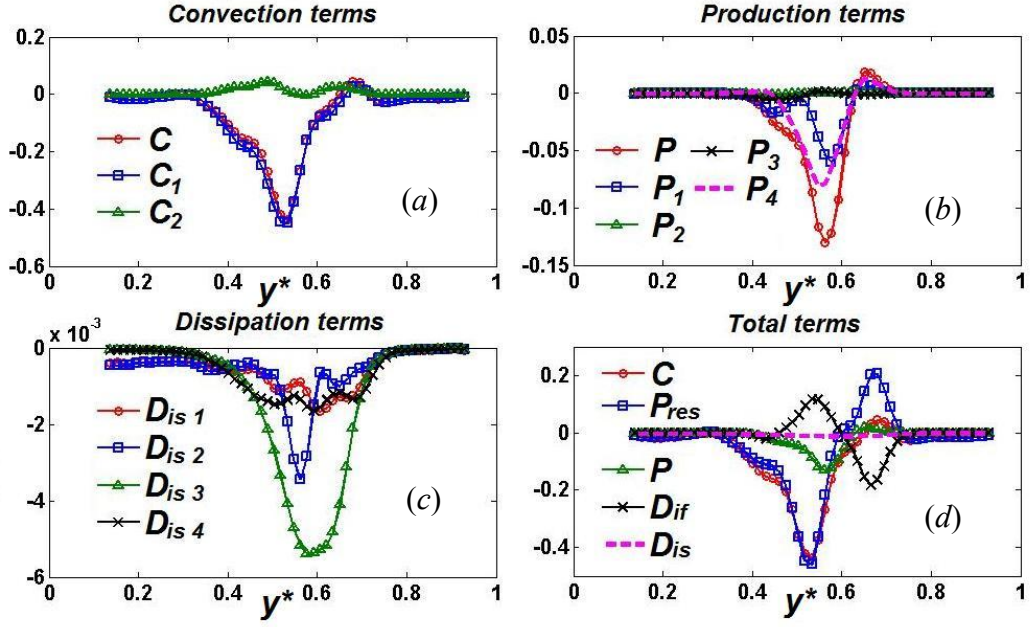

Figure 1.37 Turbulent energy terms vs y^*, 5.3 Hz, A_{fm}=21.9%. (a) Convection terms, (b) Production terms, (c) Dissipation terms, (d) Total terms.

But, this is not true for confined mixing layer when forced at 5.3 Hz and A_{fm}=21.9%.

First, as shown in Figure 1.36(*a*) and Figure 1.37(*a*), no matter averaged or not, the C and C_1 become majorly negative compared to the unforced case which exhibits the convection transport is opposite to the direction of local mean velocity. This indicates the direction of turbulent energy increasing is reverse to the mean flow velocity. In other words, the development of kinetic energy is not along with flow, but decreases with it. It's apparently not the result of K-H instability as it is convective unstable, not absolute one. This phenomenon is consistent with acoustic shedding vortex of which the initial turbulence energy is maximum and later decreases along streamwise direction. From Figure 1.36(*a*), it can be seen also the C_2 term is not neglectable. Although still much smaller than the C_1 term, it's still high enough to be comparable to other terms, such D_{is} and P. This indicates imaginable momentum and energy transport in vertical direction.

Second, the production term P becomes majorly negative as plotted in Figure 1.36(b) and Figure 1.37(b). From latter figure, we can find this is mainly caused by the highly negative P_4 term, especially at the region near the trailing edge. P_1 is not so important as in unforced flow and its value becomes more negative. The negative P indicates the existence of reverse energy transport of turbulent energy and relaminarization of flow in the FOI.

Third, from Figure 1.36(*c*) and (*d*), it can be seen the absolute value of dissipation terms are all very small compared with that of term P, especially at the smaller x^*. It is more apparent from the vertical distribution in Figure 1.37(*d*). This means most of the turbulent energy is not dissipated as heat, but transported back to the mean flow which leads to the wavy U and V profile.

(b) From cross view

As elucidated above, the vertical mean velocity is due to the streamwise vortex. And in the energy evolution from side view, the vertical mean velocity absorbs kinetic energy from velocity fluctuations. Hence, in this section, we attempt to detailed investigate the action of streamwise vortex in turbulent energy transport from cross view, and through what way, the turbulent energy is transferred to mean flow field.

All the predictable terms in cross section are listed in Table 1.3. The total dissipation D_{isc} is simply evaluated as below to estimate the contribution of cross-sectional quantities (by subscript "C"):

$$D_{isC} = D_{isC1} + D_{isC2} + D_{isC3} + D_{isC4}$$

All terms are spatially averaged in the cross-section. And the results of unforced flow and forced at 5.3 Hz where A_{fm}=11% are plotted in Figure 1.38.

In the unforced flow, as the 3-dimensionality is very weak in most of the cross-sectional region, the contribution of P_C and C_C terms to turbulent energy are considerable smaller than in the side-view plane. The P_C is still positive, but its magnitude is much smaller than that of D_{isC}. Thus, the net contribution of secondary vortex is negative, i.e. loss. This should be parts of the reason why even at high Re, the mixing layer is still stable and transient happens much later, as introduced in previous sections.

Table 1.3 The definitions of turbulent energy terms in cross section

Terms	Expressions		Contribution to turbulent energy(Sign)
Convection	$C_{C1}=W^*\partial\overline{k^*}/\partial z^*$	$C_{C2}=V^*\partial\overline{k^*}/\partial y^*$	Loss(+) Gain(-)
	$k^*=\left(w'^*\right)^2+\left(v'^*\right)^2$	$C_C=C_{C1}+C_{C2}$	
Production	$P_{C1}=-\overline{v'^*w'^*}\,\partial W^*/\partial y^*$	$P_{C2}=-\overline{v'^*w'^*}\,\partial V^*/\partial z^*$	Gain(+) Loss(-)
	$P_{C3}=-\overline{\left(w'^*\right)^2}\,\partial W^*/\partial z^*$	$P_{C4}=-\overline{\left(v'^*\right)^2}\,\partial V^*/\partial y^*$	
	$P_C=P_{C1}+P_{C2}+P_{C3}+P_{C4}$		
Dissipation	$D_{tC1}=-\overline{\left(\partial w'^*/\partial z^*\right)^2}\Big/\mathrm{Re}_D$	$D_{tC2}=-\overline{\left(\partial w'^*/\partial y^*\right)^2}\Big/\mathrm{Re}_D$	Loss(-)
	$D_{tC3}=-\overline{\left(\partial v'^*/\partial z^*\right)^2}\Big/\mathrm{Re}_D$	$D_{tC4}=-\overline{\left(\partial v'^*/\partial y^*\right)^2}\Big/\mathrm{Re}_D$	
Diffusion	$D_{tC}=-\frac{\partial}{\partial x^*}\frac{\overline{k^*u'^*}}{2}-\frac{\partial}{\partial y^*}\frac{\overline{k^*v'^*}}{2}+\frac{1}{\mathrm{Re}_D}\left(\frac{\partial^2}{\partial x^{*2}}+\frac{\partial^2}{\partial y^{*2}}\right)\overline{k^*}$		Gain(+) Loss(-)

As the 3-dimensionality becomes important, the situation is changed. While forced at 5.3 Hz and A_{fm}=11%, more than half of the terms become more negative than in unforced flow. As a result of the mean flow by streamwise vortex, the convection term, especially the C_{C2}, becomes much higher than unforced flow. The convection terms and also the diffusion terms only affect the distribution of turbulent energy. They have no contributions to the total turbulent energy.

The total turbulent energy can only be affected by both the production and dissipation terms. From the figure, it can be seen dominated by P_{C4}, the total production term P_C is highly negative. Its absolute value is about 2~3 orders than unforced case. The loss of turbulent energy caused by reversed transport is even faster than the dissipation. This is consistent with the found in side-view plane. There are two dominant terms, one is P_4, the

other is P_2. Both of them are tightly related with streamwise vortices. P_4 is controlled by the mean component of streamwise vortices, while the P_2 is related to the vorticity fluctuations, through Reynolds stress in cross section. The D_{isC} is also 3 times larger than the unforced case. In the known 4 dissipation terms, compared with the unforced case, the most rapidly increased terms are D_{isC2} and D_{isC3}, which are both related to the fluctuating streamwise vortex. The tightly relation between fluctuating streamwise vortex and the dissipation is verified in Figure 1.39 by means of the absolute value of D_{isC} and enstrophy of streamwise vorticity fluctuations.. It can be seen, the high dissipation region is highly consistent with the high enstrophy region, which verifies the supposed effect of streamwise vortex structures.

Hence, the influences of streamwise vortex can be summaried: First, through the mean streamwise vorticity, the turbulent energy is reversely transported to mean flow and cause relaminarization of flow. Second, rapid dissipation can be induced by the fluctuating streamwise vorticity.

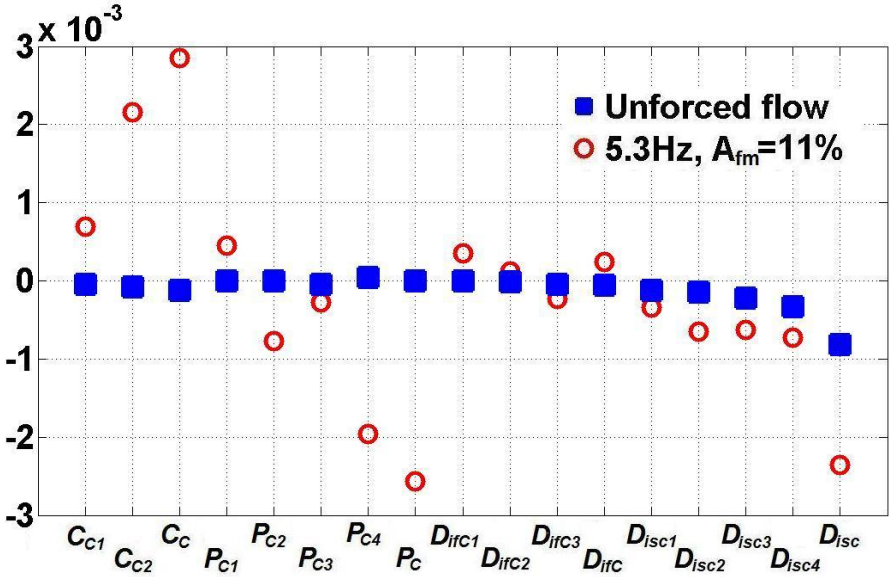

Figure 1.38 The spatial averaged terms of turbulent energy at cross-section x^*=0.85.

Re=2939, λ=1/3.

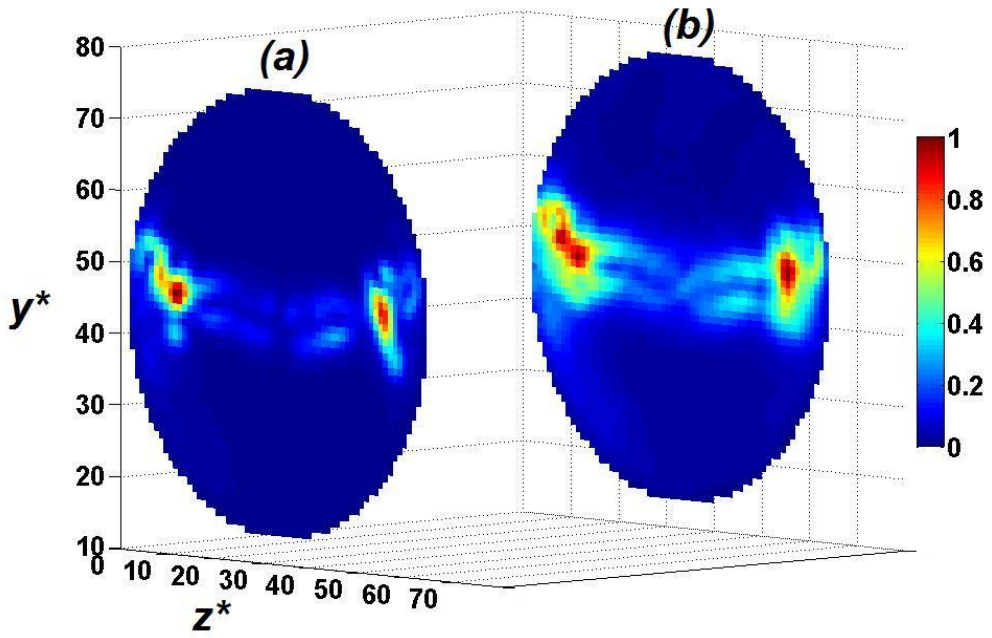

Figure 1.39 The comparison between (a) the time-averaged enstrophy of streamwise vorticity fluctuations and (b) the absolute value of D_{isC}.

1.4.2.6 Supplementary on mass transport

In free mixing layer, no matter forced or not, the mixing process and mass transportation is determined by the velocity fluctuations due to large scale spanwise vortices. However, in confined mixing layer, it can be found the high velocity fluctuations not necessarily leads to rapid mixing and high spreading ratio. For example, under A_{fm}=11%, even the fluctuation of *v'* constituent under 5.3 Hz is not so outstanding as 3.5 Hz (Figure 1.15(*a*)), the spreading angle is actually apparently larger than latter, as shown in Figure 1.40. Hence, we believe the *V* constituent of mean velocity plays important role in the spreading of mixing layer and so does the scalar transport process. This can be briefly described by the scalar transport equation, as below:

$$\frac{\partial c'}{\partial t} + U_i \frac{\partial c'}{\partial x_i} + u_i' \frac{\partial C}{\partial x_i} + \nabla \cdot (c'u' - \overline{c'u'}) = D \frac{\partial^2 c'}{\partial x_i \partial x_i}$$

$$(a) \qquad (b) \qquad (c) \qquad (d) \qquad (e) \qquad (1.15)$$

In our experiments, either the concentration of tracing particles or fluorescent dye solution is not high enough to induce apparent dynamical effect. Hence the scalar transport is a passive process and the term (*d*) in Equation (1.15) can be neglected. On large scale, the influence of diffusion term (*e*) can also be discarded due to the high Schmidt number (~2000). Thus, the mixing process is dominated by the convection terms, i.e. term (*b*) $U_i \, \partial c' / \partial x_i$, which is through the mean velocity distribution, and term (*c*) $u_i' \, \partial C / \partial x_i$ by velocity fluctuations.

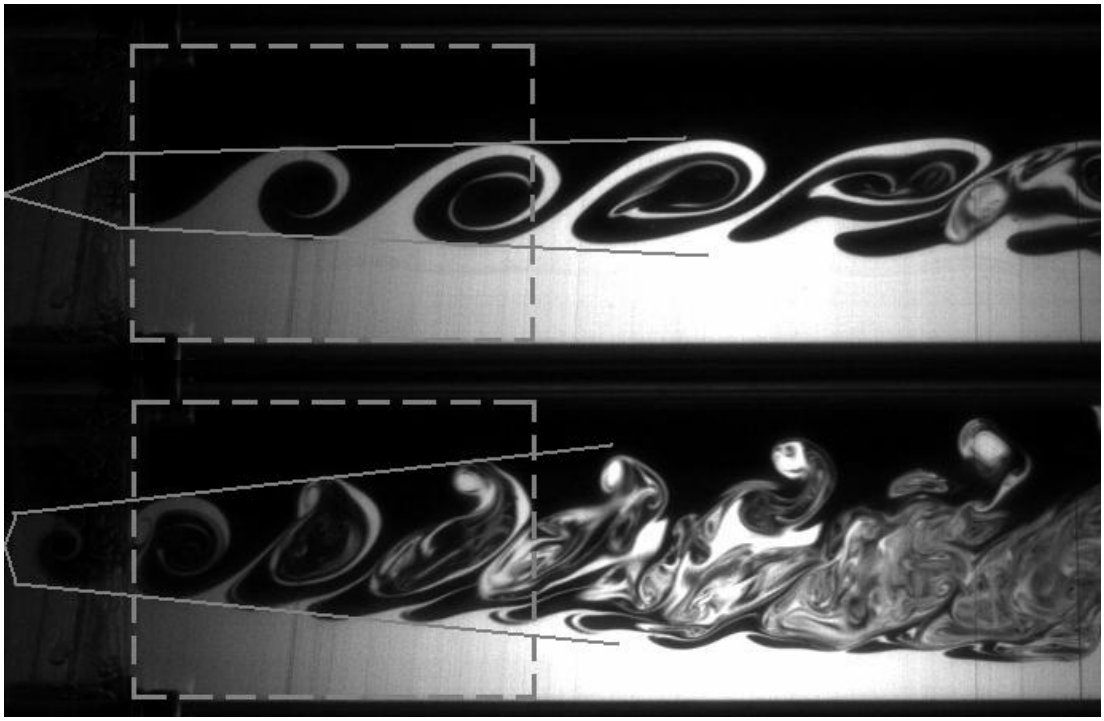

Figure 1.40 Flow visualization of forced flow when *Re*=2939, λ=1/3, A_{fm}=11%. (*a*) 3.5 Hz, (*b*) 5.3 Hz.

In forced free mixing layer, as lacking of the transverse mean velocity, the scalar transport by convection in this direction is only dominated by the *v'*. While in confined mixing layer, especially at A_{fm}=21.9%, except for the high velocity fluctuations, the vertical constituent of mean velocity is also high enough to induce intensively and continuously vertical transport. This can also be concluded through the streamline of mean flow in Figure 1.11(*c*).

Hence, the scalar transport process in forced flow can be described as: First, in the first stage, strongly spanwise vortices are generated, due to acoustically induced shedding vortex. Accompanied is the intensive velocity and scalar fluctuations, and the gradients of both *c'* and *C*. The scalar is passively transported by the velocity fluctuations and forms mixing layer with large initial spreading rate. Then, in the second stage, under the influence of $V\,\partial c'/\partial y$, the scalar is transported in vertical direction, due to the existence of mean streamwise vortex structures. Except for the convection due to mean flow, the scalar transport by velocity fluctuations such as $v'\,\partial C/\partial y$ and $w'\,\partial C/\partial z$, are also important. The former one will enhance the mixing in y-direction, and the latter one will sooner enhance the mixing in z-direction, to achieve fast mixing. Meanwhile, still under the influence of *dV/dy*, the vortices are rapidly stretched and broken which lead to astonishing uniform mixing downstream.

1.4.3 Conclusion

In this section, the rapid mixing found by Wang (Wang 2003; Wang 2006) is detailed investigated by PIV system. Compared with the traditional free mixing layer, where the

initial mixing depends on convective scalar transport by velocity fluctuations, in confined mixing layer, the mixing process can be separated into two stages. The first stage is related to acoustically induced shedding vortex, which will be introduced in section 1.5. In the second stage, both the mean and fluctuating vertical velocities work together to enhance the mass transport and the subsequent mixing process. Here, several major conclusions are summarized.

(1) The unforced confined mixing layer has similar universal law of momentum thickness ($\theta_m \sim x^{0.5}$) of mixing layer as in conventional free mixing layer. But at the equivalent Re_θ range, confined mixing layer has larger $d\theta_m/dx$ than in free mixing layer. And the confined mixing layer is more stable (require larger transient Re_θ) than free mixing layer.

(2) The receptivity of 5.3 Hz is the highest in nozzle section, but becomes much weaker in the downstream of mixing chamber. The turbulent energy is "lost". The "lost" turbulent energy is majorly converted to the mean flow energy by the reverse transport process and relaminarization, which results in the highly wavy *U* profile, and large *V* component. And minor dissipated by vortex structures.

(3) A "turn-over" point of forcing intensity is found which suggests there should be at least two different mechanisms competed with each other to dominate flow. At low forcing intensity, based on K-H instability, subharmonic mode is the dominant mechanism of mixing enhancement. While forcing at 5.3 Hz with sufficiently large forcing intensity, subharmonic mode is insignificant and the flow is dominated by the forcing frequency, not the intrinsic frequency of flow instability, and acoustically induced shedding vortex

becomes important. The short-term effect is also consistent with the existence of acoustically induced shedding vortex. The "turn-over" point can also be considered as a critical point that the flow is transferred from 2-D dominant to 3-D dominant.

(4) From vortex dynamics, the large V component is generated by streamwise vortex structures. Recently, corner vortex mechanism is a reasonable explanation, even though there are still many unsolved questions. Before these problems are solved, we cannot simply ignore other mechanisms arbitrarily, due to the complexity of flow.

(5) Strong V not only enhances the transport of momentum, scalar and energy in vertical direction, but also cause the spanwise vortex to be extremely unstable by high dV/dy. The vortices are stretched and broken down more earlier than other cases which results in faster and more homogeneous mixing.

1.5 Parametric investigation on the mechanism corresponding to the optimal frequency

1.5.1 Flow instability

In previous several sections, several instability mechanisms have been discussed, such as K-H instability, corner flow instability, traveling wave instability. As analyzed above, K-H instability and traveling wave instability are not related to the optimal frequency. Corner flow instability exhibits highest receptivity at 5.3 Hz. However, there are still many unsolved questions, especially the instability frequency of corner flow should be varying with bulk flow Re. Furthermore, even corner flow instability has receptivity at 5.3 Hz, its

velocity fluctuations should be in cross-section, not in streamwise. This is also conflict with what we found in nozzle section.

There are also some other possible mechanisms, such as Taylor-Görtler vortex and even non-model mode which is very popular recently. However, to our knowledge, no one exhibits similar behaviors and specifications as in the confined mixing layer.

1.5.2 Acoustic resonance

The major character of the optimal frequency is unchanging with Re and shear ratio, acoustic resonance is a possible mechanism of the fast mixing.

As the frequency of acoustic resonance is determined by the size and shape of cavity, changing the size and shape is the major method in this research. Due to the existence of contraction section and the optical vessel at the end of mixing chamber, the flow field can be separated into several parts from the valve to the waste water tank. First are the water supply pipes. Second is the settling chamber. Third is the mixing chamber where the mixing happens. And the last are the drain pipes. However, the influence of drain pipes can be excluded. This will be explained later.

1-D acoustic model

Due to the geometric structures of the water tunnel, the acoustic resonance can be in either axial or transverse direction. The axial resonance in pipe-like cavity can be described

using an 1-D model (Rienstra and Hirschberg 2009), if the condition of a plane wave approximation is satisfied, which is

$$f_{bd} \ll f_f < f_c \tag{1.16}$$

where f_f is the forcing frequency, $f_{bd} = 2\nu/\pi D_i^2$ is the frequency that the boundary effect cannot be neglected and $f_c = c_0/2D_i$ is the "cut-off" frequency for 1-D model. In water, the acoustic speed c_0=1450 m/s and the kinematic viscosity ν=10^{-6} m^2/s. The inner diameter of the mixing chamber is D_i = 41.3 mm. Hence, f_{bd} and f_c equals to 3.7×10^{-4} Hz and 1.8×10^4 Hz respectively. However, the frequency range we studied in is normally 1<f_f<50Hz. The condition in Equation (1.16) is apparently satisfied and the 1-D approximation is reliable here.

The resonance frequency in 1-D duct segment or pipe can be estimated by Equation (1.17) (Rienstra and Hirschberg 2009):

$$f_{r,axi} = \frac{kc_0}{2L},\ \mathrm{k} = 1,2,3\cdots \tag{1.17}$$

where $f_{r,axi}$ is the axial resonance frequency, L is the distance from nozzle to the end of optical vessel (i.e. the sum of the length of mixing chamber and optical vessel). As the convection velocity of bulk flow is much smaller than the sound speed, the change of acoustic resonance frequency due to Doppler effect is also negligible. Equation (1.17) is a proper estimation of the acoustic resonance frequency.

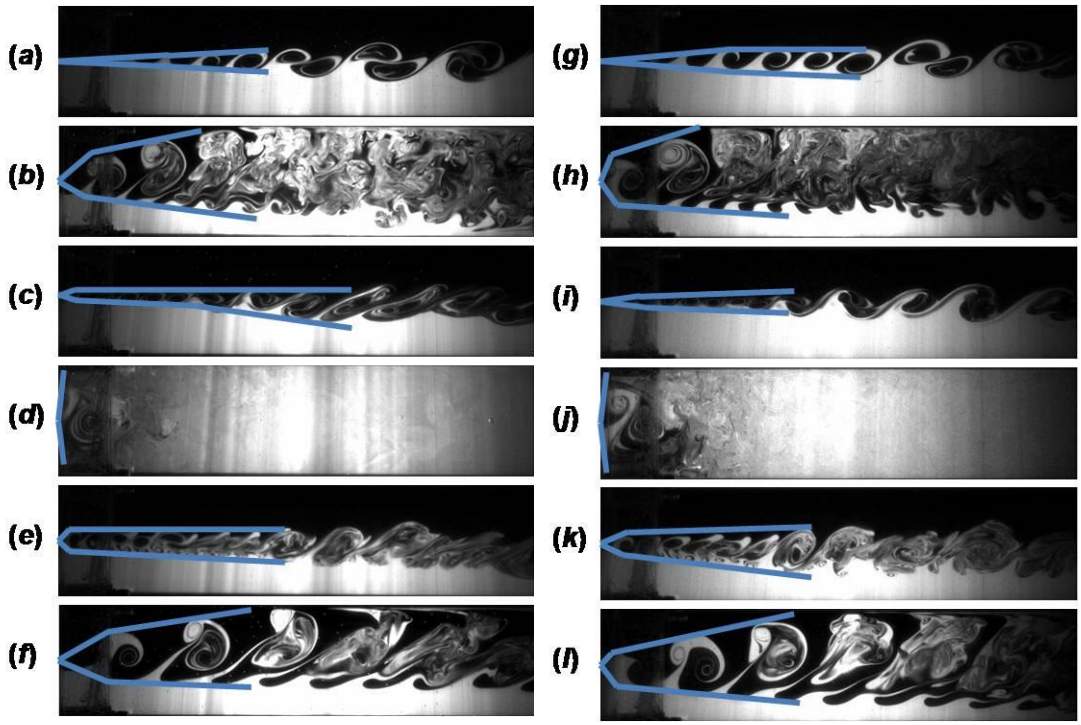

Figure 1.41. The influence of pipe length. Here, Re=2939, λ=1/3. (*a-f*) is for the pipe length equals to 0.375m, while that in (*g-l*) is 1.875m. (*a, g*) no actuating, (*b, h*) f_f=5.3 Hz, A_{fm} =21.9%, (*c, i*) f_f=10 Hz, A_{fm} =21.9%, (*d, j*) f_f=5.3 Hz, A_{fm} =94.8%, (*e, k*) f_f=10 Hz, A_{fm} =94.8%, (*f, l*) f_f=3.5 Hz, A_{fm} =21.9%.

Axial resonance in the mixing chamber

If axial resonance exists in the mixing chamber, the resonant frequencies should be varied with the lengths of mixing chamber. Hence, two mixing chambers with the same inner diameter but different lengths are employed. The shorter one is 0.375 m long, and the longer one is 1.875 m. Thus, the corresponding L for the two cases is 0.458 m and 1.958 m respectively.

The experiments are conducted under Re=2939 and λ=1/3. The unforced case is investigated first in order to make comparison. Results are shown in Figure 1.41(a) and (g). It can be seen, no matter the topology of vortex structures or the spreading angles of mixing layer (marked by blue lines), are almost the same in the two mixing chambers. The vortex

passage frequencies are both about 7 Hz. The unforced flow is still dominated by Kelvin-Helmholtz (KH) instability in the image region. Because KH instability is convectively unstable, not absolutely, the downstream velocity disturbance caused by the optical vessel due to the shortened mixing chamber cannot propagate upstream. The changing of mixing chamber won't affect the characteristics of basic flow and its instability which guarantees the validation of the comparison. This also explains why the drain pipes cannot be the resonance chamber that dominates the mixing enhancement.

In each mixing chamber, detailed investigations were conducted from 1 to 45 Hz at the same normalized forcing intensity.

Results at five actuating modes are shown in Figure 1.41, which are 3.5 Hz (sub-harmonic frequency), 5.3 Hz (optimal frequency) and 10 Hz with actuating intensity A_{fm}=21.9% and forcing at 5.3 Hz and 10 Hz while A_{fm}=94.8%, respectively. It can be seen, in the shorter mixing chamber under low forcing intensity, A_{fm}=21.9%, the optimal frequency of mixing enhancement is 5.3 Hz, as indicated in Figure 1.41(*b, c, f*). Although, at the sub-harmonic frequency, the spreading rate of mixing layer is comparable to that at 5.3 Hz. The mixing effect of small scale is definitely weaker. The inclined counter-rotation vortex pairs clearly indicate the mixing process is not governed by the well-known sub-harmonic mode (Ho and Huang 1982)(which should result in rolling co-rotation vortices downstream) in free mixing layer. While A_{fm} increases to 94.8%, the ultra fast mixing appears at 5.3 Hz as shown in Figure 1.41(*d*). The spreading rate reaches almost 180 degrees. Compared is that at 10 Hz (Figure 1.41(*e*)), the spreading rate is much smaller.

Similar phenomenon is also found in the longer mixing chamber, as shown in the right column of Figure 1.41. No matter the mixing effect or the topological structures of spanwise vortices exhibits no essential difference. It indicates the optimal frequency, 5.3 Hz, is independent of the length of mixing chamber.

This is conflicted to Equation (1.17) if the optimal frequency is the acoustic resonance. In the mixing chamber, the resonance frequencies are 1583 Hz (shorter mixing chamber) and 370 Hz (the longer one) respectively, which are far from 5.3 Hz. Even though kinder of error may exist, the inverse proportional relation between resonance frequency and L should be hold. However, such relation isn't observed either. Thus, the axial acoustic resonance should not be the reason of the rapid mixing.

Axial resonance in the settling chamber

The settling chamber provides another possible resonance cavity in the flow field. Mixing doesn't take place directly in settling chamber. However, once highly fluctuated flow is generated in the settling chamber, the disturbance may propagate downstream to the mixing chamber and induce the fast mixing.

Qualitative investigation by changing the length of settling chamber is conducted. The shortened settling chamber is schemed in Figure 1.42. All the screens and honeycombs are removed to minimize the length of the settling chamber. Only the contraction section and the splitter plate are reserved. Compared to the full settling chamber which is 494 mm long, the length of the shortened settling chamber is only 98 mm.

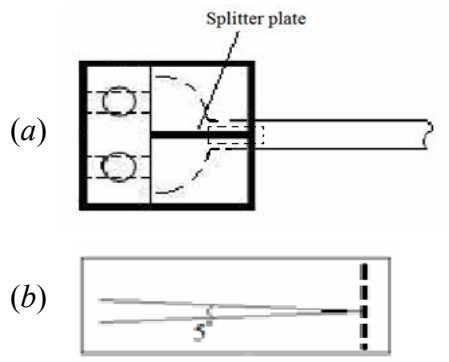

Figure 1.42 (a) The shortened settling chamber, (b) The shape of the trailing edge of splitter plate.

Figure 1.43 Mixing effect in the mixing chamber with shortened settling chamber. Here, Re=2939, λ=1/3. (a) no actuating, (b) f_f=5.3 Hz, A_{fm}=94.8%, (c) f_f=10 Hz, A_{fm}=94.8%

The experiments are carried out at Re=2939 and λ=1/3 in the longer mixing chamber as in section 3.1. The results are shown in Figure 1.43. From Figure 1.43(*a*), it can be seen removing the screens and honeycombs severely decrease the quality of unforced flow. The disturbance of unstable inlet flow is so strong that it becomes impossible to estimate the mixing enhancement effect between unforced flow and the forced flow under lower actuating intensity, such as A_{fm}=21.9%. Hence, in this section, all the comparison between forced flows are carried out at A_{fm}=94.8%. As shown in Figure 1.43(c), at f_f=10 Hz, the mixing effect is not unambiguously better than the unforced case. However, the mixing at f_f=5.3 Hz is still surprisingly fast (Figure 1.43(*b*)), just like in the full settling chamber (Figure 1.41(*j*)). Detailed investigations from 3 Hz to 45 Hz indicate 5.3 Hz is still the optimal frequency in the shortened settling chamber. Only in a narrow band of frequency around 5.3 Hz, fast mixing can be achieved. This proves 5.3 Hz should not be the frequency of axial acoustic resonance in the settling chamber.

Meanwhile, it can be seen, due to the poor quality of inlet flow, the KH instability and the spanwise vortices are indistinguishable. However, the large counter-rotation spanwise vortices related to the fast mixing are still observable. This indicates high receptivity of the flow at the optimal frequency. The insensitivity to initial conditions is very important and greatly favored in many industry fields. From this character, the mixing equipments can be extraordinarily simplified.

Transverse resonance in the mixing chamber

The fast mixing at the nozzle indicates high transverse velocity fluctuation and momentum transfer. Except the flow instability, the transverse acoustic resonance can also generate strong velocity fluctuations in the y direction. The transverse resonance of water is sensitive to both the diameter and shape of the mixing chamber(Rienstra and Hirschberg 2009). A rough but effective way to estimate the influence of transverse acoustic resonance is changing the diameter of mixing chamber, as been diagramed in Figure 1.44.

The diameter of the narrower section in the mixing chamber is 21.2 mm and the length is 82.5 mm. A custom-made tube is inserted into the inlet of the longer mixing chamber with the presence of full settling chamber. Based on the smaller diameter, the Reynolds number and λ are still 2939 and 1/3 respectively. The full settling chamber is used for better flow visualization and comparison.

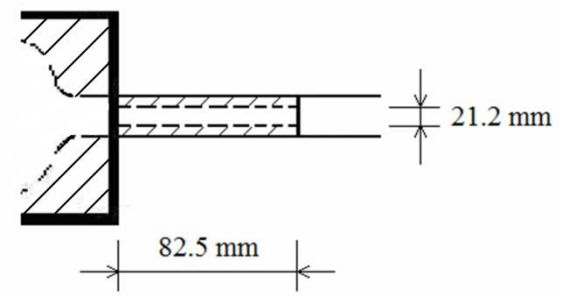

Figure 1.44 The diagram of the narrower mixing chamber

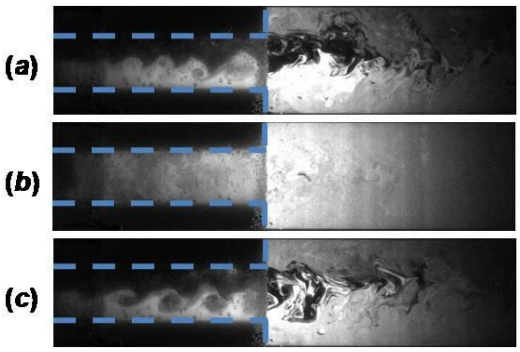

Figure 1.45 Mixing effect in the mixing chamber with new inlet section. Here, Re=2939, λ=1/3, the length of the inlet section is 82.5mm, (a) no actuating, (b) f_f=5.3 Hz, A_{fm}=62.7%, (c) f_f=11 Hz, A_{fm}=62.7%

The results are shown in Figure 1.45. Dashed lines mark the new edge of the test section. The unforced shear flow is shown in Figure 1.45(*a*). Due to the inserted narrower section, the flow and visualization quality becomes worse. However, blurred but definite vortex street can still be found in this section. The transverse resonance frequency should be inversely proportional to the local diameter of pipe. If 5.3 Hz is the transverse resonance frequency in the original mixing chamber (ID=41.3mm), the value in the inserted section should be around 11 Hz, due to the changing of inner diameter(Rienstra and Hirschberg 2009). However, the experiments clearly indicate 5.3 Hz is still the optimal frequency (Figure 1.45(*b*)). The fast mixing can be achieved at a smaller A_{fm} (62.7%, calculated by the cross-section area of the inserted section and the corresponding bulk flow velocity). Compared to forcing at 5.3 Hz, the mixing enhancement at 11 Hz is extremely limited. Therefore, the optimal frequency is not affected by the transverse size. And the influence of the transverse acoustic resonance in mixing chamber can be ignored.

Transverse resonance in the settling chamber

Similar as in mixing chamber, the influence of transverse resonance in settling chamber cannot be arbitrarily ignored, especially around the trailing edge where sloshing flow may exist. As concluded in section (iii), the shortened settling chamber will not change the optimal frequency and its mixing effect under high forcing intensity, all the experiments in this section will be carried out in the shortened settling chamber with longer mixing chamber.

The influence of nozzle size

The height in nozzle section is locally altered by inserting an aluminum plate at the high speed flow side parallel to the centerline of splitter plate, as shown in Figure 1.46. The plate is 15mm long and 0.8 mm thick which is placed 10 mm away from the splitter plate. Except changing the local dimension in nozzle, the aluminum plate also has another function — inhibiting the possible expanding of sloshing flow in transverse direction around the sharp trailing edge and the induced pre-mixing.

At this case, 5.3 Hz is still the optimal frequency as shown in Figure 1.47(*b*). The optimal frequency is not affect by the locally altered channel size. No matter the mixing effect at 5.3 Hz or 10 Hz (Figure 1.47(*c*)) are not apparently influenced by the inserted plate, compared to Figure 1.43(*b*). The influence of transverse resonance in settling chamber can be excluded.

Removing the splitter plate.

Following the last section, we are curious if the phenomenon is unique in the separated flow field. In other words, if the splitter plate is removed, how will be the mixing enhancement?

The settling chamber without splitter plate is diagramed in Figure 1.48. Without splitter plate, the original flow visualization method with dye solution in one channel and water in another is not applicable here. Instead, a dye solution is injected directly from an air vent on the top of settling chamber. It is impossible to compare the mixing effects with previous experiments that in the presence of splitter plate due to the different visualization method. Hence, what we can do is comparing with the unforced case to see if mixing becomes chaotic or not.

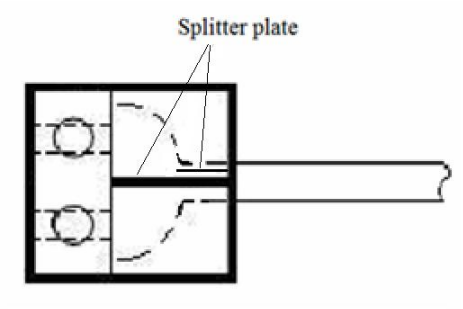

Figure 1.46 The diagram of the asymmetric nozzle section

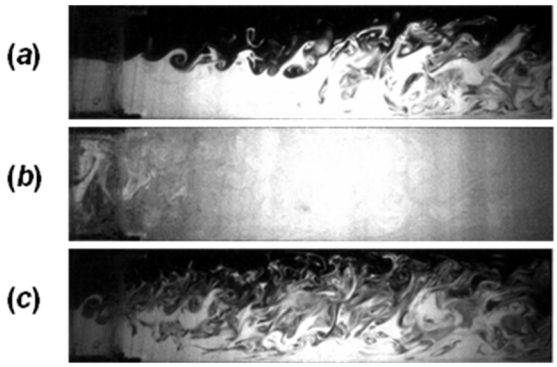

Figure 1.47 Mixing effect at this case, where Re=2939, λ=1/3 and the length of mixing chamber is 1.753 m. (*a*) No actuating, (*b*) f_f=5.3 Hz and A_{fm}=94.8%, (*c*) f_f=10 Hz and A_{fm}=94.8%.

The experiments are first carried out at about Re=600 where the flow is obviously laminar as shown in Figure 1.49. Compared with the unforced flow (Figure 1.49(*a*)), there are no essential changing of flow structures happened in Figure 1.49(*b*) and (*c*). The flow

is typically laminar and the streak-like structures are kept. When we go through from 0.5 Hz to 52 Hz, even under high actuating level, no obvious mixing enhancement is found. To avoid arbitrary, the experiments under Re = 2939 is also conducted. It can be found compared with the flow without forcing (Figure 1.50(*a*)), the forcing at 5.3 Hz with A_{fm} = 94.8% (Figure 1.50(*b*)) doesn't enhance the mixing effect at all. A detailed investigation is conducted from 3 Hz to 70 Hz. Just as under Re=600, there is no noticeable mixing enhancement found under other frequencies in the considered frequency range. Hence, the resonance of acoustic in settling chamber can be excluded

The results indicate the sufficiency of splitter plate and the two-stream flow system in the mixing enhancement.

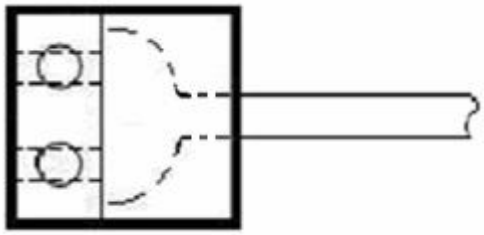

Figure 1.48 The settling chamber without splitter plate

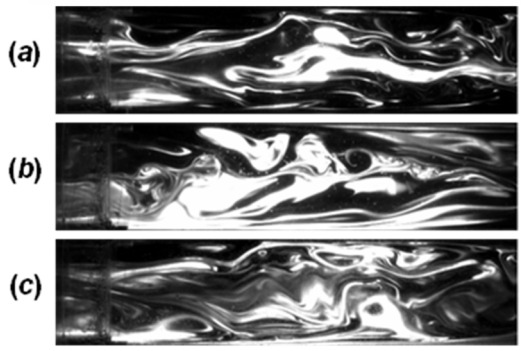

Figure 1.49 Mixing effects in shorter settling chamber without splitter plate. Here, Re=600, λ=1/3. (*a*) No actuating, (*b*) 5.3 Hz, (*c*) 10 Hz.

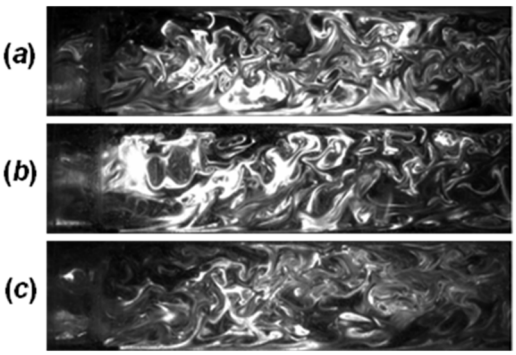

Figure 1.50 Mixing effects in shorter settling chamber without splitter plate. Here, Re=2939, λ=1/3. (*a*) No actuating, (*b*) 5.3 Hz, A_{fm}=94.8% (*c*) 10 Hz, A_{fm}=94.8%.

The influence of the shape of trailing edge

Since the receptivity is the highest at the trailing edge in mixing layers (Ho and Huerre 1984), the trailing edge and its geometry of the splitter plate should play an important role in the development of mixing layers. The geometry of the trailing edge can affect the instability property of free mixing layers (by introducing a region of absolute instability) (Huerre 1990) and their development downstream (Dziomba and Fiedler 1985). Here, we investigate if the geometry (i.e. blunt or sharpness of the trailing edge (Figure 1.51(b)) has influence on the optimal frequency, under which fastest mixing is generated.

The experiments are carried out at Re=2939 and λ=1/3 in the shortened settling chamber. It is found that without forcing (Figure 1.52(*a*)), the mixing effect using blunt trailing edge is better or equals to the case using the sharper one (Figure 1.43(*a*)). Similar result can also be found for the forced flow at 10 Hz (Figure 1.52(*c*)) compared with Figure 1.43(*c*). But at 5.3 Hz, the mixing is much slower with blunt trailing edge than with the sharp trailing edge, as shown in Figure 1.52(*b*) and Figure 1.43(*b*).

There could be two major reasons causing the weaker mixing: one is due to the changing of optimal frequency. Another is that the mixing enhancement mechanism under sharper trailing edge is inhibited. By scanning in the frequency range from 3 to 20 Hz, the first assumption is excluded. Although the mixing effect at 5.3 Hz with blunt trailing edge is much weaker than using the sharper one, it's still the optimal in the frequency range studied.

Compared to the case with sharper trailing edge (Figure 1.43(*b*)), the changing of vortex structures can be found in Figure 1.52(*b*). As shown before, the fast mixing always accompanied with the inclined CRV. However, this commonly existed inclined counter-rotation vortex pair disappeared in this case, even at A_{fm}=94.8%. The blunt trailing edge apparently inhibited the generating of large scale vortex. This is consistent with the founds on acoustically induced shedding vortex in cavity (Matta et al. 1996) and orifice (Ingård and Labate 1950; Ingard and Ising 1967; Disselhorst and Van Wijngaarden 1980; Cummings 1984). It's found when the radius of curvature of the lip is smaller than the acoustic particle displacement, there can exist acoustically induced shedding vortex due to the nonlinear effect and friction. Hence, due to the important action of large scale vortex, this mechanism becomes more attractive and will be investigated in details in future.

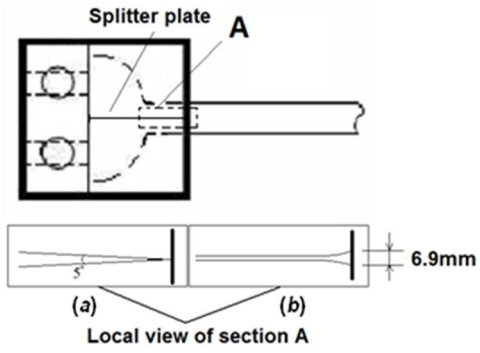

Figure 1.51 The sharp (*a*) and blunt (*b*) trailing edge in this section.

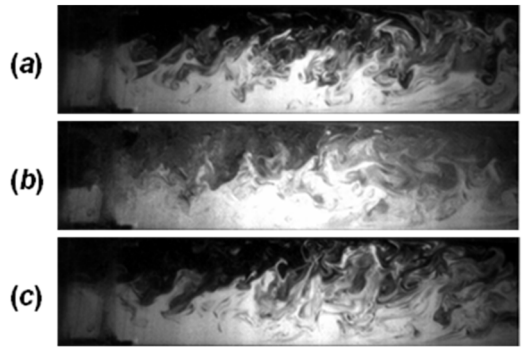

Figure 1.52 The mixing effect under blunt trailing edge. Here, *Re*=2939, λ=1/3. Long mixing chamber and shortened settling chamber are adopted. (*a*) no actuating, (*b*) f_f=5.3 Hz, A_f=94.8%, and (*c*) f_f=5.3 Hz, A_f=94.8%.

Acoustic eigenfrequency computed by Comsol software

To ensure the influence of acoustic, acoustic eigenfrequency of our flow is investigated by the pressure acoustic model of Comsol 4.3. The computing is focused on

the fluid part, not the pipe and other solid part. Hence, the computing region can be plotted as in Figure 1.53. Here, we input plane wave radiation to represent the pressure wave generated by the forcing plate. At the other three inlets and outlet, soft boundary conditions (pressure is equal to external air pressure) are applied. The thickness of split plate is 6 mm and the thickness of tip of trailing edge is 0.1 mm in computing.

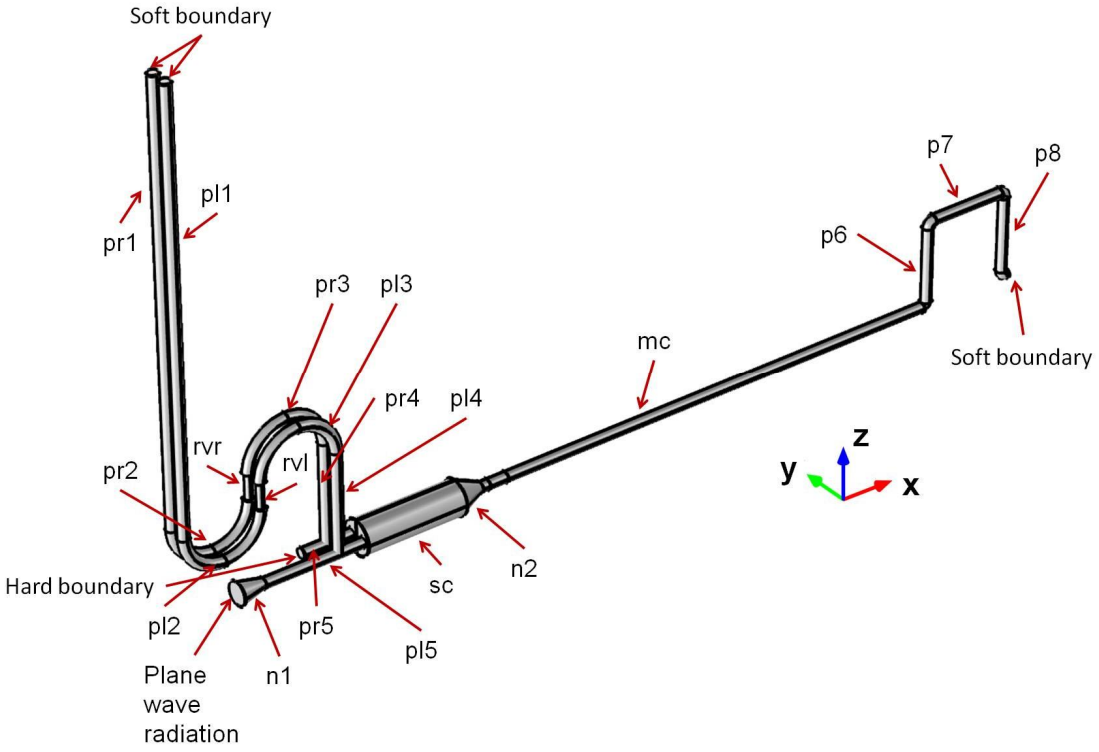

Figure 1.53 The scheme of Comsol simulation. Here, "pl" means the left pipe and "pr" is the right pipe. Single "p" means pipe. "sc" and "mc" are the settling chamber and mixing chamber respectively. "rvl" and "rvr" indicate rotameters and control valves on left and right sides respectively. "n" means nozzle part.

In the investigation, 15 different cases are computed. The details of the cases are listed in Table 1.4 Parameter of the cases computed by Comsol. In this table, "L" and "D" are the length and diameter of corresponding parts respectively. Ds and Dl are the diameter of smaller and larger end of nozzle section. Unit in mm. If no otherwise specified, D of pipes

are all 42 mm.. It can be seen from case 1, the computed solution of fundamental eigenfrequency of water tunnel system is 35.88i. The corresponding frequency is $35.88/2\pi$ = 5.71 Hz, as indicated in Table 1.4. This is consistent with what we find in experiments that the optimal frequency is 5.3 Hz. The isosurface of acoustic pressure field clearly indicates that the flow of LSS can roll back into the HSS by the driving of pressure disturbance, as shown in Figure 1.54. Therefore, the CRV can be successfully induced by the acoustic pressure field. This can explain the reason: in the nozzle section, the velocity fluctuations are still plane wave. But after trailing edge, the CRV are immediately induced when the forcing intensity is strong enough. Hence, both from the frequency and eigenmode of acoustic pressure field, our computing is consistent with what we found in experiments.

By changing the dimension of different parts, we find although slightly changing of fundamental frequency happens, generally, all the computed fundamental frequencies are still around 5.3 Hz. Because in our previous parametric experiments, we cannot changing the dimensions of water tunnel so easily as in computing, due to the restriction of experimental conditions. The small difference is hard to be distinguished by experiments. Although the changing is small, the role of each part is definitely different.

(1) If keeping the total length of downstream parts of settling chamber (i.e. mc, p6, p7 and p8) constant, but adjusting the length of each components, as shown in case 1 and 14, the eigenfrequency is not affected. But if the total length changed, as has been done in case 8 and 11, the eigenfrequency changes simultanesly. The larger the total length, the small the eigenfrequency is. This feather is qualitatively consistent with that of acoustic

resonance. However, the computed eigenfrequency is much smaller than the theoretical value of 1-D model which is introduced in section "1.5.2 Acoustic resonance".

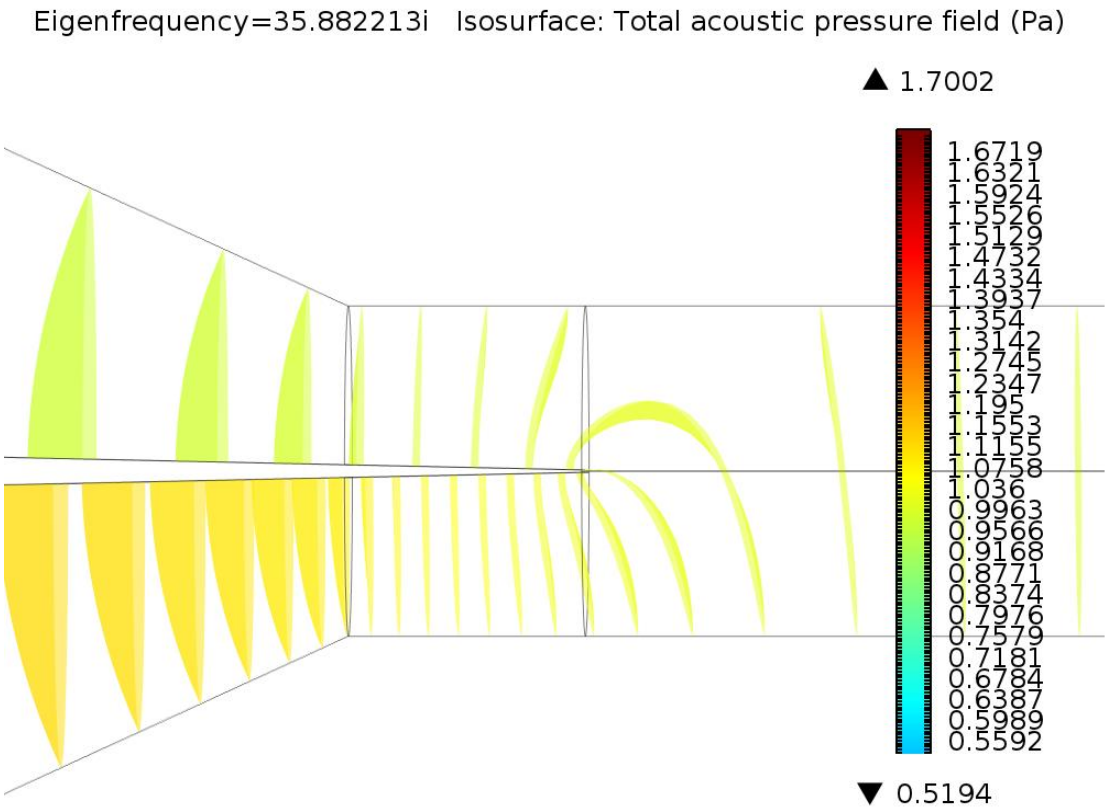

Figure 1.54 Eigenmode of acoustic pressure field under the fundamental eigenfrequency of case 1.

(2) The role of the upstream section (pl1, pl2, pl3, pl4, pr1, pr2, pr3 and pr4) of settling chamber is more complicated than that of downstream parts. When the total length of upstream parts is fixed, it can be seen: (i) the acoustic eigenfrequency decreases with the increasing length of pl1, but increases with pr1, as shown in case 2-5; (ii) pr2 has

Table 1.4 Parameter of the cases computed by Comsol. In this table, "L" and "D" are the length and diameter of corresponding parts respectively. Ds and Dl are the diameter of smaller and larger end of nozzle section. Unit in mm. If no otherwise specified, D of pipes are all 42 mm.

Case #	pl1	pr1	pl2	pr2	pl3	pr3	pl4	pr4	pl5	pr5	p6
1	L=1700	pl1	L=471	pl2	L=471	pl3	L=400	pl4	L=400	L=200	L=300
2	**L=2200**	**L=1200**	L=471	pl2	L=471	pl3	L=400	pl4	L=400	L=200	L=300
3	**L=2700**	**L=700**	L=471	pl2	L=471	pl3	L=400	pl4	L=400	L=200	L=300
4	**L=1200**	**L=2200**	L=471	pl2	L=471	pl3	L=400	pl4	L=400	L=200	L=300
5	**L=700**	**L=2700**	L=471	pl2	L=471	pl3	L=400	pl4	L=400	L=200	L=300
6	**L=3314**	pl1	L=471	pl2	L=471	pl3	L=400	pl4	L=400	L=200	L=300
7	**L=700**	pl1	L=471	pl2	L=471	pl3	L=400	pl4	L=400	L=200	L=300
8	L=1700	pl1	L=471	pl2	L=471	pl3	L=400	pl4	L=400	L=200	L=300
9	L=1700	pl1	L=471	pl2	L=471	pl3	L=400	pl4	L=400	L=200	L=300
10	L=1700	pl1	**L=1885**	pl2	**L=1885**	pl3	**L=600**	pl4	L=400	L=200	L=300
11	L=1700	pl1	L=471	pl2	L=471	pl3	L=400	pl4	L=400	L=200	L=300
12	L=1700	pl1	L=471	pl2	L=471	pl3	L=400	pl4	L=400	L=200	L=300
13	**L=500**	pl1	L=471	pl2	L=471	pl3	L=400	pl4	L=400	L=200	L=300
14	**L=500**	pl1	L=471	pl2	L=471	pl3	L=400	pl4	L=400	L=200	L=300
15	**L=850**	pl1	**L=236**	pl2	**L=236**	pl3	**L=200**	pl4	L=400	L=200	**L=150**

Continue to last page								
p7	p8	n1	n2	sc	mc	rvl	rvr	eigenfrequency
L=300	L=300	L=100, Ds=42, Dl=91	L=100, Ds=42, Dl=134	L=400	L=1875	L=100, D=25	rvl	5.71
L=300	L=300	L=100, Ds=42, Dl=91	L=100, Ds=42, Dl=134	L=400	L=1875	L=100, D=25	rvl	5.65
L=300	L=300	L=100, Ds=42, Dl=91	L=100, Ds=42, Dl=134	L=400	L=1875	L=100, D=25	rvl	5.69
L=300	L=300	L=100, Ds=42, Dl=91	L=100, Ds=42, Dl=134	L=400	L=1875	L=100, D=25	rvl	5.89
L=300	L=300	L=100, Ds=42, Dl=91	L=100, Ds=42, Dl=134	L=400	L=1875	L=100, D=25	rvl	6.22
L=300	L=300	L=100, Ds=42, Dl=91	L=100, Ds=42, Dl=134	L=400	L=1875	L=100, D=25	rvl	4.86
L=300	L=300	L=100, Ds=42, Dl=91	L=100, Ds=42, Dl=134	L=400	L=1875	L=100, D=25	rvl	6.69
L=300	L=300	L=100, Ds=42, Dl=91	L=100, Ds=42, Dl=134	L=400	**L=5875**	L=100, D=25	rvl	4.97
L=300	L=300	L=100, Ds=42, Dl=91	L=100, Ds=42, Dl=134	**L=2014**	L=1875	L=100, D=25	rvl	6.21
L=300	L=300	L=100, Ds=42, Dl=91	L=100, Ds=42, Dl=134	L=400	L=1875	L=100, D=25	rvl	4.46
L=300	L=300	L=100, Ds=42, Dl=91	L=100, Ds=42, Dl=134	L=400	**L=375**	L=100, D=25	rvl	6.85
L=300	L=300	L=100, Ds=42, Dl=91	L=100, Ds=42, Dl=134	**L=25**	**L=75**	L=100, D=25	rvl	7.51
L=300	L=300	L=100, Ds=42, Dl=91	L=100, Ds=42, Dl=134	**L=25**	**L=75**	L=100, D=25	rvl	8.37
L=1800	L=300	L=100, Ds=42, Dl=91	L=100, Ds=42, Dl=134	L=400	**L=375**	L=100, D=25	rvl	5.71
L=150	**L=150**	**L=50**, Ds=42, Dl=91	L=100, Ds=42, Dl=134	**L=200**	**L=938**	**L=50**, D=25	rvl	12.37

stronger influence on the acoustic eigenfrequency compared to pr1. It is also find from case 6 and 7, when the total length of upstream parts is increased, the acoustic eigenfrequency will decrease.

(3) The relation between the length of settling chamber and acoustic eigenfrequency is a little strange. As has been introduced in (1) and (2), normally the acoustic eigenfrequency is inversely proportional to the length of parts (except pl1, pl2, pl3 and pl4). But, comparing case 1 and 9, we find the longer the settling chamber, the higher the eigenfrequency is. This is interesting and the reason is unknown yet.

(4) The bending parts, such as pl2, pl3, pr2 and pr3, will have stronger influence on the acoustic eigenfrequency than pl1 and pr1, even if same changing of length is applied. This different influence can be found by comparing case 6 with 10.

From Table 1.4, the influence of individual parts of our water tunnel are investigated. From the results, it's hard to say how these parts exactly affect the eigenfrequency. In the considered parametric space, we find the eigenfrequency normally decreases with the increasing of pl1, pr1, pl2, pr2, pl3, pr3, pl4, pr4, sc, p6, p7, p8 and the total length (as shown in case 15), but increases with the increasing mc. As the water tunnel system can be simplified as a triple channel acoustic system (note, the acoustic resistance in each channel is different) with three open ends and one radiation input, as shown in Figure 1.56, the acoustic wave in each channel will not be alone, but related to that in other two channels. To the best of my knowledge, there is no theoretical solutions for such kind of acoustic system. One of the possible explanation is that the eigenfrequency is simultaneously close to the some subharmonic frequency of acoustic resonance in each channel. For instance, if

the total lengths of Ch1, Ch2 and Ch3 are 3342 mm, 3675 mm and 4642 respectively. the corresponding resonance frequencies are 448.8 Hz (round to 450 Hz), 408.2 Hz (round to 408 Hz) and 323.1 Hz (round to 324 Hz) as the acoustic speed in water is about 1500 m/s. Then, the most close common divisor is 6 Hz, which is consistent with the calculation.

Honestly say, our computations are based on some simplifications. Due to the limited computing capacity, in recent simulation, some local parts such as honeycomb and screens are not considered. These parts will change the local resistance and cause different damping character. The acoustic eigenfrequency would be different from what we show in Table 1.4. However, the difference should be limited as acoustic resonance is majorly determined by the large structural dimensions. In future, more researches will be focused on the acoustic eigenmode of our water tunnel.

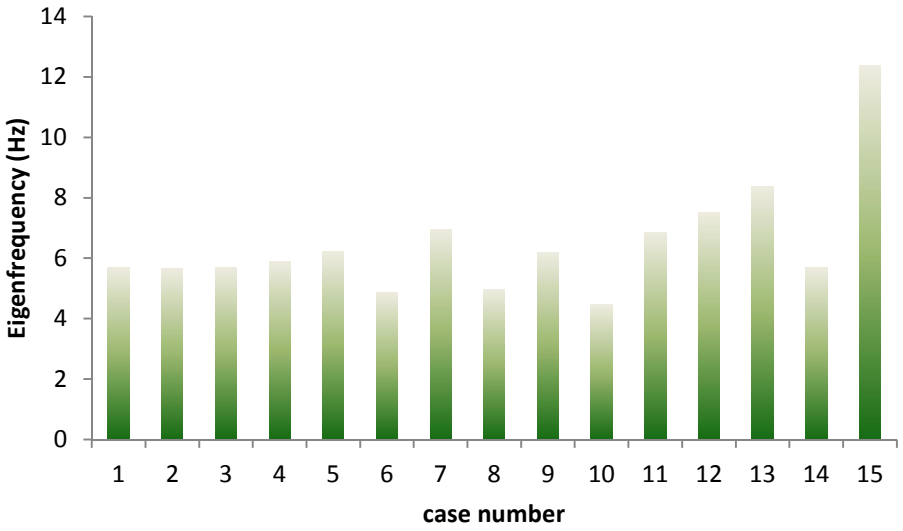

Figure 1.55 Eigenfrequency at different computing cases indicated by Table 1.4.

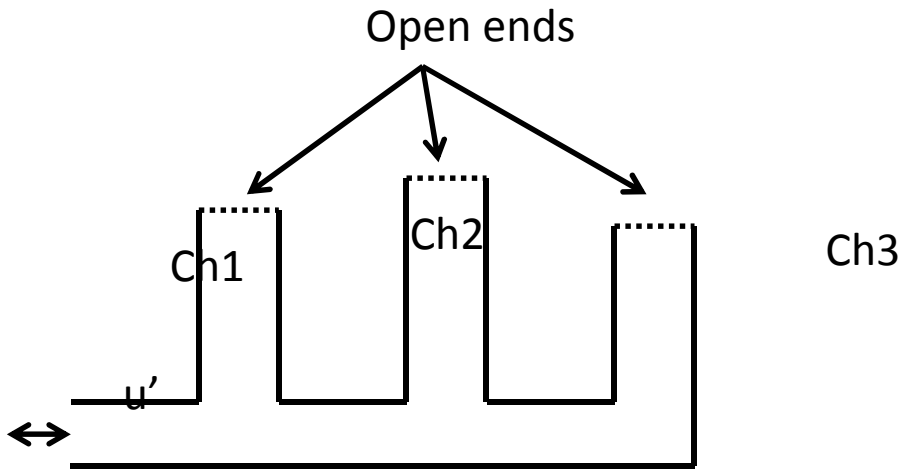

Figure 1.56 Simplified acoustic model for the water tunnel

Discussion

By computing, an acoustic eigenfrequency around 5.3 Hz is found in our water system. The acoustic resonance mechanism may be the reason of the fast mixing in confined mixing layer. However, there are still some problems unsolved, such as: (i) why in the parametric experiments, the changing of optimal frequency is not apparent. One of the possible reasons is that the parametric experiments are not explicit enough. Hence, more careful experiments should be carried out to confirm our experiments. (ii) the computing is conducted under the condition that there is no mean flow. Due to Doppler effect, the acoustic resonance frequency at this case should be different from that in a flow where mean flow velocity is not neglectable. The difference should be evaluated. (iii) Although the computed acoustic frequency is very close to the optimal frequency we found by experiments and acoustic resonance may be the reason of fast mixing, the cause of the computed eigenfrequency is still unknown. We don't know what exactly determines the eigenfrequency. More investigations are still needed in future.

1.5.3 Fluid-structural interaction

Because the optimal frequency is low, structural vibration and the corresponding resonance cannot be arbitrarily neglected without investigation. Hence, in this section, the resonance of structural vibration due to fluid is parametrically studied.

There exist three major coupling mechanisms between flow and structures, which are: Poisson coupling, friction coupling and junction coupling (Wiggert and Tijsseling 2001). Among all the three modes, junction coupling commonly exists in the mixing chamber, settling chamber and other connection pipes. In these sections, it has more apparent influence than the other two mechanisms. The Poisson coupling is also present in these sections, especially in the water supply pipes that connecting the settling chamber with water tanks. However, due to the relative large wall thickness to diameter ratio (which is not much smaller than 1), the influence of Poisson coupling is minor compared to junction coupling. Compared to the other two mechanisms, the influence of friction coupling is too small to be counted. Only the junction and Poisson couplings are discussed in this manuscript.

The junction and Poisson couplings in the mixing chamber

Due to the high length-to-diameter ratio of mixing chamber and distributed supports, the junction coupling becomes more significant than the other two coupling modes. The junction coupling is directly related to the transverse vibration of mixing chamber. When the forcing frequency happens to be the fundamental or harmonic frequencies of mixing chamber in transverse direction, the disturbance due to unsteady and asymmetric flow can

induce amplification of pipe vibration. This will in turn contribute back to the unsteady flow and form a feedback loop.

The response frequency of junction coupling can be altered by the changing of resonance frequency of mixing chamber. This can be achieved by changing the support method. As the contribution of water on vibration frequency can be simply treated as added mass due to the small vibration amplitude (compare to both the wall thickness and cross-sectional diameter), the transverse vibration frequency of mixing chamber can be estimated as below (Karnovsky and Lebed 2001):

$$f_1 = \frac{(\beta_1 l)^2}{2\pi}\sqrt{\frac{EJ}{(\rho_p A_P + \rho_w A_w) l^4}} \tag{1.18}$$

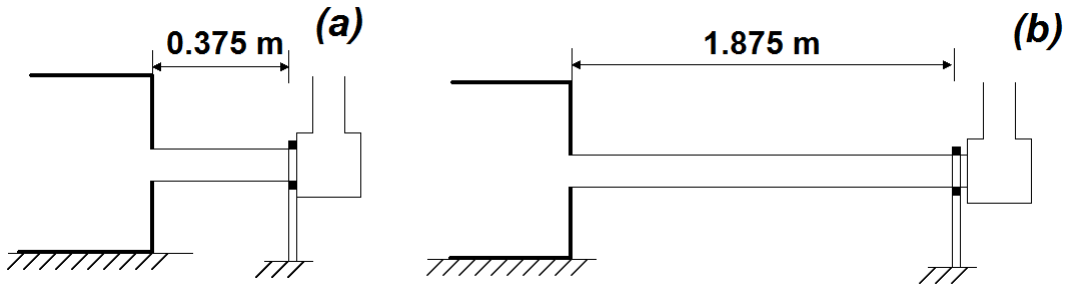

Figure 1.57 The support method. (a) The shorter mixing chamber, and (b) the longer one.

where f_1 is the first order frequency, i.e. fundamental frequency. $\beta_1 l$=4.73 due to the fixed support. l is the length of the pipe between the supports. ρ_p and ρ_w are the densities of pipe and water respectively. $A_p = \frac{\pi}{4}(D_o^2 - D^2)$ and $A_w = \frac{\pi}{4}D^2$ are the transverse areas of pipe (i.e. the solid part) and water in the mixing chamber, and D_o is its outer diameter. E is the elastic module of pipe and $J = \frac{\pi}{64}(D_o^4 - D^4)$ is the second moment of area in the cross section.

In this research, D_o=50.8 mm, D=41.3 mm, E=3.2 GPa, $\rho_p = 1200\ kg/m^3$ (Acrylic) and $\rho_w = 1000\ kg/m^3$.

For the shorter mixing chamber shown in Figure 1.57(a), l=0.375 m. Its fundamental frequency of transverse vibration is 418 Hz. For the longer one (1.875 m), depending on the support distribution, the lowest frequency can be received is 16.7 Hz (using one support on the end of optical vessel). Both the fundamental frequencies are far from 5.3 Hz. Experiments also indicate the changing of support method won't change the optimal frequency, even using only one support on the longer mixing chamber. Hence, the junction coupling in mixing chamber can be ignored.

The Poisson coupling will induce axial vibration in the wall of mixing chamber. The fundamental frequency is 2.18 KHz (the shorter mixing chamber) and 435 Hz (the longer one), respectively, due to Equation (1.19):

$$f_{axi} = \frac{1}{2l}\sqrt{\frac{E}{\rho_p}} \tag{1.19}$$

Moreover, as stated by Wiggert (Wiggert and Tijsseling 2001), the acoustic speed in Poisson coupling can be larger than in the case without FSI. Hence, the actual fundamental frequency should be even larger than the estimations above. Apparently, both of them are far from the optimal frequency in this research.

The FSI related to the settling chamber

Because of the much larger D_o and D_o/D, the magnitude of J of the settling chamber can be expected to be much larger than that of mixing chamber. Meanwhile, its length is

only 594 mm. The Poisson coupling cannot function well on this rigid object with thick wall. Hence, only the junction coupling should be considered. For the mixing chamber with this length, the transverse resonance frequency is about 166.5 Hz. However, concerning the much larger J, the transverse fundamental frequency of settling chamber should be much larger than 166.5 Hz. Hence, the vibration of settling chamber can be easily excluded.

The influence of total mass of the water tunnel system

If all the clamps are released from the experimental table, the water tunnel will slightly vibrate in vertical direction. Its vibration behaves as a harmonic oscillator and the natural frequency is proportional to $m^{-1/2}$ (Meirovitch 1986). When the water tunnels are clamped on the experimental, the mass of the harmonic oscillator is more than 20 times larger than the unclamped case. The natural frequency should be at least 4.5 times smaller than the latter. The mixing enhancement should be seriously affected. However, this is not found in the experiments and this possibility can be ignored.

The FSI in the water supply pipes of settling chamber

For flexible purpose, the water supply pipes which connect the settling chamber and control valves are all constituted by bendable plastic pipes. The influences of FSI on these parts are much more significant than the rigid pipes. While forcing on the flow, the vibrations of pipes can be easily observed, even though three clamps have been used on each pipe. To test the influence of FSI, forcing is directly applied on the most flexible point of the pipe on the low-speed side. We first measured the amplitude generated at the most

flexible point when the forcing is directly applied on water as normal. Then, the equivalent forcing amplitude at each frequency is employed on these points. The flow visualization is listed in Figure 1.58.

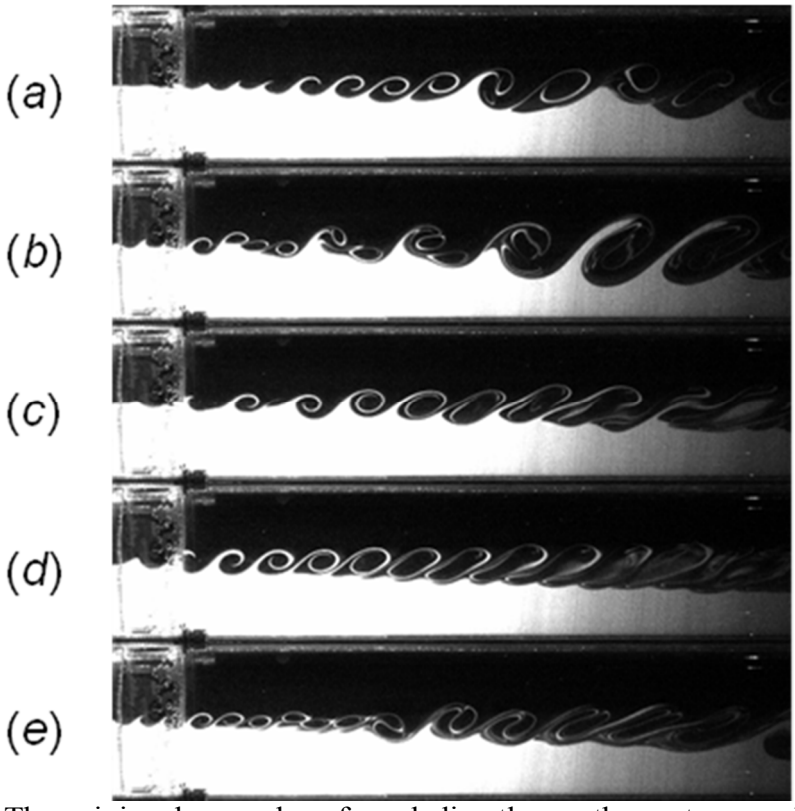

Figure 1.58 The mixing layer when forced directly on the water supply pipes. (a) unforced, (b) 3.5 Hz, (c) 5.3 Hz, (d) 7 Hz and (e) 10 Hz.

At the selected frequencies, the mixing enhancement is far from the situation when directly forcing on water as shown in Figure 1.41. Subharmonic vortex merging can be easily found at 3.5 Hz in Figure 1.58(*b*), compared to other cases. This is consistent to the vortex evolution on forced traditional mixing layer, as stated by Ho et al(Ho and Huang 1982). At 5.3 Hz, the vortex merging process is not clearly found. But the frequency lock region do exist, although is very short as shown in Figure 1.58(*c*). At 5.3 Hz, the expected

fast mixing doesn't appear. Apparently, the contribution of FSI on the mixing enhancement is very weak. The FSI of the pipe cannot be the reason of the drastic flow mixing.

Conclusion

In this section, the possible causes of the optimal frequency related to the fast mixing have been parametrically investigated. It's found changing the sizes and shapes of water tunnel won't affect the optimal frequency. From the authors' knowledge, the acoustic resonance mechanisms can be excluded. Meanwhile, two factors are located to be necessary in the mixing enhancement: one is sufficiency of the existence of separated flow. The other is the sharpness of trailing edge.

The structural vibration due to FSI is also investigated. However, the influence of FSI is only equivalent to the inlet flow disturbance. Its effect is negligible compared to the fast mixing process.

1.5.4 Acoustic induced vortex

Through the numerical investigations by Comsol, we found close to 5.3 Hz, there do exist an acoustic eigenfrequency. Hence, acoustic resonance is the most probable mechanism of causing fast mixing in confined mixing layer. Also, by experiments, we notice that the CRV structures are very important on enhance mixing. Hence, how could the CRV structures be generated by acoustics should be investigated.

As introduced by Rienstra and Hirschberg (2009), to form acoustically induced vortex shedding, the following condition is required:

$$\frac{s}{r} \geq O(1)$$

where r is the curvature radius of trailing edge and s is called Acoustic particle displacement (APD), which is expressed as:

$$s = \sqrt{\overline{u'^2 + v'^2}}/\omega = \sqrt{\overline{u'^2 + v'^2}}/2\pi f_w \tag{1.20}$$

In their case, the thickness of acoustic boundary layer is much smaller than the geometry of orifice, which is neglectable. But in our case, the thickness of acoustic boundary layer can be even larger than the radius of sharp trailing edge. Hence, the condition needed to be revised as:

$$\frac{s}{r+\delta} \geq O(1) \tag{1.21}$$

where δ is the thickness of acoustic boundary layer (also known as viscous laminar boundary layer or Stokes layer) that can be expressed as:

$$\delta = \sqrt{2\nu/\omega} = \sqrt{\nu/\pi f_w} \tag{1.22}$$

where f_w is the frequency of u' in stream 1 (LSS) of nozzle section while forced and can be approximately equal to f_f. $\omega = 2\pi f_w$ is the corresponding angle frequency. In this investigation, we consider two kinds of trailing edge, one is sharp trailing edge (r_s =0.1 mm) and the other is blunt trailing edge(r_b =3.4 mm). In our experiments, as investigated by PIV, the velocity fluctuations in LSS is stronger than that of HSS. APD in LSS is more

critical than that in HSS. Hence, in this section, all the APD are directly measured from LSS.

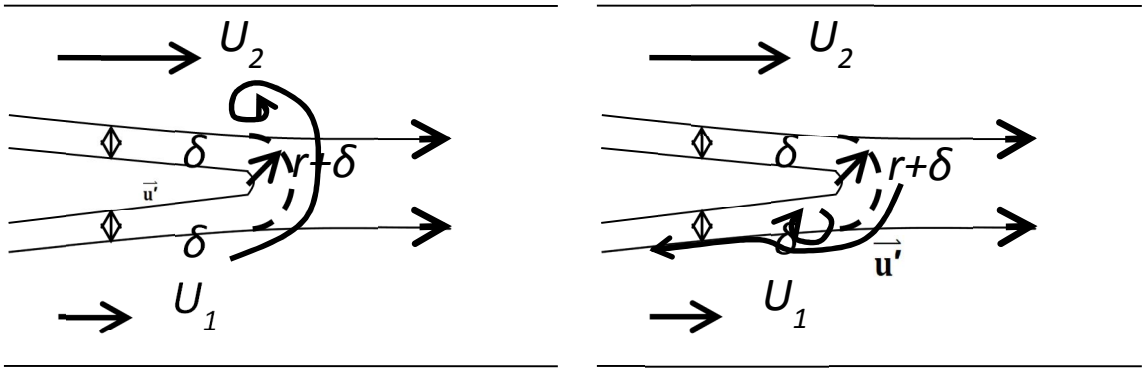

(a) (b)

Figure 1.59 Schematic of acoustic induced vortex shedding. (a) Counter-clockwise vortex generated by positive u'_1 and negative u'_2. The vorticity of mean flow is overcome. (b) Clockwise vortex generated by negative u'_1 and positive u'_2, combined with the vorticity of mean flow.

To form CRV, the mean vorticity of shear layer right after the trailing edge in unforced flow should be overcome. This process can be described by Figure 1.59. In the first half period of periodic forcing, i.e. during pushing, a positive u'_1 and negative u'_2 are generated. The velocity fluctuations will simutaneously cause CRV (positive vorticity in spanwise direction) at a result of the boundary layer. When the counter-clockwise vortex is strong enough, the mean vorticity of unforced shear layer can be conquered. A shedding vortex of counter-clockwise could be produced. In the second half period of periodic forcing, due to pulling, u'_1 and u'_2 are negative and positive respectively. In this case, the shedding vortex of clockwise will be enhanced. This is why in our experiments, when the velocity ratio is larger than 0, the CRV is always asymmetric. If wake flow is applied as basic flow, the CRV becomes more symmetric.

Hence, physically say, to generate CRV, it is required:

$$\frac{\sqrt{\overline{u'^2 + v'^2}}}{\delta} \geq \frac{U_H - U_L}{\delta_m}$$

where $\sqrt{\overline{u'^2 + v'^2}}$ is measured in LSS, δ_m is the width of the unforced mixing layer right after the trailing edge. To evaluate the ratio between velocity gradient due to acoustic induced flow and the gradient of mean flow, a parameter (γ) is introduced as below:

$$\gamma = \frac{\sqrt{\overline{u'^2+v'^2}}\delta_m}{(U_H-U_L)\delta} \tag{1.23}$$

To generate CRV, both of the Equation (1.21) and $\gamma > 1$ should be satisfied. When Re=2939 and λ=1/3, δ_m is estimated to be around 0.8 mm. It can be seen from Figure 1.60(a) and (b), when A_{fm}=11%, only at 5.3 Hz, both the Equation (1.21) and condition $\gamma > 1$ are achieved. This is also consistent with the flow visualization as shown in Figure 1.60(c). Although around 7 Hz, the second condition $\gamma > 1$ is also satisfied, the APD generated at this frequency is too small to induce counter-rotation shedding vortices. Thus, there is no CRV generated at this frequency and forcing intensity. The forcing at 7 Hz only causes faster transition of mixing layer from linearly unstable state to nonlinear state indicated by the rolling up of vortex.

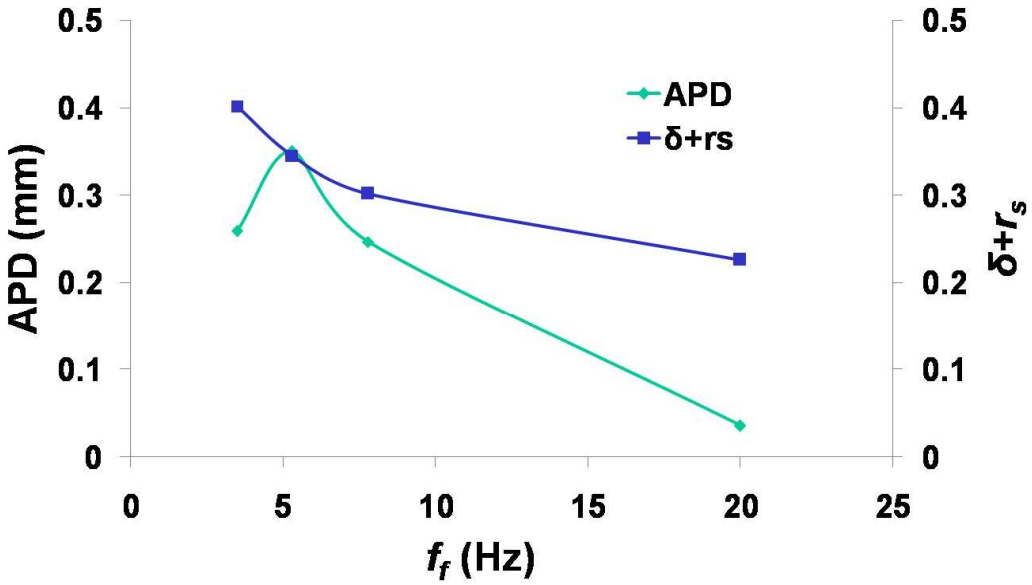

(a)

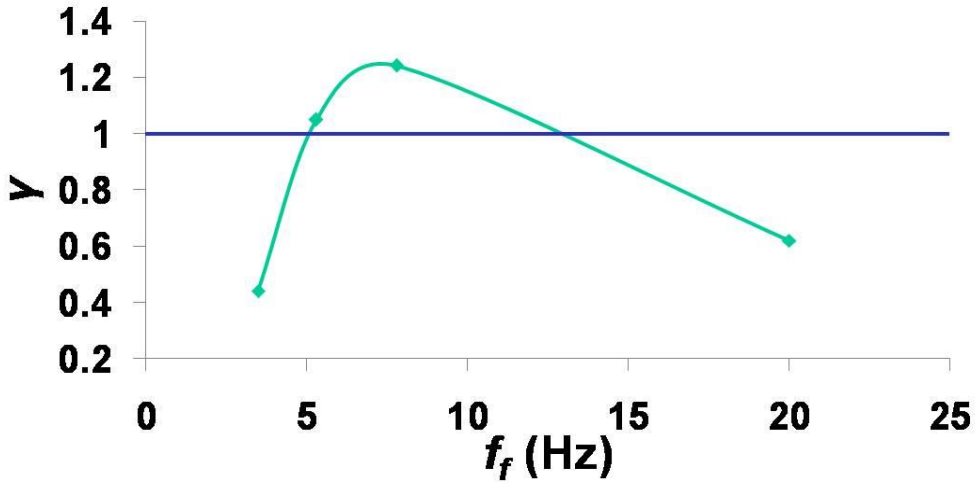

(b)

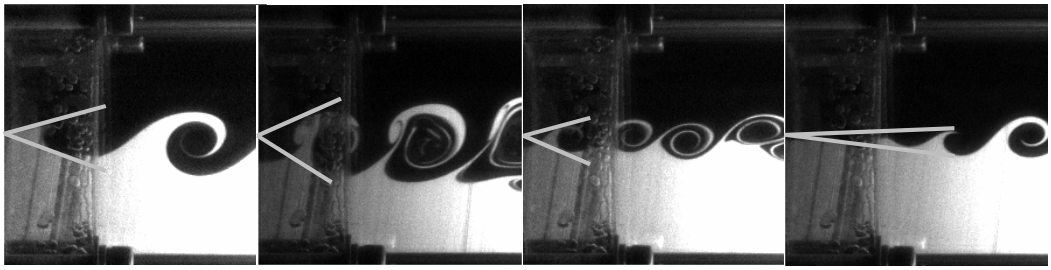

(c)

3.5 Hz 5.3 Hz 7.8 Hz 20 Hz

Figure 1.60 Re=2939, λ=1/3, A_{fm}=11%, (a) APD compared with $\boldsymbol{r+\delta}$, (b) γ at different frequency, (c) the corresponding vortex structures at different frequencies.

In the aforementioned two conditions, we can see they are determined by the forcing intensity, frequency and mean flow velocity. Hence, at different Re and velocity ratio, the critical forcing intensity that causing CRV should be different. This is also initially investigated and the results are shown in Figure 1.61. In the figure, A'_{fm} is a normalized critical forcing intensity related to CRV and defined as:

$$A'_{fm} = A_{fm} * \mathrm{Re}_{\mathrm{ref}}/\mathrm{Re}$$

where $\mathrm{Re}_{\mathrm{ref}} = 3000$ is the reference Re number. It can be seen, after normalization, the critical forcing intensity of CRV can approximately fall upon a line. A'_{fm} is proportional to both Re and λ. In a flow with large Re and λ, to generate CRV and the corresponding fast mixing, a higher forcing intensity is required.

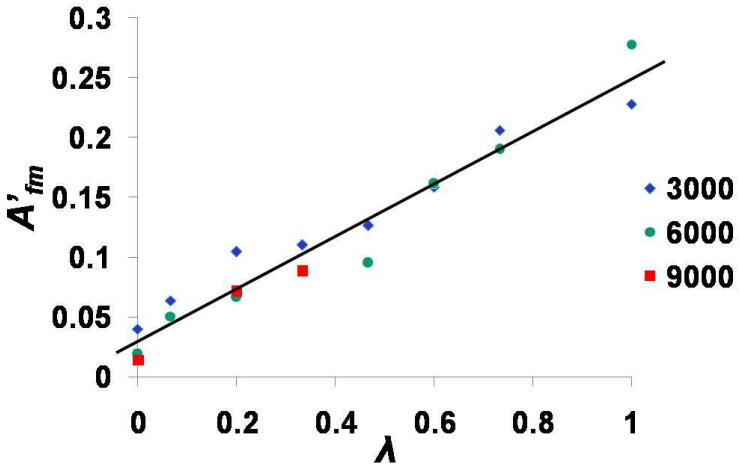

Figure 1.61 The critical normalized forcing intensity A'_{fm} varies with velocity ratio λ

1.6 Conclusion

In this section, the rapid mixing found by Wang (Wang 2003; Wang 2006) is detailed investigated by PIV system. Compared with the traditional free mixing layer, where the initial mixing depends on convective scalar transport by velocity fluctuations, in confined

mixing layer, the mixing process can be separated into two stages. The first stage is related to acoustically induced shedding vortex. In the second stage, both the mean and fluctuating vertical velocities work together to enhance the mass transport and the subsequent mixing process. Here, several major conclusions are summarized.

(1) The unforced confined mixing layer has similar universal law of momentum thickness ($\theta_m \sim x^{0.5}$) of mixing layer as in conventional free mixing layer. But at the equivalent Re_θ range, confined mixing layer has larger $d\theta_m/dx$ than in free mixing layer. And the confined mixing layer is more stable (require larger transient Re_θ) than free mixing layer.

(2) The receptivity of 5.3 Hz is the highest in nozzle section, but becomes much weaker in the downstream of mixing chamber. The turbulent energy is "lost". The "lost" turbulent energy is majorly converted to the mean flow energy by the reverse transport process and relaminarization, which results in the highly wavy *U* profile, and large *V* component. And minor dissipated by vortex structures.

(3) A "turn-over" point of forcing intensity is found which suggests there should be at least two different mechanisms competed with each other to dominate flow. At low forcing intensity, based on K-H instability, subharmonic mode is the dominant mechanism of mixing enhancement. While forcing at 5.3 Hz with sufficiently large forcing intensity, subharmonic mode is insignificant and the flow is dominated by the forcing frequency, not the intrinsic frequency of flow instability, and acoustically induced shedding vortex becomes important. The short-term effect is also consistent with the existence of

acoustically induced shedding vortex. The "turn-over" point can also be considered as a critical point that the flow is transferred from 2-D dominant to 3-D dominant.

(4) From vortex dynamics, the large V component is generated by streamwise vortex structures. Recently, corner vortex mechanism is a reasonable explanation, even though there are still many unsolved questions. Before these problems are solved, we cannot simply ignore other mechanisms arbitrarily, due to the complexity of flow.

(5) Strong V not only enhances the transport of momentum, scalar and energy in vertical direction, but also cause the spanwise vortex to be extremely unstable by high dV/dy. The vortices are stretched and broken down more earlier than other cases which results in faster and more homogeneous mixing.

(6) The optimal frequency, i.e. 5.3 Hz here, is not related to FSI mechanisms, but some unknown low frequency acoustic resonance of fluid, as shown by Comsol computation. Generally say, the acoustic eigenfrequency decreases with the increasing length of all the parts, except the mixing chamber. But, the theoretical and physical reason is still unclear. One of the possible reasons is due to the superposition of indivial subharmonic mode of each channel. To confirm this conclusion, a significant changing of water tunnel should be made in future investigation.

(7) The important counter-rotation vortex structures is due to the acoustically induced vortex shedding. The requirement of generating CRV is discussed and compared with experiments. To achieve CRV, the periodic acoustic boundary layer under external forcing should meet two conditions: (a) The APD should be larger than the sum of the curvature

radius of trailing edge and the thickness acoustic boundary layer; (b) The velocity gradient due to acoustic induced flow should be large enough to conquer the gradient of mean flow.

Although the flow dynamics of the fast mixing and many parameters that may related to the optimal frequency are detailed investigated in this section, there are still many unsolved problems.

(1) First, which is also one of the most important is the cause of optimal frequency. A possible explanation has been given in section 1.5. However, more and detailed investigations are still required.

(2) The fast transition of flow from laminar to turbulence right after the trailing edge. As the flow is strongly nonlinear, linear instability research may not be able to make a sufficient investigation. Recently, only the non-model instability may solve the problem.

(3) The flow instability under the presence of low frequency large scale velocity structures. Traditionally, people investigate the instability of flow under a "fixed" flow profile or flow geometry, for example based on mean flow profile. This is unnecessary in fact. When a flow meets the following conditions:

    a. The flow has energy injected by external forcing at low frequency components.

    b. The low frequency components due to external forcing is much smaller than the spectrum region of turbulence developed downstream

c. The low frequency components due to external forcing and the spectrum region of turbulence, i.e. the high frequency ones, are uncorrelated.

The instability of flow can be investigated under the time frame of low frequency forcing. For example, if we forced at 5 Hz, and the time request for flow instability to achieve maximum is only 0.1 s, then we can approximately consider the flow to be quasi-steady under the periodic forcing and the acceleration of flow at 5 Hz is approximately ignored. But, if the time cost for flow instability to achieve maximum is 1 s, we can not use the quasi-steady approximation.

(4) The influence of periodic low frequency flow (i.e. the acceleration of flow profile) on flow instability should be considered.

Chapter 2

LOW REYNOLDS NUMBER TURBULENCE IN MICROFLOW

2.1 Introduction

In chemical engineering, the relatively slow mixing process is often a bottleneck that restricts the reaction process, especially when the reaction rate is high. For this purpose, short mixing time is crucial and highly required to avoid the reactive process being delayed by relatively slow mixing process. Essentially say, the principle of mixing enhancement is to accelerate the process that large scale scalar structures is broken into small scale structures where molecule diffusion starts dominate. In macroflow, this can be achieved by generating turbulent flows which can rapidly rupture the large scale scalar structures into small scales through cascade process because of instability of large vortices, such as in the cases of agitated tanks (Ali et al. 1981; Chang et al. 1981; Armenante and Huang 1992; Tsouris and Tavlarides 1994; Kresta 1998; Alvarez et al. 2002; Ascanio et al. 2002; Paul et al. 2003; Rudolph et al. 2007), mixing layer (Wygnanski and Fiedler 1970; Dimotakis and Brown 1976; Ho and Huang 1982; Ho and Huerre 1984; Koochesfahani and Dimotakis 1985; Koochesfahani and Dimotakis 1986; Koochesfahani and Mackinnon 1991; Fiedler et al. 1998; Wang 2003; Dimotakis 2005; Wang 2006) or jet flow (Catrakis and Dimotakis 1996; Dimotakis 2005). However, in microreactor and other lab-on-a-chip applications, where Reynolds number is normally on the order of or below unity and fast mixing is still required, only chaotic flows are

normally used to enhance mixing, because so far it is believed that there is no turbulence in microfluidics at such a low Re (Brody et al. 1996).

The reason why it is believed that there is no turbulence at such low Re flows in microfluidics is because the classical understanding of turbulence is a feature of high Re flows, and the lack of fundamental theory to generate turbulence in low Re flows. In microchannel, due to the strong viscosity effect, any initially generated velocity fluctuation will dissipated in a short time. Hence, to achieve turbulent flow, there should be a mechanism of generating high and long-lasting turbulent energy. Normally, the turbulent energy can be generated by flow itself through some instability mechanisms, or from external force. However, the former one requires extreme high pressure drop to generate high velocity flow which is impossible in most microfluidics applications. Hence, many efforts have been explored in generating flow disturbance by external forces, such as active method like electrokinetic (EK) flow (Baygents and Baldessari 1998; Ramos et al. 1998; Chen et al. 2005; Park et al. 2005; Huang et al. 2006; Posner and Santiago 2006; Chang and Yang 2007) and passive ways by specially designed geometry of channel (Stroock et al. 2002; Hessel et al. 2005). Although there can be elastic turbulence in polymer solutions at low *Re* (Groisman and Steinberg 2000), it is conventionally believed that the flow in microfluidics, where typical *Re* is on the order of 1 or lower and the fluids are often approximately seen as Newtonian, can only be laminar (Stroock et al. 2002; Janasek et al. 2006) and cannot be turbulent (Simonnet and Groisman 2005; Ahn et al. 2008; Balasuriya 2010; Capretto et al. 2011). According to recent review, Chang and Yang (2007) implied that so far many efforts have been explored to enhance mixing in microfluidics, e.g. using sufficiently high DC or AC voltage to force flow in a microchannel based on electrokinetic

instability (Oddy et al. 2001; Burghelea et al. 2004; Chen et al. 2005; Park et al. 2005; Huang et al. 2006; Hu et al. 2008), but the forced flows in these studies are chaotic advection, not turbulence (Lee et al. 2011).

Another reason that till now no one discovered turbulence in microfluidics, is due to the lack of effective velocimeter that can quantitatively detect turbulent signal at high frequency in microflows. Previously, in microfluidics, the most successful and widely used velocimetry in microfluidics is micro Particle Image Velocimetry (μPIV) and its derivatives, which have the capability of measuring 2-D and 3-D microflow field on mean flow field, if the flow is steady or at most weakly disturbed (Santiago et al. 1998; Meinhart et al. 1999; Meinhart et al. 2000; Westerweel et al. 2004; Kinoshita et al. 2007; Klein and Posner 2010; Wereley and Meinhart 2010; Raben et al. 2013). However, for unsteady flows with random high velocity gradients, e.g. chaotic or turbulent flows where u' could be strong, continuously measurement of u' with sufficiently high spatiotemporal resolution becomes challenging for current μPIV, which has difficulty in exploring the spatial structure of flows down to sufficiently small spatial scales, because of its limited resolution (Burghelea et al. 2004). To our knowledge, there is even no published power spectrum density (PSD) of u' in microfluidics for frequency higher than 100 Hz.

For the widefield microscope, to reach a high spatial resolution, a large NA and magnification lens is necessary. To ensure the capture of particles in interrogation spots, high particle volume fraction is also required. However, this will cause (1) more serious out-of-focus noise which limits the signal-noise ratio (SNR) of image (2) worse SNR of correlation field that leads to high probability of erroneous velocity, and (3) change of viscocity of fluids (due to microviscosity, especially in non-Newtonian fluids (Suh et al.

2005). In fact, even using a large NA lens cannot apparently increase the spatial resolution by reducing depth of correlation and the out-of-focus influence (Rossi et al. 2012).

To reduce the out-of-focus influence and achieve high temporal resolution, Kinoshita (Kinoshita et al. 2007) used confocal microscope with high-speed rotating Nipkow disk to capture the instant particle images in moving droplets. Continuum lasers are used as light source. This work claimed 2000 Hz capture rate could be achieved. However, to increase the relatively low SNR, ensemble-average of correlation fields was applied which restricts the temporal resolution. Later Klein (Klein and Posner 2010) applied similar facilities with high power laser in electrokinetic instability (EKI) experiments. A great improvement was achieved and instant velocity fields were successfully measured. But the local structures are not reliable due to the erroneous velocity, which also makes continuous measurement for spectrum analysis unreliable. To reduce the percentage of erroneous velocity, (Raben et al. 2013) combined confocal based μPIV with Robust Phase Correlation (RPC) and tested in steady Poiseuille flow. These authors found this combination could apparently reduce the erroneous vectors in steady flow. However, for a highly fluctuated flow, such as electrokinetic (EK) flow with high electric field intensity and high conductivity ratio, to our knowledge, there are no reliable measurements on velocity field published.

This situation becomes worse when μPIV is used in EK or near wall flows, since it suffers from several uncertainties. For instance, in EK flows, the infilled particles may not monitor the fluid flow faithfully, because they will experience electric force (e.g. dielectrophoresis due to the different permittivity and conductivity of particle from solution and Coulomb force) and have different velocity from local fluids (Kirby 2010). The presence of particles in flow can change the local electric field, and thus flow as well. The

well-known particle lagging makes it difficult to measure strong and high frequency u'. Since most particles may have more or less charge, erroneous velocity due to electrostatic force cannot be avoided, not only in the presence of EK, but also in flows without EK when particles are close to the polarized wall (Sadr et al. 2007). These uncertainties, especially when we are talking about measuring flow velocity fluctuations, are hard to distinguish and unable to removed. This makes μPIV measurement dubious in electrokinetic flow. In addition, these PIV based methods also require expensive pulse laser and camera.

Although there are also many other velocimeter developed in microfluidics (Flamion et al. 1991; Nguyen 1997), all of them, to our knowledge, are incapable to measure u' with high fluctuation frequency in unsteady microflows as found by Wang et al(Wang et al. 2014). For this reason, Wang (Wang 2005) developed a new velocity measurement technique called Laser Induced Fluorescence Photobleaching Anemometer (LIFPA) based on the relation between fluorescence intensity and velocity of flow due to photobleaching process. This technique has several advantages: (1) non-invasive; (2) high spatiotemporal resolution; (3) capable for far-field nanoscopic measurement (Kuang and Wang 2010; Kuang et al. 2010). And it has been successfully used on measuring velocity power spectrum in EK microflow (Wang et al. 2014).

However, similar to single-wire HWA measurement, LIFPA cannot distinguish individual velocity components in different directions. And due to the much smaller aspect ratio, intuitively, the 3-D flow effect may become more severe and cause significant bias errors on: (1) mean velocity; (2) velocity fluctuations and the higher order statistics; (3) first derivatives variance (FDV) of velocity fluctuations, which will create discrepancies on calculating characteristic spatial scales of turbulence later. These will all cause

misunderstanding of people on flow dynamics. Hence, proper correction method on statistical results is necessary.

In recent years, via LIFPA method, we successfully discovered turbulent signals in pressure-driven EK flow with external AC electric field. A lot of high Re characters in macroflow are also found in this microfluidics channel flow, for instance, Kolmogorov -5/3 spectrum of velocity fluctuations, Obukhov-Corrsin -5/3 spectrum of scalar (concentration in these experiments), exponential tail of probability density function (PDF), scaling laws of both velocity and scalar structure functions, exponential evolution of scalar variance in streamwise direction, and so on. Besides these classical phenomenon. We also discovered many new phenomena, and one of the most important is a new scaling law for EK turbulence.

In this manuscript, the principle of LIFPA measurement on velocity fluctuations and its temporal resolution (TR) is discussed first. Then, the statistical correction on LIFPA measurement is analyzed. Later, the theory of generating turbulence in microfluidics by EK flow is introduced. The experimental results and the corresponding physical processes are presented. Finally, a new scaling law of EK turbulence is advanced.

2.1.1 What is Turbulence?

Before introducing the mechanism of generating turbulence in microfluidics, we have to know first what turbulence is. Many renowned researchers had try to give explicit definition for turbulence (Frisch 1995; Lesieur 2007), however, this is not achievable due to the new discoveries on turbulence. Although it is difficult to give an accurate definition of turbulence, there are some common features in turbulence (Tennekes and Lumley 1972):

fast diffusion, random motion, high dissipation rate, continuous flow, multiscale eddies, 3-D and high *Re*. Based on these features, common knowledge is that the critical Reynolds number — Re_c is 2100~2300 in pipe flow. In microfluidics, turbulence is hard to be generated unless the pressure head is high enough (Kirby 2010; Tabeling 2010). As we know, Re_c in microchannels is similar to that in macroflows, although debates exist (Sharp et al. 2002). This turbulence is induced by hydrodynamics, so it is also called hydrodynamic (HD) turbulence. There are also several other turbulence mechanism, such as (1) turbulent Rayleigh-Bénard (RB) convection driven by buoyancy due to temperature difference, (2) magnetohydrodynamic (MHD) turbulence due to the driven of magnetic force, (3) elastic turbulence, a kind of polymer turbulence disturbed by the non-Newtonian stress, (4) weak turbulence, which is also called turbulence but essentially not, such as electric turbulence that has only random phase of signal. Compared with chaotic flow, which is normally either spatially or temporally random, turbulence is a highly random system both spatially and temporally.

In macroflows, we have realized turbulence and ultrafast mixing at relatively low *Re* based on receptivity (Wang 2006; Wang 2013). In the present work, we demonstrate that turbulence can be achieved in an electrokinetically forced pressure-driven flow in microchannels with bulk flow *Re* on the order of 1.

2.1.2 Mechanism of electrokinetic (EK) turbulence in microflow

Previously, many investigations have been conducted to generate disordered and irregular flows in microchannel by electrokinetic method, such as periodic electroosmotic

flow (Lim et al. 2010), dielectrophoretic flow (Lee et al. 2001; Deval et al. 2002; Campisi et al. 2009; Choi et al. 2009; Lee et al. 2011; Zhao and Yang 2011), electrothermal flow (Ng et al. 2009) and so on. One of the most important methods is based on electrokinetic instability (EKI). The EKI mechanism is very common and can be induced by placing an external electric field either parallel (Baygents and Baldessari 1998) or perpendicular (Chen et al. 2005) to solution conductivity gradient. Whether the disordered flow can be generated depends on the so-called critical electric Rayleigh number ($Ra_{e,c}$). By increasing the electric Rayleigh number (using higher voltage), Posner and Santiago (Posner and Santiago 2006) experimentally find the transition of flow from periodic to chaotic (a kind of disordered flow, but not turbulent).

By increasing external electric field intensity, higher electric-inertial velocity (u_e, the velocity scale when electric body force is balanced with inertial terms of Navier-Stokes equations, a relatively large scale quantity where viscosity effect is ignored) can be generated which could cause the flow to be unstable. If the electric-inertial velocity is increased sufficiently high, even though the bulk flow Re is still low, the corresponding electric Reynolds number, Re_e ($= du_e/\upsilon$, where d is the width of the interface between different electric conductivity solutions, υ is the kinematic viscosity) can be very large, and it is possible to generate a turbulent flow region before the kinetic energy of velocity fluctuation is completely dissipated by viscosity. Hence, the key issue is how to generate higher u_e. u_e can be estimated by dimensional analysis from the Navier-Stokes equation with electric body force, which is (Baygents and Baldessari 1998; Ramos et al. 1998; Ramos 2011):

$$\rho\left(\frac{\partial\vec{u}}{\partial t}+\vec{u}\cdot\nabla\vec{u}\right)=\nabla p+\eta\nabla^2\vec{u}+\vec{F}_e \tag{2.1}$$

where ρ, $\vec{u}$, p, η and $\vec{F}_e$ are the fluid density, flow velocity, pressure, dynamic viscosity and electrical body force, respectively. $\vec{F}_e=\rho_f\vec{E}$, where $\vec{E}$ is the electric field and $\rho_f=-\varepsilon\vec{E}\cdot\nabla\sigma/\sigma$ denotes the initial free charge density in solution (Chen et al. 2005), where ε is the permittivity of the electrolyte, σ is the electric conductivity of medium and $\nabla\sigma$ is the conductivity gradient. From Equation (2.1), we can easily find u_e is of the order $\sqrt{\left|d\varepsilon\left(\vec{E}\cdot\nabla\sigma\right)\vec{E}/\sigma\right|}$. Obviously, u_e can be increased by (1) increasing high conductivity ratio between the two streams; (2) high electric field intensity; (3) or aligning the external electric field to be in the same direction of the conductivity gradient.

Assume in the indiffusible limit, i.e. at extreme small effective diffusivity D_e, (about 1.5×10^{-9} m^2/s for the buffer solution), the scalar diffusion will only be effective at a much smaller scale than the momentum diffusion due to viscosity (Kolmogorov scale). The scalar structures can be sustained to Batchelor's scale by inertial and viscous convection (Batchelor 1959; Batchelor 1959), where the flux of scalar variance is constant. Hence, the local conductivity ratio of scalar structure will keep constant down to Batchelor's scale and so does the u_e.

For a given length scale l_e, we have the convective time scale $\tau_e = l_e/u_e$, which in turn, is much smaller than the related viscous diffusion time $\tau_d=\rho l_e^2/\mu$ for large l_e. In this case, viscous effect is negligible compared with convection effect, which due to shear stress and nonlinear effect, can generate smaller scale structures. As l_e becomes smaller, τ_d decreases faster than τ_e. At sufficiently small l_e, $\tau_d = \tau_e$. The viscous effect is directly

balanced by the inertial and electric effect which gives a possibly smallest length scale as (Wang et al. 2014):

$$l_{de} = \sqrt{\mu^2 \sigma_1 / \rho \varepsilon E_0^2 (\sigma_2 - \sigma_1)} = \sqrt{d^2 / \mathrm{Gr_e}} \tag{2.2}$$

where Gr_e is the nominal electric Grashof number and $Gr_e = \rho \varepsilon d^2 E_0^2 (\sigma_2 - \sigma_1)/\sigma_1 \mu^2$, σ_1 and σ_2 are the conductivity of the two streams, E_0 is the nominal electric field intensity in the interface. When Gr_e is increased, from Equation (2.2), l_{de} can be significantly decreased. On length scale $l \gg l_{de}$, the electric body force has stronger effect than viscous dissipation which results in a large contribution to inertial effect. Due to the inhomogeneous distribution of scalar structures, vortex structure can be generated by the external electric body force. While $l < l_{de}$, viscosity becomes dominant and electric body force will be immediately overcome by viscosity force. The flow at this scale is dominated by fluctuations of strains. l_{de} is an important length scale which reveals what smallest scales the velocity structures can be reduced to. From the introduction above, we can see l_{de} should be larger than Batchelor's scale, but smaller than Kolmogorov scale. As the largest vortex scale in microchannels is restricted by the geometry, decreasing l_{de}, will reduce the lower limit of energy cascade range and generate a large energy cascade range for the flow structures to evolve from large scale to small scale. In other words, to generate turbulence region, l_{de} should be small enough.

In light of aforementioned argument, following steps have recently been carried out to achieve turbulence (Wang et al. 2014): (1) An AC Electric field is applied through conductive sidewalls of the microchannel. As the conductivity gradient of two streams at the interface is perpendicular to the streamwise direction, this arrangement of electric field

can maximize $\vec{E} \cdot \nabla\sigma$ and thus Gr_e as well. (2) There is a 5° divergent angle between the two conductive sidewalls of the microchannel. The setup has two benefits. One is the flow can be more unstable compared to parallel sidewall, since the critical Reynolds number from the Jeffery-Hamel flow in a diffuser is smaller than a rectangular channel flow (Sahu and Govindarajan 2005). The other is the slightly inclined sidewalls will introduce a non-uniform electric field in streamwise direction. The high frequency and non-uniform AC electric field will again disturb the flow, especially near the sidewall where streamwise component of electric field is relatively strong. (3) Increase the conductivity ratio to 1:5000 to generate a steep conductivity gradient at the interface of the two streams. After these arrangement, the maximum nominal Gr_e can be up to 7×10^5, if let d=130 μm and $E_0 = 1.1 \times 10^5$ V/m.

2.2 Measurement method ─ Laser Induced Fluorescence Photobleaching Anemometer (LIFPA)

In this section, we first theoretically analyze and experimentally demonstrate the high TR of LIFPA (Rička 1987; Sugarman and Prud'homme 1987; Wang 2005; Kuang and Wang 2009) for *u'* measurement in unsteady EK flows. Then the results are compared with μPIV measurement.

2.2.1 Principle of LIFPA measurement

LIFPA bases on the photobleaching phenomenon of a small molecular fluorescent dye tracer (not micro- or nanoparticles) under the illuminating of laser beam. When an electrically neutral dye is used, it can avoid aforementioned issues with particles in μPIV. Generally, if laser power density (P_d) is uniform in focus area, the fluorescence intensity I_f decreases exponentially in a quiescent fluid with bleaching time t as:

$$I_f = I_{f0} e^{-t/\tau} \tag{2.3}$$

where I_{f0} is the initial I_f at $t = 0$ and τ is a half decay time constant. Both I_{f0} and τ are determined by P_d, dye concentration, fluorescent efficiency, and quantum yield of photobleaching of dye at the laser wavelength and pH etc. With Galilean transformation on Equation (2.3), I_f can be related to the instantaneous flow velocity u, as: $I_f(u; x, y) = I_{f0} e^{-x/u\tau}$

where x is the streamwise position in the laser focus along the direction of u, which is perpendicular to laser axis; y is the lateral position. If P_d is not uniform, but Gaussian. I_{f0}

and τ cannot be assumed to be constant as they depend on the bleaching history along pathline due to non-uniform P_d. A weight function $\psi(u;x,y)$ is introduced to account the influence of non-uniform P_d and we have:

$$I_f(u;x,y) = I_{f0}\psi(u;x,y)e^{-x/u\tau} \tag{2.4}$$

Approximating the exposure region to be a square with width of d_f (not accurate, but sufficient to evaluate the influence of high P_d region), the total $I_f(u;x,y)$ in the laser focus area, i.e. $I_{f,total}$ can be calculated as below:

$$I_{f,total}(u) = \int_0^{d_f}\int_0^{d_f} I_f(u;x,y)dx\,dy + I_{f,end}$$

where $I_{f,\,end}$ is a positive constant. As $\psi(u;x,y) > 0$ and is continuous in the region, $x \in (0, d_f)$ and $y \in (0, d_f)$, then:

$$I_{f,total}(u) = I_{f0}\psi_s(u)\int_0^{d_f}\int_0^{d_f} e^{-x/(u\tau)}dx\,dy + I_{f,end}$$

$$= \psi_s(u)d_f I_{f0}u\tau\left(1 - e^{-d_f/u\tau}\right) + I_{f,end} \tag{2.5}$$

Here, $\psi_s(u)$ is a slowly varying function compared to $u\left(1 - e^{-d_f/u\tau}\right)$ for evaluating the overall effect of non-uniform P_d, with $\psi_s(0) = \psi_s(\infty)$. Hence, $I_{f,total}(u)$ is a monotonically increasing function of u.

In highly and rapidly fluctuated flows, the temporal response of a velocimeter to u variation is of most interests. It should be sufficiently fast to capture the instantly varying u structures. Since the bleaching is behind the mechanism of LIFPA and the bleaching t can be approximately seen as the residence time of the dye within the laser beam, LIFPA's

TR, or temporal response to u variation, is normally determined by τ and d_f, and can be equivalently estimated from the bleaching process in a quiescent flow. At an arbitrary u, we can have a corresponding $I_{f,\,total}$, which in turn, corresponds to t in quiescent flow. If u changes in du, a corresponding change in time interval (i.e. dt) will cause $I_{f,\,total}$ to relocate under the bleaching process. The maximum du/dt should correspond to the highest acceleration that LIFPA can measure.

The relation of $I_{f,total,quie}{\sim}t$ in quiescent flow can be described as:

$$I_{f,total,quie}(t) = \psi_s(0)\int_0^{d_f}\int_0^{d_f} I_{f0}e^{-t/\tau}dx\,dy + I_{f,end} = \psi_s(0)d_f^2 I_{f0}e^{-t/\tau} + I_{f,end}$$

Let $I_{f,total}(u) \equiv I_{f,total,quie}(t)$, we find:

$$\psi_s(u)d_f I_{f0}u\tau\left(1 - e^{\frac{-d_f}{u\tau}}\right) = \psi_s(0)d_f^2 I_{f0}e^{-t/\tau} \tag{2.6}$$

From Equation (2.6), u can be related directly to t by a $u{\sim}t$ curve. Its slope determines the maximum temporal change of u LIFPA can measure. If

$$\left|\left(\frac{du}{dt}\right)_{LIFPA}\right| \geq \left|\left(\frac{du}{dt}\right)_{flow}\right| \tag{2.7}$$

i.e. the actual temporal change of u ($\left|(du/dt)_{flow}\right|$) is smaller than the slope ($|(du/dt)_{LIFPA}|$) of $u{\sim}t$curve, LIFPA can measure faithfully the variation of u. Reversely, if

$$\left|\left(\frac{du}{dt}\right)_{LIFPA}\right| < \left|\left(\frac{du}{dt}\right)_{flow}\right| \tag{2.8}$$

LIFPA cannot grasp *u* structures and results in underestimated of *u'*. $|(du/dt)_{LIFPA}|$ can be estimated by taking time derivatives on both sides of Equation (2.6), with plugging Equation (2.6) in as:

$$\left(\frac{du}{dt}\right)_{LIFPA}\left[\frac{d\psi_s(u)}{du}u\tau\left(1-e^{\frac{-d_f}{u\tau}}\right)+\psi_s(u)\tau\left(1-e^{\frac{-d_f}{u\tau}}\right)-\psi_s(u)\frac{d_f}{u}e^{\frac{-d_f}{u\tau}}\right]=$$

$$-\psi_s(u)u\left(1-e^{\frac{-d_f}{u\tau}}\right) \tag{2.9}$$

If $d_f/(u\tau) \gg 1$, i.e. for low *u*, and suppose $d\psi_s(u)/du \sim 0$ (as $\psi_s(u)$ is slowly varying function of *u*), it's obtained:

$$(du/dt)_{LIFPA} = -u/\tau \tag{2.10}$$

If $d_f/(u\tau) \ll 1$, i.e. for much larger *u*, and assume we only take into account the first order of exponential term ($e^{-d_f/u\tau} = 1 - d_f/u\tau$), then:

$$(du/dt)_{LIFPA} = -u^2/d_f \tag{2.11}$$

This means, at small magnitude of *u*, the response speed of LIFPA to *u* variation is proportional to *u* by a factor of -1/τ, and $u \sim t$ curve is exponential. While at high *u*, $(du/dt)_{LIFPA}$ is dominated by d_f and *u* itself, and *u*~*t* curve becomes power-law. A simplified $u \sim t$relation can further illustrate the mechanism of high TR of LIFPA. Let $\tilde{t} = t/\tau$, $\tilde{u} = u\tau/d_f$, and arbitrarily assume $\psi_s(u)$ to be a constant, from Equation (2.6) we have dimensionless equation:

$$\tilde{t} = -ln\left[\tilde{u}\left(1-e^{-\frac{1}{\tilde{u}}}\right)\right] \tag{2.12}$$

The $\tilde{u}\sim\tilde{t}$ relation is plotted in Figure 2.2(a). Here, $\tilde{t}$ can also be related to the resident time $t_r = d_f/u$ as:

$$\tilde{t} = -ln\left[\left(1 - e^{-\widetilde{t_r}}\right)/\widetilde{t_r}\right] \tag{2.13}$$

where $\widetilde{t_r} = t_r/\tau$. Larger *u* and smaller t_r are equivalent to shorter *t* in quiescent flow, and vice versa. $|d\tilde{u}/d\tilde{t}|\sim\tilde{u}$ curve is plotted in Figure 2.2(b).

A monotonic increasing relation can be found between $|d\tilde{u}/d\tilde{t}|$ and $\tilde{u}$. The higher *u*, the faster LIFPA responds. Normally, if no reverse flow exists, TR of LIFPA won't suffer from smaller *u* as long as τ is sufficiently small.

2.2.2 LIFPA setup

The LIFPA measurement system is consisted of a confocal microscopy system (CMS) and data acquisition system (DAS), as shown in Figure 2.1(b). Briefly say, the CMS is consist of a light source (405 nm continuous laser), self-assembled confocal microscope, high accuracy nano-translation stage (Physik Instrumente (PI) Piezo NanoCube 3-D positioning stage P-611.3SF) and Olympus objective of PlanApo100x NA 1.4 oil immersions. The laser power at its output is 50 mW.

The DAS is also shown in Figure 2.1(b) schematically. After an optical band-pass filter (to eliminate noise) and pinhole (as spatial filter), the fluorescence signal is collected by a high sensitive photomultiplier (PMT, HAMAMATSU, R-928). The current signal is amplified and filtered (low-pass) by a low-noise current preamplifier SR570 (Stanford

Research System) which generates a voltage signal. The signal is later sent to the computer by an NI A/D convertor and recorded by LabVIEW SignalExpress.

In this experiment, the spatial resolution of LIPFA dictated by the diffraction limit at focus is 203 nm in diameter and 812 nm in depth of focus. The sampling rate is 12.8 kHz to compatible to the spatial resolution at the recent bulk flow velocity.

2.2.3 μPIV measurements

For comparison, the velocity fluctuation measured by μPIV is also conducted. The μPIV system is consisted with PCO Sensicam high sensitivity camera, NewWave SOLO III pulse laser, self-assembled microscope with 60x NA 0.85 Plan microscope objective and Newport 3-D precision translation stage. 1 μm polystyrene fluorescent particle (Thermo Scientific Fluoro-Max Red) is used as tracer. The velocity field is calculated by Davis 7 software (by LaVision Inc.). The interrogation window size is 64pixels × 64 pixels (8.1μm×8.1μm) with 50% overlap. The depth of correlation should be larger than 30 μm if estimated from the work of Rossi (Rossi et al. 2012). The measured plane is z=-4 μm from centerline (Bown et al. 2006) which is a sufficient approximation of flow at centerline. For calculating the root-mean-square of velocity fluctuations, 200 velocity fields are processed in this manuscript.

2.2.4 AC EK flow in microchannel

In our research, an unsteady, EK forced pressure driven flow in a microchannel with external AC electric field, is investigated to demonstrate the high TR of LIFPA. A quasi T-channel with side walls of 5º divergent angle was fabricated as shown in Figure 2.1(a). Both top and bottom layer of the channel are made by transparent acrylic plastic substrates. The sidewalls of the microchannel are conductive (gold) so that they are used as electrodes for forcing a pressure driven flow electrokinetically. The channel has a rectangular cross section. At entrance, the width (w) is 130 μm. The height is 240 μm which is constant for the entire 5mm long channel.

The two streams are pumped into the channel by a Harvard Apparatus PHD 2000 infusion pump. They are separated by a plastic (Acrylic) splitter plate that have a sharp trailing edge. The two streams have different conductivities, one side is approximately 1 μS/cm, the other side is 5000 μS/cm. The flow rate of each stream is about 2 μL/min. Hence, the bulk flow Reynolds number (Re=$U_b d/v$, where U_b=2 mm/s is the bulk flow velocity, d is the hydraulic diameter of channel at the entrance and v is the kinematic viscosity of water) is around 0.4.

While forced, an AC signal by Tektronix function generator, Model AFG3102 is applied on the pressure driven flow. Two channels of the function generator are separately connected to the two electrodes of the microchannel's sidewalls. Sinusoidal signals with the same amplitude and frequency but 180º phase difference are applied to maximum the disturbance and increase velocity fluctuations.

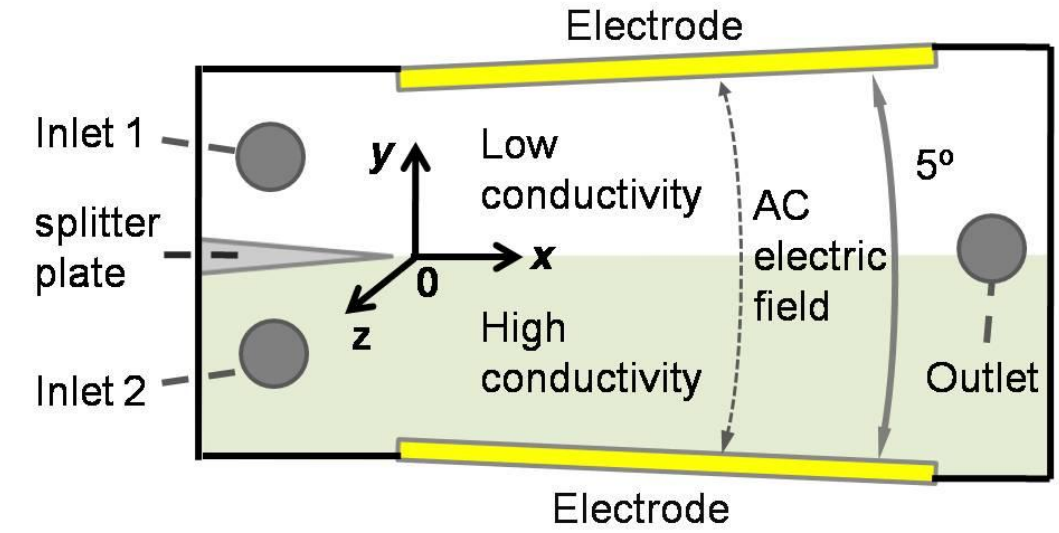

(a)

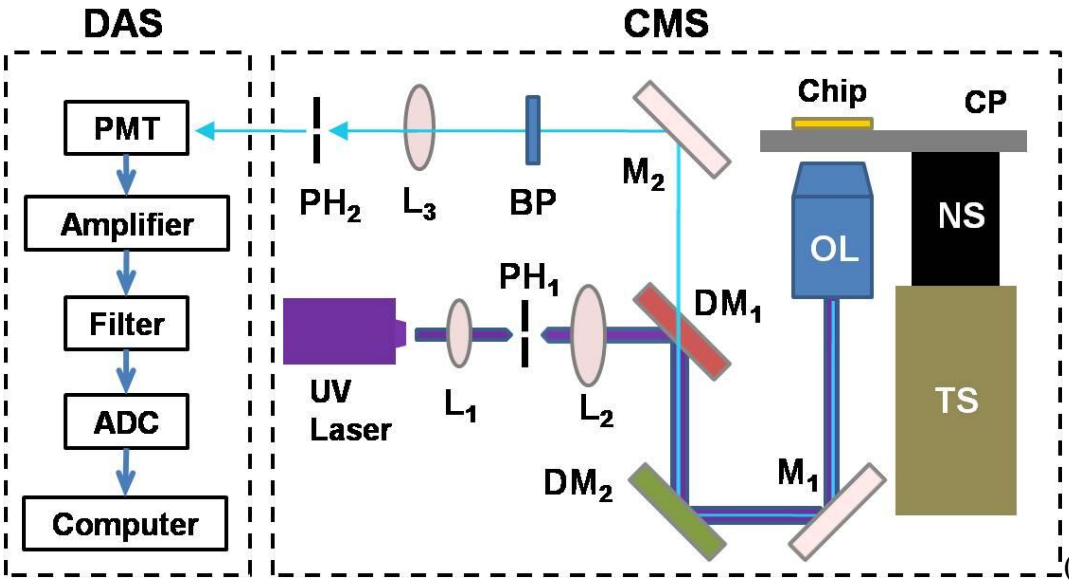

(b)

Figure 2.1 (a) Schematic of microchannel. AC electric field is applied on the two gold electrodes by function generator. Basic flow is supplied by syringe pump. (b)Setup of LIFPA system in this experiment. L1, L2 and L3: lenses; PH1 and PH2: pinholes; DM1 and DM2: dichroic mirrors; MOF: multi-mode optical fiber; M1 and M2: mirrors; BP: bandpass filter; OL: objective lens from Olympus; CP: carrier plate; NS: Nano cube piezostage (PI, 3-D); TS: manual translation stage (Melles-Griot, 3-D); ADC: NI A/D converter; PMT: photomultiplier (HAMAMATSU, R-928); Amplifier: SR570; Filter: SR570 built-in.

2.2.5 Experimental results

Similar as hot-wire anemometer (HWA), LIFPA should be calibrated before measurement. In this experiments, LIFPA is calibrated in the same microchannel that experiments will be conducted. To avoid the inaccurate syringe pump, the flow velocity is also calibrated by particle tracing method. The calibration curve $u = u(I_{f,total})$ is nonlinearly fitted by both 5th order polynomial curve ($u(I_{f,total}) = \sum_{n=0}^{5} a_n I_{f,total}^n$) and the theoretical curve from Equation (2.5), where the effect $\psi_s(u)$ is assumed to be a constant. Both methods exhibit good fitting as shown in Figure 2.2(c). The 5th order polynomial is adopted for u calculation because of the better fitting.

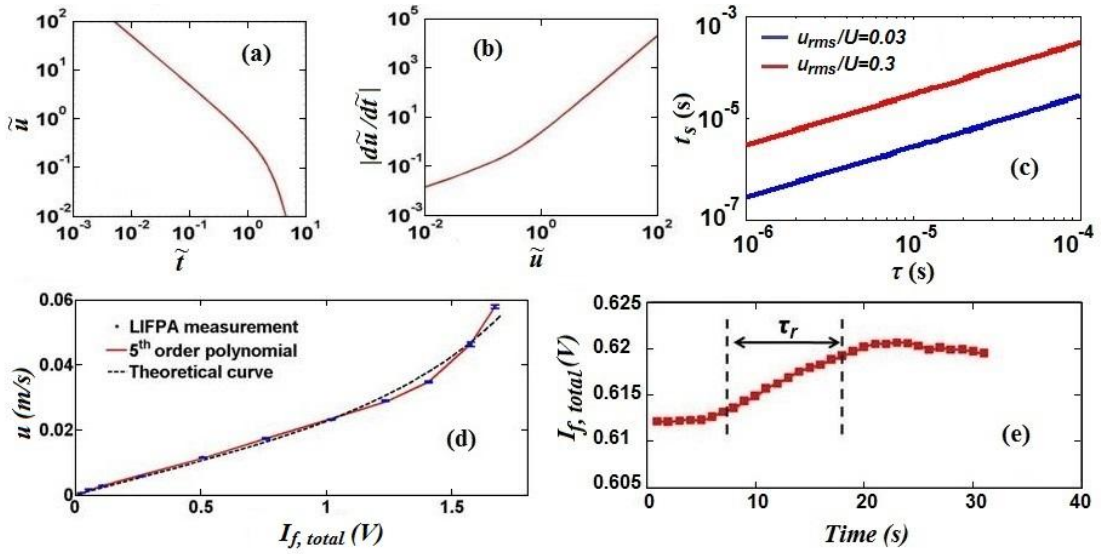

Figure 2.2 (a) Typical relation between $\tilde{u}$ and $\tilde{t}$, (b) $|d\tilde{u}/d\tilde{t}|$ vs $\tilde{u}$. (c) t_s vs τ at different velocity fluctuation intensities. (d) LIFPA calibration curve fitting by both theoretical curve (Equation (3)) and 5th order polynomial. (e) Rise time of EOF. The transient process of the initial stage of the EOF with time step of 1 μs during a 15 μs period. The result shows that TR of the LIFPA is better than 5 μs, because values can be easily discriminated during the 5 μs time intervals.

The time series of u is plotted in Figure 2.3(a), where three cases are investigated. Without forcing, u is nearly constant with negligible small fluctuations due to vibration of

the setup and shot noise. Under forcing with voltage V=8 $V_{p\text{-}p}$, f=100 kHz, the flow is slightly and randomly disturbed. However, when V is increased to 20 $V_{p\text{-}p}$, u signal becomes random with large and rapid fluctuation, and large local gradient as shown in Figure 2.3(b).

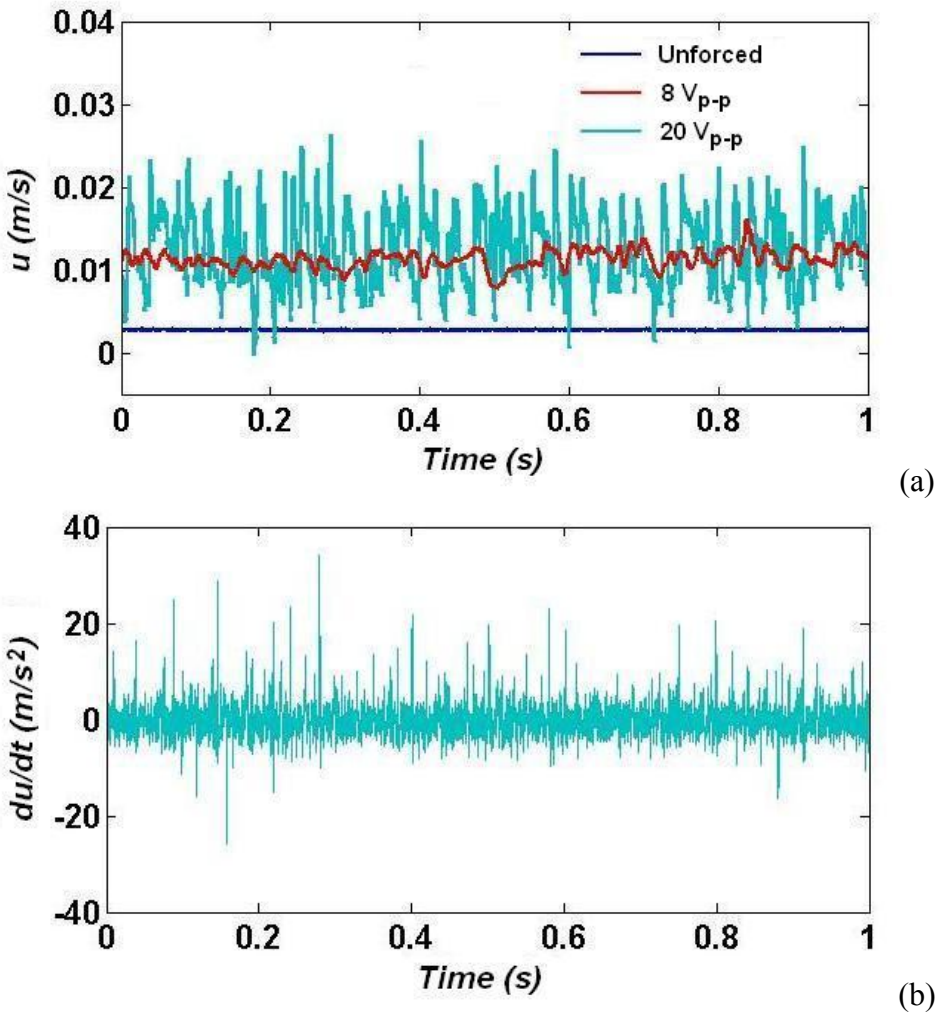

Figure 2.3 Time series of (a) u at different voltages and f=100. (b) du/dt at V=20 $V_{p\text{-}p}$ along center line of the channel at x=10 μm downstream from trailing edge.

By fitting Equation (2.5) (as shown in Figure 2.2(c)), τ is found to be about 4 μs. As $d_f/(u\tau) \gg 1$, the $|(du/dt)_{LIFPA}|$ is estimated to be 500 m/s^2 according to Equation

(2.10), when $u = 2$ mm/s. This is much larger than the maximum $|(du/dt)_{flow}|$ (about 35 m/s^2) in Figure 2.3(b). Hence, the LIPFA measurement is theoretically fast enough to measure *u'* in this flow. Although $|(du/dt)_{LIFPA}|$ decreases to 50 m/s^2 when *u* is reduced to 0.2 mm/s (already a small value for most lab-on-a-chip applications), it is still sufficiently fast to measure at least 2 kHz signal.

To ensure the high TR character of LIFPA, the rise time τ_r of DC electroosmotic flow (EOF) under sudden applied electric field is also investigated. (The flow rate of each stream is still 2 μL/min. Two electrodes were placed at the inlets and outlet with 20 $V_{p\text{-}p}$ voltage. Two streams has same conductivity of 1 μS/cm to generate a larger electric double layer. Measured at 1 μm from bottom. The sampling rate of signal in this experiment is 1 MHz.) As shown in Figure 2.2(d), the rise time of EOF flow is about 10 μs. Although due to the relatively weak electric field intensity, the velocity increment caused by EOF (about 0.3 mm/s) is limited. But the influence of EOF still can be clearly distinguished from basic flow. Hence, the rapid response of LIFPA is undisputed.

$u^*_{rms}(= \sqrt{\overline{u'^2}}/U_b$, where the bar means ensemble averaging) at V=20 $V_{p\text{-}p}$, f=100 kHz is measured by both LIFPA and μPIV (via fluctuation of velocity module to compare with LIFPA data as LIFPA cannot distinguish velocity directions) and compared at different streamwise positions, as plotted in Figure 2.4. Adjacent to the inlet, u^*_{rms} is very large. Here, u^*_{rms} measured from μPIV is at leaset 24% smaller than that from LIFPA. After x/w=0.4 downstream, where u^*_{rms} is much weaker due to rapid viscous dissipation, μPIV exhibits consistent value as LIFPA. This comparison directly indicates high TR of LIFPA. In Figure 2.5, the PSD of u' is plotted. The detectable *u* structure in

micro EK forced flows can be up to 2 kHz (whose corresponding wave-number is about 6×10^6 1/m), which to our knowledge, cannot be measured by μPIV recently. The reason why the measured u^*_{rms} by μPIV is lower than that measured by LIFPA is not clear and has several possibilities. One could be because μPIV has difficulty in measuring the fast fluctuated u' due to intrinsic particle lagging (although the discrepancy is small if estimated from Adrian (Adrian 1991)), for the especially high frequency small scale structures, which is crucial for transport phenomena. Another cause could be EK force (e.g. dielectrophoresis (DEP), electrophoresis et al) loaded on the particles. In this experiments, the DEP effect is inevitablethe. The real part of Clausius-Mossotti factor is between -0.5 to 0.74 and varies at different positions with time, due to the varying solution conductivity and permittivity. The local DEP effect will varies spatially and temporally and results in an unpredictable varying DEP force which may drive the particles in a different direction as flow. Besides, as the particle is slightly negatively charged, the influence of AC electric body force on particles are also unpredictable. These influences will also cause the μPIV measurement departure from the actual flow veocity. The third reason may be due to the relatively low spatial resolution of μPIV, not only in xy plane, but also the large depth of correlation in z-direction (Rossi et al. 2012). All these uncertainties could cause smaller magnitude of velocity fluctuations measured by μPIV in this EK flow, compared to LIFPA method.

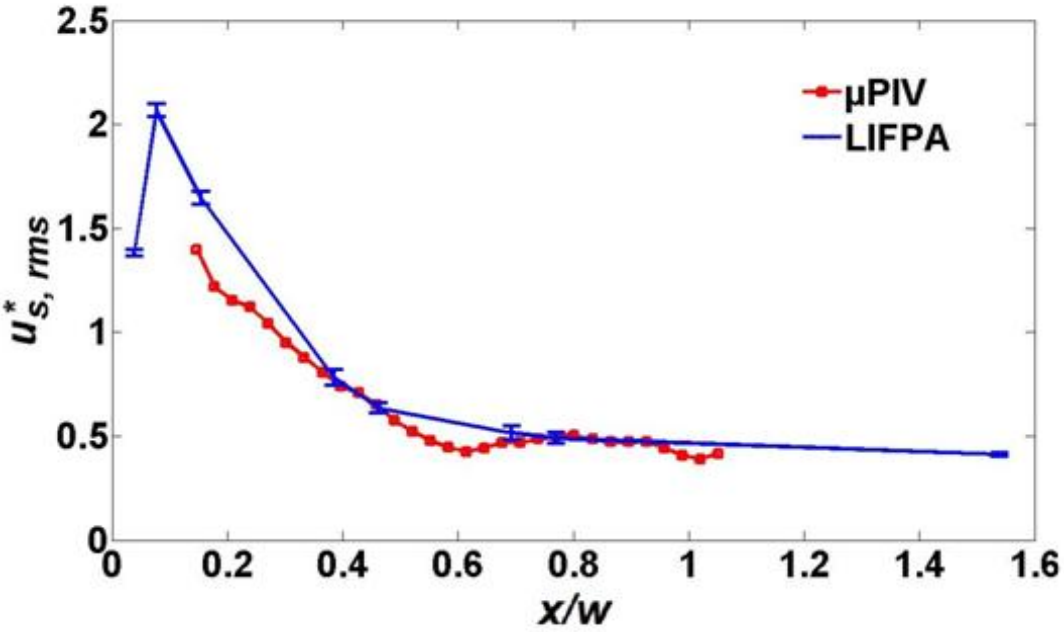

Figure 2.4 Comparison of u^*_{rms}measured along x-direction by both LIFPA and μPIV at the centerline of channel under V=20 $V_{p\text{-}p}$, f=100 kHz.

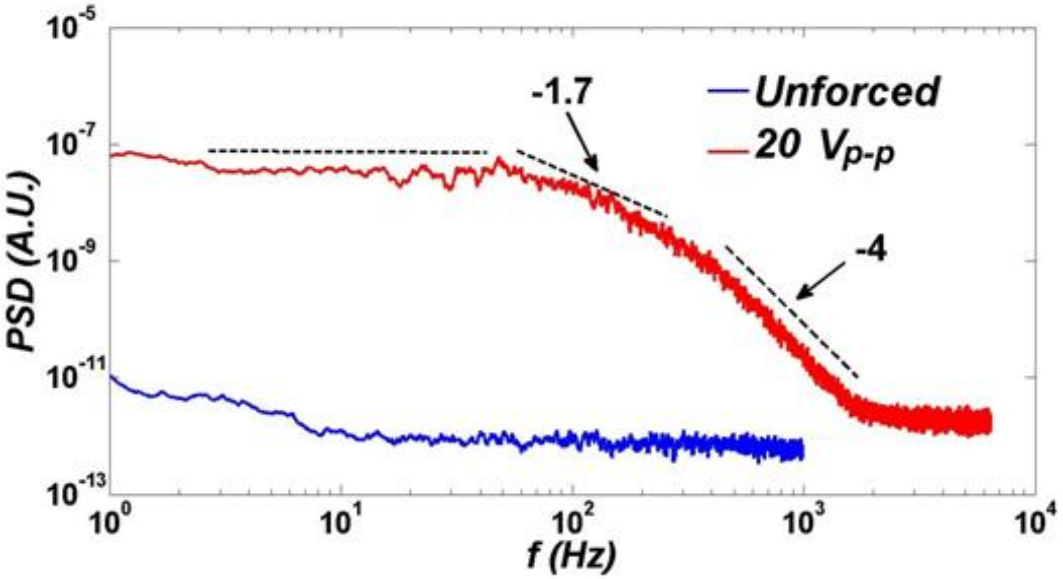

Figure 2.5 Velocity PSD along centerline at x=10 μm.

2.2.6 Discussion

In section 2.2, the TR of LIPFA is theoretically investigated and compared to μPIV measurement. Recently, LIFPA technique is still on its early stage and has large development potency. By increasing laser intensity at focus point or developing new

fluorescent dye, τ can be further reduced and significantly increase TR. The limit of τ is life time of fluorescence, which can be on the order from nanosecond to microsecond. Since the neutral dye is molecularly dissolved in the fluid, there are always sufficient "particles" of molecular size as flow tracer to avoid the issues of particle seeding and interaction with electric field in μPIV, and to ensure continuously high frequency sampling with long time measurement. Therefore LIFPA can be a new technique for statistical measurement of high frequency u' with simultaneously high spatiotemporal resolution in complex flows in microfluidics.

2.3 Comparison and correction

In this section, we focused on the correction of statistical velocity quantities in a microchannel that has moderate velocity fluctuations. The corrections of mean flow velocity and standard deviation of velocity fluctuations are introduced. The FDV of velocity fluctuation is first evaluated by Local Taylor Hypothesis (LTH) suggested by Pinton (Pinton and Labbé 1994) and compared to the conventional Taylor Hypothesis (TH). Then the statistical errors due to 3-D flow effect at different turbulent intensities are estimated later.

2.3.1 Correction of velocity measurement

(1) Basic relations

Briefly say, LIFPA can be simply considered as an optical version of hot-wire anemometer, but is a non-invasive method with much high spatial resolution. It is also unaffected by the presence of electric field, since electrically neutral dye can be used as molecular scale tracer. In LIFPA measurement, the measured instant velocity can be determined as below (Ewing 2004):

$$u_m = (a_i^2 u_i^2)^{1/2} \tag{2.14}$$

where the subscript "m" indicates the measured value. u_i is the true instantaneous velocity. u_1 is in the direction (x_1) of mean flow velocity; u_2 is in the transverse direction (x_2), i.e perpendicular to both the laser beam and x_1. And u_3 is parallel to thelaser beam (x_3). a_i is the directional correction factor in each direction for LIFPA measurement. The repeated subscripts indicate summation convention from 1 to 3, if no otherwise specified. In this manuscript, we only investigate the flow where the mean velocity is perpendicular to the laser beam. And hence, the velocity components can be expressed as $u_i = U\delta_{1i} + u_i'$, where U is mean flow velocity, (Note: here, x_i is not necessary to be global constant and can change with positions locally.)

(2) Relations of kinetic energy

Take the square of Equation (2.14), and because $u_m = U_m + u'_m$, where, $U_m$and u'_m are the measured mean velocity and velocity fluctuation, respectively, we have the equation for kinetic energy:

$$U_m^2 + \langle u'^2_m \rangle = U^2 + \langle a_i^2 u'^2_i \rangle \tag{2.15}$$

where, <> indicates ensemble averaging.

(3) Estimation of U

Based on Equation (2.14) and (2.15), the real mean velocity *U* can be estimated. Rewrite Equation (2.14) in dimensionless form, we have:

$$\frac{u_m}{a_1 U} = \left(1 + 2\widetilde{u'}_1 + \widetilde{u'}_1^2 + \frac{a_2^2}{a_1^2}\widetilde{u'}_2^2 + \frac{a_3^2}{a_1^2}\widetilde{u'}_3^2\right)^{1/2} = (1+M)^{1/2}$$

where $M = 2\widetilde{u'}_1 + \widetilde{u'}_1^2 + \frac{a_2^2}{a_1^2}\widetilde{u'}_2^2 + \frac{a_3^2}{a_1^2}\widetilde{u'}_3^2$ and $\widetilde{u'}_\iota = u'_i/U$. In the flow field where |M|<1 is satisfied, by applying binomial expansion, we have:

$$\frac{u_m}{a_1 U} = 1 + \widetilde{u'}_1 + \frac{\frac{a_2^2}{a_1^2}\widetilde{u'}_2^2}{2} + \frac{\frac{a_3^2}{a_1^2}\widetilde{u'}_3^2}{2} + O\left(\widetilde{u'}^3\right)$$

where $\widetilde{u'} = \left(\widetilde{u'}_\iota \widetilde{u'}_\iota/3\right)^{1/2}$. In isotropic flow, the mean value of measured velocity U_m and the real mean velocity *U*,

$$\frac{U_m}{U} = a_1 + \frac{\langle \widetilde{u'}_1^2 \rangle}{2a_1}(a_2^2 + a_3^2)$$

Or alternatively in dimensional expression,

$$a_1 U^2 - U_m U + \frac{1}{2a_1}(a_2^2 + a_3^2)\langle u'^2_1\rangle = 0 \tag{2.16}$$

Plug Equation (2.15) into (2.16) and easily we can find,

$$U = \frac{C_2 U_m \pm \sqrt{C_3 U_m^2 - C_1(a_2^2+a_3^2)\langle u\prime_m{}^2\rangle}}{C_1} \tag{2.17}$$

where $C_1 = 2a_1^4 + 2a_1^2a_2^2 + 2a_1^2a_3^2 - a_2^2 - a_3^2$, $C_2 = a_1(a_1^2 + a_2^2 + a_3^2)$, $C_3 = a_1^3 + (a_1 - 1)(a_2^2 + a_3^2)$. In the solution, only the positive sign is selected to meet the constraint of |M|<1.

For the anisotropic case, the corrections of mean velocity and velocity variance are also available. This can be simply achieved by replacing a_i (i= 2, 3) with $a_i\sqrt{\langle u'^2_i\rangle/\langle u'^2_1\rangle}$ to count the anisotropy into directional correction factors.

After calculating U, $\langle u'^2_1\rangle$ can be obtained as

$$\langle u'^2_1\rangle = \frac{U_m^2 + \langle u\prime_m^2\rangle - U^2}{a_i a_i} \tag{2.18}$$

Experimental results will be introduced later.

2.3.2 Correction on first derivative variance

(1) The influence of LTH

In moderately fluctuated flow, the FDV of velocity fluctuations, i.e. $\langle(\partial u_1'/\partial x_1)^2\rangle$, is very important for calculating dissipation rate and characteristic spatial and temporal scales. However, similar as HWA, directly measure u_1' is impossible and error can exist while using u_m' instead of u_1' to calculate FDV. The error primarily comes from two sources. One is the improper use of Taylor Hypothesis due to the relatively large velocity fluctuations. The other is the 3-D velocity fluctuations due to the indistinguishable velocity components. In this section, the influence of the first reason on $\langle(\partial u_1'/\partial x_1)^2\rangle$ is investigated.

Conventionally, the calculation of $\langle(du'_m/dx_1)^2\rangle$ by TH can be expressed as (Monin and Yaglom 1975):

$$\langle\left(\frac{du'_m}{dx_1}\right)^2\rangle = \langle\left(\frac{du'_m}{U_m dt}\right)^2\rangle \tag{2.19}$$

This is a reasonable approximation while local turbulent intensity is much smaller than 1 (Tennekes and Lumley 1972). But, if this condition is not satisfied, TH cannot be arbitrarily applied, as the spatial velocity distributions may be not correctly calculated by velocity time series and its mean value. Hence, the influence of relatively large-scale velocity fluctuations which have most influences on positioning of velocity should be evaluated by LTH.

LTH is first suggested by Pinton (Pinton and Labbé 1994) while transferring the energy spectrum of velocity from frequency region to wavenumber region. In the scheme,

the spatial position is determined by the time interval and locally averaged velocity (named advection average velocity) which is calculated by:

$$\widehat{U}_m(t) = \frac{1}{T}\int_{t-T/2}^{t+T/2} u_m(\tau)\, d\tau$$

where T is a characteristic time scale. These authors defined T as the period of an external force. However, in many practical cases, such as our investigation here, the forcing frequency of electric field is higher than the cut-off frequency of velocity signal that can be measured in the flow, such as high-frequency AC EK flow(Wang et al.). We cannot simply use the period of the electric field as T. Instead, an arbitrary time scale related to large-scale energy containing structure is used. If Kolmogorov spectra exists, T is the reciprocal of the frequency, where -5/3 slope starts. If not, such as in cases of chaotic flows, the reciprocal of frequency, where steeper descending of power spectrum (related to the viscous diffusion region) starts, is applied.

Then, FDV of velocity fluctuations via LTH can be calculated as:

$$\langle\left(\frac{d\widehat{u'}_m}{dx_1}\right)^2\rangle = \langle\left(\frac{d\widehat{u'}_m}{\widehat{U}_{m,LTH}(t)dt}\right)^2\rangle \tag{2.20}$$

where $u_m(t) = \widehat{U}_m(t) + \widehat{u'}_m(t)$. The results of FDV calculated by TH and LTH will be introduced in section 2.3.3. Here, the reference mean velocity for TH is U_m, not U. This is because we cannot directly estimate the advection average velocity U.

(2) 3-D flow effect

In LIFPA measurements, a_3 is not negligible because the aspect ratio between depth of focus and diameter of focus is relatively small (4~5), which is mainly determined by the microscope objective. Therefore the contribution of $u_3^{'}$ cannot be simply ignored as always done in HWA. Hence, we expand Ewing's work (Ewing and George 2000) for HWA to LIFPA for the 3-D velocity fluctuations and their derivatives with the influence of directional correction factor a_i. This leads to:

$$\left\langle\left(\frac{\partial u_m}{\partial x}\right)^2\right\rangle = \frac{1}{U^2}\left\langle\frac{a_l^2 a_n^2 a_i a_j u_{l,LW} u_{n,LW} u_{i,LW} u_{j,LW}}{a_1^2 u_{1,LW}^2 + a_2^2 u_{2,LW}^2 + a_3^2 u_{3,LW}^2}\right\rangle \left\langle\frac{\partial u'_{l,HW}}{\partial x_i}\frac{\partial u'_{n,HW}}{\partial x_j}\right\rangle \tag{2.21}$$

where, l, n, i, j are summed from 1 to 3. $u'_i = u'_{i,LW} + u'_{i,HW}$ and $u_{i,LW} = U\delta_{1i} + u'_{i,LW}$. Here, subscript '*LW*' means the low-wavenumber components of velocity fluctuations which are related to the energy containing structures, i.e. large scale vortex structures. This part dominates the kinetic energy of velocity fluctuations. '*HW*' indicates the high-wavenumber parts of velocity fluctuations which locates in inertial and dissipation subrange (Lumley 1965). It dominates the FDV of velocity fluctuations. Applying binomial expansion to the 3rd order, the first denominator of Equation (2.21) can be written as:

$$\frac{1}{a_1^2 u_{1,LW}^2 + a_2^2 u_{2,LW}^2 + a_3^2 u_{3,LW}^2}$$

$$= \frac{1}{a_1^2 U^2}\left[1 - 2\left(\frac{u'_{1,LW}}{U}\right) + 3\left(\frac{u'_{1,LW}}{U}\right)^2 - 4\left(\frac{u'_{1,LW}}{U}\right)^3 - \frac{a_2^2}{a_1^2}\left(\frac{u'_{2,LW}}{U}\right)^2 - \frac{a_3^2}{a_1^2}\left(\frac{u'_{3,LW}}{U}\right)^2 + 4\frac{a_2^2}{a_1^2}\left(\frac{u'_{1,LW}}{U}\right)\left(\frac{u'_{2,LW}}{U}\right)^2 + 4\frac{a_3^2}{a_1^2}\left(\frac{u'_{1,LW}}{U}\right)\left(\frac{u'_{3,LW}}{U}\right)^2 + \cdots\right]$$

Hence, up to the second order of $u'_{i,LW}$, Equation (2.21) becomes:

$$\left\langle\left(\frac{\partial u'_m}{\partial x_1}\right)^2\right\rangle = a_1^4\left(1+\left\langle\frac{u'^2_{1,LW}}{U^2}\right\rangle-\frac{a_2^2}{a_1^2}\left\langle\frac{u'^2_{2,LW}}{U^2}\right\rangle-\frac{a_3^2}{a_1^2}\left\langle\frac{u'^2_{3,LW}}{U^2}\right\rangle\right)\left\langle\left(\frac{\partial u'_{1,HW}}{\partial x_1}\right)^2\right\rangle$$

$$+\left\langle\frac{u'^2_{2,LW}}{U^2}\right\rangle\left[a_2^4\left\langle\left(\frac{\partial u'_{2,HW}}{\partial x_1}\right)^2\right\rangle+a_1^2a_2^2\left\langle\left(\frac{\partial u'_{1,HW}}{\partial x_2}\right)^2\right\rangle\right.$$

$$\left.+2a_1a_2^3\left(\left\langle\frac{\partial u'_{1,HW}}{\partial x_2}\frac{\partial u'_{2,HW}}{\partial x_1}\right\rangle+\left\langle\frac{\partial u'_{1,HW}}{\partial x_1}\frac{\partial u'_{2,HW}}{\partial x_2}\right\rangle\right)\right]$$

$$+\left\langle\frac{u'^2_{3,LW}}{U^2}\right\rangle\left[a_3^4\left\langle\left(\frac{\partial u'_{3,HW}}{\partial x_1}\right)^2\right\rangle+a_1^2a_3^2\left\langle\left(\frac{\partial u'_{1,HW}}{\partial x_3}\right)^2\right\rangle\right.$$

$$\left.+2a_1a_3^3\left(\left\langle\frac{\partial u'_{1,HW}}{\partial x_3}\frac{\partial u'_{3,HW}}{\partial x_1}\right\rangle+\left\langle\frac{\partial u'_{1,HW}}{\partial x_1}\frac{\partial u'_{3,HW}}{\partial x_3}\right\rangle\right)\right]$$

$$+2\left\langle\frac{u'_{1,LW}u'_{2,LW}}{U^2}\right\rangle\left[a_1^2a_2^2\left\langle\frac{\partial u'_{1,HW}}{\partial x_1}\frac{\partial u'_{2,HW}}{\partial x_1}\right\rangle+a_1^3a_2\left\langle\frac{\partial u'_{1,HW}}{\partial x_1}\frac{\partial u'_{1,HW}}{\partial x_2}\right\rangle\right]$$

$$+2\left\langle\frac{u'_{1,LW}u'_{3,LW}}{U^2}\right\rangle\left[a_1^2a_3^2\left\langle\frac{\partial u'_{1,HW}}{\partial x_1}\frac{\partial u'_{3,HW}}{\partial x_1}\right\rangle+a_1^3a_3\left\langle\frac{\partial u'_{1,HW}}{\partial x_1}\frac{\partial u'_{1,HW}}{\partial x_3}\right\rangle\right]$$

$$+2\left\langle\frac{u'_{2,LW}u'_{3,LW}}{U^2}\right\rangle\left[a_1a_2^2a_3\left(\left\langle\frac{\partial u'_{1,HW}}{\partial x_3}\frac{\partial u'_{2,HW}}{\partial x_1}\right\rangle+\left\langle\frac{\partial u'_{1,HW}}{\partial x_1}\frac{\partial u'_{2,HW}}{\partial x_3}\right\rangle\right)+\right.$$

$$a_1a_2a_3^2\left(\left\langle\frac{\partial u'_{1,HW}}{\partial x_2}\frac{\partial u'_{3,HW}}{\partial x_1}\right\rangle+\left\langle\frac{\partial u'_{1,HW}}{\partial x_1}\frac{\partial u'_{3,HW}}{\partial x_2}\right\rangle\right)+a_1^2a_2a_3\left\langle\frac{\partial u'_{1,HW}}{\partial x_2}\frac{\partial u'_{1,HW}}{\partial x_3}\right\rangle+$$

$$\left.a_2^2a_3^2\left\langle\frac{\partial u'_{2,HW}}{\partial x_1}\frac{\partial u'_{3,HW}}{\partial x_1}\right\rangle\right]+\text{H.O.T.} \qquad (2.22)$$

Besides,

$$\langle u'_i u'_j\rangle = \langle\left(u'_{i,LW}+u'_{i,HW}\right)\left(u'_{j,LW}+u'_{j,HW}\right)\rangle$$

$$= \langle u'_{i,LW} u'_{j,LW} \rangle + \langle u'_{i,LW} u'_{j,HW} \rangle + \langle u'_{i,HW} u'_{j,LW} \rangle + \langle u'_{i,HW} u'_{j,HW} \rangle \quad (2.23)$$

Because the correlation between LW and HW parts can be ignored (Lumley 1965) and $\langle u'_{i,HW} u'_{j,HW} \rangle$ is much smaller than $\langle u'_{i,LW} u'_{j,LW} \rangle$, the Equation (2.23) can be rewritten as:

$$\langle u'_{i,LW} u'_{j,LW} \rangle \approx \langle u'_i u'_j \rangle$$

Similarly, as the FDV is normally dominated by high-wavenumber fluctuations (Lumley 1965; Wyngaard and Clifford 1977), we have:

$$\langle \frac{\partial u'_{l,HW}}{\partial x_i} \frac{\partial u'_{n,HW}}{\partial x_j} \rangle \approx \langle \frac{\partial u'_l}{\partial x_i} \frac{\partial u'_n}{\partial x_j} \rangle$$

To simplify the analysis here, the flow is assumed to be homogeneous and isotropic as,

$$\langle \frac{\partial u'_l}{\partial x_i} \frac{\partial u'_n}{\partial x_j} \rangle = 2 \langle \left(\frac{\partial u'_1}{\partial x_1} \right)^2 \rangle \left[\delta_{ij} \delta_{ln} - \frac{1}{4} \left(\delta_{il} \delta_{jn} + \delta_{in} \delta_{jl} \right) \right]$$

Expression (7) can be simplified as,

$$\langle \left(\frac{\partial u'_m}{\partial x_1} \right)^2 \rangle = a_1^4 \langle \left(\frac{\partial u'_1}{\partial x_1} \right)^2 \rangle + \frac{\langle u'^2_1 \rangle}{U^2} [a_1^4 + a_2^4 + a_3^4 + a_2^2 (a_1 - a_2)^2 + a_3^2 (a_1 -$$

$$a_3)^2] \langle \left(\frac{\partial u'_1}{\partial x_1} \right)^2 \rangle \quad (2.24)$$

It can be seen, the measured FDV of velocity will be contaminated by both the 3-D velocity components and the different direction factors of LIFPA. This will inevitably introduce an error when a_i (i=1, 2, 3) is close to 1 in high turbulent intensity flows, while |M|<1 is satisfied. However, compared to the previous works (Wyngaard and Clifford 1977;

Ewing and George 2000), Equation (2.24) indicates a smaller error, if assume a_i (i=1, 2, 3) is 1. And the error can be even smaller if $a_3 << 1$. This is interesting and means in isotropic flow, if consider all the component effects, the error is not that large as mentioned by Wyngaard and Ewing. Here, we only expand the equation to the 2nd order of *u'* and this may cause the error being underestimated compared to Ewing who approximate Equation (2.22) to third order, when $\widetilde{u'}$ is not small. But instead, as the influence of velocity component in x_3 direction is included, ignoring the higher order terms of Equation (2.22) should have negligible influence.

In fact, Ewing (2000) has also taken account of the TH influence for moderate turbulent intensities. But compared to the LTH, the limit of binomial expansion restricts the application of Ewing's theory from much higher turbulent intensity. Hence, Ewing (2000) and Equation (2.24) in this manuscript is only proper for moderate or small velocity fluctuations, while LTH can be used for the flow which has large velocity fluctuations, even reverse flow existed as introduced by Pinton (1994).

(3) Estimate the coefficients a_i

The coefficients a_i are normally determined by the photobleaching character of LIFPA system, i.e. dimensions of laser focus, laser power, fluorescent dye and velocity range. As LIFPA has good linearity of velocity with fluorescence intensity, the difference of velocity fluctuations in x_1 and x_2 directions is very small and negligible. a_2 should be close to a_1. Here, the streamwise factor a_1 and transverse factor a_2 are both 1, as the symmetry of laser beam and linearity of velocity calibration curve of LIFPA at low velocity. Due to the low

aspect ratio of laser focus, in LIFPA measurement, the correction factor of parallel-beam direction, i.e. a_3, may have apparent different from the HWA. In HWA measurement, the smaller the aspect ratio of hot wire, the larger the value of a_3. And the flow parallel to laser beam will have larger contribution to velocity measurement which is undesired. Also due to the existence of prongs, the flow in x_3 direction can generate additional flow disturbance in other two directions, and the measured velocity signals will be contaminated. However, in LIFPA measurement, even though the aspect ratio is only 4, the influence of flow in parallel-beam direction is still negligible. The value of a_3 can be estimated by the comparing photobleaching process of a dye in orthogonal and parallel directions of the laser beam.

The fluorescence intensity normally decreases with time exponentially, as below:

$$I = I_0 e^{-t/\tau}$$

where, I_0 is the initial value of I.

In the case where the uniform flow is perpendicular with laser beam (i.e. x_1 or x_2 direction) with velocity magnitude $u_\perp$, as shown in Figure 2.6(a) and (c), the spatial distribution of I in the laser focus is:

$$I_\perp(l) = I_0 e^{-l/u_\perp \tau}$$

where l is the distance from where the dye enters laser focus region, along the direction of velocity. However, if the flow direction is parallel to the laser beam (i.e. x_3 direction with magnitude of $u_\parallel$), as the dye solution has been more or less pre-photobleached before

entering the focus (as schemed in Figure 2.6(b) and (d)), assume the pre-photobleach length is d_{pp}, the spatial distribution of fluorescence intensity along the laser focus is:

$$I_{\parallel}(l) = I_0 e^{-(l+d_{pp})/u_{\parallel}\tau}$$

Here, as a roughly approximation, the focus region is simplified to rectangular cube with uniform laser intensity, with transverse width d_f and depth of focus d_{pf}. Then, in the perpendicular case, the total fluorescence intensity can be calculated by:

$$I_{\perp} = d_{pf} d_f \int_0^{d_f} I_{\perp}(l) dl = u_{\perp}\tau d_{pf} d_f I_0 \left(1 - e^{-\frac{d_f}{u_{\perp}\tau}}\right) \tag{2.25}$$

While for the parallel case, the total fluorescence intensity is:

$$I_{\parallel} = d_f^2 \int_0^{d_{pf}} I_{\parallel}(l) dl = u_{\parallel}\tau d_f^2 I_0 e^{-\frac{d_{pp}}{u_{\parallel}\tau}} \left(1 - e^{-\frac{d_{pf}}{u_{\parallel}\tau}}\right) \tag{2.26}$$

To evaluate the influence of different flow direction on LIFPA measurement, we let $u_{\perp} = u_{\parallel}$ which both have the magnitude of u. Then, for the case where $u\tau \gg d_{pf} \sim d_{pp} > d_f$, expend the exponential term to the second order, we have:

$$I_{\perp} \approx d_{pf} d_f^2 I_0 \left(1 - \frac{d_f}{2u\tau}\right)$$

$$I_{\parallel} \approx d_{pf} d_f^2 I_0 \left(1 - \frac{d_{pp}}{u\tau} - \frac{d_{pf}}{2u\tau}\right)$$

And, the ratio (R) between $I_{\parallel}$ and $I_{\perp}$ can be simplified as:

$$R = \frac{I_{\parallel}}{I_{\perp}} = \frac{1 - d_{pp}/u\tau - d_{pf}/2u\tau}{1 - d_f/2u\tau} = 1 - \frac{d_{pf} + 2d_{pp} - d_f}{2u\tau - d_f} \tag{2.27}$$

For the case while $u\tau \ll d_f < d_{pf} \sim d_{pp}$:

$$R = \frac{I_{\parallel}}{I_{\perp}} = \frac{d_f e^{-\frac{d_{pp}}{u\tau}}\left(1-e^{-\frac{d_{pf}}{u\tau}}\right)}{d_{pf}\left(1-e^{-\frac{d_f}{u\tau}}\right)} \approx \frac{d_f}{d_{pf}} e^{-\frac{d_{pp}}{u\tau}} \tag{2.28}$$

R is actually equivalent to the direction correction factor in x_3 direction, i.e. a_3. This can be simply proved as below. As the velocity calibration curve is normally calibrated in the x_1 direction, i.e. $u_1 = u_1(I_{\perp})$, a velocity in x_3 direction with actual magnitude of u_3 can exhibit an apparent value as:

$$u_1[I_{\parallel}(u_3)] = u_1[RI_{\perp}(u_3)]$$

In LIFPA, as in most ranges of calibration curve, especially at low velocity magnitude, the calibration curve has excellent linearity, hence:

$$u_1[RI_{\perp}(u_3)] = Ru_1[I_{\perp}(u_3)] = Ru_3 = a_3u_3$$

It's readily seen, a_3=R.

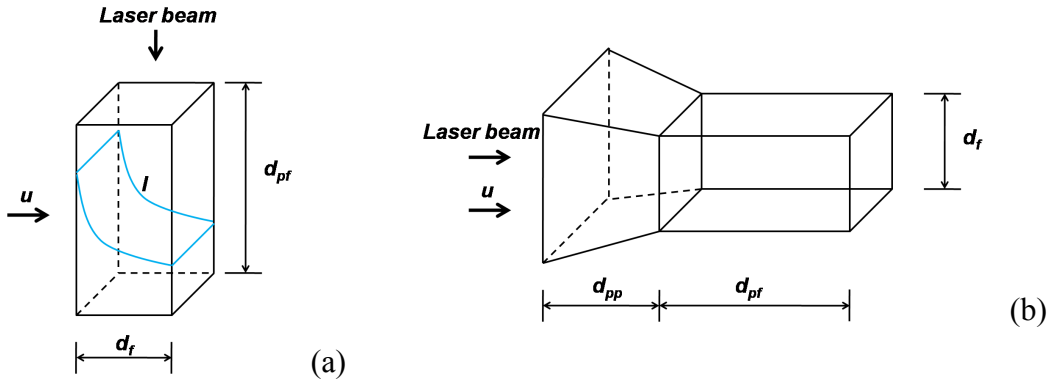

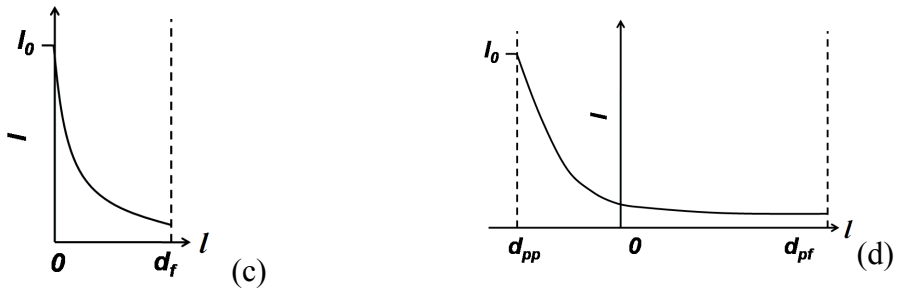

Figure 2.6 Schemes of photobleaching process. (a) Laser beam is orthogonal to flow. (b) Laser beam is parallel to flow. (c) Fluorescence intensity varies with l when laser beam is orthogonal to flow. (d) Fluorescence intensity varies with l when laser beam is parallel to flow. The influence of pre-photobleaching can be clearly indicated.

2.3.3 Experimental results

From previous investigations (Kuang and Wang 2010; Kuang et al. 2010), the dimension of laser beam at focus was d_f=203nm and d_{pf}=812 nm. The time constant τ is estimated to be less than 10 μs ((Wang et al.); Zhao, Yang, Wang). Hence, in the flow where in x_3 direction the velocity fluctuation is limited and on the order of 1 mm/s, $u\tau \ll d_f < d_{pf}$ is satisfied. If we further assume $d_{pf} = d_{pp}$, for a typical velocity fluctuation of 1 mm/s, a_3 (Equation (2.28)) is approximately to be 0. In fact, even d_{pp} is down to $u\tau$, a_3 is still no more than 0.1. This clearly indicates, even though the aspect ratio of LIFPA is much smaller than HWA, a_3 of LIFPA is not larger than that of HWA, due to the short photobleaching time of LIFPA. Furthermore, as LIFPA is a non-invasive velocimeter, there is no additional flow disturbance generated. The velocity fluctuation components in the direction orthogonal to laser beam can be truely evaluated.

In this section, we use x_1, x_2 and x_3 to represent streamwise, spanwise and vertical positions. And assume mean flow velocity is in streamwise direction.

(1) Errors of U and u'_{1_rms}

The mean velocity and the root-mean-square (rms) values of velocity fluctuations at different voltages are investigated respectively. The influences of different a_2 and a_3 on error (Equation (2.29)) are plotted in Figure 2.7. The flow is assumed to be isotropic for simplifying the analysis. At 10 $V_{p\text{-}p}$, the measured turbulent intensity u'_{m_rms}/U_m is only 1.7%. In this case, the errors of both mean velocity and rms values are very small.

$$\text{Error (\%)} = \left|\frac{\text{real value} - \text{measured value}}{\text{real value}}\right| \times 100 \tag{2.29}$$

The influence of 3-D flow on velocity fluctuations is even smaller than that on *U*. Compared to the corresponding measured values, the actual magnitude of *U* is normally smaller, with relatively larger u'_{1_rms}.

Keep increasing the voltage to 20 $V_{p\text{-}p}$, much larger velocity fluctuations can be generated. The measurement turbulent intensity is about 11.1%. Even though, both the errors of mean velocity and velocity fluctuations are less than 2% as shown in Figure 2.7 (c) and (d). These errors are limited and won't cause much difference from the actual values.

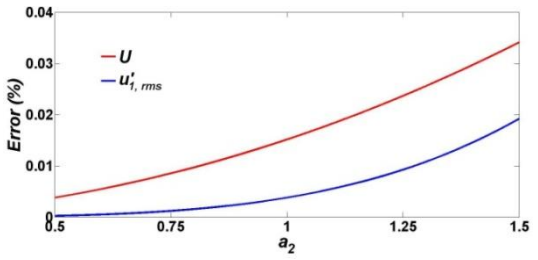

(a)

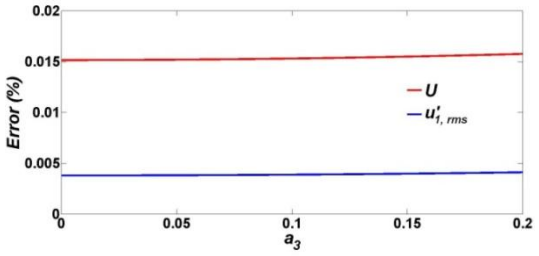

(b)

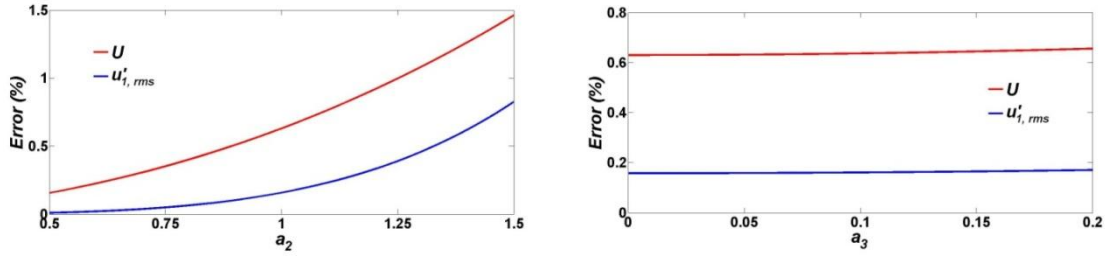

(c) (d)

Figure 2.7 The relative error of U and u'_{1_rms} influenced by a_2 and a_3. Measured at x_1=100 μm from trailing edge, and x_2=x_3=0, i.e. the centerline of channel. (a) a_2 influence when a_3=0.01, 10 $V_{p\text{-}p}$. (b) a_3 influence when a_2=1, at V = 10 $V_{p\text{-}p}$. (c) a_2 influence when a_3=0.01, 20 $V_{p\text{-}p}$. (d) a_3 influence when a_2=1, at V = 20 $V_{p\text{-}p}$.

(2) FDV of velocity fluctuations by TH and LTH

Both the FDV of velocity fluctuations by TH and LTH are investigated at different streamwise positions and voltages. As plotted in Fig. 4, the differences between TH and LTH are very small and hard to distinguish. No matter at different streamwise positions along centerline (20 $V_{p\text{-}p}$) (Figure 2.8(b) and (d)) or under different voltages at x_1=100 μm (Figure 2.8(a) and (c)), the relative errors ($|(\mathrm{LTH}-\mathrm{TH})/\mathrm{LTH}|\times 100\%$) are less than 5%. Hence in most cases, using TH won't cause large error. This is similar to most cases in conventional turbulent flows when turbulent intensity is much smaller than 1(Tennekes and Lumley 1972). Compared to the error caused by 3-D flow, the LTH won't give much improved corrections, even if at x_1=10 μm where turbulent intensity is high. Normally, correction on TH by using LTH is not necessary, except ultra high turbulent intensities, which are not achievable in this research.

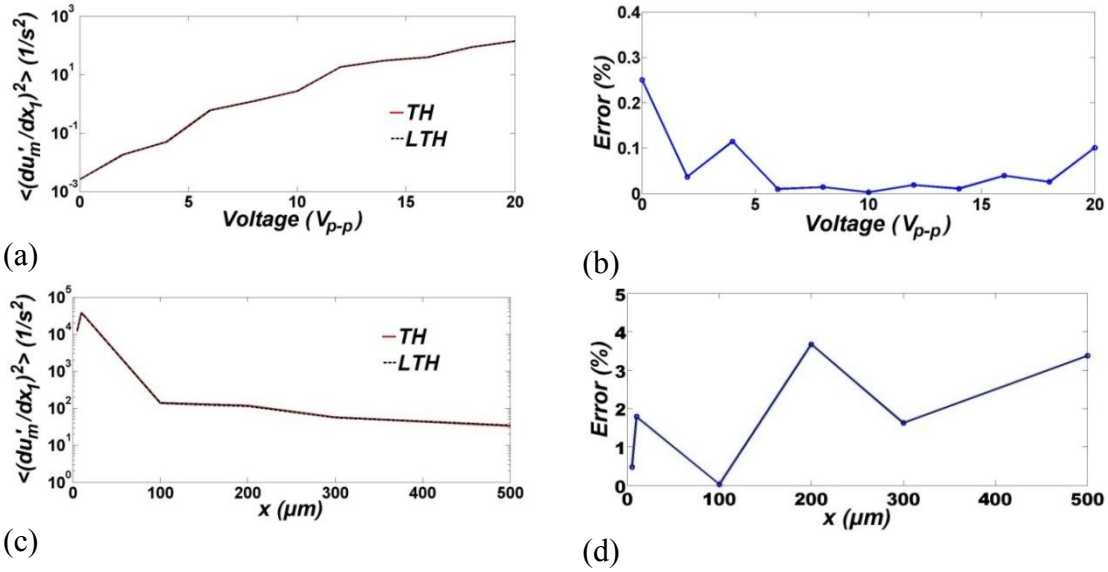

(a) (b) (c) (d)

Figure 2.8 (a) $\langle(du'_m/dx_1)^2\rangle$ calculated by TH and LTH, under different voltages at x_1=100 μm, x_2=x_3=0. (b) The relative errors corresponding to (a). (c) $\langle(du'_m/dx_1)^2\rangle$ calculated by TH and LTH, at different streamwise positions at 20 V_{p-p}, x_2= x_3= 0. (d) The relative errors corresponding to (c).

As the calculation of TH is based on the measured mean velocity, not the actual one, the TH should be smaller than the actual value. And the actual relative error between TH and LTH should be larger than the estimation here. Compared to the 3-D flow effect which will be introduced, LTH is not restricted by |M|<1. Hence it can be applied even in high turbulent intensity flow if there is a specific large energy injection scale.

(3) The cross flow effect on variance of velocity derivative

Still assuming the flow to be homogeneous and isotropic, the relative error of FDV of velocity fluctuations can be estimated from Equation (2.30), as:

$$\text{Error (\%)} = \left|1 - a_1^4 - [a_1^4 + a_2^4 + a_3^4 + a_2^2(a_1 - a_2)^2 + a_3^2(a_1 - a_3)^2]\frac{\langle u'^2_1\rangle}{U^2}\right| \times 100 \quad (2.30)$$

The relative errors influenced by both a_2 and a_3 are investigated at three different cases and plotted in Figure 2.9. It can be seen, in the directional correction factor range, error are monotonically increasing with a_2 and a_3. Under 10 $V_{p\text{-}p}$ at x_1=100 μm, due to the small velocity fluctuations, the error attributed to the 3-D velocity fluctuations is very small and can be simply ignored. However, as the voltage increased to 20 $V_{p\text{-}p}$, $\langle u'^2_1 \rangle / U^2$ is enhanced due to the larger electric body force. The actual turbulent intensity after correction increases to 11.3%. This results in a larger error around 3%. But at x_1=10 μm, i.e. adjacent to the entrance of channel, where the flow is highly disturbed, the error becomes significant. While forced at 20 $V_{p\text{-}p}$, the actual turbulent intensity is about 26.4% which is comparable to the turbulent mixing layer (George and Hussein 1991). The FDV error can be up to 26% depends on a_2 and a_3. At such cases, the errors cannot be arbitrarily ignored and should be carefully corrected, especially when $u\tau \gg d_{pf} \sim d_{pp} > d_f$ is satisfied (in other words, a_3 approaches 1).

While evaluating the influence of u'_3, the error is actually smaller than what estimated by Lumley (Lumley 1965) and Ewing (Ewing and George 2000). For example, considering the case at x_1=10 μm and V = 20 $V_{p\text{-}p}$, assuming a_i=1 for i=1, 2, 3 (for comparing with Ewing's work). The error estimated from Lumley's work is 34.8%, and 27.9% by Ewing. Both of them are larger than our calculation which is 23.9%. As in this LIFPA system, $a_3 \ll 1$, the error can be low to 13.7%. Hence, the measured FDV by LIFPA can have smaller difference from the actual values, compared to HWA.

From Equation (2.24) and assume a_1 is always 1, it can be estimated that $\langle (\partial u'_m / \partial x_1)^2 \rangle$ should be always larger than $\langle (\partial u'_1 / \partial x_1)^2 \rangle$. This is completely different from the variation of $\langle u'^2_1 \rangle$ which is always larger than $\langle u'^2_m \rangle$. It indicates the different

influence of 3-D effect on calculating large and small scale velocity components. And the actual Taylor scale should be underestimated.

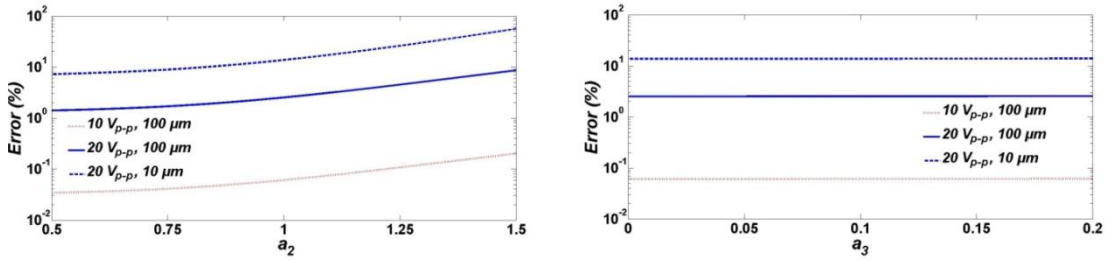

(a) (b)

Figure 2.9 The relative error of $\langle(\partial u'_1/\partial x_1)^2\rangle$ influenced by a_2 and a_3. (a) a_2 influence when a_3=0.01. (b) a_3 influence when a_2=1.

2.3.4 Discussion

In section 2.3, the directional correction factor in x_3 direction is discussed in detail. The small aspect ratio of laser focus won't generate a large a_3 which means the measurement won't be contaminated by the velocity fluctuations in x_3 direction. This is astonishing and completely different as in HWA, where the aspect ratio should be large enough to avoid parallel flow effect. The small a_3 should be caused by two as reasons: (1) non-invasive character of LIFPA that no support structures (which is inevitable in HWA) induce additional flow fluctuations; (2) The fast photobleaching of dye and small photobleaching time.

Based on the theoretically predicted a_3, the relation between some statistics of measured velocity via LIFPA and the actual values are studied both theoretically and experimentally. It can be seen, in the investigated turbulent intensities (below 11.1%), the actual mean velocity and velocity rms value are not seriously affected by the relatively small aspect ratio of the laser focus. The differences from the measured values are

negligible. In the turbulent intensity range of no more than 11.1%, LTH does not have much improvement in the correction of FDV of velocity fluctuations. And the error of FDV due to 3-D flow is also negligible. But for the high turbulent intensities of 26.4%, the 3-D flow effect on FDV cannot be ignored and can cause inevitable errors. However, compared to HWA, the influence of 3-D flow on FDV that measured by LIFPA is much smaller.

2.4 Measurement for scalar turbulence and mixing

Another two commonly used flow diagnostic techniques are used in our experiments to monitor the mixing process through scalar (concentration) variation. One is Laser Induced Fluorescence (LIF) for high spatial-temporal resolution measurement of concentration, the other is flow visualization for coarse view of concentration distribution.

2.4.1 LIF measurement

The LIF measurement shares the same optical and data acquisition system with LIFPA system. The only difference is: LIFPA uses a fast photobleaching dye with high concentration, while for LIF measurement, the dye should be very slowly photobleached with low concentration. Hence, we selected CF405 fluorescent dye with 1 μM concentration here. In LIF measurement, only the stream of high conductivity side has the fluorescent dye.

2.4.2 Flow visualization

To have a straightforward understanding on the mixing process, flow visualization is also conducted. In this experiment, the images are captured on an Olympus microscope (using Olympus UPlanFL 10x NA 0.3 objective lens) with high sensitivity camera (PCO

SENSICAM QE). The stream of DI water has no dye and the other stream is filled with fluorescent dye (Fluorescein Sodium Salt) solution, which is excited by blue light (around 473 nm) and emits green light (around 520 nm).

2.5 Experimental results on micro EK turbulence

2.5.1 Experimental facilities and methods

In the investigation, we used LIFPA and μPIV to measure the velocity field of flow. Meanwhile, LIF and flow visualization are both used to detect the scalar variation of mixing process. The microchip, electric filed applied and measurement system are exactly the same as introduced in section 2.2, if no otherwise mentioned.

2.5.2 The proof of existence of micro EK turbulence

Fast diffusion

Figure 2.10 shows the fast diffusion feature without and with AC forcing, when bulk flow *Re* at the entrance is 0.4 without forcing. Figure 2.10(a) is the case without forcing. Clearly, the flow is laminar and there is almost no mixing except for the negligible molecular diffusion at the interface between the two streams. With forcing at $V = 8\ V_{p\text{-}p}$, mixing is decidedly enhanced, but not so dramatically, as shown in Figure 2.10(f). While at $V = 20\ V_{p\text{-}p}$, the mixing becomes extraordinarily fast even near the entrance, as shown in Figure 2.10 (b), where the mixing is so rapid that the visualization cannot display the correspondingly detailed kinematic process. Apparently this indicates that there are

relatively strong disturbances and vortex motions in the flow, which cause large convection in the transverse direction between the two electrodes. Note in Figure 2.10(b), where a little upstream of the trailing edge, there is no mixing at all. Hence, the flow seems to undergo a sudden transition from laminar to turbulent motion once the two streams converge. After merely 65 μm downstream of the entrance, the concentration almost becomes uniform (at least on a "large scale") in the entire *y*-direction. The mixing time on large scale under forcing is estimated to be about 33 ms, nearly 10^3 times faster compared to that only by molecular diffusion in the unforced case. Normally, such a rapid mixing only happens in turbulence.

Another feature of turbulence is that there are vortices of different scales. These vortices can also be visualized by using polystyrene particles as tracers as shown in Figure 2.11(a) and (b). The conditions are consistent to Figure 2.10(a) and (b) respectively. Vortices of different sizes can be clearly found in Figure 2.11(b), which corresponds to the flow of Figure 2.10(b).

High dissipation

A high turbulent diffusion rate is normally accompanied with high turbulent dissipation caused by viscous shear stresses at small scales. In macroflows, right beyond Re_c, the turbulent dissipation (or pressure drop) will increase rapidly and nonlinearly. Since turbulent kinetic energy will be eventually dissipated, we used turbulent energy $T_e = \langle {u_s}'^2 \rangle$ to represent the dissipation feature equivalently and qualitatively, where $u_s = \sqrt{u^2 + v^2}$ is the instantaneous velocity measured by LIFPA (*u* and *v* are the instantaneous velocity components in the streamwise (*x*) and transverse (*y*) direction respectively, ${u_s}' = u_s - < u_s >$ and "< >" indicates ensemble averaging). Since it is the electrokinetic force

that causes the turbulence and corresponding high dissipation, the relationship between T_e and nominal Ra_e (when d=w, $\varepsilon = 7.1 \times 10^{-10}$ F/m, μ=10^{-3} kg/m·s, $D_e = 1.5 \times 10^{-9}$m^2/s) are used to describe the feature of dissipation in the flow as shown in Figure 2.12. As V varies from 0 $V_{p\text{-}p}$ to 20 $V_{p\text{-}p}$, E_0 changes from 0 to 1.1×10^5 V/m.

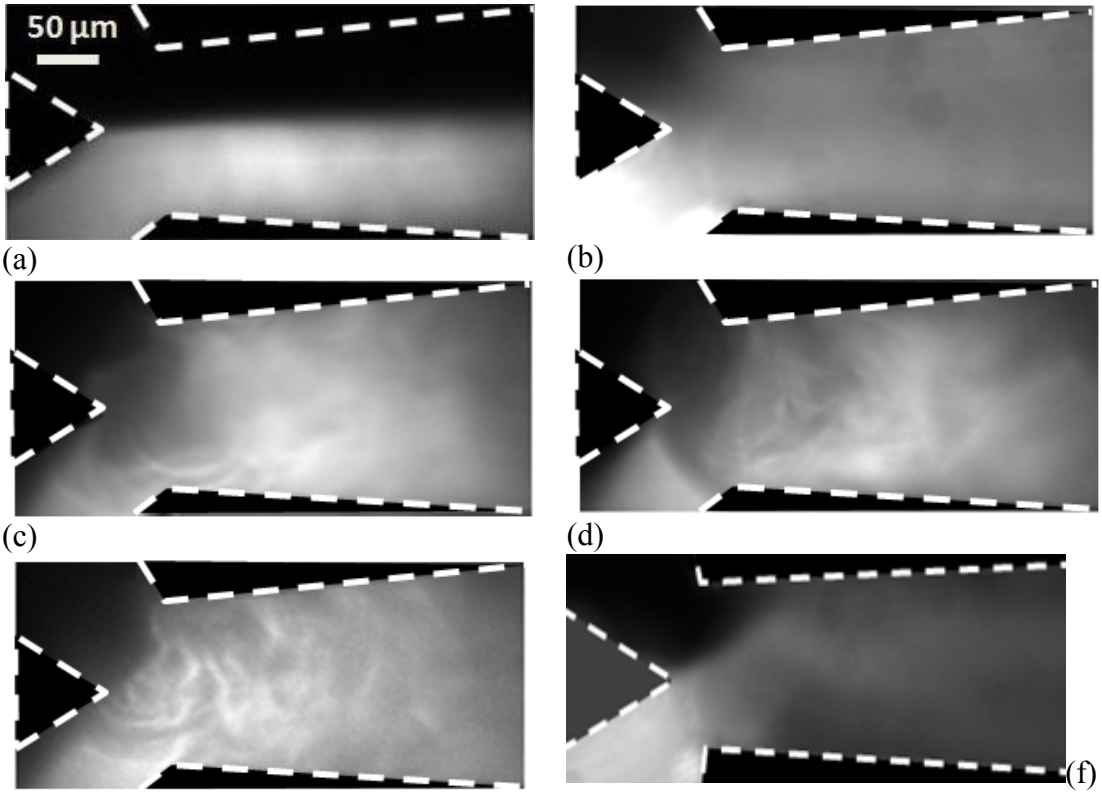

Figure 2.10 (a)-(f) Flow visualizations. (a) mixing in unforced flow, 0.3 ms exposure time. (b)-(e) mixing in 20 $V_{p\text{-}p}$ and f=100 kHz with different expousre time. (b) 100 ms, (c) 1.5 ms, (d) 0.3 ms and (e) 0.1 ms. (f) 8 $V_{p\text{-}p}$ and f_f=100 kHz, 100 ms exposure time.

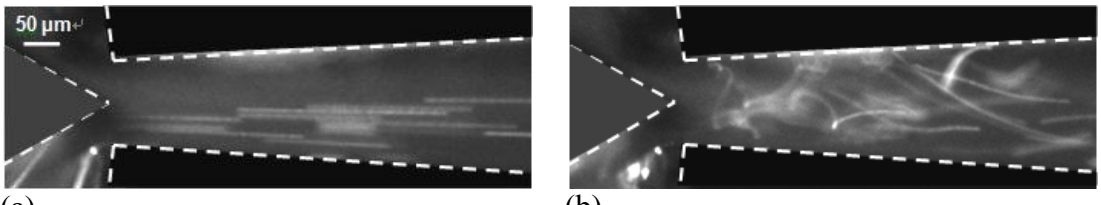

Figure 2.11 (a) Visualization of the unforced flow with polystyrene particles of 1 µm in diameter. The particles are premixed only with the bottom stream. Straight pathlines indicates the flow is laminar. (b) The corresponding violent vortex motion of the particles with various sizes of vortices for the flow under 20 $V_{p\text{-}p}$ and f_f=100 kHz.

It can be seen, a critical value of Ra_e, i.e. Ra_{ec}, is located between 1.9×10^7 and 4.3×10^7, Below which, T_e increases slowly with a log-log slope of 0.16. However, beyond the critical point, T_e increases much faster. The slope is estimated to be about 3.03, which is 19 times larger than that of laminar regime. The relation between T_e and Ra_e is very similar to that between pressure drop and Re around the transitional regime in macroflows. In general, Figure 2.12 indicates that, as Ra_e is increased, the forced microflow also has a dramatically nonlinear increase in dissipation in the turbulent flow compared with that of the laminar flow. Figure 2.12 shows the typical transition behavior around $Ra_e = 2.5 \times 10^7$ and high dissipation feature of turbulence at $Ra_e = 4.7 \times 10^8$.

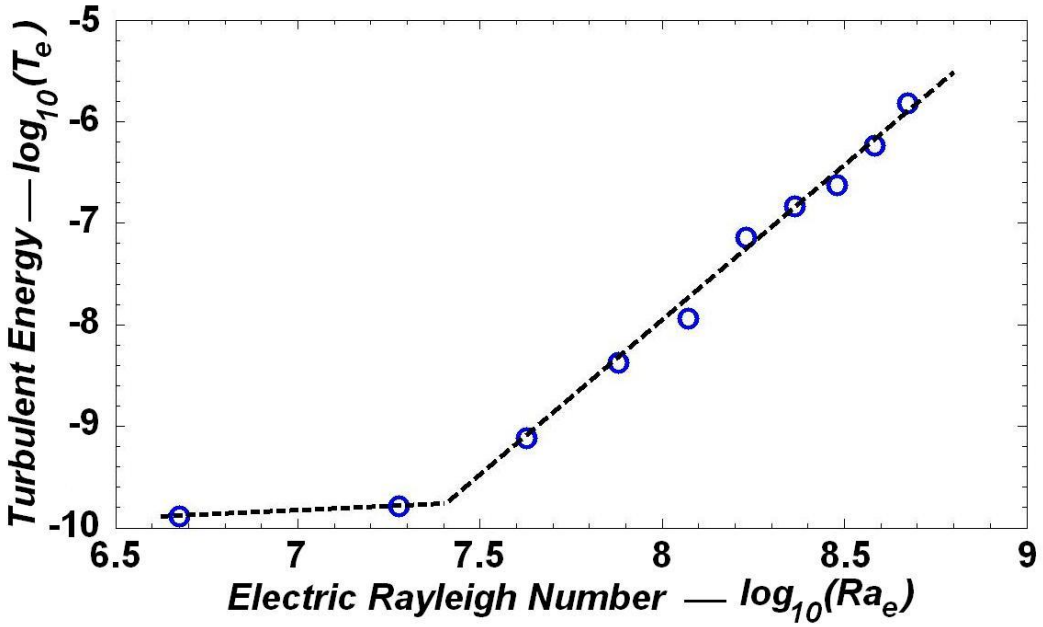

Figure 2.12 Relationship between turbulent energy T_e and Ra_e. Data are measured at $y = 0$, $z = 0$ and $x = 100$ μm.

Irregularity

Another feature of turbulence is the irregularity, which can be characterized by time trace of velocity at a fixed spatial point**.** Time traces of u_s in Figure 2.10(a), (b) and (f) at x = 100 μm (streamwise position is evaluated from the trailing edge) are recorded in Figure 2.13. Without forcing, u_s is almost a constant. With forcing of V = 8 $V_{p\text{-}p}$, u_s has small fluctuations. In this case, u_s already shows some slight irregularity, but not strong. However, as V is further increased to 20 $V_{p\text{-}p}$, the flow pattern becomes quite different, and u_s is highly fluctuated and random. Note the forced u_s is much higher than the unforced one, because what LIFPA measured directly is the magnitude of velocity, which includes the additional contribution from spanwise velocity component v.

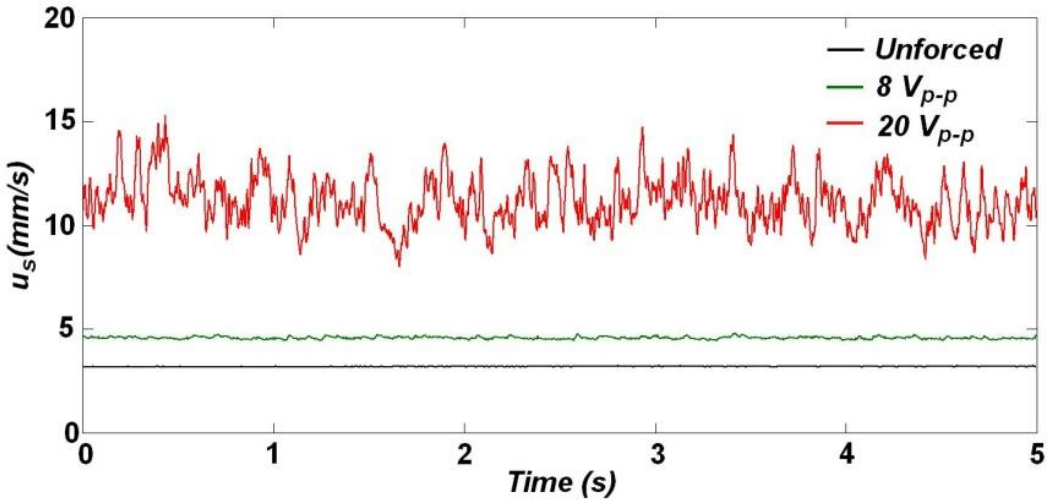

Figure 2.13 Time series of u_s at position x = 100 μm, y = 0 and z =0. Based on the measured calibration curve between flow velocity and fluorescence intensity, the measured mean velocity of u_s is about 11.2 mm/s, i.e. 5.3 times larger than unforced bulk velocity U. Therefore, Re based on this forced mean u_s and the hydraulic diameter of channel at inlet is about 2.

Multiscale eddies

An intrinsic feature in turbulence is the multiscale eddies that can be described in the spectral space by a power spectrum density (PSD) $E(f)$ of u_s, where f is the fluctuation

frequency of u_s. *E(f)* without and with different V at various streamwise positions is given in Figure 2.14. At $x = 10$ μm, without forcing, *E(f)* is nearly flat as background noise, since there is no fluctuation of u_s. The reason that *E(f)* at low frequency is not completely flat could be because of the vibration of the pump. With forcing of $V = 8$ $V_{p\text{-}p}$, *E(f)* at x_2 has significantly increased. However, *E(f)* at high f, e.g. 100 Hz, that corresponding to "small" scale eddies, is relatively weak.

As V is further increased up to 20 $V_{p\text{-}p}$ at $x = 10$ μm, *E(f)* at high f, the bandwidth and cut-off frequency f_c of *E(f)*, where noise starts to dominate, also increase both rapidly and significantly. However, at $x = -10$ μm, *E(f)* under forcing at $V = 20$ $V_{p\text{-}p}$ is similar to that without forcing, indicating that the flow is still laminar just 10 μm upstream of the inlet. This again indicated a possible sudden transition from laminar to turbulent flow. Note, there is no sharp peak for *E(f)* at 100 kHz, although the forcing frequency f_f is 100 kHz and the temporal resolution of LIFPA is sufficient to measure 100 kHz signal when both sampling rate and f_{sc} are 1 MHz. In particular, while f_c at $V = 8$ $V_{p\text{-}p}$ is about 200 Hz, it increases approximately to 1.5 kHz at $V = 20$ $V_{p\text{-}p}$. This could indicate that the forcing at $V = 20$ $V_{p\text{-}p}$ generates velocity fluctuations that produce relatively "large scale" eddies, which in turn produce small scale eddies down to dissipation scale l_{de}, where viscous force dominates. The energetic large velocity fluctuations also induce higher dissipation rate and smaller eddies. This could explain why f_c moves toward high frequency regime under forcing of $V = 20$ $V_{p\text{-}p}$, compared to that under forcing of $V = 8$ $V_{p\text{-}p}$. At $V = 20$ $V_{p\text{-}p}$, within 3-60 Hz *E(f)* is almost a constant and about four orders higher in magnitude than that of the unforced flow. Furthermore, although *E(f)* continuously decreases with the increasing of f beyond about 60 Hz at a slope of approximately -5/3 (Note that turbulence does not

always require the existence of -5/3 inertial range of high *Re* turbulence, and many macro turbulent flows do not have the inertial range in the spectrum.), i.e. it does not fall sharply. Only when *f* is higher than 300 Hz, starts *E(f)* to decay sharply with a slope of about -5. Since the velocity power spectrum with $V = 20\ V_{p\text{-}p}$ decays much slower than f^{-3} in the range from 1 to 300 Hz, Figure 2.14 could exclude the possible temporally random but spatially smooth chaotic flow normally observed at the very low *Re*, which requires *E(f)* decay fast than f^{-3} (Fouxon and Lebedev 2003; Burghelea et al. 2004). Hence, although it is not clear if the flow forced at $V = 8\ V_{p\text{-}p.}$ is turbulence or not, the flow forced at $V = 20\ V_{p\text{-}p}$ should be turbulence, considering that there are multiscale eddies corresponding to the wide bandwidth from 1 through 300 Hz, where *E(f)* has no sharp decrease, another typical feature of turbulence.

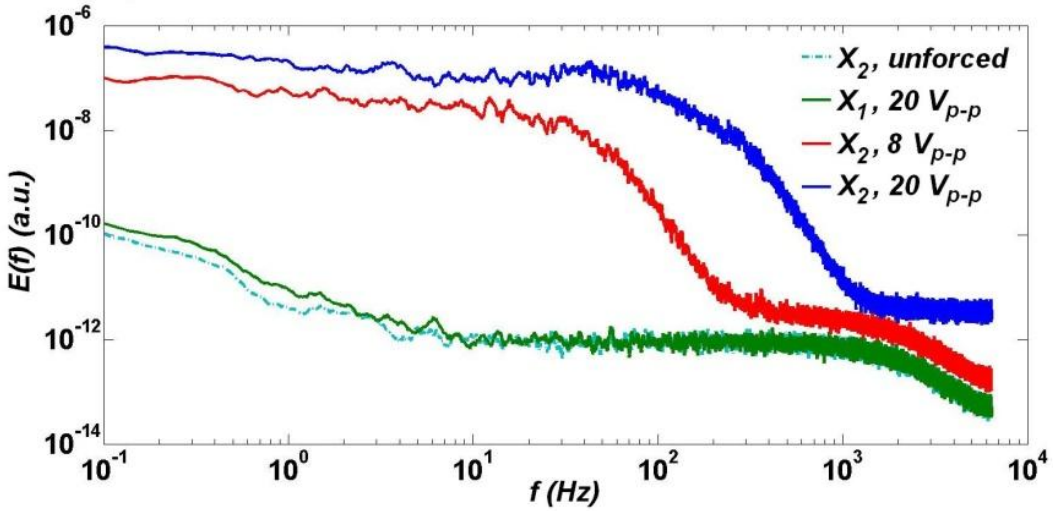

Figure 2.14 *E(f)* of u_s under different voltages and streamwise positions. *E(f)* without and with forcing under different *V* (8 and 20 $V_{p\text{-}p}$) at $x = 10$ μm display significantly different behaviors.

Continuity

To evaluate the continuity of the flow, we use Knudsen number, i.e. the ratio of mean free path ξ of water and the estimated smallest structure l_{de}, as the criterion (Tennekes and

Lumley 1972). Based on Figure 2.14, the l_{de} corresponding to the forced flow at $V = 20$ $V_{p\text{-}p}$ is estimated to be about 0.2-1 μm. ξ is about 0.02 nm (Kirby 2010). Thus, the ratio $\xi/l_{de} << 1$. This confirms that the flow in Figure 2.10(b) is still continuous, although the channel's size is in microscale.

3-D flow

The 3-D of instant flow is a basic feature of turbulence. Actually, the inhomogeneity of flow in *x*-direction is apparent from both Figure 2.10(b) and Figure 2.14. What we need is to measure the inhomogeneity in y-z plane. For this purpose, the distributions of T_e along the transverse *y*-direction were measured at two different *z*-positions (spanwise) at downstream (x= 100 μm) as shown in Figure 2.15. While T_e in the unforced flow (caused by the low frequency noise, such as pump vibration and negligible shot noise) is very small and negligible, T_e in the forced flow at $V = 20$ $V_{p\text{-}p}$ is increased by 3-4 orders, and the flow becomes highly fluctuated and 3-D. From Figure 2.15, it can be found that while for $y = 0$ μm in the *z*-direction, T_e at $z = 0$ μm is about 2.7 times larger than that at $z = -100$ μm. For $z = 0$ μm in the *y*-direction, T_e at $y = 0$ μm is about 30 times higher than that at $y = 30$ μm. The variation of T_e in *y*-direction is much larger than that in *z*-direction. This is reasonable as the flow disturbance is generated by $\vec{F}_e = -\frac{\varepsilon \vec{E} \cdot \nabla \sigma}{\sigma} \vec{E}$, and $\nabla \sigma$ is maximum at the centerline in y-direction. It implies the local ratio of electrokinetic force to viscosity force, i.e. Gr_e, changed much faster in *y*-direction than in *z*-direction, which is because of the 3-D variation of conductivity structures. This indicates the intrinsic 3-D nature of the flow.

Since rapid time periodic forcing (100 kHz) is used to force the flow, it is not clear whether the large scale structures (low frequency signals) and small structures (high frequency signal) in Figure 2.14 are resulted from viscous damping of much smaller scale structures (i.e. much higher frequency signal) caused by f_f = 100 kHz. If this is true, then what we have in Figure 2.14 could not be turbulence, but actually a chaotic flow and mixing generated in a 3-D geometry through viscous diffusion of the forced smaller structures produced at high f_f. To address this issue, we first recall what Ottino (1990) mentioned "It is simplistic to seek a clean answer to the questions of whether turbulence is chaotic or chaos is turbulent". We need to make it clear that studying the difference between chaotic flow and turbulence, a difficult topic, is out of the scope of the present work. To ensure that spectrum *E(f)* in Figure 2.14 with V = 20 $V_{p\text{-}p}$, including the large scale low frequency and small scale high frequency signal, is not just the consequence of the viscous damping of the higher frequency signal at such a low *Re* flow, we first measured the *E(f)* with f_{sc} = 1 MHz for the flow in Figure 2.10(b), and found no signal at all, but noise at 100 kHz although the flow was forced at this frequency. For such a high $f_{sc,}$ the noise is higher than that in Figure 2.14, because shot noise increase with frequency (Wang and Fiedler 2000). Then, forcing at a low f_f of 15 Hz is also investigated to ensure that *E(f)* has both high and low frequency signal without high f_f.

As electrolysis could create bubbles at such a low f_f, we reduced the conductivity ratio to 10 and increased the forcing voltage V to 36 $V_{p\text{-}p}$. The Ra_e is about 2.8×10^6 in this case. Nevertheless, the principle of generating turbulence in this type flow is similar for all f_f used. The result is shown in Figure 2.16, where f_c is still about 1 kHz, more than sixty times of f_f. Figure 2.16 indicates that, the *E(f)* generated at f_f = 15 Hz is similar to that at f_f

= 100 kHz qualitatively. The length scale estimated from f_f and bulk velocity, i.e. U/f_f is in the same order of the channel width. Therefore, in this case, both low and high frequency signal in the $E(f)$ should not be created by the viscous damping of higher frequency signal, but probably because of the loss of flow stability under strong forcing and the resulted in l_{de}. In fact, our experiment also finds that this type flow normally becomes more unstable at lower f_f, and the lower the f_f, the more unstable the flow for a given voltage. The reason we select the high frequency is mainly because of its potential future application in lab-on-a-chip to avoid the possible bubble generation at a low frequency.

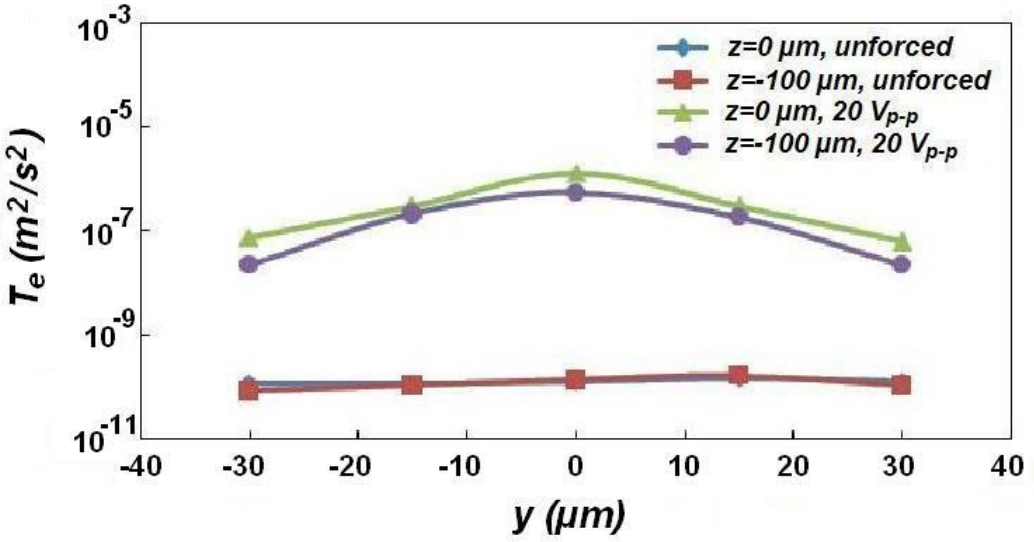

Figure 2.15 T_e distribution along the transverse direction at two vertical positions without and with forcing of $V = 20$ $V_{p\text{-}p}$ at $x = 100$ μm.

In macroflows, low *Re* elastic turbulence has been reported (Groisman and Steinberg 2000), where the fluid has to be polymer, but no elastic turbulence has, to the best of our knowledge, been reported in microfluidics. In the present work, the fluid is not the non-Newtonian, but the common Newtonian, i.e. water solution with small ions. Electrokinetic forcing has also widely been applied in microfluidics. However, no publication has claimed

that turbulence flow has been observed in *Re* below 10 in electrokinetically forced flows with Newtonian fluid. Burghelea *et al* (Burghelea et al. 2004) reported that the most popular velocimeter, μPIV has difficulty in exploring the properties of the flow down to sufficiently small spatial scales about its spatial structure because of its limited resolution. Here we have not only used unique method to generate turbulence, but also developed new method to be able to measure turbulence in microchannels. Since the origin of the transition to turbulence is not mainly because of the pressure driven pipe or channel macroflows, but the electrokinetic forcing in microchannel, we name the flow as micro electrokinetic turbulence (or μEK turbulence) to distinguish it from "micro turbulence" used already in other field(Jager 1954; Heidbrink et al. 2009).

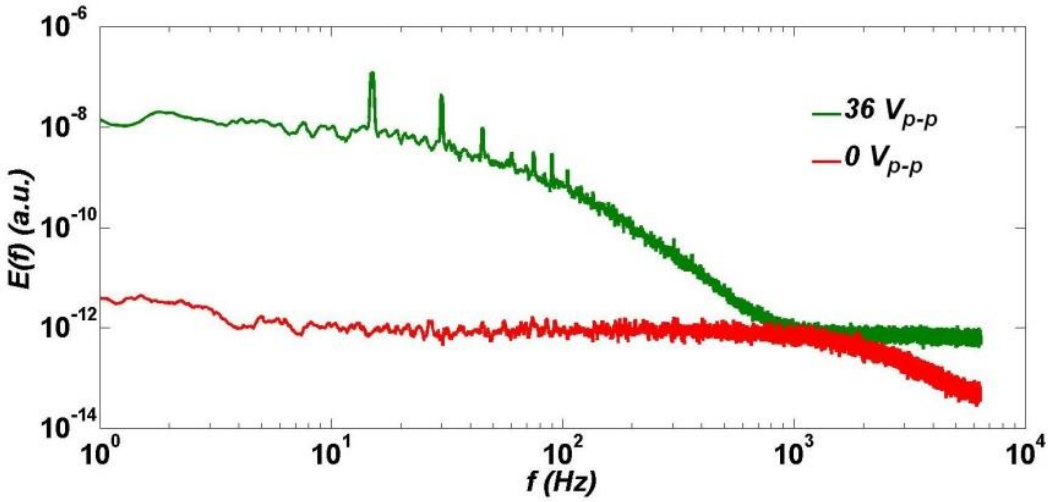

Figure 2.16 *E(f)* with low forcing frequency of 15 Hz at position x = 100 μm. Compared with the unforced one, the *E(f)* of the forced one is much higher at frequency from 10 Hz through 500 Hz.

2.5.3 The characters of high Reynolds number turbulence in μEK turbulence

2.5.3.1 Mean velocity

Before introducing our finds in μEK turbulence, it's necessary to know the character of basic flow first. The U distribution along y direction at x=100 μm is shown in Figure 2.17. Without forcing, the measured U matches very well with the numerically calculated Jeffery-Hamel (J-H) flow (Joneidi et al. 2010). However, under forcing, for a given z position, U is no more symmetric along y-direction, but higher in the side of the stream with lower σ, since $\vec{E}$ and $\vec{F}_e$ decrease with increase of σ. In addition, U is increased along y direction near the center region and decreased near the wall region, resulting in a steeper U distribution, compared to the unforced case. The reason is unknown yet. One possible explanation is that the entire flow is within turbulent boundary layer, which is normally steeper than laminar boundary layers in closed channel flows. Another one is due to the unexpected DEP effect on the particles which results in a doubtable measurement. Personally say, the second reason has higher possibilities. However, recently, there is no valid and reliable measurement or simulations on such kind of strongly disturbed EK flow. μPIV is the most commonly used technique in microfluidics. That's why we plot the velocity profile with μPIV measurement.

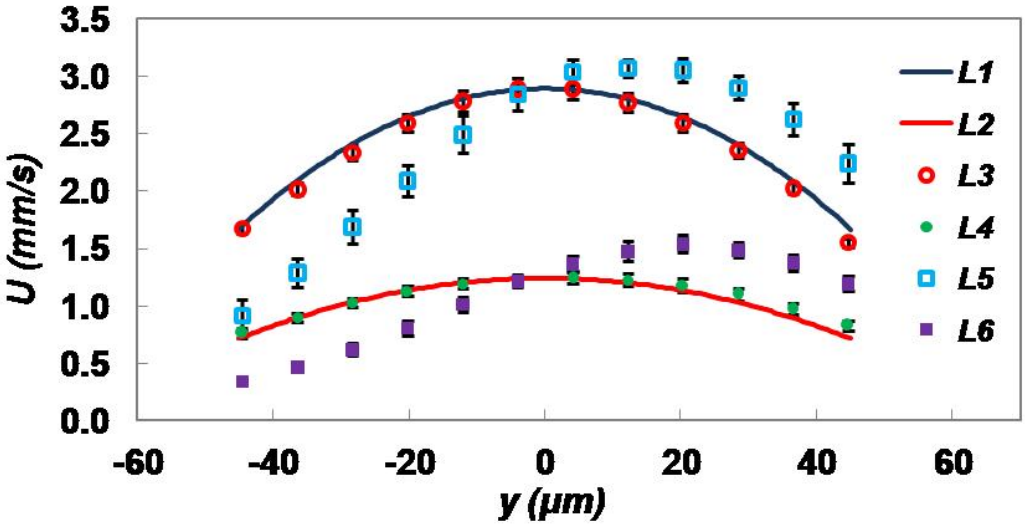

Figure 2.17 *U* distribution along the transverse direction at x = 100 μm measured by μPIV and compared with J-H profile. L1: z = 0, J-H profile; L2: z = -90 μm, J-H profile; L3-L6 are measured by μPIV. L3: z = 0 μm, unforced; L4: z = -90 μm, unforced; L5: z = 0 μm, 20 $V_{p\text{-}p}$; L6: z = -90 μm, 20 $V_{p\text{-}p}$. The flow becomes 3-D under forcing.

2.5.3.2 PSD of velocity fluctuations

Figure 2.18(a) shows the PSD *E(f)* of u_s' for various voltages at spatial position x = 100 μm. When V is increased from 10 $V_{p\text{-}p}$ up to 20 $V_{p\text{-}p}$, *E(f)*, its bandwidth and cut-off frequency f_c, where noise starts to dominate, also increase. *E(f)* gradually develops a similar slope with the increase of V. Of particular interest is, at 20 $V_{p\text{-}p}$ the PSD is not only continuously spanned in f, but also exhibits a -5/3 slope roughly from 3 to 60 Hz in a span of more than one decade! In fact, there is already the -5/3 slope at 14 $V_{p\text{-}p}$, and reaches the longest bandwidth at 20 $V_{p\text{-}p}$ (the highest V we can provide). This is really a surprising, since the -5/3 slope corresponds to the Kolmogorov spectrum, whose existence requires very high Taylor scale Re (Re_λ) on the order of 100 or more {Sreenivasan, 1996 #79}. However, the measured $Re_\lambda = u_{s,rms}\lambda/\upsilon$, where $u_{s,rms} = \sqrt{\langle u'^2_s \rangle}$, $\lambda = \sqrt{\langle u'^2_s \rangle / \langle (du'_s/dx)^2 \rangle}$ is the Taylor scale measured from 1-D measurement, $u'_s = u_s -$

$\langle u_s \rangle$, $dx = U_b * dt$ (dt is the time interval of LIFPA sampling), for 20 $V_{p\text{-}p}$ at x_4 is estimated to be only 0.03! From section 2.3, we know $\langle u'^2_s \rangle$ is normally smaller than the real $\langle u'^2 \rangle$, and $\langle (du'_s/dx)^2 \rangle$ is larger than $\langle (du'/dx)^2 \rangle$. Hence, the measured Taylor scale λ should be smaller than the actual value. However, as discussed in section 2.3, the errors on calculating $\langle u'^2 \rangle$ and $\langle (du'/dx)^2 \rangle$ is very small. Hence, the λ and corresponding Re_λ should be accurate enough to the actual values.

The evolution of *E(f)* along the streamwise direction is shown in Figure 2.18(b). At x= -10 μm, i.e. upstream of the trailing edge, *E(f)* is almost flat and the flow remains laminar. However, at x=5 μm the PSD changes dramatically and f_c rapidly increases to about 2,000 Hz. There is an energy accumulation to eddy scale corresponding to about 50 Hz, indicating an unsteady or non-equilibrium process in the entrance region. At x_3 = 40 μm, a narrow subrange with -5/3 slope from 40 to 200 Hz appears (Note, in this streamwise region, the slope of PSD is very sensitive to the external circumstance and initial conditions. In different measurements, the slope can change from -7/5 to -5/3. In the experiments introduced in this section, the slope is approximate -5/3). The -5/3 spectrum continues developing to x_4 with a span of more than one decade. However, f_c and *E(f)* are all much lower than that upstream. At this position f_c is about 200 Hz. The reason could be (1) the fast diffusion would decrease the σ gradient at the interface of the two fluids, which then reduces $\vec{F}_e$ that causes the μEKT. (2) At x = 5 μm, the flow has already generated smaller eddies and the corresponding scalar (σ or ion concentration here) structures, which decay rapidly by the high viscous dissipation and molecular diffusion to smear the fine structures in this low Re flow. Nevertheless, it seems the energy transfer from large to small scale reaches equilibrium, and hence, with continuous development the random flow persistently

possesses the -5/3 slope. Further downstream at x = 200 μm, 300 μm and 500 μm, both *E(f)* and f_c continuously decay, but the -5/3 slope is kept although the bandwidth decreases continuously. In this sense, the flow downstream from x = 40 μm behaves similar to the free decaying turbulence. In addition, although the flow is forced at 100 kHz, there is no peak or distinguish signal in PSD at this forcing frequency. Our LIFPA's temporal resolution is high enough to measure 100 kHz signal, if it existed, Figure 2.18(b) shows no inverse cascade signal. In fact, the forcing frequency may not play a key role on the spectra, since similar spectra can be observed, no matter if the flow is forced at a high frequency of 100 kHz or a low frequency of only 15 Hz as described before (Wang et al. 2014). Thus, the power law may not be from the direct injection of 100 kHz forcing. This indicates the external energy input is accepted by the flow and converted into unstable vortices. The large ones are cascaded into the small ones rapidly, a direct energy cascade.

Normally the -5/3 slope is in the inertial range that ends at $(f/U) * \eta \approx 0.1$ (Chen et al. 1993; Saddoughi and Veeravalli 1994), and beyond -5/3 spectrum, *E(f)* decays exponentially. From Figure 2.18, η is estimated to be 3.3 μm at x_4. These scales are at least one order smaller than the channel width. This could support why the span of *E(f)* with -5/3 slope can be one decade wide. In addition, in Figure 2.18 beyond -5/3 spectrum, *E(f)* has an averaged slope of -6.3, which is within the range between -5.2 (Saddoughi and Veeravalli 1994) and -7.2 (Comte-Bellot and Corrsin 1971) in high Re turbulent flows. Note, although the flow is strongly non-homogeneous and anisotropic, the measured spectrum is expected to be reliable. This is because LIFPA is similar to the hot-wire anemometer with single wire probe, which is more accurate than a x-wire probe for the 1-D spectra measurement (Saddoughi and Veeravalli 1994; Ewing 2004).

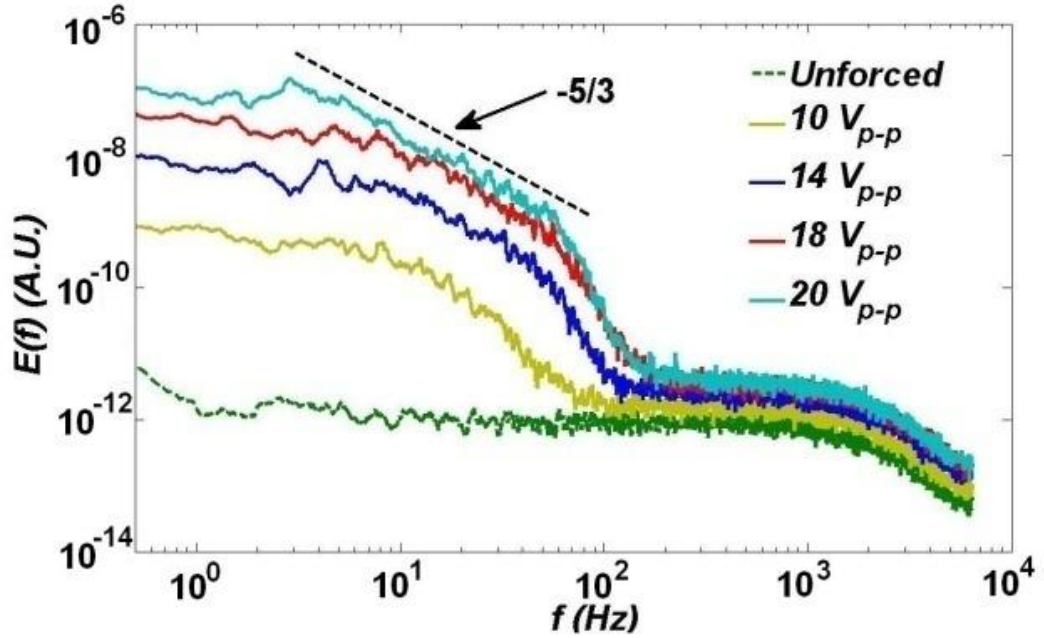

(a)

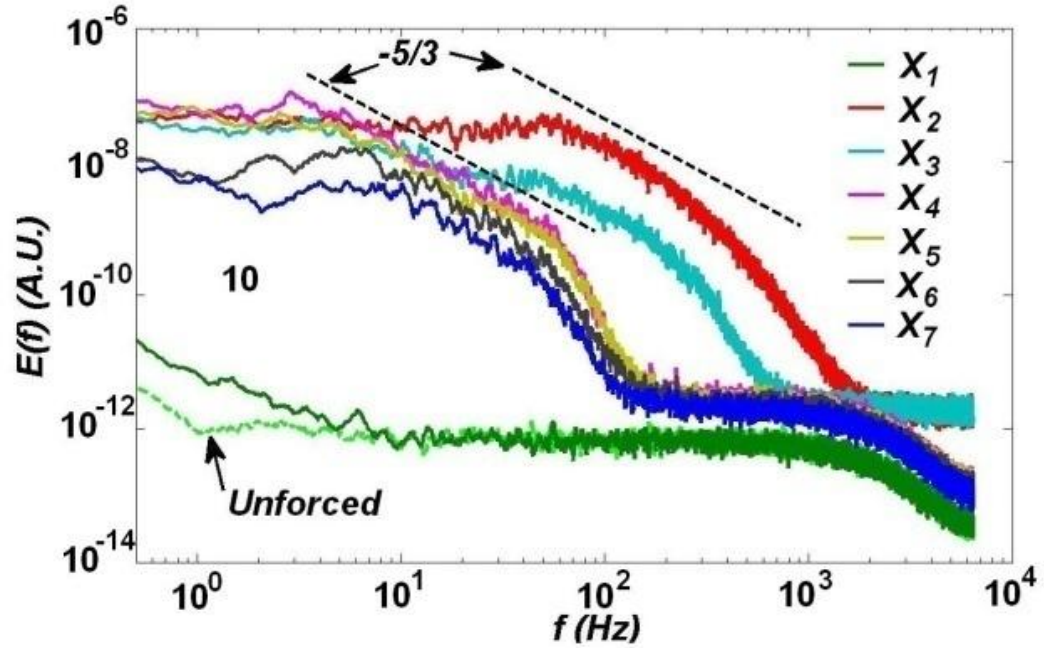

(b)

Figure 2.18 Power spectra of velocity *E(f)* under various conditions at y = z = 0. (a) *E(f)* under various voltages at x = 100 μm. Without forcing, *E(f)* is flat, resulted from background noise, since there is no fluctuation of u_s. With forcing of 10 V_{p-p}, *E(f)* is increased, but not significantly. However, a -5/3 slope of *E(f)* is obtained when V = 20 V_{p-p}. The span of the -5/3 slope increases with V. (b) PSD development at various streamwise positions under V = 20 V_{p-p}. The measuring positions along streamwise direction relative to the trailing edge are, x_1 = -10 μm, x_2 = 5 μm, x_3 = 40 μm, x_4 = 100 μm, x_5 = 200 μm, x_6 = 300 μm, and x_7 = 500 μm, respectively. The unforced

PSD is used for reference. -5/3 spectrum starts at x_3 and persists in at x_7. The observed PSD here excludes the possible temporally random but spatially smooth chaotic flow (elastic turbulence) normally observed at the very low *Re*, which requires *E(f)* decay faster than f^{-3} (Groisman and Steinberg 2000; Burghelea et al. 2004).

2.5.3.3 Velocity structure function and scaling law

Velocity structure function $\Delta u(r) = u(x+r) - u(x)$ ($r = U_b \Delta t$, is the spatial distance and Δt is the time interval) at high Re macroflow has the following scaling relation: $\langle |\Delta u(r)|^p \rangle \sim r^{\xi_p}$, where ξ_p is the scaling exponent of p^{th} order moment. According to Kolmogorov's second similarity hypothesis (K41), $\xi_p = p/3$. For low p, ξ_p is close to $p/3$ and the scaling relation of $\Delta u(r)$ matches K41 theory well, but for high p, ξ_p is lower than $p/3$, i.e. deviates from K41 prediction because of the intermittency of dissipation structure. When u_s is used to represent u, similar scaling exponents are also observed at 20 $V_{p\text{-}p}$ by calculating $\Delta u(r)$ in the inertial subrange regions at two different streamwise positions along $y = z = 0$, as shown in Figure 2.19(a). For $p \leq 4$, the measured scaling exponent ξ_p is very close to K41 prediction. However, for $p \geq 4$, the difference between K41 prediction and measured ξ_p increases with the increase of p. Figure 2.19(a) shows the similar scaling to that of Benzi et al (Benzi et al. 1996) in high Re flow. Note, at x_4 as $p \geq 6$, ξ_p is even lower than that of Benzi et al. This could indirectly imply $\overrightarrow{F_e}$ has effect on small scale structures, where σ is not uniform, and thus, increases the intermittency and the departure from known models (such as Log-Poisson).

2.5.3.4 Probability density function of du_s'/dx

Another feature of high Re turbulence is the existence of an exponential tail of probability density function (PDF) of velocity derivative in physical space also because of intermittency at small scales. PDF of $(du_s'/dx)/(du_s'/dx)_{rms}$ (i.e. $(du_s'/dt)/(du_s'/dt)_{rms}$, rms means "root mean square") is investigated at various streamwise positions, as given in Figure 2.19(b). Without forcing, the measured PDF caused by the noise of the detector is similar to the Gaussian distribution. With forcing at x_2, there is a clear exponential tail, corresponding to the small scale eddies shown in Figure 2.18. The exponential tails persist in at x_4 and x_5, although they are weaker compared with that at x_2, indicating fast diffusion and dissipation are smearing the smaller structures. This is identical with the PSD shown in Figure 2.18.

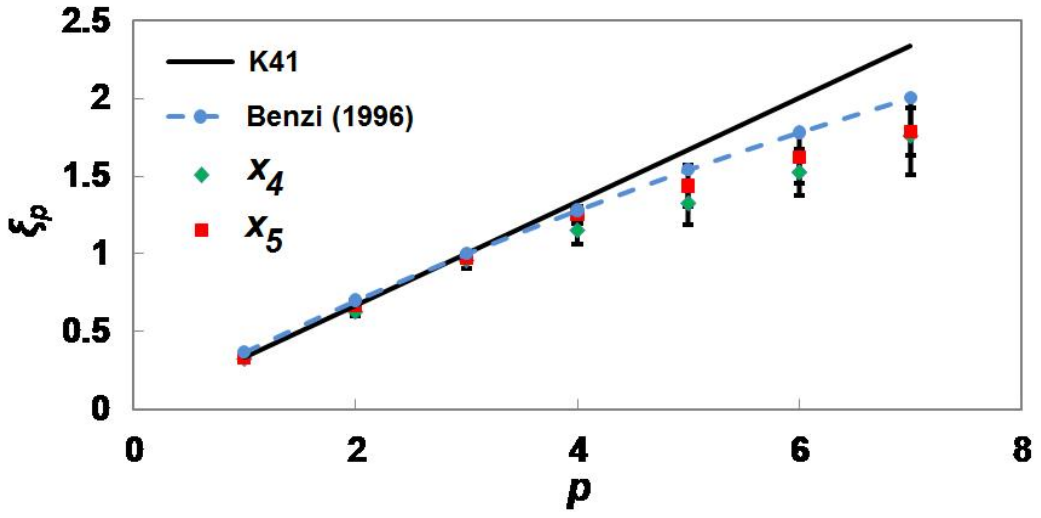

(a)

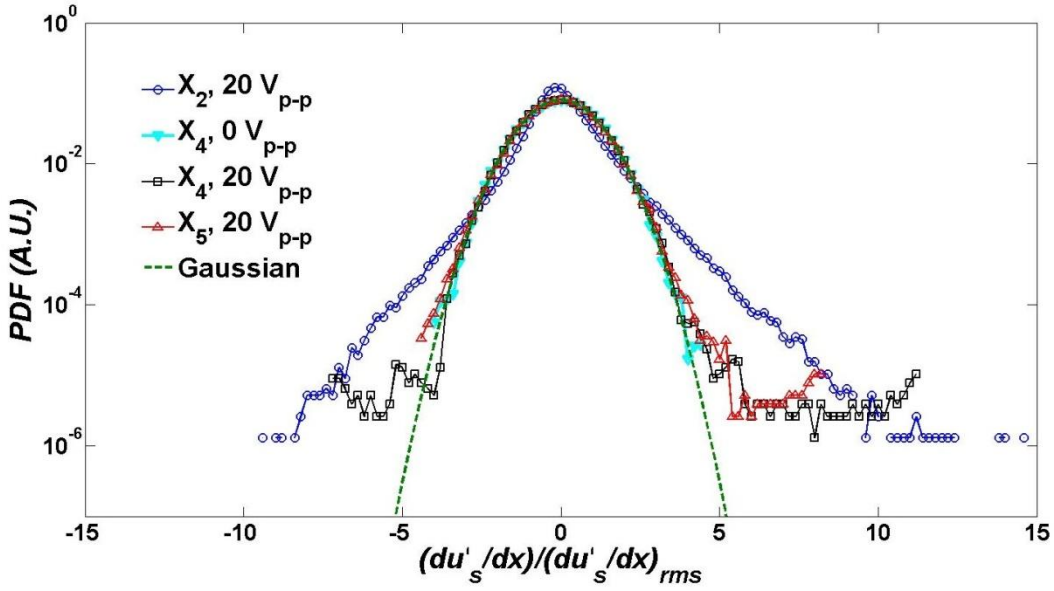

(b)

Figure 2.19 Velocity structure function and PDF of flow in Figure 2.10(e) at different positions along $y = z = 0$. (a) Scaling exponents of velocity structure function at x_4 = 100 μm and x_5 = 200 μm. The solid line is the prediction of K41. For $p = 3$, the scaling exponent ξ_p is close to 1.01 for all two positions, similar to the predicted 1.00 from K41. However, for $p = 6$, the measured ξ_p is 1.62 and 1.78 at x_4, and x_5 respectively, similar to the scaling law of velocity structure function at high Re flows. (b) PDF of velocity derivative $(du_s'/dx)/(du_s'/dx)_{rms}$ at x_3, x_4 and x_5. The PDF exhibits an exponential tail of high Re flows. Note the amount of data for calculating was about 10^6, which is enough to estimate approximately up to only the 7th standard deviations and 7th order moment.

On the one hand, the spectra, structure function and PDF indicate that the low Re flow can have features of high Re. On the other hand, since Re_λ under forcing is lower than one, conventional scaling relation, i.e. $\eta/\lambda \sim Re_\lambda^{-1/2}$ seems no more valid. This should not be surprise, since the low Re should not be the only major parameter for the scaling, but Gr_e or Ra_e as well, similar to the role of thermo-Rayleigh number (Ra) in turbulent Rayleigh-Bénard convection (Lohse and Xia 2010), where the scaling relies on Ra, which is nonlinearly proportional to Re. Compared with turbulent Rayleigh-Bénard convection where Re is also very high for the high Ra, the Re here is very low. Even if as mentioned

before (Wang et al. 2014), $\langle u_s \rangle$ is larger under forcing than that without forcing and increases with voltage (but decreases downstream). Re based on $\langle u_s \rangle$ is not higher than 10 in the entire flow field, still very low.

2.5.4 Concentration

(a) Evaluation of mixing effect

From Figure 2.10(b), a fast mixing can be easily found. However, this can be misleading, because the long exposure time can smear unmixed fine structures and the actual molecular mixing is not completely finished. Although the mixing index is large (will be introduced later), there are still many unmixed concentration (evaluated by fluorescence intensity) structures which exhibit strong temporal fluctuations. These unmixed small structures become more visible when the exposure time is shortened from 100 ms to 0.1 ms as shown in Figure 2.10(b) to (e) through "freezing" the structures. In fact, these small spatial scale and high frequency concentration structures are crucial in chemical engineering applications, especially when the desired reaction has short reaction time.

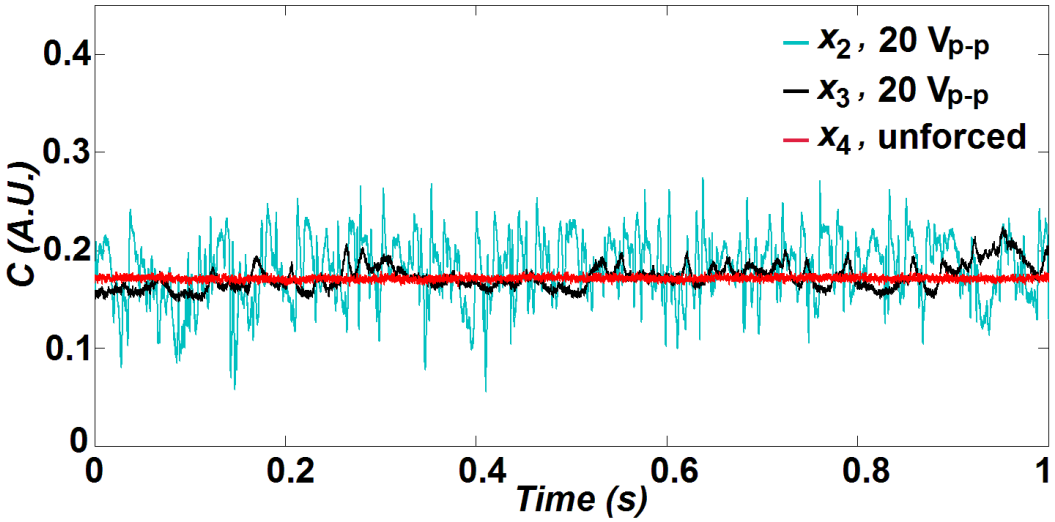

Figure 2.20 Time series of concentration by LIF. x_2 = 10 μm, x_3 = 100 μm, x_4 = 500 μm

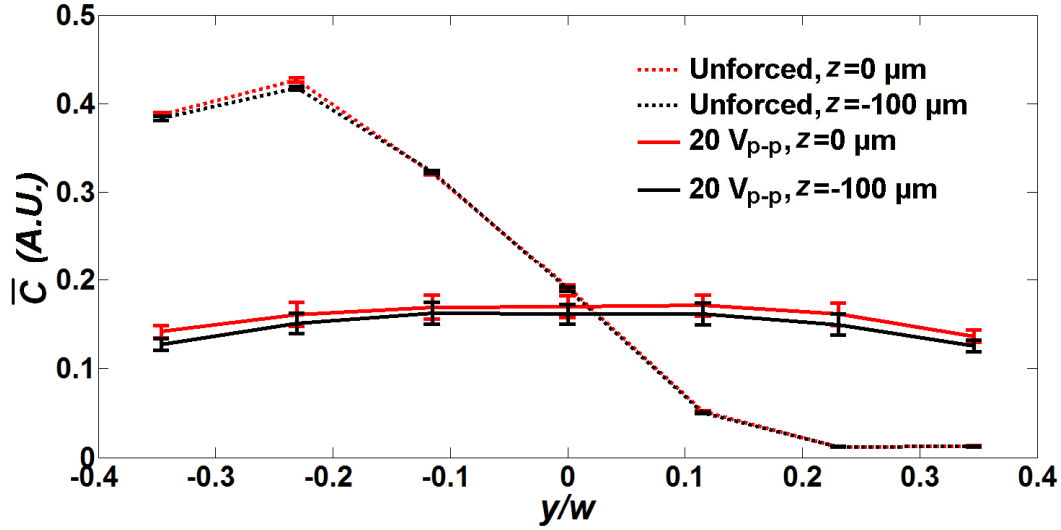

Figure 2.21 Mean concentration profile with and without forcing at x = 100 μm and different z positions.

The concentration fluctuations C' are more accurately measured by LIF with the confocal microscope with ultrahigh spatiotemporal resolution, and expressed in time series as shown in Figure 2.20. The small scale high frequency components can be directly observed from the time trace.

The mean concentration profiles at x=100 μm are plotted in Figure 2.21. While unforced, the high and low concentration streams can be easily distinguished by a steep

interface. The large concentration gradient indicates the concentration is far from uniform and the fluid is not mixed. However, under forcing, the mean concentration profiles become flat at two different z positions, which indicates a good mixing effect from the sense of temporal averaging.

Evolution of segregation intensity of dye concentration, $I_s = \langle C'^2 \rangle / \langle C \rangle^2$, along streamwise direction is later given in Figure 2.22, where, C is local concentration, $<C>$ is the ensemble average of C, and $<C'^2>$ is the variance of concentration fluctuation C' ($=C-<C>$). Under forcing, I_s increases both rapidly and significantly at the inlet of the channel. After achieving its maximum approximately at x = 10 μm, I_s starts to decrease rapidly and exponentially downstream similar to the case predicted in the near field of a turbulent pipe flow (Guilkey et al. 1997) or in an isotropic turbulent mixer (Corrsin 1964).

To evaluate the mixing effects on the entire cross section, the distribution of $C'_{rms}/\langle C \rangle_s$ is shown in Figure 2.23, where $C'_{rms} = \sqrt{\langle C'^2 \rangle}$ and $<>_s$ is the spatially averaged quantity along the entire width of the channel. Hence, $<C>_s$ is equivalent to the concentration while the streams are perfectly mixed. From Figure 2.23, it can be seen the measured $C'_{rms}/\langle C \rangle_s$ is very small and almost comparable to the unforced case (due to noise). The mixing based on the spatial resolution is at least 92% finished at x=100 μm, if estimated from the temporal variation.

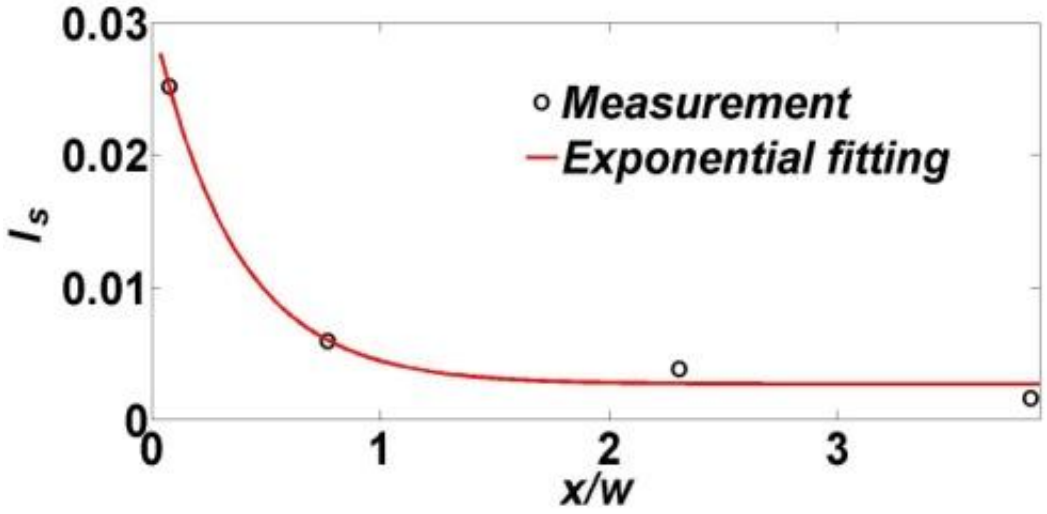

Figure 2.22 Evolution of I_s along x-direction at $y = z = 0$.

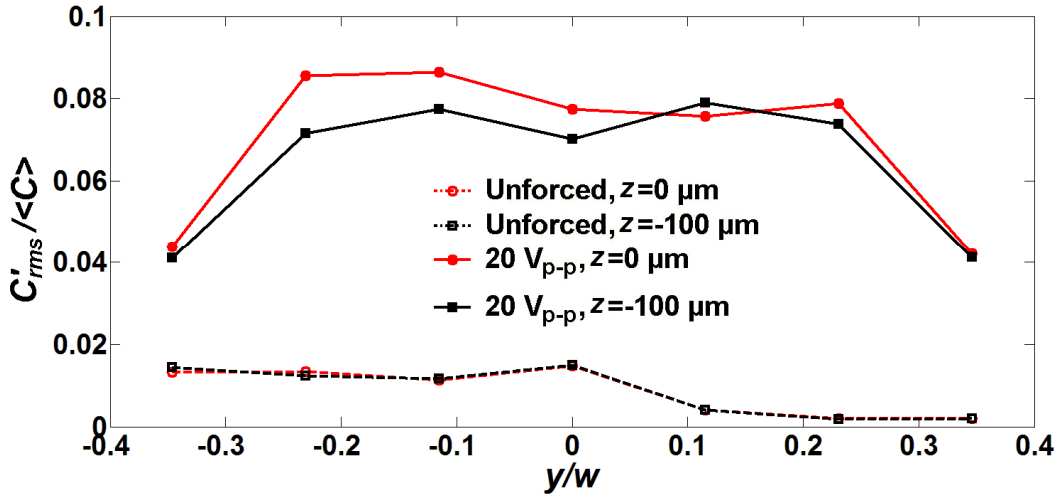

Figure 2.23 $C'_{rms}/\langle C\rangle$ with and without forcing at $x = 100$ μm and different z positions

However, although I_s is often used in statistical analysis for turbulence, where temporal average is used, there is difference between the temporal averaged concentration ($\langle C\rangle$) and the value of the perfectly mixed state (i.e. $\langle C\rangle_s$) in most cases. Therefore, C' cannot accurately reflect the variation from the perfectly mixed state. In other words, when $\langle C\rangle$ and $\langle C\rangle_s$ has large difference, even though C'_{rms} is very small, the mixing can be far from completed (a special and extreme case can be related to unforced flow), because of the existence of the inhomogeneity of concentration at large scale. To avoid this issue in

mixing evaluation, the degree of mixedness (λ) (Erol and Kalyon 2005) is used, which is defined as:

$$\lambda = 1 - C''_{rms}/C_{ref}$$

where $C''_{rms} = \sqrt{\langle C''^2 \rangle}$, $C'' = C - \langle C \rangle_s$ and $C_{ref} = \sqrt{\langle C \rangle_s (C_0 - \langle C \rangle_s)}$ with C_0 the initial concentration of dye.

From Figure 2.24, it can be seen, 77% mixing has been reached just x = 10 μm downstream of trailing edge, from which the two streams begin to meet each other, and take only 5 ms for them to flow to x = 10 μm. This is amazingly fast. As the distance from trailing edge increases, λ keeps increasing and reaches 90% at x = 100 μm and 95% at x = 500 μm, respectively.

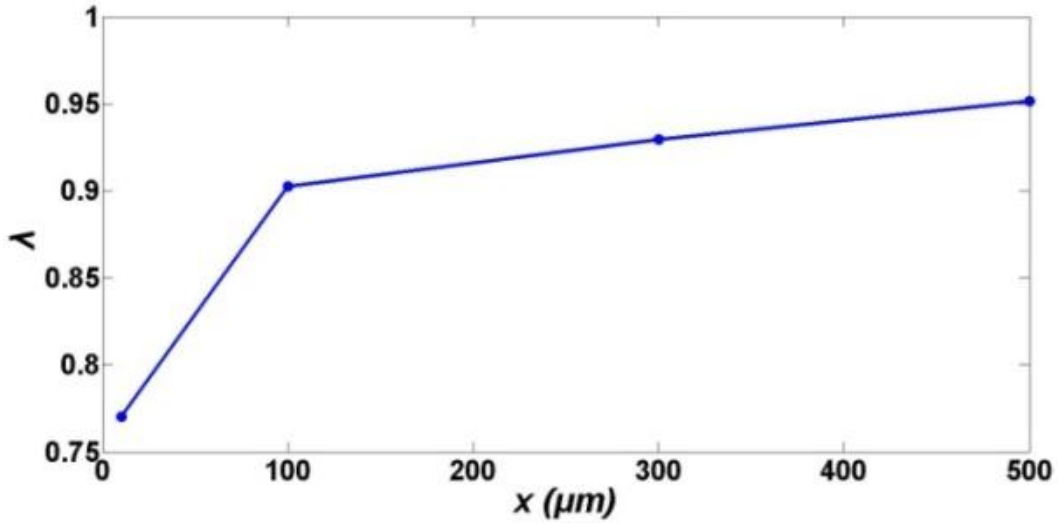

Figure 2.24 Mixing index along streamwise direction at the centerline with forcing at 20 $V_{p\text{-}p}$.

The fast mixing is not only realized at the centerline, but also in almost the whole area of the cross section. At x = 100 μm, on most of the cross-sectional area, more than 90%

mixing can be easily found, as shown in Figure 2.25. Furthermore, near y=0 μm, the mixing near the bottom (z=-100 μm) of channel even exhibits better mixing effect than at the centerline (z=0 μm). This really exceeds our expectation and maybe the result of AC electroosmotic flow which enhance the mixing in *y* direction near bottom. All these indicate the mixing is amazingly fast.

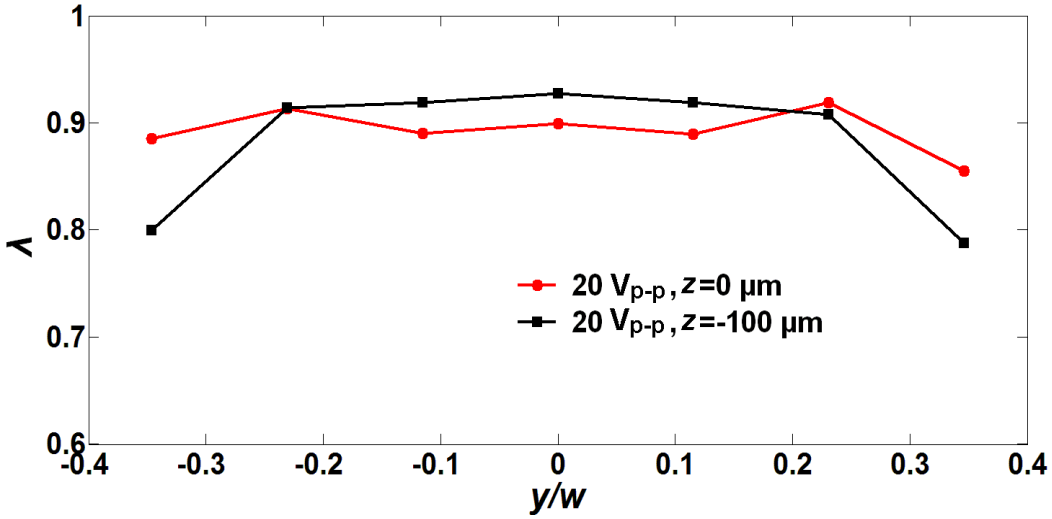

Figure 2.25 Mixing index at x = 100 μm with forcing.

(b) PSD of concentration

PSD of *C'* (also called E_c) for various forcing voltages at x=100 μm is given in Figure 2.26(a), which shows both PSD and the cut-off frequency f_c where noise starts to dominate, increase with the voltage. Without forcing, the PSD is very low, although there are some peaks which could be caused by the vibration of the interface of the two streams. With forcing at 10 $V_{p\text{-}p}$ ($Gr_e = 1.8 \times 10^5$), there are some fluctuations in the spectrum and PSD increases within the range of 1 to 100 Hz. At 14 $V_{p\text{-}p}$ ($Gr_e = 3.5 \times 10^5$), the PSD not only increases, but also starts to exhibits a slope of -5/3 within the range of 7-50 Hz. As voltage is further increased to 20 $V_{p\text{-}p}$, both the magnitude and bandwidth of PSD increase, and the

bandwidth that possesses the -5/3 slope increases to the range of 4-60 Hz, i.e. more than one decade. In macroflows, the -5/3 spectrum is the so-called Obukhov-Corrsin (O-C) (Obukhov 1949; Corrsin 1951) spectrum, which normally can only be observed when Re is very high, e.g. the corresponding Taylor microscale Reynolds number $Re_\lambda > 2{,}000$ is required before the -5/3 spectrum occurs in shear flow (Sreenivasan 1996), although it is possible to achieve it at lower Re_λ, i.e. ~500 for shear-free grid generated turbulent flows (Mydlarski and Warhaft 1998). However, in μEK turbulence, as introduced previously, the Re_λ at x=100 μm is estimated to be only 0.032.

In the turbulent transport, the concentration structures cascade from large scale to small scale and then are eliminated by diffusion (or in other words, the turbulent mixing transfers $\langle C'^2 \rangle$ from low frequency components to high frequency components and then $\langle C'^2 \rangle$ is dissipated by molecule diffusion). This should cause two phenomena: (1) The low frequency components of PSD will continuously decrease downstream due to energy cascading; (2) the cut-off frequency, where noise starts to dominate, will also continuously decrease due to diffusion. Both of them are consistent with the development of PSD in x-direction, as shown in Figure 2.26(b). At x = -10 μm, i.e. upstream of the trailing edge, the PSD is similar to that of the unforced flow, indicating that the flow is still laminar. However, at x = 10 μm, the PSD has dramatically increased, and is about three orders higher than that of the unforced one in the range of 30-100 Hz and the f_c is increased to more than 1 kHz. At x=100 μm, the PSD has developed the -5/3 spectrum. Further downstream at x = 500 μm, both PSD and f_c decrease, but there is still a range of spectrum of -5/3 slope although its bandwidth decreases. To understand the cause of the scalar PSD, the PSD of velocity is also given in Figure 2.26(b). The PSDs of scalar are very similar to that of velocity, both

slope and bandwidth at the same *x*-positions, indicating that the scalar fluctuation is directly caused by eddies.

From scalar PSD, we can also discover a large homogeneous region around *x*=100 μm, as shown in Figure 2.26(c) where the scalar PSD measured at different *y* and z positions on cross-section of *x*=100 μm is plotted. It can be seen, while unforced, E_c of three different transverse and vertical positions are all flat at most of the frequency range, except low frequency noises caused by the possible oscillation of the interface between the two streams. While forced, at these positions, all the three E_c exhibit almost the same cut-off frequencies, which indicates the simultaneous and uniform mixing on small scale is achieved in this cross-section. At z=0 and z= -100 μm, the scalar PSD exhibit almost the same slope and shape, which implies the existence of homogeneous region of flow. And compared to y-direction, homogeneous flow field, no matter characterized by velocity and corresponding scalar, are easier to achieve in z-direction, even though the detection position is very close to the bottom wall. The homogeneous scalar field implies the homogeneity of velocity field which is not affected by the strong wall viscosity. This is surprising compared to conventional HD turbulence, but reasonable for an electrically driven flow in a closed system, where the driven force is determined by conductivity gradient which is unaffected by wall viscosity and easier to achieve homogeneity.

In Figure 2.26, although the -5/3 slope is achieved, beyond it no Batchelor -1 spectrum (Batchelor 1959) of viscous-convective subrange is observed. Spatial resolution of the measurement should not be the cause, although the spatial resolution may not be high enough for the entire Batchelor spectrum of the forced flow at *x*=100 μm. The Kolmogorov scale is estimated to be about 3.3 μm based on measured PSD of velocity at *x*=100 μm, and

the corresponding Batchelor scale is about 0.07 μm, since the Schmidt number of fluorescent dye is about 2000. The resolution of the measuring system is about 0.2 μm. Therefore, the resolution is sufficient to measure at least part of the Batchelor spectrum, if it at all existed. In Figure 2.26, beyond the -5/3 subrange, the slope is about -5.6, much steeper than -1. Actually this slope is almost the same for all spectra at streamwise positions downstream of x=100 μm.

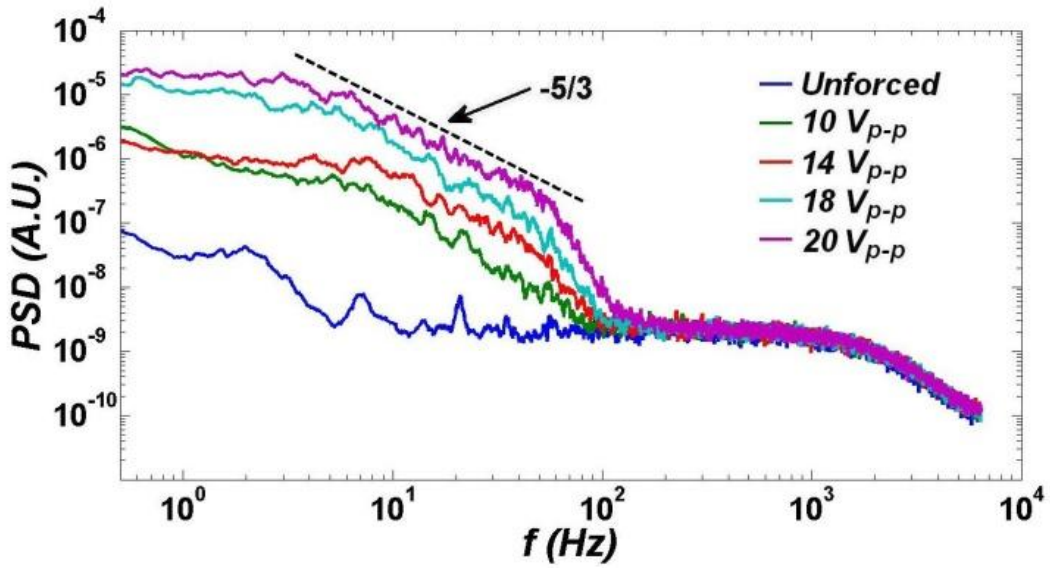

(a)

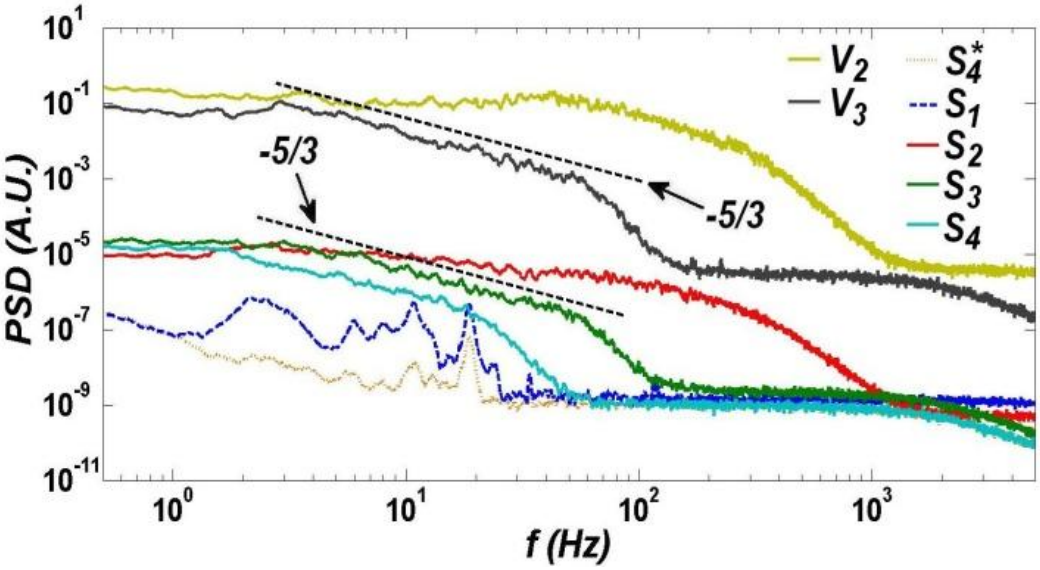

(b)

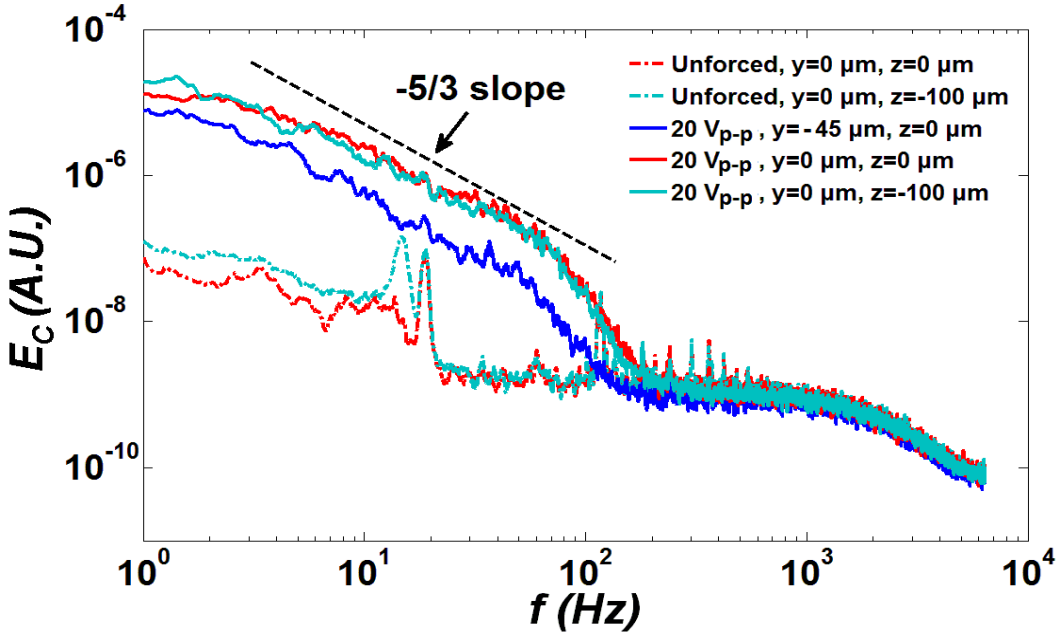

(c)

Figure 2.26 PSD under various conditions at $y = z = 0$. (a) PSD under various voltages at $x = 100$ μm . (b) PSD development along x-direction. "S" indicates scalar and "V" means velocity. Subscripts indicate the x positions and '*' means unforced case. All the other cases without '*' are measured under 20 $V_{p\text{-}p}$. S_1 means scalar PSD at x=-10 μm under 20 $V_{p\text{-}p}$, S_2 is at x=10 μm, S_3 is at x=100 μm and S_4 is at x=500 μm, while S_4^* means unforced scalar PSD at x=500 μm. -5/3 spectrum starts at x=100 μm and persists in at x=500 μm. To make it easier to read, PSD of velocity is shift up for six orders, but this will not affect reading of the slope and f_c. (c) PSD of C' in cross-section at x=100 μm with and without forcing. The peaks in unforced flow are caused by noise.

Batchelor theory(Batchelor 1959) on small scalar structures has been perceived for more than five decades. However, so far, no reliable experiment in a laboratory can validate it, although some earlier pioneering measurements have supported it(Gibson and Schwarz 1963; Nye and Brodkey 1967). There are also other experiments that show no Batchelor's -1 slope (Miller and Dimotakis 1996; Williams et al. 1997; Wang 2000). It seems that the debate if there is the -1 Batchelor spectrum beyond -5/3 spectrum, has not received its conclusion yet. As Batchelor mentioned that the -1 spectrum does not require Re to be so

large that an inertial subrange exists. Hence, the relatively low Re and anisotropic flow may not be the reason why there is no -1 Batchelor spectrum beyond the -5/3 spectrum.

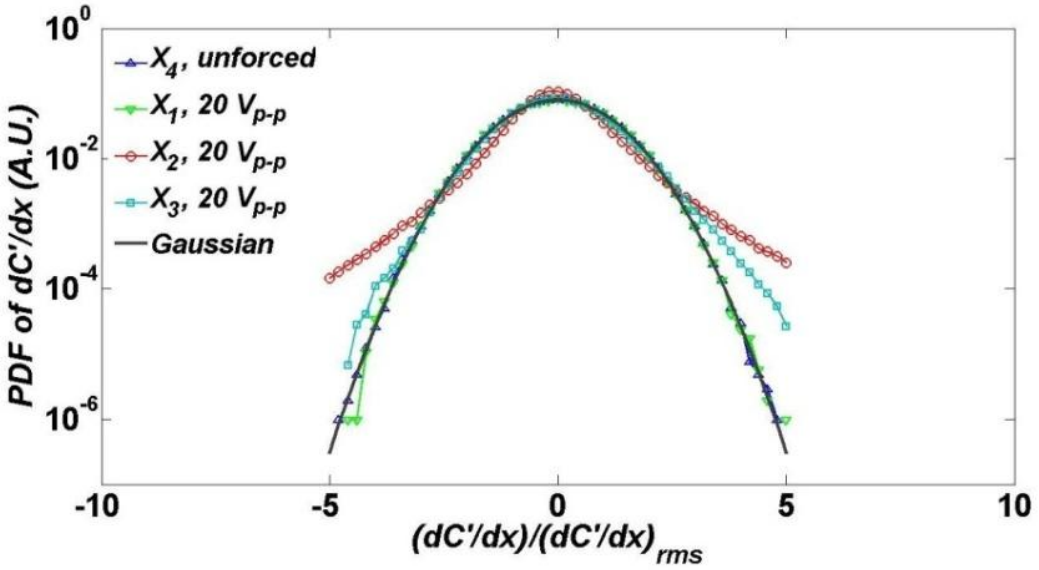

Figure 2.27 The PDF of d*C'/dx* at various x-positions without and with forcing at 20 V_{p-p} along $y = z = 0$. Without forcing there is no exponential tail. However, while the flow is forced, an exponential tail appears at x=10 μm and decays along x-direction.

(c) PDF of dC'/dx

The PDF of d*C'/dx* at various positions, is given in Figure 2.27 for the unforced and forced flow at 20 V_{p-p}. While without forcing, PDF of d*C'/dx* at x = 500 μm is a Gaussian distribution as expected (The reason of using the unforced flow at x=500 μm, not other positions, is to lower down the vibration noise by the smaller concentration gradient at x=500 μm), the PDF of the forced flow at x=10 μm does not display a Gaussian distribution, but an exponential tail. Usually the exponential tail is resulted from the intermittency of the small scale structures (Warhaft 2000). The strongest exponential tail is near x=10 μm, beyond which it degrades along the streamwise direction. The reason is probably that near x=10 μm the scalar has the smallest structures (see spectrum in Figure 2.26(b)), and thus

high local scalar gradient. In this case, the molecular diffusion becomes very important at x=10 μm where small scale structures have already been generated. Downstream of x=10 μm, due to unknown mechanism, the intermittency of small-scale scalar structures becomes weaker and thus, the exponential tail of PDF becomes insignificant. This is inconsistent with what we find in velocity structures, where at x=100 μm, strong intermittency can still be found. The "smooth" small-scale scalar structures are also indicated by the scaling exponents of scalar structure functions, as be introduced in next section.

(d) Scalar structure function and scaling law

Scaling similarity of scalar structure function is another feature of high Re turbulent flow (Ruiz-Chavarria et al. 1996). Such a behavior is also observed in the forced flow as shown in Figure 2.28, Structure function is $S_p(r)=<|C(x+r)-C(x)|^p>\sim r^{\zeta_p}$, where p is the order of moment, r is spatial distance and ξ_p is the scaling exponent. Here, we use the second order moment (i.e. p = 2) to show the scaling similarity at x=100 μm. In the inertial subrange, the scaling exponent of $S_2(r)$ is approximately 0.68, which is consistent to the O-C law. The scaling relation between ξ_p and p for $p \leq 5$ is given in Figure 2.28(b). Here the scaling relation fits O-C law very well, i.e. $\xi_p = p/3$. But similar to the PDF of dC'/dx, the supposed intermittency phenomenon (i.e. ξ_p departures from $p/3$) of the scalar structures is not observed, which could indicate the relatively weak intermittency of small-scale scalar structures due to rapid diffusion.

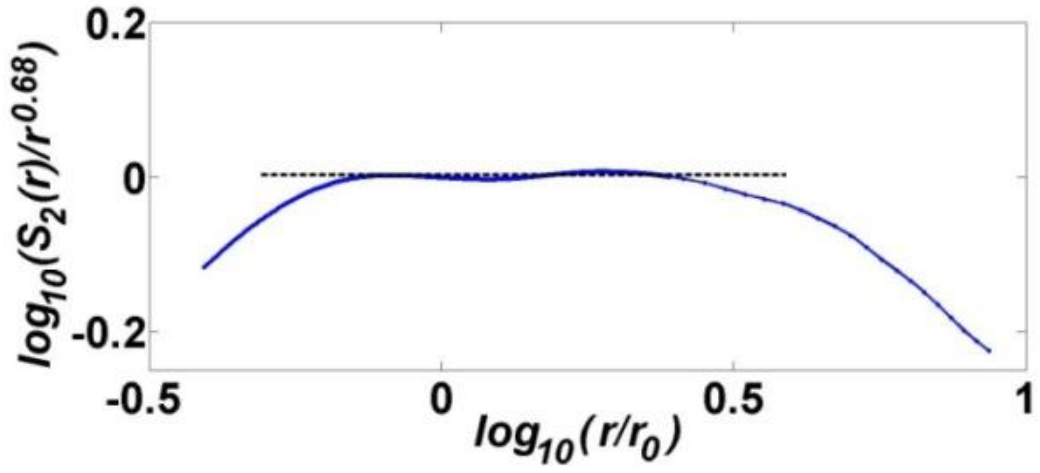

(a)

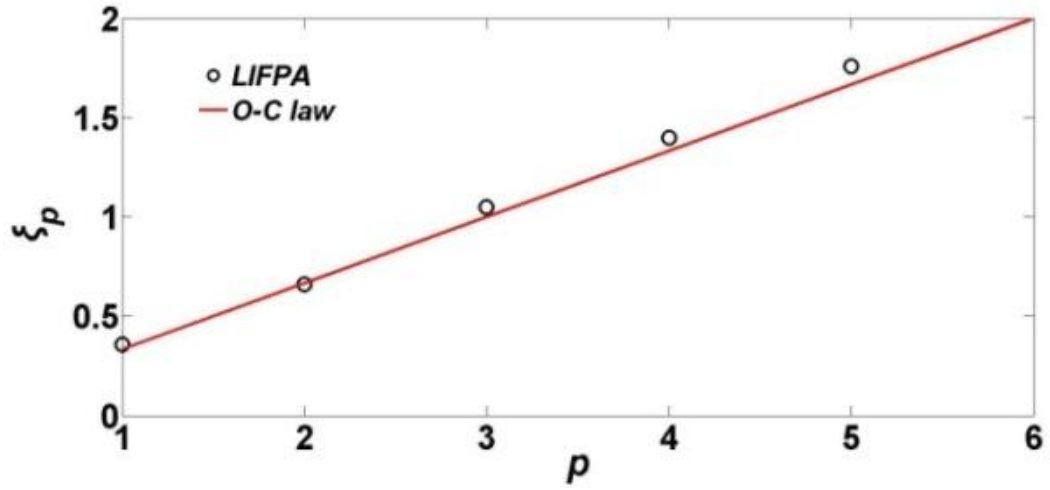

(b)

Figure 2.28 Scaling behavior of scalar structure function of the second order moment and scaling exponent. (a) $S_2(r)$ vs r at x=100 μm , $y = z = 0$, matches well with O-C scaling as the existence of plateau indicated by dashed line. Here r_0 is a reference length scale. (b) The scaling exponent fits well with O-C scaling, but no intermittency is observed at x=100 μm and $y = z = 0$.

(e) Discussion and Conclusion

In the light of conventional mixing criterion, as plotted in Figure 2.24 and Figure 2.25, the turbulent mixing is observed to achieve the ultrafast mixing. To reach the equivalent mixing, shown at x=10, 100 and 500 μm by molecular diffusion alone, it normally takes 4 s, 7 s and 9 s respectively (calculated by solving the 1-D diffusion equation with Neumann boundary conditions, i.e. the concentration gradients at walls are 0). However, to these

positions by convection transport, the time cost is 5 ms, 50 ms and 250 ms respectively. This indicates that the mixing is two to three orders faster by generating the EK turbulent mixing. To the best of our knowledge, so far no other method can have such a fast mixing process (Lee et al. 2011). The EK turbulence mixing initially has exponential increasing with streamwise distance from trailing edge (Wang et al. Submitted), which is consistent with initial behavior in high Re stirred tank (Nye and Brodkey 1967) and turbulent pipe flow (Kerstein and McMurtry 1994; Guilkey et al. 1997). It means the mixer we developed not only has overall fast mixing, but also has a much faster initial mixing, as evaluated at x=10 μm. This is especially preferred for many specific applications where mixing effect is not highly required, but mixing time or dimensions of mixing chamber is limited.

Although the experiments are carefully carried out, there are still many inevitable problems, such as errors and noise signals. For example, in Figure 2.26(c), the signal on dye side is relatively larger than twice the concentration of the forced case. This may be caused by either the fabrication error of entrance positions, or different flow rates by syringe pump error. Due to background noise, the signal on DI water side cannot be exactly 0. It can also be found in Figure 2.21, that even for the unforced case, a large C'_{rms} exists on the dye side. This is caused by shot noise of PMT. Even though there can be many problems, the extremely fast mixing is undisputed.

In this section, we have investigated scalar transport in μEK turbulence. Although the physical mechanism of μEK turbulence is far from clear, the presence of the turbulence is undisputed. The mixing is significantly enhanced by the generated EK turbulent flow. By evaluating with the degree of mixedness λ, a two to three orders faster mixing is achieved, compared to the one through purely molecular diffusion. Large scale concentration

structures are broken down immediately downstream the trailing edge, and transferred to small scale ones by passive turbulent transport mechanism. In the process, several characters of high Re scalar turbulence, such as O-C spectrum, exponential tail of PDF have been discovered. Meanwhile, we also find several differences from conventional HD turbulence. The most important is the weaker intermittency indicated from scalar than from velocity. This is contrary with conventional HD turbulence, where normally small-scale scalar structures have stronger intermittency than the corresponding velocity structures (Sreenivasan 1997). What kind of physical mechanism causes the abnormal intermittency behavior is still unknown. Further investigations are required.

2.5.5 A new scaling region in micro EK turbulence

Kolmogorov (1941) established the classical and graceful self-similarity law (K41 law) of turbulence in high Reynolds number limit. In the theory, based on the homogeneous and isotropic hypothesis of turbulence, in the inertial subrange, the 2nd order streamwise velocity structure function ($\Delta u(l) = u(x+l) - u(x)$) is directly related to the corresponding spatial scale — l as below:

$$S_u^2(l) = \langle \Delta u(l)^2 \rangle \sim \epsilon_u^{2/3} l^{2/3} \tag{2.31}$$

where $S_u^p(l)$ is the p^{th} order structure function of u,$\epsilon_u = 2\nu s_{ij} s_{ij}$ is turbulent energy dissipation rate, υ isthe kinematic viscosity and s_{ij} is strain-rate tensor (Davidson 2004). Later, Obukhov (1949) and Corrsin (1951) extended his work to the scalar structure function ($\Delta\varphi(l) = \varphi(x+l) - \varphi(x)$) in inertial subrange of scalar turbulence by passive convection, as:

$$S_{\varphi}^{2}(l) = \langle \Delta\varphi(l)^{2} \rangle \sim \epsilon_{\varphi} \epsilon_{u}^{-1/3} l^{2/3} \tag{2.32}$$

where $\epsilon_{\varphi} = 2D_{\varphi} \langle \left(\frac{d\varphi}{dx}\right)^{2} \rangle$ is the scalar dissipation rate of φ and D_{φ} is the diffusivity of scalar φ. Later, Bolgiano (1959) and Obukhov (1959) discovered the BO59 scaling in RB convection respectively, as shown below:

$$S_{u}^{2}(l) \sim \epsilon_{T}^{2/5} (\alpha\rho)^{4/5} l^{6/5}$$

$$S_{T}^{2}(l) \sim \epsilon_{T}^{4/5} (\alpha\rho)^{-2/5} l^{2/5}$$

where T is temperature. Niemela et al. (2000) experimentally observed the temperature spectrum corresponding to BO59 law, which supports its existence. However, to our knowledge, there is no experimental data on velocity so far which supports BO59, except the numerical simulation by Boffetta et al. (2012).

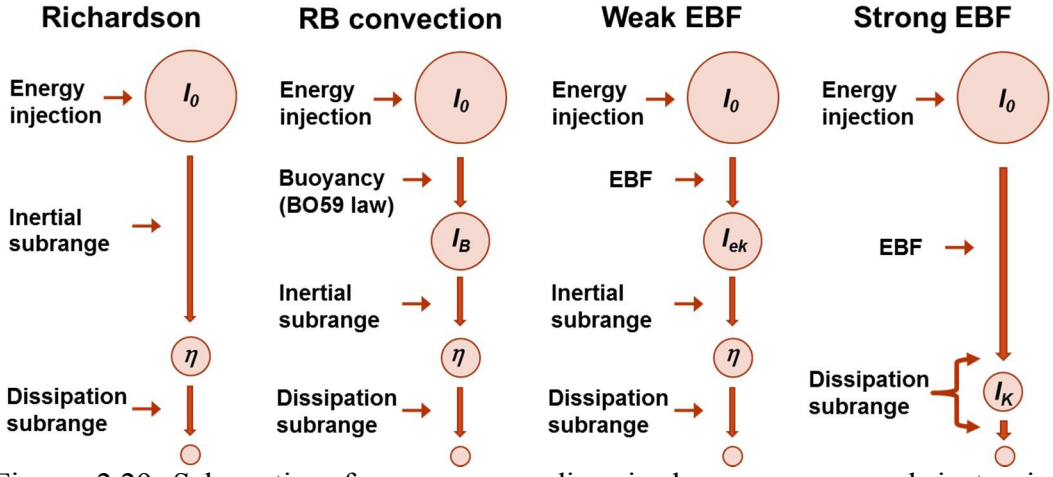

Figure 2.29 Schematic of energy cascading in homogeneous and isotropic hydrodynamic turbulence, turbulent RB convection and EK turbulence with different EBFs. l_B is the Bolgiano scale (Bolgiano 1959) in RB convection.

Compared to RB turbulence, Wang et al. (2014) discovered turbulence-like power spectrum density (PSD) of velocity fluctuation in micro-EK flow by applying high AC

electric field and streams with large initial ratio of electric conductivity. The energy cascade process is similar to that of RB flow by replacing buoyancy force to EBF, as shown in Figure 2.29. The large scale velocity fluctuations are initially generated by EBF, and the associated turbulence energy is cascading to small scale, with the continuous injection of energy by EBF. The difference between the energy cascades in RB convection and EK turbulence is: the effect of buoyancy decreases with scale very fast ($\sim l^{4/5}$) (Lohse and Xia 2010), hence, it can only affect the large scale velocity structures. However, EBF, which depends on the gradient of conductivity, is actually increasing with decreased *l*, indicating significant influence deep into small scale velocity structures.

The increasing of EBF with decreasing *l* is actually slower than the increasing of viscous dissipation with decreasing *l*. This results in two different power spectrum behaviors: (1) When the EBF is weak, its influence is more important on large scales conductivity structures. We can predict the existence of EBF dominant spectrum region at the low frequency part of inertial subrange. Or in other words, the power spectrum can be separated into 4 subranges. From low frequency to high frequency, they are energy containing subrange, EBF dominant subrange, inertial subrange and dissipation subrange, as shown in Figure 2.29. (2) When EBF is very strong, the inertial subrange will be replaced and covered by the EBF dominant region. EBF can deep into dissipation subrange. The conventionally defined Kolmogorov scale should be replaced by another microscale which can describe the balance between EBF induced velocity fluctuations and viscosity. The detailed deviations will be introduced later.

In EK flow, even in microchannels, the fluid can still be assumed to be continuum and incompressible. Then the momentum equation is (Ramos 2011):

$$\rho \frac{D\boldsymbol{u}}{Dt} = -\nabla p + \mu \nabla^2 \boldsymbol{u} + F_e \tag{2.33}$$

where $\boldsymbol{u} = u\vec{\imath} + v\vec{\jmath} + w\vec{k}$ is the instant velocity vector (u, v and w are the velocity in streamwise (x), spanwise (y) and vertical (z) directions respectively. And $\vec{\imath}$, $\vec{\jmath}$ and $\vec{k}$ are the unit vector in these 3 directions), $D/Dt = \partial/\partial t + \boldsymbol{u} \cdot \nabla$. In AC electric field, when the frequency of AC electric field (f_f) is much smaller than the frequency corresponding to the charge relaxation time ($f_r = \sigma/\varepsilon$, where σ and $\varepsilon = \varepsilon_r \varepsilon_0$ are the conductivity and permittivity of solution respectively. ε_r is the relative permittivity and ε_0 is vacuum permittivity), the electric field is quasi-electrostatic. Normally $\boldsymbol{E} = |\boldsymbol{E}|e^{i\omega t}$ ($\omega = 2\pi f_f$ is the angle frequency), $F_e = \mathrm{Re}(\rho_e)\mathrm{Re}(\boldsymbol{E}) - \frac{1}{2}[\mathrm{Re}(\boldsymbol{E}) \cdot \mathrm{Re}(\boldsymbol{E})]\nabla\varepsilon$ (the flow is assumed to be incompressible and Re indicates real part of complex function) is the EBF and $\rho_e = \nabla \cdot (\varepsilon \boldsymbol{E}) = \nabla\varepsilon \cdot \boldsymbol{E} + \varepsilon \nabla \cdot \boldsymbol{E}$ is the net charge**.** μ and ρ are dynamic viscosity and density of fluid.

Here, we consider a simple 1D AC electric field in y-direction to simplify analysis. Then, $\nabla\varepsilon = \partial\varepsilon/\partial y$. When the characteristic frequency of conductivity fluctuation f_σ is much smaller than f_f, the electric field intensity can be described as $\boldsymbol{E} = E(y,t)\vec{\jmath} = E_m(y,t_s)e^{i\omega t}\vec{\jmath}$, ($E_m(y,t_s)$ is a slowly and slightly varying function of time compared to the influence of AC signal. $E_m(y,t_s)$ is determined by conductivity structures and $t_s = 1/f_\sigma$). Hence, $\partial E_m(y,t_s)/\partial t \approx 0$and $\partial^2(\varepsilon E)/\partial t \partial y \approx \partial(i\omega\varepsilon E)/\partial y$. As normally the convection velocity is limited, the charge transport equation $\partial\rho_e/\partial t + \nabla \cdot (\sigma \boldsymbol{E}) + \nabla \cdot (\rho_e \boldsymbol{u}) = 0$ becomes:

$$\frac{\partial i\omega\varepsilon E}{\partial y} + \frac{\partial \sigma E}{\partial y} = \frac{\partial \sigma^* E}{\partial y} = 0$$

where $\sigma^* = \sigma + i\omega\varepsilon$ Hence, for 1D case,

$$\sigma^* E = J^*(t) \tag{2.34}$$

which is constant for *y*.

For clarity, we use E_R to demonstrate the real part of $E(y,t)$, we have:

$$F_e = \left(\frac{\partial \varepsilon}{\partial y} E_R + \varepsilon \frac{\partial E_R}{\partial y}\right) E_R - \frac{1}{2} E_R^2 \frac{\partial \varepsilon}{\partial y} = \frac{\partial}{\partial y}\left(\frac{1}{2}\varepsilon E_R^2\right) \tag{2.35}$$

For conductivity structure of scale *l*, the averaged EBF is:

$$F_{e,l} = \langle F_e \rangle_l = \frac{1}{2l} \varepsilon E_R^2 |_y^{y+l} \tag{2.36}$$

where $\langle f \rangle_l = \frac{1}{l}\int_y^{y+l} f\, dy$ and *f* is arbitrary function. By plugging Equation (2.34) into (2.36) with $E_R = \left(E + \tilde{E}\right)/2$ ("~" means complex conjugate), $F_{e,l}$ becomes:

$$F_{e,l} = \frac{\varepsilon}{8l}\left(\frac{J^{*2}}{\sigma^{*2}} + \frac{\widetilde{J^*}^2}{\widetilde{\sigma^*}^2} + 2\frac{|J^*|^2}{|\sigma^*|^2}\right)\Big|_y^{y+l} \tag{2.37}$$

Here assume linear variation of σ in this scale *l* structure, we can find:

$$\begin{cases} \left.\dfrac{J^{*2}}{\sigma^{*2}}\right|_y^{y+l} = -2J^{*2}\dfrac{1}{\sigma_{m,l}^{*\,2}}\dfrac{\theta_l^*}{\left[1-\frac{1}{4}\theta_l^{*2}\right]^2} \\ \left.\dfrac{\widetilde{J^*}^2}{\widetilde{\sigma^*}^2}\right|_y^{y+l} = -2\widetilde{J^*}^2\dfrac{1}{\widetilde{\sigma_{m,l}^*}^2}\dfrac{\widetilde{\theta_l^*}}{\left[1-\frac{1}{4}\widetilde{\theta_l^{*2}}\right]^2} \\ \left.\dfrac{|J^*|^2}{|\sigma^*|^2}\right|_y^{y+l} = -2\dfrac{|J^*|^2}{\sigma_{m,l}^2}\dfrac{\theta_l}{\left[1+\frac{1}{4}\theta_l^2+\beta_l^2\right]^2-\theta_l^2} \end{cases} \tag{2.38}$$

where $\sigma_{m,l}^* = [\sigma^*(y+l) + \sigma^*(l)]/2$, $\sigma_{m,l} = [\sigma(y+l) + \sigma(l)]/2$, $\Delta\sigma(l) = \sigma(y+l) - \sigma(l)$, $\theta_l = \Delta\sigma(l)/\sigma_{m,l}$, $\theta_l^* = \Delta\sigma^*(l)/\sigma_{m,l}^*$, $\beta_l = \omega\varepsilon/\sigma_{m,l}$.

Furthermore, when $\beta_l \ll 1$, as $|\theta_l| \in [0,2], |\theta_l^*| \in [0,2]$, by nominal expansion and Taylor expansion, we have:

$$\begin{cases} \frac{\theta_l^*}{\left[1-\frac{1}{4}\theta_l^{*2}\right]^2} \sim \theta_l - \theta_l\beta_l^2 + \frac{1}{2}\theta_l^3 - i\theta_l\beta_l \\ \frac{\widetilde{\theta_l^*}}{\left[1-\frac{1}{4}\widetilde{\theta_l^*}^2\right]^2} \sim \theta_l - \theta_l\beta_l^2 + \frac{1}{2}\theta_l^3 + i\theta_l\beta_l \\ \frac{\theta_l}{\left[1+\frac{1}{4}\theta_l^2+\beta_l^2\right]^2-\theta_l^2} \sim \theta_l\left(1 + \frac{1}{2}\theta_l^2 - 2\beta_l^2\right) \end{cases} \tag{2.39}$$

To estimate the influence of J^*, a new quantity that evaluating the averaging influence of conductivity on scale l is introduced as below:

$$\sigma_l^* = 1/\langle 1/\sigma^* \rangle_l \tag{2.40}$$

Accompanied with the scale based electric field intensity:

$$E_l = \langle E \rangle_l \tag{2.41}$$

Which has the relation:

$$\sigma^* E = \sigma_l^* E_l = \sigma_w^* E_w = J^* \tag{2.42}$$

where "w" is the width of channel. By plugging Equation (2.41), (2.42) and (2.45) into Equation (2.37), we have:

$$F_{e,l} = -\frac{\varepsilon}{4l}\left[(\sigma_w^* E_w)^2 \frac{\theta_l}{\sigma_{m,l}^{*\,2}}\left(1 - \beta_l^2 + \frac{1}{2}\theta_l^2 - i\beta_l\right)\right.$$

$$+\left(\widetilde{\sigma_w^*}\widetilde{E_w}\right)^2 \frac{\theta_l}{\widetilde{\sigma_{m,l}^{*\,2}}}\left(1 - \beta_l^2 + \frac{1}{2}\theta_l^2 + i\beta_l\right)$$

$$\left.+\frac{E_w\widetilde{E_w}\sigma_w^*\widetilde{\sigma_w^*}}{\sigma_{m,l}^2}\theta_l\left(1 + \frac{1}{2}\theta_l^2 - 2\beta_l^2\right)\right] \tag{2.43}$$

Furthermore, considering equilibrium condition of conductivity structures (similar as the definition given by Kolmogorov for velocity field (Kolmogorov 1941), no mean conductivity gradient, scalar variance cascade from large scale to small scale) with small conductivity fluctuations, i.e. $\theta_l \ll 1, \ \forall l$, we have following approximations:

$$\begin{cases} \sigma_{m,l} \approx \sigma_{m,w} \approx \sigma_l \approx \sigma_w \\ \sigma^*_{m,l} \approx \sigma^*_{m,w} \approx \sigma^*_l \approx \sigma^*_w \\ \sigma^*_{m,l_l} \approx \sigma^*_{m,w} \approx \widetilde{\sigma^*_l} \approx \widetilde{\sigma^*_w} \end{cases} \tag{2.44}$$

Thus, $\beta_l = \beta_w \approx \omega\varepsilon/\langle\sigma\rangle_w$ and $\sigma^*_w\widetilde{\sigma^*_w} = \sigma^2_{m,w} + \omega^2\varepsilon^2$. Note that $E_w = V^*/w = E_{amp}e^{i\omega t}$, and neglecting $O(\theta_l^3)$, Equation (2.51) becomes:

$$F_{e,l} = -\frac{\varepsilon E^2_{amp}\theta_l}{2l}[(1-\beta_w^2)\cos(2\omega t) + \beta_w \sin(2\omega t) + (1-\beta_w^2)] \tag{2.45}$$

By further taking short-time averaging (indicated by $\bar{\cdot}$),

$$\overline{\overline{F_{e,l}}}(y, t_s) = \frac{1}{t_s}\int_t^{t+t_s} F_{e,l}\, dt = -\frac{\varepsilon E^2_{amp}\theta_l}{2l}(1-\beta_w^2) \tag{2.46}$$

Hence, $\overline{\overline{F_{e,l}}}$ is the effective EBF that applied on the spatial-temporal varying conductivity structures of scale *l*.

Further, assume the scalar structure function has the self-similarity as $S^1_\sigma(l) = \langle|\Delta\sigma(l)|\rangle \sim \langle|\Delta\sigma(l_0)|\rangle(l/l_0)^{\delta_{\sigma,1}}$ or in another form:

$$\langle|\theta_l|\rangle \sim \langle|\theta_{l_0}|\rangle l^{*\delta_{\sigma,1}}$$

where l_0 is a reference large scale, $0 < l^* = l/l_0 \leq 1$, and $\delta_{\sigma,p}$ is the scaling exponents of p^{th} order structure function of σ, $\langle\rangle$ means spatial averaging in the equilibrium region of

flow field. Then the electric-inertial velocity (Baygents and Baldessari 1998) on scale l can be approximate as below,

$$\langle {u_l}^2 \rangle \sim S_u^2(l) \sim \langle \left| \overline{\overline{F_{e,l}}} \right| \rangle l/\rho \sim \Lambda \, {l^*}^{\delta_{\sigma,1}}/\rho \sim {l^*}^{\delta_{\sigma,1}} \tag{2.47}$$

where $\Lambda = \langle \left| \theta_{l_0} \right| \rangle \varepsilon E_{amp}^2 (1 - \beta_w^2)/2$ is large-scale reference function. As $\langle {u_l}^2 \rangle = S_u^2(l) \sim {l^*}^{\delta_{u,2}}$, we have:

$$\delta_{u,2} = \delta_{\sigma,1} \; or \; \delta_{\varepsilon,1} \tag{2.48}$$

As in the assumed subrange, $\langle \Delta\sigma(l)^2 \rangle \langle \Delta u(l)^2 \rangle^{1/2}/l$ is constant, which is equivalent to $l^{2.5\delta_{\sigma,1}} \sim l$, then:

$$\delta_{u,2} = \delta_{\sigma,1} = 2/5 \text{ and } \delta_{\sigma,2} = 4/5 \tag{2.49}$$

where intermittency is not considered. Meanwhile, from Equation (2.47):

$$\langle \left| \overline{\overline{F_{e,l}}} \right| \rangle \sim \Lambda l_0^{-2/5} l^{-3/5} \tag{2.50a}$$

$$Gr_{e,l} \sim \langle \left| \overline{\overline{F_{e,l}}} \right| \rangle l^3/\rho\nu^2 \sim \Lambda l_0^{-2/5} l^{12/5}/\rho\nu^2 \tag{2.50b}$$

$$Ra_{e,l} = Gr_{e,l} Sc \sim \Lambda l_0^{-2/5} \, l^{12/5}/\rho\nu D_\sigma \tag{2.50c}$$

where $Gr_{e,l}$ and $Ra_{e,l}$ are the scale based electric Grashof number and electric Rayleigh number respectively. $Sc = \nu/D_\sigma$ is the Schmidt number of buffer solution (used to changing σ) and D_σ is the effective diffusivity. Furthermore, due to the similar energy cascading process to RB flow (where the cascading process is dominated by scalar dissipation rate of electric permittivity which is dominated by σ/ω, external electric field

intensity and medium density), Equation (2.49) can also be reached by similar as by Bolgiano (Bolgiano 1959) and Obukhov (Obukhov 1959), which is:

$$S_u^2(l) \sim \epsilon_\sigma^{2/5} E_{amp}^{8/5} \omega^{-4/5} \rho^{-4/5} l^{2/5} \tag{2.51}$$

where $\epsilon_\sigma = D_\sigma \langle (\partial\sigma/\partial x)^2 \rangle$ is the dissipation rate of electric conductivity. And the 2nd order structure function of electric permittivity is:

$$S_\sigma^2(l) \sim \epsilon_\sigma^{4/5} E_{amp}^{-4/5} \omega^{12/5} \rho^{2/5} l^{4/5} \tag{2.52}$$

Hence, the dimensional analysis is consistent with what we found in Equation (2.49).

By comparing Equation (2.47) and (2.51), and arbitrarily assuming $G\left(\langle|\theta_{l_0}|\rangle; \beta_w\right) \sim \left[\langle|\theta_{l_0}|\rangle(1-\beta_w^2)/2\right]^{5/2}$ (a dimensionless function that evaluating the influence of large scale σ structures and forcing frequency), the large scale l_0 can be estimated as:

$$l_0 \sim G \rho^{-1/2} \varepsilon^{5/2} E_{amp} \epsilon_\sigma^{-1} \omega^2 \tag{2.53}$$

Similar to the Bolgiano scale, there exists a length scale l_{ek}, at which EBF becomes in-significant. However, compared to buoyancy in RB convection ($\sim l^{4/5}$), the scale based EBF will increase with decreased l as shown in Equation (2.50a), which indicates much larger influence of EBF on small scale velocity structures. This causes two different characteristic length scales.

If the EBF effect is too weak to reach the dissipation subrange and the inertial subrange still exists, a large length scale similar to Bolgiano scale can be found by balancing Equation (2.31) and (2.51), as:

$$l_{ek} \sim \epsilon_\sigma^{3/2} \epsilon_u^{-5/2} E_{amp}^6 \omega^{-3} \rho^{-3} \tag{2.54}$$

So these two length scales have relation:

$$l_{ek}/l_0 \sim G^{-1} \omega^{-5} \left(E_{amp}^2/\rho\varepsilon\right)^{5/2} (\epsilon_\sigma/\epsilon_u)^{5/2} \tag{2.55}$$

However, if the EBF effect is very strong, its influence can deep into the dissipation subrange and directly works on the strain of fluid, an alternative Kolmogorov scale l_K can be defined by using the electric-inertial velocity as:

$$l_K/\sqrt{\langle u_l{}^2 \rangle} = l_K^2/\nu \tag{2.56}$$

By plugging Equation (2.51) into (2.56), and similarly assuming $\epsilon_\sigma = D_\sigma \left(\frac{\sigma_2 - \sigma_1}{w}\right)^2 Sh$ as in RB convection(Lohse and Xia 2010), then:

$$l_K \sim Ra_e^{-1/3} Sh^{-1/6} \beta_w^{1/3} Sc^{1/2} w \tag{2.57}$$

where $Ra_e = \varepsilon w^2 E_{amp}^2 (\sigma_2 - \sigma_1)/\rho\nu D_\sigma \langle\sigma\rangle_w$ is the nominal electric Rayleigh number, $Sc = \nu/D_\sigma$ is Schmidt number, and $Sh = Kw/D_\sigma$ is Sherwood number. In this case, there will be no inertial subrange existed and the EBF dominant subrange directly connects with dissipation subrange.

The detailed derivations of the theoretical parts in this section can be found in the appendix of dissertation.

In Figure 2.30, the 2nd order moment of velocity structure function is investigated with spatial scale *l* (using Taylor Hypothesis to transfer time series to spatial one) at different streamwise positions. At x = 40 μm, a short but EBF dominant subrange could be found in

Figure 2.30. The slope is approximately 2/5, which is consistent with Equation (2.47) and (2.51). In our experiments, this subrange only exists in a small flow region in streamwise (about 20 μm long). After that, this subrange disappears at x=100 μm, instead is the well-known K41 law. Here, the l_0 evaluated from Equation (2.53) is much smaller even compared to the scale of inertial subrange. The EBF dominant subrange cannot be distinguished from the dissipation subrange.

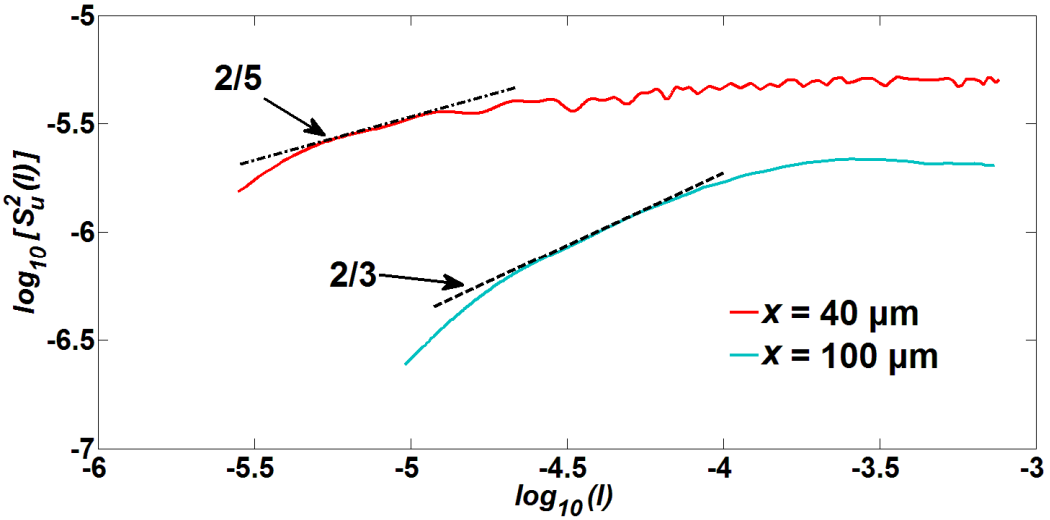

Figure 2.30 2nd order velocity structure function vs l. l=$U\Delta t$, where U is bulk flow velocity and Δt is time intervals.

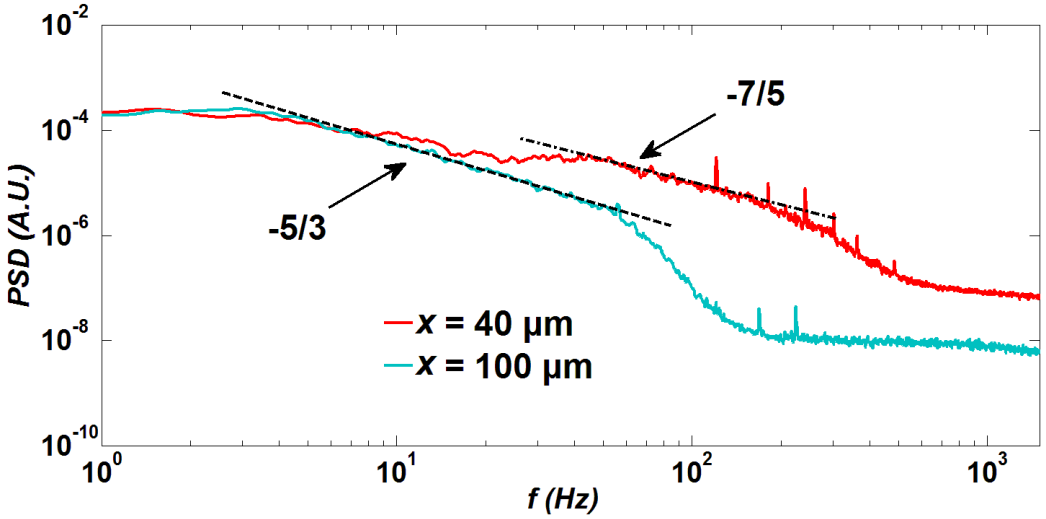

Figure 2.31 PSD of velocity fluctuation at different x-positions

The scaling behavior can also be found in frequency domain by the PSD of velocity fluctuation, as shown in Figure 2.31. At x = 100 μm, Kolmogorov -5/3 spectrum can be found. While at x = 40 μm, the slope is about -7/5, which is consistent with the prediction of Equation (2.47) and (2.51) in physical space. Also, the EBF dominate subrange from PSD space has longer decades compared to the one demonstrated by $S_u^2(l)$, this is conceptually consistent with the researches of Davidson and Krogstad (2008) who find $S_u^2(l)$ has defection on describing turbulent inertial subrange compared to PSD.

In this section, we present the theoretically predicted the scaling of both velocity and conductivity structures in EBF dominant subrange, and experimentally verify it in micro EK turbulence. Both the scaling and spectrum behavior of velocity fluctuations are determined by Ra_e, Sh and Sc etc. Different from buoyancy, EBF increases with decreasing length scales and hence, its influence can deep into small scale. However, the scale based Gr_e and Ra_e actually decrease with length scale, and the effect of EBF is later eliminated by the faster increasing of viscosity effect.

Similar as BO59 which is hard to be discovered as mentioned by Lohse (2010), the electric-inertial subrange in microfluidics EK turbulence is also a fleeting show. It only exists in a small region and we didn't find the co-existence of both electric-inertial scaling and K41 scaling at the same position. This could be because the small geometric scale of microchannel, which restricts the simultaneous development of the energy cascade process in both scale ranges.

2.6 Some characters of μEK turbulence for discussion

2.6.1 Extended self-similarity and abnormal intermittency factor of hierarchical structures

Self-similarity and extended self-similarity (ESS)

In 1993, Benzi et al. (1993) established another form of similarity between velocity structures, i.e. extended self-similarity (ESS), which can be expressed as:

$$S_p(r) = \langle |u(x+r) - u(x)|^p \rangle = \langle |\Delta u(r)|^p \rangle \sim S_3(r)^{\zeta_p} \tag{2.58}$$

In the ESS frame, a much wider inertial subrange can be found, which implies a long-lasting hierarchical cascading progress. The intermittency factor advanced by K62 theory and suggested by Frisch et al. (Frisch 1995) is also consistent with the found in ESS model. Then, all these experimental results are well explained by the She-Leveque model (also called SL94) (She and Leveque 1994) using 3 parameters, which are scaling exponents of most singular structures (γ), co-dimensions (C) and intermittency factor (β). The SL94 model has the following expression:

$$\xi_p = \gamma p + C(1 - \beta^{p/3}) \tag{2.59}$$

Further researches indicate the SL94 model is also established in ESS frame, with the same expression in homogeneous and isotropic turbulence. Here, in an electrically driven microscale flow, the scaling exponents of velocity structures are investigated by ESS. The β factor in SL94 model is then investigated by β-test.

The existence of inertial subrange implies the possible self-similarity of velocity structures can be present in a microscale low Re flow. This is verified as shown in Figure 2.32. In the Figure 2.32(a), the Kolmogorov self-similarity law is investigated. The relation between $S_2(r)$, $S_3(r)$ and $S_6(r)$ with spatial scale r are plotted separately. A clear self-similarity behavior can be found. The inertial subrange, compared to the found by the velocity power spectrum in Wang's work which is more than a decade long, is a little shorter. Here, due to the low signal-noise ratio (SNR) of small scale signals, the spatial scale r is truncated at the cut-off frequency which is estimated from the velocity power spectrum. And the upper bound is restricted to the depth of channel. In streamwise, the $S_3(r)$ vs r at different x positions are investigated and shown in Figure 2.32(b). The width of inertial subrange is almost the same from x = 100 μm to 200 μm, and then decreases in streamwise direction. To x = 300 μm, the power-law region is smaller than half a decade. In this closed system, as the continuously decaying of large scale conductivity structures, the external work input due to electric body force is not sufficient to support the inertial subrange. Meanwhile, the dissipation due to small scale electric body force can sustain longer time as the high Schmidt number (Sc) of conductivity solute. Therefore, after x = 200 μm, the inertial subrange is rapidly and continuously shrinked and the flow will later return to chaotic. The turbulent stage is a local phenomenon and its persistence time is more than 0.15s (considering the distance from inlet to x = 300 μm). This is much larger than the lifetime of turbulence in macroscale pipe flow, the value of which at this low Re (~0.4) is only $3*10^{-25}$ s (Hof, Nature, 2006; Eckhardt, Annu. Rev. Fluid Mech., 2007). The sustained turbulent flow region can only be attributed to the influence of electric body force and relatively large local Grashof number.

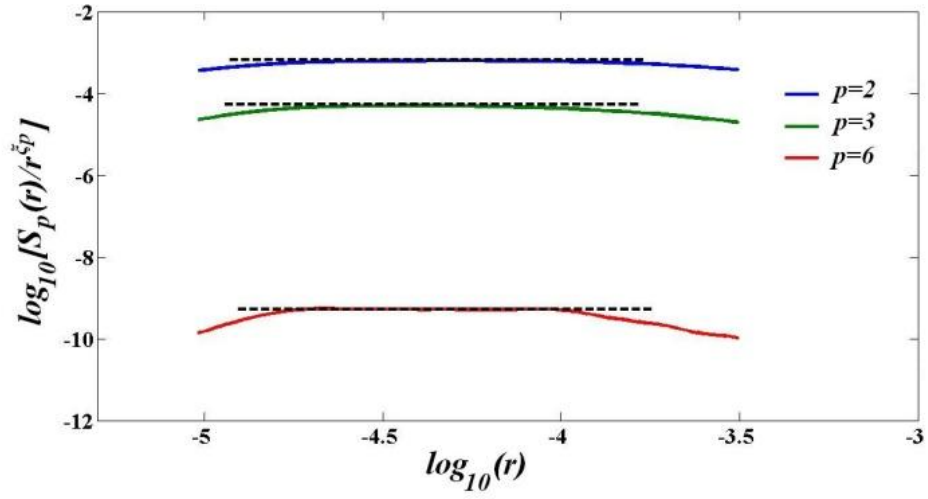

(a)

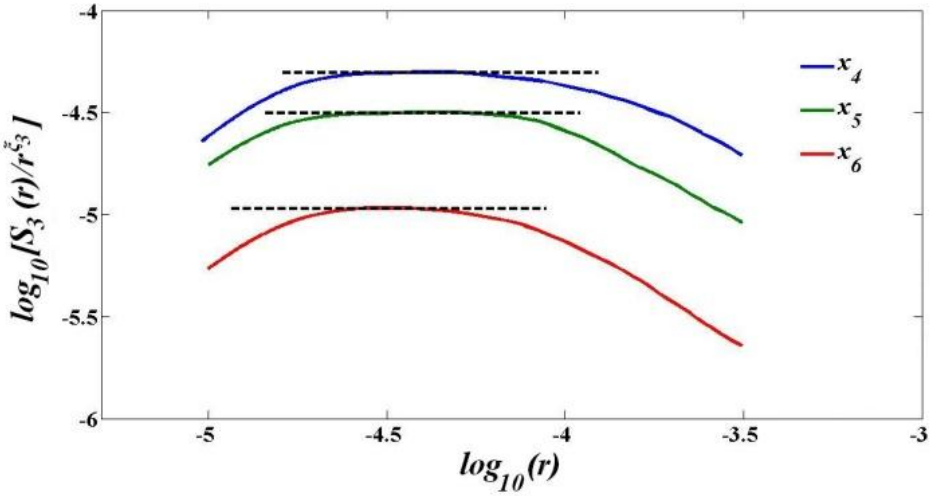

(b)

Figure 2.32 (a) $S_p(r)$ vs r at x=100 μm; (b) $S_3(r)$ vs r at three different positions. x_4=100 μm, x_5=200 μm and x_6=300 μm.

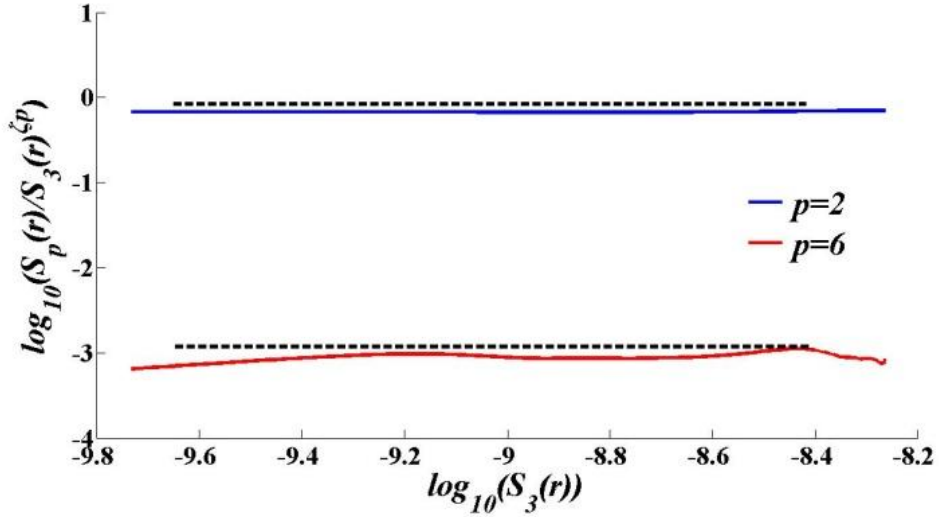

Figure 2.33 ESS relation at x=100 μm

The scaling behavior has an apparent degenerating along the streamwise position after x = 200 μm. However, the ESS of velocity structures exhibits much longer self-similarity region, as it shows in macroscale flow field. As shown in Figure 2.33, at x = 100 μm, the ESS can sustain from large scale (approximate channel depth, the larger one compared to channel width) to small scale (cut-off scale). The inertial subrange due to ESS frame has almost double decades of the K41 law.

Table 2.1 Scaling exponents in inertial subrange of electrically driven turbulent flow at two different streamwise positions. x_4 = 100 μm and x_5 = 200 μm.

p	ξ_p		ζ_p		*K41*	*Benzi, 1996*		
						Hydrodynamic turbulence	*MHD*	*RB convection*
	x_4	x_5	x_4	x_5	ξ_p	$\xi_p(\zeta_p)$	ζ_p	ζ_p
1	0.352	0.342	0.345	0.36	0.333	0.37	0.37	0.37
2	0.637	0.697	0.665	0.7	0.667	0.7	0.7	0.7
3	1.015	1.007	1	1	1	1	1	1
4	1.254	1.31	1.27	1.26	1.333	1.28	1.28	1.28
5	1.475	1.56	1.49	1.5	1.667	1.54	1.54	1.54
6	1.62	1.777	1.56	1.71	2	1.78	1.78	1.78

The scaling exponents in inertial subrange are listed in Table 2.1 and compared to the classical theories and measurements at different type of turbulence. As the number of samples is $1.15*10^6$, a reliable calculation of scaling exponent can reach up to 6^{th} order. It

can be seen, at x = 100 μm, the intermittency factor ($\mu = 2 - \xi_6$) is apparently larger than that at x = 200 μm and the high Re measurements. The statistics at the position should have larger departure from Gaussian process. After 100 μm, as measured at x = 200 μm, the flow becomes more comparable with the high Re turbulence. Both the scaling exponents of self-similarity and ESS are consistent with the Benzi's measurements (Benzi et al. 1996). This is an astonishing result that traditionally believe no turbulence can exist in low Re microchannel flow. It is also the first time of discovering this kind of self-similarity in microfluidics.

The intermittency factor of most singular structures—β

The higher intermittency at x = 100 μm exhibits kinder of difference from the traditional turbulence and the most important characteristics—hierarchical structures. In the investigation on hierarchical structures, the intermittency factor of most singular structures— β (She, Leveque, 1994) is very important on describing the cascading hierarchical structures.

The intermittency factor β is calculated by the so-called *β-test* (She et al. 2001), as below:

$$H_{p+1,m+1}(l) = H_{p,m}(l)^{\beta} \tag{2.60}$$

where $H_{p,m}(l) = \frac{F_p(l)}{F_m(l)} \frac{F_m(l_0)}{F_p(l_0)}$ and $F_p(l) = S_{p+1}(l)/S_p(l)$, $S_p(l) = \langle |u(x+l) - u(x)|^p \rangle = \langle |\Delta u(l)|^p \rangle$. l_0 is a reference scale which is the upper limit of inertial subrange here. (Note: in this flow, the upper bound of scale of inertial subrange is not integral length

anymore, but some other scales which has not been determined yet.) In SL94 model, β should be between 0 and 1. And the dissipation structure has a hierarchical expression as (She and Leveque 1994):

$$\varepsilon_l^{(p+1)} = A_p \varepsilon_l^{(p)^\beta} \varepsilon_l^{(\infty)^{1-\beta}} \tag{2.61}$$

where $\varepsilon_l^{(p)} = \langle \varepsilon_l^{p+1} \rangle / \langle \varepsilon_l^p \rangle$ and $\varepsilon_l^{(\infty)} \sim l^{-2/3}$ is the most intermittent structure in hydrodynamic turbulence.

However, from Figure 2.34, it can be seen the averaged value of β is around 1.1 at x = 100 μm and 1.2 at x = 200 μm. Both of them are larger than the value in homogeneous and isotropic turbulence (about $(2/3)^{1/3} \approx 0.87$) and in magnetohydrodynamic turbulence (between $(1/2)^{1/4}$ and 1). They are both larger than 1 which is the upper bound of β in SL94 model, no matter at x = 100 μm or x = 200 μm. This indicates the original hypothesis of SL94 model is not totally valid in this electrically driven microscale turbulent flow.

Plotting equation (2.60) by log-log curve, we do find there exist a linear region and its slope is related to β. This indicates the hierarchical structures advanced by She and Leveque (1994) have similarity. But, the successive dissipation structures, i.e. $\varepsilon_l^{(p)}$, does not monotonically increase with p, but in a reverse way. The most intermittent structures in this flow is doubtable to be $\varepsilon_l^{(\infty)}$ any more. If a monotonic behavior is still present, the most singular structure should be determined by $\varepsilon_l^{(0)}$, instead of $\varepsilon_l^{(\infty)}$.

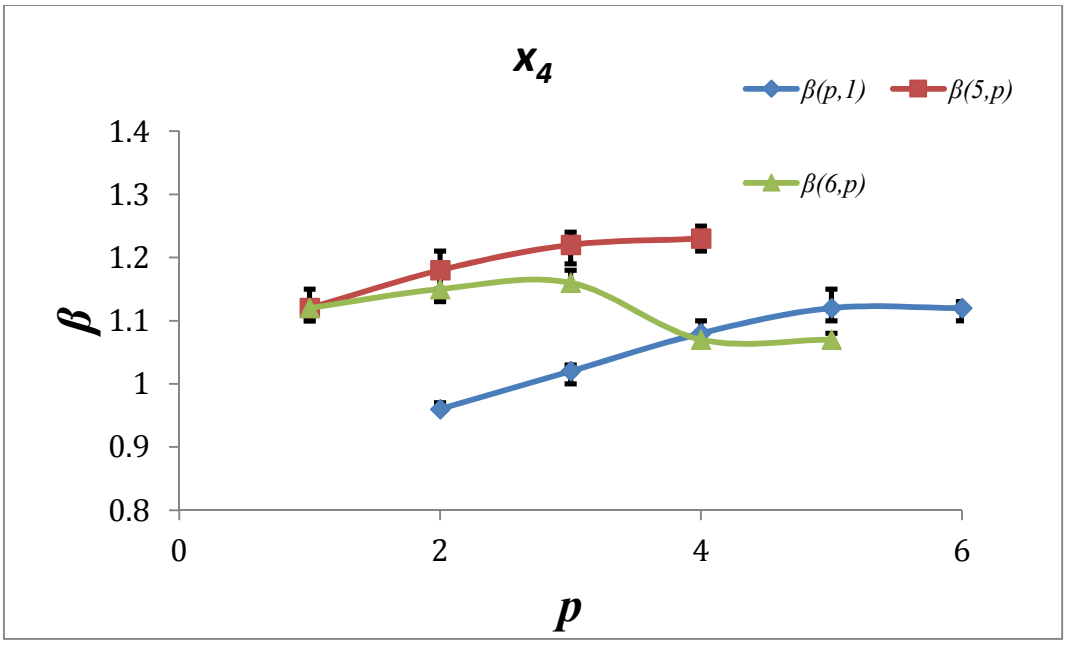

(a)

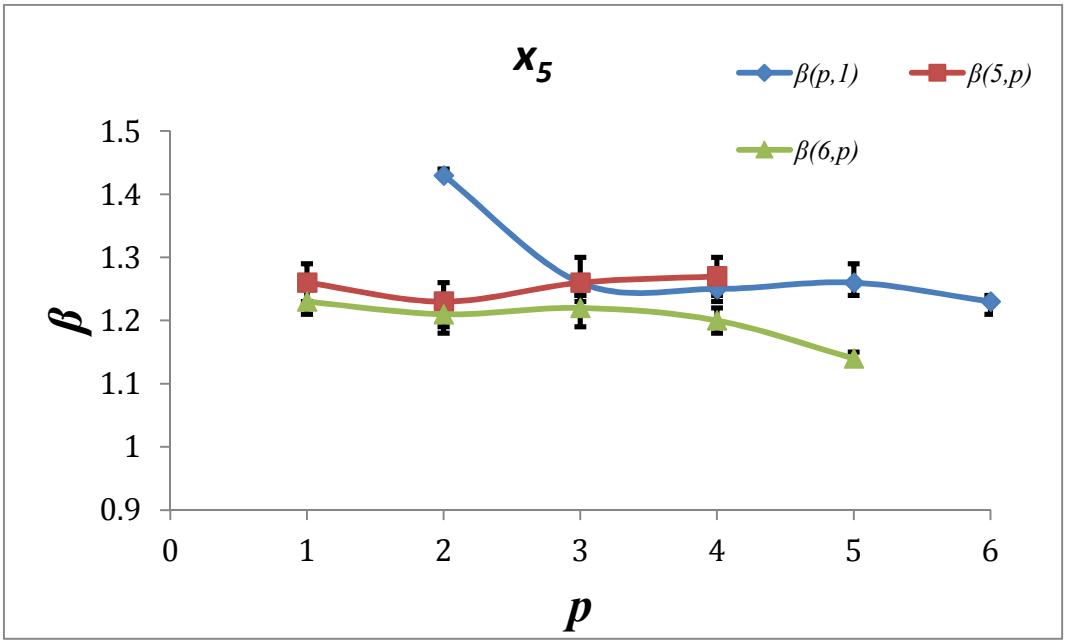

(b)

Figure 2.34 The intermittency factor β calculated from hierarchical structures at different conditions, (a) x_4=100 μm, (b) x_5=200 μm.

Similar as what has been done by She (She and Leveque 1994) and Politano (Politano and Pouquet 1995), we hypothesize:

$$\varepsilon_l^{(0)} \sim {u_l}^2/t_l$$

Where $u_l{}^2 \sim l^\delta$ is the energy input by electric body force on spatial scale l, and the time scale:

$$t_l \sim l^\alpha \ (\alpha > 0)$$

Compared to the high Re number hydrodynamic turbulence or magnetohydrodynamic (MHD) turbulence, the electrically driven turbulent flow in microscale flow field has an apparent difference: the existence of conductivity gradients and more scales of scalar structures due to large Schimdt number (Sc). This means the energy input by electric body force will be effective for all the scale range, from large scale to dissipation subrange. (Here, we tried to avoid equivalent the large scale to the integral scale as what is always done in hydrodynamic turbulence. This is because the integral scale in EK turbulence is not that "large" any more and even comparable with the conventional Kolmogorov scale. The range of inertial subrange seems to be not determined by the integral scale, but something else, which is still under investigation.)

2.6.2 Flatness, skewness and universal law

The control equation of kinetic energy

The control equation of turbulent energy in EK flow actually depends on the frequency of AC electric field.

(1) When the frequency of AC electric field is much higher than the cut-off frequency of velocity fluctuations, we have:

$$\rho\left[\frac{\partial\bar{k}}{\partial t}+\overline{(\boldsymbol{U}\cdot\nabla)k}+\overline{(\boldsymbol{u'}\cdot\nabla)k}+\overline{\boldsymbol{u}'\cdot(\boldsymbol{u'}\cdot\nabla)\boldsymbol{U}}\right]=\overline{-\boldsymbol{u}'\cdot\nabla p'}+\mu\nabla^2\bar{k}-2\mu\bar{\Omega}+$$

$$\overline{\boldsymbol{u}'\cdot\overline{\overline{(\nabla\varepsilon'\cdot\boldsymbol{E}_{\boldsymbol{h}}')\boldsymbol{E}_{\boldsymbol{h}}'}}}+\overline{\boldsymbol{u}'\cdot(\nabla\varepsilon'\cdot\boldsymbol{E}_{\boldsymbol{l}}')\boldsymbol{E}_{\boldsymbol{l}}'}+\overline{\boldsymbol{u}'\cdot(\nabla\bar{\varepsilon}\cdot\boldsymbol{E}_{\boldsymbol{l}}')\boldsymbol{E}_{\boldsymbol{l}}'}+\overline{\varepsilon'\boldsymbol{u}'}\cdot\overline{\overline{(\nabla\cdot\boldsymbol{E}_{\boldsymbol{h}}')\boldsymbol{E}_{\boldsymbol{h}}'}}+$$

$$\overline{\varepsilon'\boldsymbol{u}'\cdot(\nabla\cdot\boldsymbol{E}_{\boldsymbol{l}}')\boldsymbol{E}_{\boldsymbol{l}}'}+\bar{\varepsilon}\overline{\boldsymbol{u}'\cdot(\nabla\cdot\boldsymbol{E}_{\boldsymbol{l}}')\boldsymbol{E}_{\boldsymbol{l}}'}-\frac{1}{2}\left[\overline{\boldsymbol{u}'\cdot\left(\overline{\boldsymbol{E}_{\boldsymbol{h}}'\cdot\boldsymbol{E}_{\boldsymbol{h}}'}\right)\nabla\varepsilon'}+\overline{\boldsymbol{u}'\cdot(\boldsymbol{E}_{\boldsymbol{l}}'\cdot\boldsymbol{E}_{\boldsymbol{l}}')\nabla\varepsilon'}+\right.$$

$$\left.\overline{\boldsymbol{u}'\cdot(\boldsymbol{E}_{\boldsymbol{l}}'\cdot\boldsymbol{E}_{\boldsymbol{l}}')}\nabla\bar{\varepsilon}\right] \tag{2.62}$$

where $\boldsymbol{u}=\boldsymbol{u}'+\boldsymbol{U},\ \boldsymbol{E}=\boldsymbol{E}'+\bar{\boldsymbol{E}},\ \boldsymbol{E}'=\boldsymbol{E}_{\boldsymbol{h}}'+\boldsymbol{E}_{\boldsymbol{l}}',\ p=p'+P,\ \varepsilon=\varepsilon'+\bar{\varepsilon},\ \bar{\boldsymbol{E}}=\boldsymbol{0},\ k=\boldsymbol{u}'\cdot\boldsymbol{u}'/2$ is the kinetic energy and $\Omega=\frac{1}{2}\boldsymbol{\omega}'\cdot\boldsymbol{\omega}'$ is the enstropy and $\boldsymbol{\omega}'=\nabla\times\boldsymbol{u}'$ is the vorticity of velocity fluctuations. In the equation, two different temporal averaging methods are used. One is short time averaging ($\bar{\bar{\cdot}}$), i.e. averaging for high frequency components. The other is the ensemble averaging ($\bar{\cdot}$) for low frequency components.

(a) In the case where the changing of electric field due to the changing of conductivity distribution is much smaller than the influence of AC electric field, and the temperature effect is not neglectable, we have:

$$\overline{\boldsymbol{E}_{\boldsymbol{l}}'\cdot\boldsymbol{E}_{\boldsymbol{l}}'}\ll\overline{\overline{\boldsymbol{E}_{\boldsymbol{h}}'\cdot\boldsymbol{E}_{\boldsymbol{h}}'}}\ \text{ and }\ \nabla\bar{\varepsilon}\ll\nabla\varepsilon'$$

Then, equation (2.62) becomes:

$$\rho\left[\frac{\partial\bar{k}}{\partial t}+\overline{(\boldsymbol{U}\cdot\nabla)k}+\overline{(\boldsymbol{u}'\cdot\nabla)k}+\overline{\boldsymbol{u}'\cdot(\boldsymbol{u}'\cdot\nabla)\boldsymbol{U}}\right]=\overline{-\boldsymbol{u}'\cdot\nabla p'}+\mu\nabla^2\bar{k}-2\mu\bar{\Omega}$$

$$+\overline{\boldsymbol{u}'\cdot\overline{\overline{(\nabla\varepsilon'\cdot\boldsymbol{E}_{\boldsymbol{h}}')\boldsymbol{E}_{\boldsymbol{h}}'}}}+\overline{\varepsilon'\boldsymbol{u}'}\cdot\overline{\overline{(\nabla\cdot\boldsymbol{E}_{\boldsymbol{h}}')\boldsymbol{E}_{\boldsymbol{h}}'}}-\frac{1}{2}\overline{\boldsymbol{u}'\cdot\left(\overline{\boldsymbol{E}_{\boldsymbol{h}}'\cdot\boldsymbol{E}_{\boldsymbol{h}}'}\right)\nabla\varepsilon'} \tag{2.63}$$

As

$$\overline{\boldsymbol{u}'\cdot\left(\overline{\boldsymbol{E}_{\boldsymbol{h}}'\cdot\boldsymbol{E}_{\boldsymbol{h}}'}\right)\nabla\varepsilon'}=\overline{2\boldsymbol{u}'\cdot\nabla\Pi'}-\overline{\boldsymbol{u}'\varepsilon'}\cdot\nabla\overline{(\boldsymbol{E}_{\boldsymbol{h}}'\cdot\boldsymbol{E}_{\boldsymbol{h}}')}$$

where Π is the fluctuating energy density of electric field (Griffiths 2007) on the time scale of ε', i.e. low frequency. It has the expression:

$$\Pi' = \frac{1}{2}\varepsilon'\overline{\overline{\boldsymbol{E}\cdot\boldsymbol{E}}} \approx \frac{1}{2}\varepsilon'\overline{\overline{\boldsymbol{E}_{\boldsymbol{h}}'\cdot\boldsymbol{E}_{\boldsymbol{h}}'}}$$

Also $\overline{\overline{\boldsymbol{E}_{\boldsymbol{h}}'\cdot\boldsymbol{E}_{\boldsymbol{h}}'}} = \overline{\boldsymbol{E}_{\boldsymbol{h}}'\cdot\boldsymbol{E}_{\boldsymbol{h}}'}$. Then,

$$\rho\left[\frac{\partial\bar{k}}{\partial t} + \overline{(\boldsymbol{U}\cdot\nabla)k} + \overline{(\boldsymbol{u}'\cdot\nabla)k} + \overline{\boldsymbol{u}'\cdot(\boldsymbol{u}'\cdot\nabla)\boldsymbol{U}}\right] = \overline{-\boldsymbol{u}'\cdot\nabla p'} + \mu\nabla^2\bar{k} - 2\mu\bar{\Omega} -$$

$$\overline{\boldsymbol{u}'\cdot\nabla\Pi'} + \overline{\boldsymbol{u}'\cdot\overline{\overline{(\nabla\varepsilon'\cdot\boldsymbol{E}_{\boldsymbol{h}}')\boldsymbol{E}_{\boldsymbol{h}}'}}} + \overline{\varepsilon'\boldsymbol{u}'}\cdot\overline{(\nabla\cdot\boldsymbol{E}_{\boldsymbol{h}}')\boldsymbol{E}_{\boldsymbol{h}}'} + \frac{1}{2}\overline{\boldsymbol{u}'\varepsilon'}\cdot\nabla\overline{(\boldsymbol{E}_{\boldsymbol{h}}'\cdot\boldsymbol{E}_{\boldsymbol{h}}')} \qquad (2.64)$$

If there exists steady state, equation (2.64) can also be written as:

$$\rho\left[\overline{(\boldsymbol{U}\cdot\nabla)k} + \overline{(\boldsymbol{u}'\cdot\nabla)k} + \overline{\boldsymbol{u}'\cdot(\boldsymbol{u}'\cdot\nabla)\boldsymbol{U}}\right] = \overline{-\boldsymbol{u}'\cdot\nabla p'} + \mu\nabla^2\bar{k} - 2\mu\bar{\Omega} - \overline{\boldsymbol{u}'\cdot\nabla\Pi'} +$$

$$\overline{\boldsymbol{u}'\cdot\overline{\overline{(\nabla\varepsilon'\cdot\boldsymbol{E}_{\boldsymbol{h}}')\boldsymbol{E}_{\boldsymbol{h}}'}}} + \overline{\varepsilon'\boldsymbol{u}'}\cdot\overline{\overline{(\nabla\cdot\boldsymbol{E}_{\boldsymbol{h}}')\boldsymbol{E}_{\boldsymbol{h}}'}} + \frac{1}{2}\overline{\boldsymbol{u}'\varepsilon'}\cdot\nabla\overline{(\boldsymbol{E}_{\boldsymbol{h}}'\cdot\boldsymbol{E}_{\boldsymbol{h}}')} \qquad (2.65)$$

In equation (2.65), compared to the conventional hydrodynamic turbulence, there are 4 more terms, which are:

- $\overline{\boldsymbol{u}'\cdot\nabla\Pi'}$: the transport of electric field energy
- $\overline{\boldsymbol{u}'\cdot\overline{\overline{(\nabla\varepsilon'\cdot\boldsymbol{E}_{\boldsymbol{h}}')\boldsymbol{E}_{\boldsymbol{h}}'}}}$: Coulomb force due to the permittivity gradient (results from temperature gradient)
- $\overline{\varepsilon'\boldsymbol{u}'}\cdot\overline{\overline{(\nabla\cdot\boldsymbol{E}_{\boldsymbol{h}}')\boldsymbol{E}_{\boldsymbol{h}}'}}$: Coulomb force due to local net change
- $\frac{1}{2}\overline{\boldsymbol{u}'\varepsilon'}\cdot\nabla\overline{(\boldsymbol{E}_{\boldsymbol{h}}'\cdot\boldsymbol{E}_{\boldsymbol{h}}')}$: This term has the same expression as dielectrophoresis (DEP) effect

These terms indirectly indicate the influence of high frequency AC electric field on velocity fluctuations which are at low frequency, especially the fourth term which is successfully used to describe the particle motion in AC electric field under DEP. The equation (2.65) can help us indirectly understand why we use 100 kHz AC electric field, but the velocity response is below 2 kHz.

For more details, please read section A10.

(2) When the forcing frequency is smaller than the cut-off frequency of velocity fluctuations, we have another expression as:

$$\rho\left[\frac{\partial \bar{k}}{\partial t}+\overline{(\boldsymbol{U}\cdot\nabla)k}+\overline{(\boldsymbol{u'}\cdot\nabla)k}+\overline{\boldsymbol{u}'\cdot(\boldsymbol{u'}\cdot\nabla)\boldsymbol{U}}\right]=\overline{-\boldsymbol{u}'\cdot\nabla p'}+\mu\nabla^2\bar{k}-2\mu\bar{\Omega}+$$

$$\overline{\boldsymbol{u}'\cdot\left(\nabla\varepsilon\cdot\boldsymbol{E}_l'\right)\boldsymbol{E}_l'}+\overline{\varepsilon\boldsymbol{u}'\cdot\left(\nabla\cdot\boldsymbol{E}_l'\right)\boldsymbol{E}_l'}-\frac{1}{2}\overline{\boldsymbol{u}'\cdot\left(\boldsymbol{E}_l'\cdot\boldsymbol{E}_l'\right)\nabla\varepsilon} \qquad (2.66)$$

In this case, the velocity fluctuations have strong correlation with the electric field disturbance. In other words, the electric body force will vary with velocity fluctuations and show kinder of consistency. Recently, it's difficult to predict how strong the correlation is. Also, the contribution of each term is hard to distinguish.

From both cases, we can see compared to the conventional turbulent energy equation without forcing, the energy equation of EK turbulence has more terms and complicated relations between electric field, conductivity and flow field. These cause many interesting phenomena which will be introduced below.

The evolution of kinetic energy and energy dissipation

Under the strong AC electric field, the initially laminar flow experiences a sudden transition process which is accomplished in only 100 μm distance from the entrance. This can be viewed from the turbulent kinetic energy ($T_e = \overline{u_m'^2}$, where $u_m' = u_m - \overline{u_m}$) evolution in streamwise direction as shown in Figure 2.35.

At the beginning, the turbulent energy exhibits extremely fast increasing. From undisturbed region (x = -10 μm) to strongest disturbance region (x = 10 μm), it only cost 15μm spatial distance (or 7.5 ms time scale if estimated by bulk flow velocity). After increasing to a peak value, the turbulent energy first experiences a fast damping until x = 100 μm. Then decrease slowly downstream. In this short progress from x=-10 μm to 100 μm, continuous and multiscale flow structures have been developed. This cannot be realized in traditional turbulence and the AC electric field should play a very important role in the evolution process. Accompanied with the fast turbulent kinetic energy variation is the fast turbulent energy dissipation rate (ε_u) evolution. The calculation of ε_u can be expressed as:

$$\varepsilon_u = 15\nu \left\langle \left(\frac{du_m'}{dx}\right)^2 \right\rangle \approx \frac{15\nu}{U_b^2} \left\langle \left(\frac{du_m'}{dt}\right)^2 \right\rangle$$

Here homogeneous and isotropic (HI) hypothesis of turbulence is adopted for simplification without lost of generality. The hypothesis will cause error, but won't lead to the error of quantity order. In Figure 2.36 (ε_u variation in x direction), similar as the T_e, ε_u also increases from x=-10 μm to 10 μm and then decreases in x direction. However, the

kinetic energy variation ΔT_e cannot be simply balanced by the dissipation terms $\Delta T_{e,\varepsilon}(x_i)$ at considered streamwise positions, i.e. $\Delta T_{e,\varepsilon}(x_i) \neq \Delta T_e$, where:

$$\Delta T_{e,\varepsilon}(x_i) = \frac{[\varepsilon(x_i)+\varepsilon(x_{i+1})](x_{i+1}-x_i)}{2U_b} \text{ and } \Delta T_e(x_i) = T_e(x_{i+1}) - T_e(x_i)$$

"i" is the indices of streamwise position and i=3 to 6. The estimated kinetic energy changing due to ε_u, i.e. $\Delta T_{e,\varepsilon}$, is about 4 orders larger than ΔT_e, as shown in Figure 2.37 (ΔT_e vs energy dissipation. This implies two possible reasons: (1) the dissipation is directly balanced with works of electric body force at small scales; (2) Continuous energy input from electric body force at large scales.

Actually, from our introduction in section 2.5.5 and the control equation of kinetic energy, we can see both of the reasons are present in the flow.

First, the electric body force is strong enough to affect small scale velocity fluctuations, as shown in section 2.5.5. The electric body force is directly balanced by the viscous force and in turn generates a strong virtual energy dissipation rate. Because this portion of energy is not cascading from large scale to small scale, the turbulent energy calculated from velocity fluctuations is significantly smaller than expected.

Second, for the conductivity, as there is no new solutions with different conductivities injected downstream, the variance of conductivity becomes smaller and smaller. The velocity fluctuations generated by electric body force is too weak to support the flow. This can also cause the big difference between $\Delta T_{e,\varepsilon}$ and ΔT_e.

Third, compared to the conventional hydrodynamic turbulence, in the energy equation of EK turbulence, there are four more terms. In these terms, because $\nabla \times \boldsymbol{E_h'} = 0$, $\overline{\varepsilon' \boldsymbol{u}'} \cdot \overline{(\nabla \cdot \boldsymbol{E_h'})\boldsymbol{E_h'}} = \frac{1}{2}\overline{\varepsilon' \boldsymbol{u}'} \cdot \nabla\overline{(\boldsymbol{E_h'} \cdot \boldsymbol{E_h'})} = \overline{\varepsilon' \boldsymbol{u}'} \cdot \nabla(\overline{\boldsymbol{E_h'} \cdot \boldsymbol{E_h'}})$.

Hence,

$$\overline{\varepsilon' \boldsymbol{u}'} \cdot \overline{(\nabla \cdot \boldsymbol{E_h'})\boldsymbol{E_h'}} + \frac{1}{2}\overline{\boldsymbol{u}'\varepsilon'} \cdot \nabla\overline{(\boldsymbol{E_h'} \cdot \boldsymbol{E_h'})} = \overline{\boldsymbol{u}'\varepsilon'} \cdot \nabla(\overline{\boldsymbol{E_h'} \cdot \boldsymbol{E_h'}})$$

In the low conductivity half plane, $\overline{\boldsymbol{E_h'} \cdot \boldsymbol{E_h'}}$ would decrease downstream. While in the high conductivity half plane, $\overline{\boldsymbol{E_h'} \cdot \boldsymbol{E_h'}}$ would increase downstream. Thus, $\nabla(\overline{\boldsymbol{E_h'} \cdot \boldsymbol{E_h'}})$ has different signs at different y positions. However, the flow itself seems to be symmetric, due to the symmetric boundary conditions and conductivity fluctuations. Hence, we hypothesize $\overline{\varepsilon' \boldsymbol{u}'}$ to be symmetric along centerline. This results in different signs of $\overline{\boldsymbol{u}'\varepsilon'} \cdot \nabla(\overline{\boldsymbol{E_h'} \cdot \boldsymbol{E_h'}})$ at different y positions. In other words, the electric body force sometimes enhances the velocity fluctuations, but in other regions, it inhibit velocity fluctuations. This is another possible reason that the turbulent energy is so small.

Viscous diffusion effect The decreasing of T_e along streamwise direction is not the result of turbulence advection or diffusion, as both of them have been completed before x_3 as can be seen in Figure 2.10(e). In other words, the T_e transport in spanwise direction, no matter by advection or viscous diffusion, is very fast and costs only a few microseconds. This process can be finished even before x_3. The fast decreasing cannot be due to the re-

distribution of T_e in y-direction. Similarly, the possibility of fast variation of T_e by advection of velocity and pressure can be excluded.

Dissipation terms of turbulent kinetic energy Hence, from above discussion, the fast kinetic energy decreasing should be the result of negotiating between electric work terms and energy dissipation due to viscosity. But, the question is, is the electric work only contribute to the production of kinetic energy?

It is clear that in free decaying turbulence, the second order moment of velocity structures—a measure of kinetic energy, can be split into two parts: the large scale parts attributed to kinetic energy and the small scale parts contributed to enstrophy, or finally dissipated. It is similar in the electrically driven turbulent flow.

As known, the effective diffusivity of ions is much smaller than the kinematic viscosity of water. So the scalar structures have more scales than that of velocity structures, as the large Schmidt number. This indicates the electric body force will be also effective at smaller spatial (or equivalent temporal) scales than the inertial effect.

From both the velocity and scalar spectrums, as indicated by Figure 2.26, it can be seen the flow are separated into 3 regions.

The first one locates at low frequency region which is about the large scale energy (or variance) where electric work is transferred to large scale flow structures. The second one is the electric-inertial sub-region which locates in the intermediate range of frequency. Here, the energy of large scale velocity structures will cascade into smaller scales and kinetic

energy will be transferred primarily from large scale velocity structures and secondarily by the work of electric body force. Hence, the scalar and velocity power spectrum have the same slope, almost -5/3. After that, the slopes of both scalar and velocity spectrums become much steeper. The slopes of scalar spectrum and velocity spectrum are both around -6. The latter is consistent with the found in the dissipation region of free decaying turbulence (Saddoughi and Veeravalli 1994). But the Batchelor regime (i.e. -1 slope) is not found in the former. This exhibits a different physical process of dynamics. Also, because in the concentration measurement, we use fluorescent dye as tracer. For the dye molecule, the convection is passive. But as the source of electric body force, the transport of solution with different conductivities should be more like active transport process. Thus, it is still questionable whether the fluorescent dye can follow the conductivity and describe the transport process of fluid particle with different conductivities.

As elucidated previously (about the self-similarity of scalar and velocity), while the mixing becomes homogeneous and the scalar structures has self-similarity, the scaling exponent of velocity structures is smaller than that of scalar. The relation is:

$$|\Delta\sigma(l)| \sim l^{\zeta} \sim |\Delta u(l)|^2$$

Hence, the power spectrum of scalar and velocity can be described as:

$$E_c(k) \sim k^{-2\zeta-1} \text{ and } E_{ue}(k) \sim k^{-\zeta-1}$$

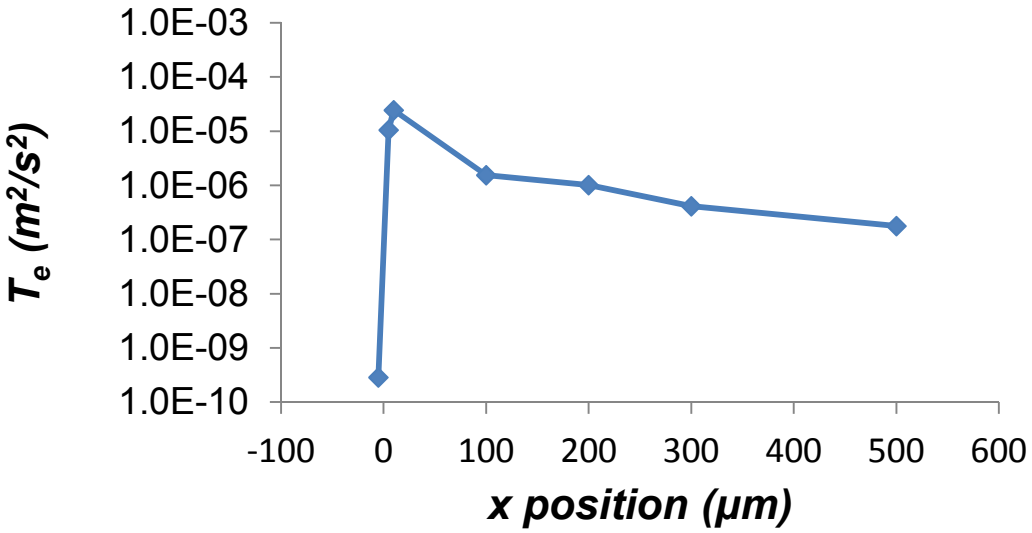

Figure 2.35 Turbulent energy evolution along streamwise direction

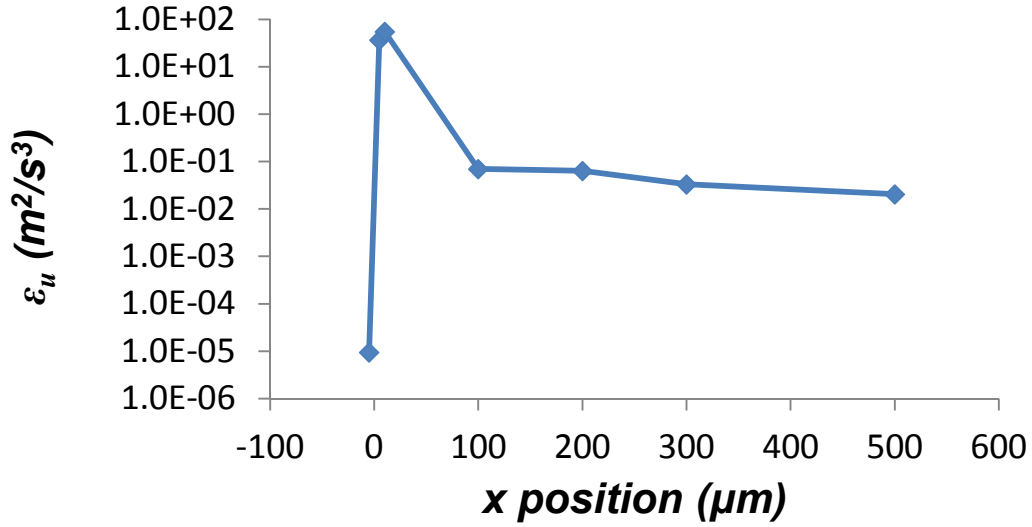

Figure 2.36 Turbulent kinetic energy dissipation rate in x-direction

Estimated from the slope of scalar spectrum, it can be seen ζ=4 and the power spectrum of electrically-driven velocity in the sub-regime is -5, regardless the intermittency of scalar structures. This is consistent to the velocity measurement.

The electrically-driven velocity at small scales will have tremendous contribution to the spectrum of enstrophy, as $E_{ens}(k) = k^2 E_{ue}(k)$. Hence, there exists a balanced scale l_T (or wavenumber k_T). Above l_T, the work of electric body force will contribute to the

kinetic energy. And below it, the electric body force will enhance the dissipation. This is similar as in free decaying turbulence, where the l_T can be roughly estimated by Taylor microscale. However, in μEK turbulence, the determination of l_T is not unique and varies with positions. There is no generalized form as the contribution of electrical body force is hard to evaluate. But, qualitatively, the portion of wavenumber range that related to dissipation should be much larger in electrically-driven turbulent flow than in other hydrodynamic turbulence.

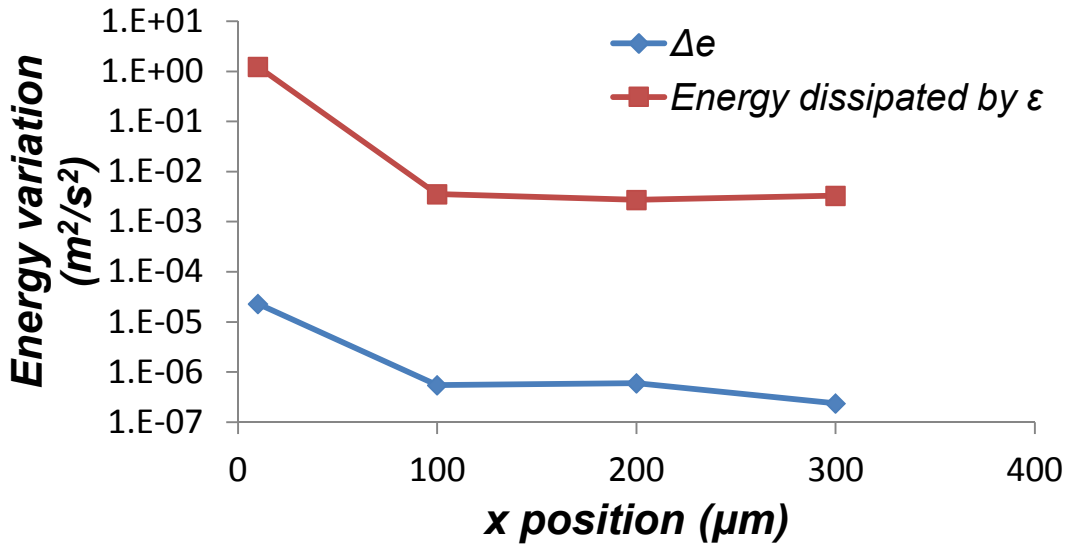

Figure 2.37 The energy variation along x-direction. Δe is directly measured. The red line is estimated by energy dissipation rate ε_u and convection time.

The intermittency and bias along x-direction

The fast transition is not only a simply accumulation of kinetic energy, but also a rapid evolution of flow structures, especially at the small scale where intermittency becomes important. This can be easily found from the streamwise variation of flatness factor (Figure 2.38), which is defined as below:

$$F_n = \langle (du'_m/dx)^4 \rangle / \langle (du'_m/dx)^2 \rangle^2 = \langle (du'_m/dt)^4 \rangle / \langle (du'_m/dt)^2 \rangle^2 \qquad (2.67)$$

At x = -10 μm, where only -10 μm from inlet, the flatness of velocity gradient is 3. This indicates the velocity gradient we measured has Gaussian distribution and the small scale signal fluctuations are the result of multiple source of noise, such as background noise (light noise or temperature noise) and a small portion of shot noise. The flow here is weakly or even not affected by the electric field. Then, about 15μm downstream from x = -10 μm, the flow exhibits strong small-scale intermittency. The intermittency reaches the peak at x = 10 μm. The value of flatness is about 14 which is only reached in high Re turbulence (Tabeling et al. 1996). After that, F_n decreases to 4 rapidly and keep decreasing to about 3 at far downstream from entrance.

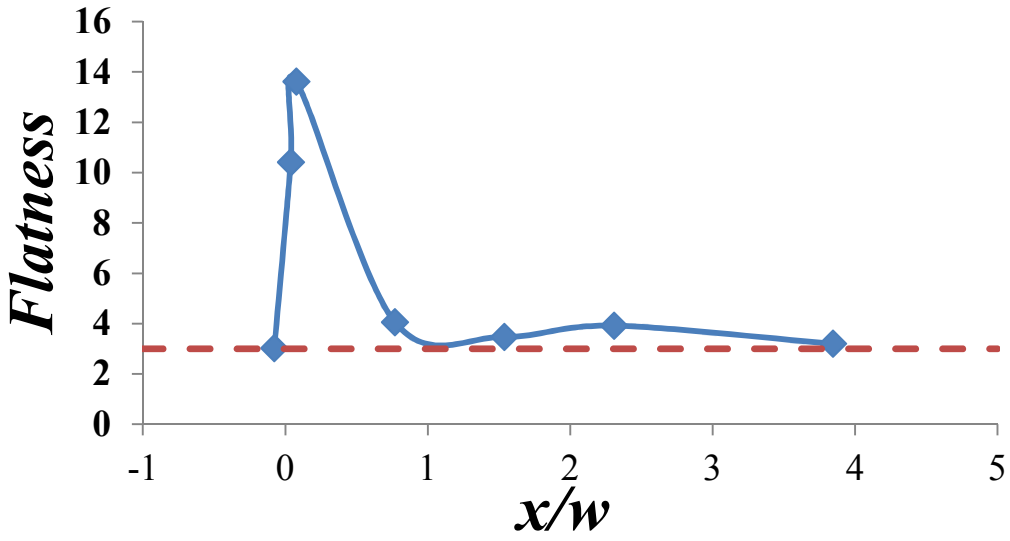

Figure 2.38 F_n along x-direction

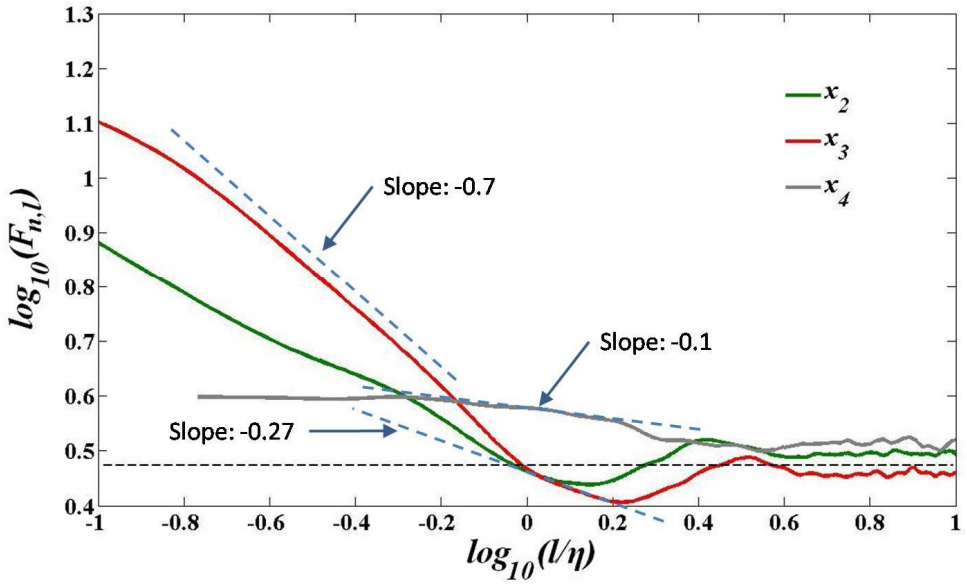

Figure 2.39 Flatness factors of velocity structures at different spatial intervals. x_2=5 μm, x_3=10 μm, x_4=100 μm.

The fast variation of F_n indicates the changing of flow structures. This can be investigated by the flatness of velocity structures on scale l at different streamwise positions, i.e.:

$$F_{n,l} = \frac{\langle \Delta u'_m(l)^4 \rangle}{\langle \Delta u'_m(l)^2 \rangle^2} \tag{2.68}$$

where $\Delta u'_m(l) = u'_m(x+l) - u'_m(x)$. At x=5 μm, where the flow is experiencing the transition from laminar to turbulence, there is no inertial range ($F_{n,l}$ displays a power-law relation with l as $F_{n,l} \sim l^{\zeta_F}$) can be found above l/η=1. However, at x=10 μm, a short but clear linear region can be found, with a slope of m_f=-0.27. The steeper slope indicates a stronger departure from K41 scaling law. Accompanied is the smaller F_n compared to 3 which is corresponding to Gaussian process. In this region, the velocity structures are smoother than at both larger and smaller scales. The randomness is inhibited and flow

exhibits organization under electric field. We believe this region is the major range of energy input due to the work of electric body force at this streamwise positions. Furthermore, at smaller spatial scales, where is called near-dissipation range, a more negative slope can be found which is agree with Chevillard's argument (Chevillard et al. 2005). However, in our case, the mf in near-dissipation range is about -0.7 which is also much steeper than in Chevillard's work.

Relative to the large difference of slope, the ratio of their slopes in dissipation range to inertial range is very close. In our case, the ratio is about 2.6. While in Chevillard's paper (Chevillard et al. 2005), it is estimated to be around 2.8. Since the slope itself indicates the multifractal structures in the scale range, and the ratio implies the transfer process of multifractal structures in different scale ranges, the flow at x=10 μm has similar behavior transiting from inertial to dissipation range.

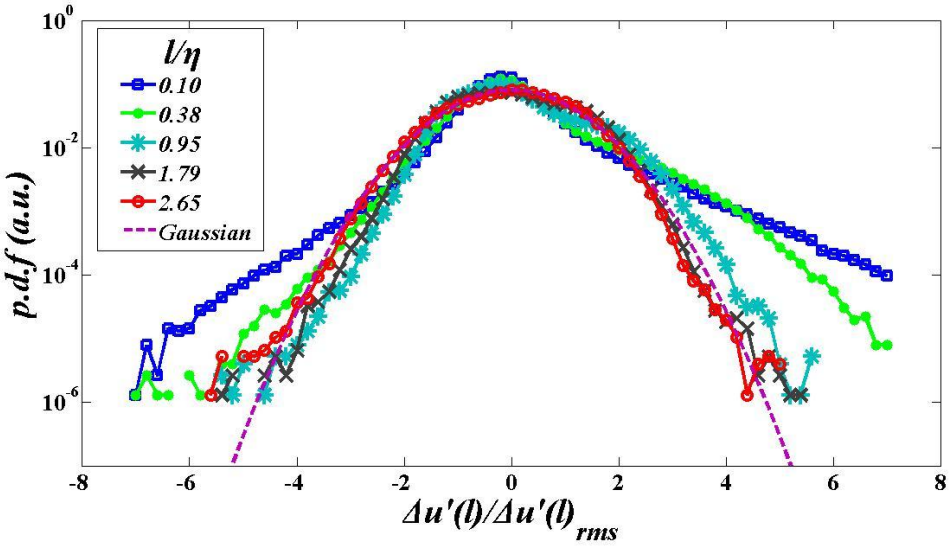

Figure 2.40 The PDF of velocity increment of differnet spatial intervals at x=10 μm

At x=100 μm, the m_f of inertial range is further reduced to -0.1 which is perfectly consistent with the hydrodynamic turbulence. From the power spectrum, a long and -5/3 slope is also found which fits Kolmogorov -5/3 law very well. The flow exhibits a typical character of turbulence. Unfortunately, F_n in dissipation subrange has apparently different with the hydrodynamic turbulence. It is saturated at relatively larger l/η, compared to that of x=10 μm. The mechanism of changing of dissipation range from x=10 μm to 100 μm is still unknown. One of the possible explanations is the velocity accompanied with conductivity structures exhibit kinder of similarity where the electric body force dominates.

The variation of F_n is consistent with what we found in probability density function (PDF) as shown in Figure 2.19(b). At x=10 μm, a representatively exponential tail can be found. At downstream, the departure from Gaussian distribution becomes smaller. This intermittency is dominated by small scale velocity structures, not large one, as established in Figure 2.40. Here, the PDF of velocity structures of different scales ($P[\Delta u'_m(l)]$) at x=10 μm is plotted. It can be seen, as the spatial scale increases, the PDF becomes closer to Gaussian distribution and the intermittency becomes smaller. However, this variation is not a simple approximation process. The PDF first becomes narrower till $l/\eta=1.79$ where the PDF is even sharper than Gaussian distribution. Then recover at larger scales. In the positive half side of PDF curve, additional one inflection point can be found which indicates the correction of asymmetric physical process. This recovery process is not found in hydrodynamic turbulence. We believe, the narrower PDF that causes the low $F_{n,l}$ should be due to the electric modulation.

In this process, the apparently asymmetric distribution is slowly diminished, both in streamwise direction and spatial scales, which can be easily found by the skewness factors S_n as below:

$$S_n = \frac{\langle (du'/dx)^3 \rangle}{\langle (du'/dx)^2 \rangle^{3/2}} \tag{2.69}$$

From Figure 2.41, it can be seen there is a large S_n at x=10 μm which is even more than 1. And before x/w=2, the skewness factors are all positive. This is consistent with the found in turbulent dissipation range (Chevillard et al. 2006). Be aware, the bias is not due to the undistinguished sign of velocity, as S_n is determined by the small scale velocity structures which will not be affected by the uncertainty of measurement of large structures.

The variation of S_n is also due to small scale structures, as elucidated by the $S_{n,l}$:

$$S_{n,l} = \langle \Delta u'_m(l)^3 \rangle / \langle \Delta u'_m(l)^2 \rangle^{3/2} \tag{2.70}$$

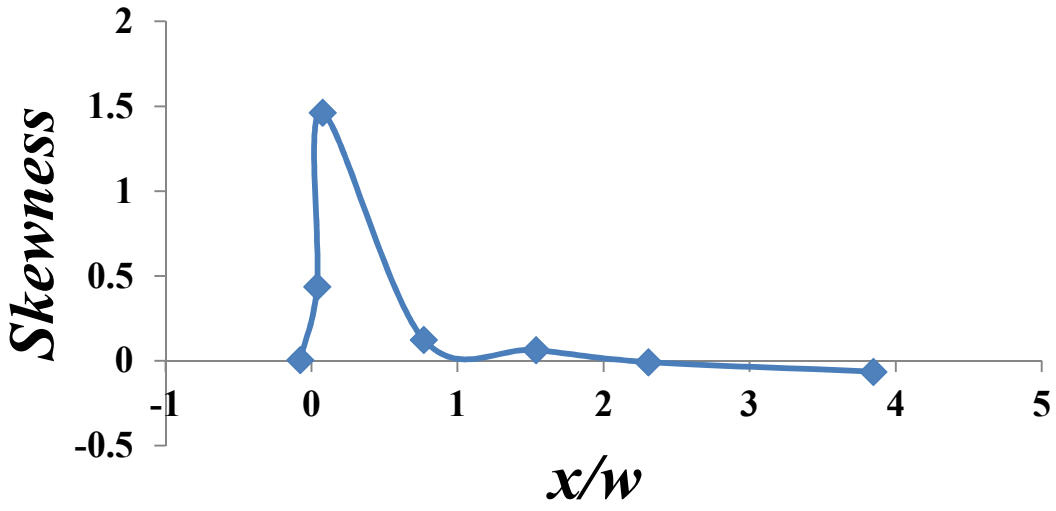

Figure 2.41 Skewness factors along streamwise direction.

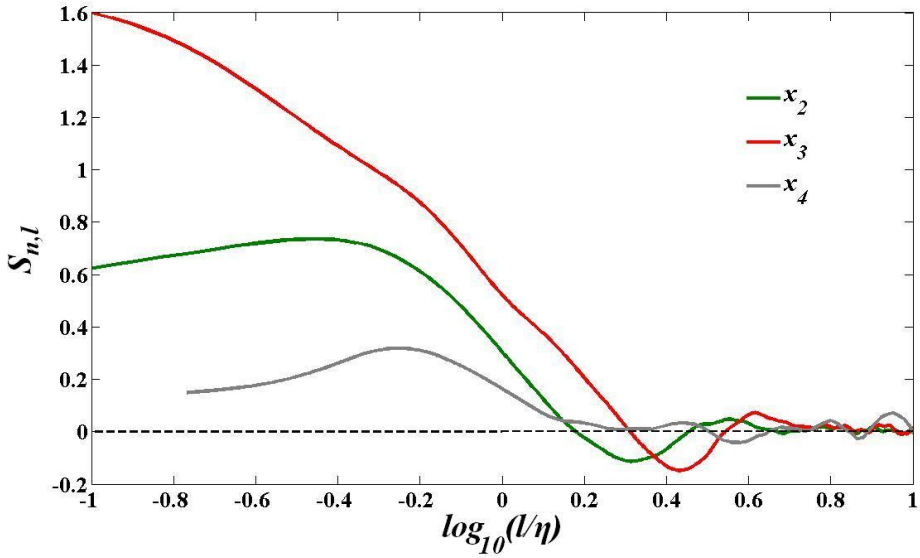

Figure 2.42 Skewness factors vs spatial scales at different streamwise positions. x_2=5 μm, x_3=10 μm, x_4=100 μm.

As plotted in Figure 2.42, in the development region of flow, the scale range of positive $S_{n,l}$ is extended in streamwise locations. Accompanied is the continuously shrinkage of negative range. Normally, in hydrodynamic turbulence, above l/η=1 the skewness factors should be negative, as predicted by Karman-Howarth equation and measured by experiments (Tabeling et al. 1996). And in the dissipation range, the $S_{n,l}$ should be positive with a maximum value of about 0.5 at high Reynolds number. Here, we suppose the Karman-Howarth equation (Davidson 2004) that in homogeneous and isotropic turbulence is still established for our flow, as below:

$$\frac{\partial}{\partial t}[u^2 l^4 f(l,t)] = u^3 \frac{\partial}{\partial r}[l^4 K(l)] + 2\nu u^2 \frac{\partial}{\partial r}[l^4 f'(l)] \tag{2.71}$$

or in the format with velocity structure functions,

$$-\frac{2}{3}l^4\varepsilon - \frac{l^4}{2}\frac{\partial}{\partial t}\langle[\Delta u(l)]^2\rangle = \frac{\partial}{\partial l}\left[\frac{l^4}{6}\langle[\Delta u(l)]^3\rangle\right] - \nu\frac{\partial}{\partial l}\left[l^4\frac{\partial}{\partial l}\langle[\Delta u(l)]^2\rangle\right] \tag{2.72}$$

Neglecting the temporal derivative term and $\langle[\Delta u(l)]^2\rangle \approx \langle \Delta u_m^{'}(l)^2\rangle = Cl^{\zeta}$, $\langle[\Delta u(l)]^3\rangle \approx \langle \Delta u_m^{'}(l)^3\rangle$, $\varepsilon(l) = 15\nu\langle \Delta u_m^{'}(l)^2\rangle l^{-2}$, then the relation between S_n, scale l and scaling exponent ζ in dissipation range can be write into a simple expression:

$$S_{n,l}(\zeta) = \frac{\langle \Delta u_m'(l)^3\rangle}{\langle \Delta u_m'(l)^2\rangle^{\frac{3}{2}}} = 6\left(\zeta - \frac{10}{3+\zeta}\right) l^{-1-\zeta/2} C^{-1/2}\nu \tag{2.73}$$

The critical value of ζ_c when S_n is zero can be easily calculated as 2 (another solution, -5, which means both positive slope of $E(k)$ and $k^2E(k)$ in high wavenumber region, is abandoned due to the convergence of $\langle \Delta u_m^{'}(l)^2\rangle$). Above this value, S_n will be positive. And below it, S_n will be negative. As introduced previously, the slope of $E(k)$ in dissipation range is about -5.8, nearly -6 which means ζ is around 5. Hence, a positive S_n is consistent with our prediction and the high Reynolds number characteristics. From equation (2.73), $S_n \sim l^{-1-\zeta/2}$. However, no such fast decreasing can be found in hydrodynamic turbulence or in this electrically-driven turbulent flow. Chevillard et al tried to explain it with multifractal theory as $\zeta = \zeta(l)$ which is out of scope of this paper. We only want to qualitatively elucidate the existence of high Re characteristics in this low Re flow.

Skewness is an important factor in turbulence which is introduced from Karman-Howarth equation which is well-known in conventional high Re turbulence. However, Karman-Howarth equation is an equation to describe turbulent flow dominated by inertial force, not by external force. Also the sign of skewness is controlled by the 3rd order momentum of velocity structure function. Yakhot {Yakhot, 1992 #832} preliminarily discussed on the 3rd order momentum of velocity structure function in high-Rayleigh-number Bénard convection. In the paper, he found:

$$S_3(l) = -\frac{4}{5}\varepsilon_u l + 6\nu\frac{\partial S_2(l)}{\partial l} + \frac{6}{l^4}\int_0^l l'^4\langle \Delta u(l')\Delta f(l')\rangle dl'$$

where *f* is the external force. From the equation, we can see if no external force, the 3rd order momentum of velocity structure function at small scale l is dominated by $-\frac{4}{5}\varepsilon_u l$ and definitely to be negative. But when *f* exists, such as the F_e in our experiments, $S_3(l)$ may not be negative. As expressed previously, $F_{e,l}$ actually increases with decreased l. This indicates a positive correlation velocity fluctuations and EBF is possible, i.e. $\langle \Delta u(l')\Delta F_e(l')\rangle > 0$. Also, $\langle \Delta u(l')\Delta F_e(l')\rangle \sim l'^{\xi}$, where $\xi < 0$ is a undetermined scaling exponents. At this case, $\frac{6}{l^4}\int_0^l l'^4\langle \Delta u(l')\Delta f(l')\rangle dl' \sim l^{1+\xi}$. The sign of $S_3(l)$ is more significantly affected by the external forcing term, as $\xi < 0$. When $\xi \ll 0$, $S_3(l)$ will become positive even at a large scale. Hence, in EK turbulence, skewness can be positive. This is a character which is different from hydrodynamic turbulence.

Kolmogorov scale and l_{TS}

The variation of S_n along streamwise direction is tightly related to the values of Kolmogorov scale and electric Kolmogorov scale as which determine the range of dissipation subregion. The definition of Kolmogorov scale is as below:

$$\eta = (\nu^3/\varepsilon_u)^{1/4}$$

As the displacement from inlet increasing, η decreases very fast initially and then gradually increases, as shown in Figure 2.43. Relatively, the upper limit of dissipation subregion in wavenumber space, i.e. k_η will increase first and then decrease.

Being noted, after x=10 μm, the calculated η becomes even larger than the values in most hydrodynamic turbulence. The η is also much larger than $l_{TS} = \sqrt{\langle u_m'^2 \rangle / \langle (du_m'/dt)^2 \rangle}/U_b$. Both of these are the characteristics of microscale electrically-driven turbulent flow. It indicates eddies in intermediate wavenumber range, doesn't majorly rely on the energy input from large scale vortex, but dominated by the continuously energy production through electric body force. The commonly used l_{TS} based Reynolds number is not a proper dimensionless parameter to characterize flow.

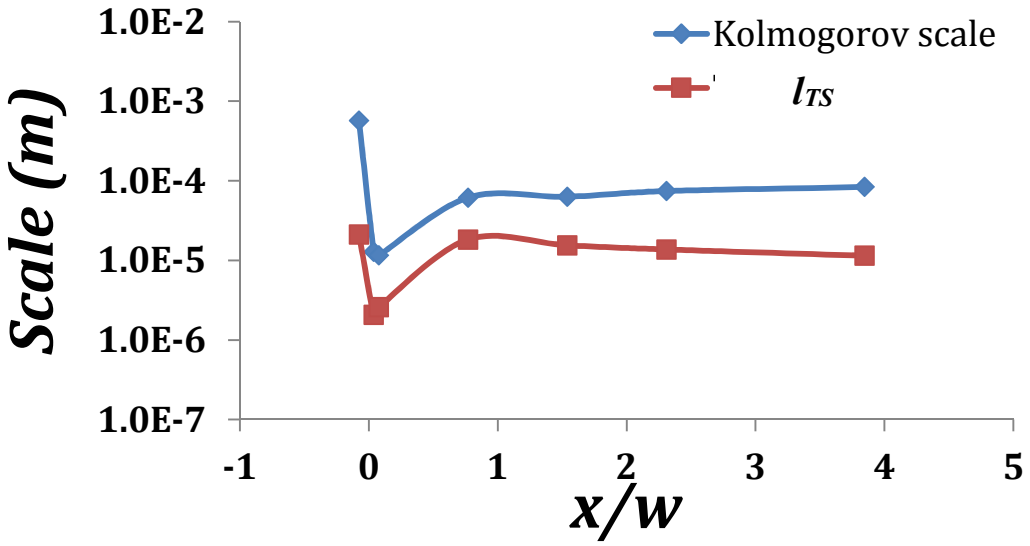

Figure 2.43 Microscales at different streamwise positions

As the flow and the carried conductivity advecting downstream, we can see: (1) the gradient of velocity fluctuations keeps decreasing along streamwise direction. This causes the decreasing of ε_u and increasing of η. (2) the turbulent energy decreases even faster than ε_u that the l_{TS} becomes decreasing in streamwise direction after x_4=100 μm. In this region, as no new conductivity variance is imported downstream, the mixing is conducted in a closed system and the spatial conductivity fluctuations becomes much smaller. The

electric body force is not strong enough to support the flow to conquer viscosity effect and the flow becomes decaying turbulence. Just due to the fast decreasing of the influence of electric body force, the inertial subrange can be found in the microfluidics flow. Or, what we see will be the electric body force dominated region as shown in Figure 2.30 and Figure 2.31.

Nominal electric Kolmogorov scale

As introduced previously, the TED calculated from the gradient of velocity fluctuations is an apparently underestimation. The work of electric body force are not completely transfer to kinetic energy of flow. Hence, the conventionally calculation of Kolmogorov scale is not a valid micro scale in EK turbulence. In this section, we tried to advance a new micro scale in EK turbulence.

Still assume the effective diffusivity D_e (about 1.5×10^{-9} m^2/s for the buffer solution) is much smaller than the kinematic viscosity of fluid, as what we have done in section 2.1, the scalar diffusion will be much slower than the momentum diffusion. The scalar structures can be sustained to Batchelor's scale by both inertial and viscous convection (Batchelor 1959; Batchelor 1959). In this progress, the flux of scalar variance is constant. Therefore, the conductivity ratio on each local interface of scalar structure will keep constant down to Batchelor's scale and so does the u_e.

For simplifying analysis, 1-D model is used here as shown in Figure 2.44. At the initial stage (say x_0), the conductivity distribution is on large scale, as described by solid line. After convection downstream to x, by either vortex motion or stretching and folding, the

large-scale conductivity structures are broken into small scales, but the variance of conductivity is constant. This means the following relations are satisfied:

(1) $\sigma_w^* = const$, at x_0

(2) $\langle\sigma^*\rangle_{l,x} = \langle\sigma^*\rangle_{l_0,x_0}$, $\theta_{l,x} = \theta_{l_0,x_0}$, $\beta_{l,x} = \beta_{l_0,x_0}$, for each inclined sides, such as *a* and *b* in Figure 2.44

By taking short time averaging and because $E_w = E_{amp}e^{i\omega t}$, we have the averaged electric body force on scale *l* as:

$$\overline{\overline{F_{e,l}}} = -\frac{\varepsilon}{4l}\left[\overline{\overline{(\sigma_w^* E_w)^2}}\frac{\theta_l}{\langle\sigma^*\rangle_l^2}\left(1-\beta_l^2+\frac{1}{2}\theta_l^2-i\beta_l\right)\right.$$
$$+\overline{\overline{\left(\widetilde{\sigma_w^*}\widetilde{E_w}\right)^2}}\frac{\theta_l}{\langle\widetilde{\sigma^*}\rangle_l^2}\left(1-\beta_l^2+\frac{1}{2}\theta_l^2+i\beta_l\right)$$
$$\left.+\,2\overline{\overline{E_w\widetilde{E_w}\frac{\sigma_w^*\widetilde{\sigma_w^*}}{\langle\sigma\rangle_l^2}}}\theta_l\left(1+\frac{1}{2}\theta_l^2-2\beta_l^2-\frac{1}{2}\theta_l^2\beta_l^2-\frac{1}{16}\theta_l^4-\beta_l^4\right)\right]$$

$$=-\frac{\varepsilon}{2l}\left[E_{amp}^2\frac{\sigma_w^*\widetilde{\sigma_w^*}}{\langle\sigma\rangle_l^2}\theta_l\left(1+\frac{1}{2}\theta_l^2-2\beta_l^2-\frac{1}{2}\theta_l^2\beta_l^2-\frac{1}{16}\theta_l^4-\beta_l^4\right)\right]$$

The details of derivation can be found in section A4. From the condition (1) and (2) above, we can see:

$$\overline{\overline{F_{e,l}}}_x l = \overline{\overline{F_{e,l_0}}}_{x_0} l_0$$

Or in other words, the electric body force on the gradients of conductivity is inversely proportional to spatial scale *l*, when the effective diffusivity is neglectable.

On the scale *l*, the electric inertial velocity can be expressed as:

$$u_{e,l} = \sqrt{\frac{F_{e,l} l}{\rho}}$$

Hence,

$$u_{e,l_x} = u_{e,l_{0_{x_0}}}$$

This means the electric inertial velocity can be sustained in the cascading process of conductivity structures. For a given length scale l, we have the convective time scale $\tau_e = l/u_{e,l}$, and the related viscous diffusion time $\tau_d = l^2/\nu$. At sufficiently small l, when $\tau_d = \tau_e$, the viscous effect is directly balanced by the inertial and electric effect which gives a possibly smallest length scale as (Wang et al. 2014):

$$\frac{l}{\sqrt{\frac{F_{e,l} l}{\rho}}} = \frac{l^2}{\nu} \tag{2.74}$$

Then,

$$l = \left(\frac{\nu^2 \rho}{F_{e,l}}\right)^{\frac{1}{3}}$$

As

$$\langle u_{e,l}^2 \rangle = \langle |F_{e,l}| \rangle \frac{l}{\rho} \tag{2.75}$$

where <> is spatial averaging. For a homogeneous flow with zero electrically-induced mean flow, i.e. $\langle u_{e,l} \rangle = 0$, and further assuming the velocity fluctuations are dominant by electric body force ($\langle u_{e,l}^2 \rangle = \langle u'^2 \rangle_{>l}$, $\langle u'^2 \rangle_{>l}$ is the velocity variance from low

wavenumber components or the large scale structures), then we have the so-called electric Kolmogorov scale, which is:

$$\eta_e = \frac{\nu}{\sqrt{\langle u_{e,l}^2 \rangle}} = \frac{\nu}{\sqrt{\langle u'^2 \rangle_{>l}}} \approx \frac{\nu}{u_{rms}} \tag{2.76}$$

Note, to have the above expression, two additional approximations are used: (1) because the flow is homogeneous and ergodic, $\langle u'^2 \rangle = \overline{u'^2} = u_{rms}$; (2) normally the turbulent energy is dominated by large scale structures, when l is small enough, $\langle u'^2 \rangle \approx \langle u'^2 \rangle_{>l}$.

Because in the assumed indiffusible condition, σ_w^* is kept constant as initial value. $\langle \sigma \rangle_l$ on the side edge is also equal to $\langle \sigma \rangle_w$ and kept constant. Also the θ_l and β_l. Then,

$$\overline{\overline{F_{e,l}}} = -\frac{\varepsilon}{2l}\left[E_{amp}^2 \frac{\sigma_w^* \widetilde{\sigma_w^*}}{\langle \sigma \rangle_l^2} \theta_l \left(1 + \frac{1}{2}\theta_l^2 - 2\beta_l^2 - \frac{1}{2}\theta_l^2\beta_l^2 - \frac{1}{16}\theta_l^4 - \beta_l^4\right)\right] = \overline{\overline{F_e}}/l$$

where $\overline{\overline{F_e}} = -\frac{\varepsilon}{2}\left[E_{amp}^2 \frac{\sigma_w^* \widetilde{\sigma_w^*}}{\langle \sigma \rangle_l^2} \theta_l \left(1 + \frac{1}{2}\theta_l^2 - 2\beta_l^2 - \frac{1}{2}\theta_l^2\beta_l^2 - \frac{1}{16}\theta_l^4 - \beta_l^4\right)\right]$ is kept constant along the cascading process. From the definition of equation (2.75) and (2.76), we have:

$$\eta_e = \left(\frac{\nu^2 \rho}{\langle |\overline{\overline{F_e}}| \rangle}\right)^{1/2}$$

We name it nominal electric Kolmogorov scale. This is the theoretically smallest spatial scale that EK turbulence may have. It is not achievable in practical as the diffusivity cannot be zero. In equilibrium state, the electric Kolmogorov scale should be referred to the l_K in section 2.5.5.

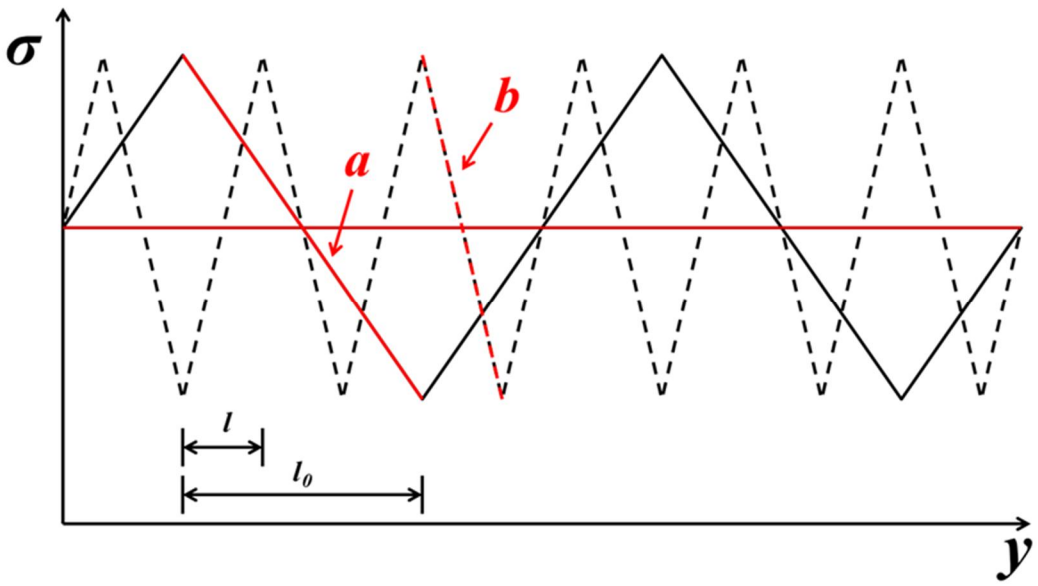

Figure 2.44 Diagram of the cascade process of conductivity structures due to inertial and viscous convections without diffusion.

Auto-correlation function

The auto-correlation coefficient has been plotted in Figure 2.45, which is defined as:

$$f(l) = \frac{\int_{-\infty}^{\infty} u'_m(x+l)u'_m(x)dx}{\int_{-\infty}^{\infty} u'_m(x)^2 dx} \tag{2.77}$$

As the lack of universal law in different streamwise positions, absolute coordinate is used instead of dimensionless coordinate. Turbulent flow doesn't have a universal expression of auto-correlation coefficient. But compared to that of laminar flow (*f(l)* decays very fast with *l* due to the noise signal) or elastic turbulence (*f(l)* doesn't approach to zero and has a large integral length), the auto-correlation curve in this paper is apparently of turbulence. However, compared to the traditional turbulence and other four points, the auto-correlation curves at x = 100 μm and x = 200 μm have obvious difference. The curves are not smooth but can be separated into two linear segments. For instance at x = 100 μm,

the slopes of both segments are smaller than the values at x = 5 μm, 10 μm, 300 μm and 500 μm. And the slopes at smaller scales (dissipation range) are smaller than that at larger scales (inertial range and above). This shows a stronger correlation and more deterministic of flow. The scale of intersection of two line segments is consistent with the upper limit of wavenumber what we found from the *E(k)* where the -5/3 slope ends. This elucidates the essence of electrically driven turbulent flow and its inertial subrange which is the result of electric modulation.

Rayleigh number effect and cut-off frequencies

The cut-off frequency at fixed position varies with the applied electric field intensity and also the nominal electric Rayleigh number, as found by Wang et al(Wang et al. 2014). However, the dimensionless cut-off frequency, i.e. Strouhal number (*St*) is invariant with the electric field intensity, as shown in Figure 2.46. The definition of *St* is introduced below:

$$St = \frac{f_c * d}{u_{e,d}} \tag{2.78}$$

The $u_{e,d}$ is the initial electric inertial velocity, which is:

$$u_{e,d} = \sqrt{\frac{F_{e,d} d}{\rho}}$$

Where f_c is the cut-off frequency of velocity power spectrum, $d = \sqrt{4 D_e t}$ is the initial thickness of interface, t is the convection time. The definition of $F_{e,d}$ can be found in equation (D22).

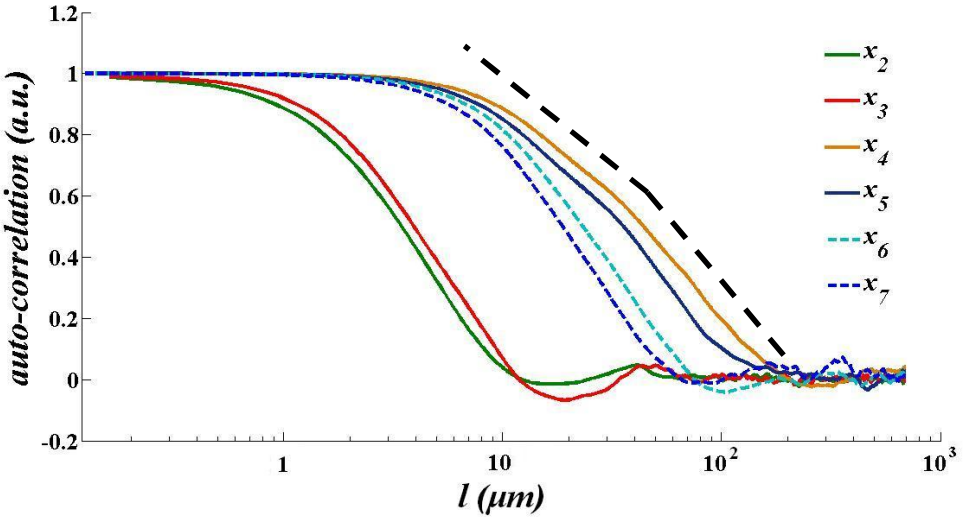

Figure 2.45 Auto-correlation of velocity fluctuations at different streamwise positions. x_2 = 5 μm, x_3 = 10 μm, x_4 = 100 μm, x_5 = 200 μm, x_6 = 300 μm, x_7 = 500 μm.

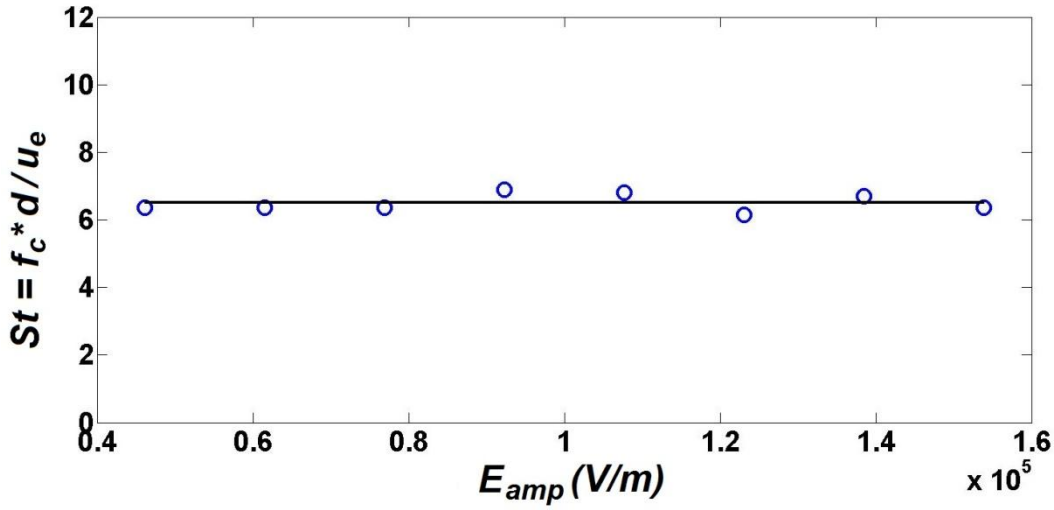

Figure 2.46 The Strouhal number varies with Rayleigh number at x = 100 μm

From Figure 2.46, it can be seen, at x = 100 μm, *St* fluctuates around 6.5 in the considered range of electric field intensity (the equivalent voltage range is from 6 $V_{p\text{-}p}$ to 20 $V_{p\text{-}p}$ and the low voltage cases are neglected because turbulent transition starts from 6 $V_{p\text{-}p}$ as introduced before). This implies the existence of a universal law between the scale of small scale structures and the initial electric field intensity (or Ra_e). Here, we are unable to test the influence of *d* which is fixed in our experiments. Hence, a universal expression of *St* is still under investigation. Thus, so far we can only say, stronger electric field

intensity will generate larger initial $u_{e,d}$. This furthermore causes the kinetic energy of fluid to be transported to smaller scales and exhibits larger cut-off frequency of velocity fluctuations.

The results indicate that increasing electric field intensity is an effective way to enhance turbulent mixing. Also, the bandwidth of turbulent energy cascading process can be expanded.

2.7 Discussions and prospects of further investigations

Discussions on the spatial resolution of LIFPA

In section 2.2.1, the temporal resolution of LIFPA system has been discussed. In this part, the spatial resolution is believed to be the diameter of confocal detection area. However, this argument is not exactly.

In LIFPA measurement, when the flow velocity is large or the photobleaching time constant τ is large (slow photobleaching), the photobleaching process can be schemed by the sold line in Figure 2.47. When the fluorescent dye molecule leaves the focus area of laser, i.e. at $x > d_f$, because the photobleaching is not completely finished, the $I_{f,\ total}$ is determined by the total fluorescent intensity in the detection area of confocal microscope. Hence, the spatial resolution (l_{sr}) of LIFPA of this case is d_f. However, when the flow velocity is small or the photobleaching time constant τ is small (fast photobleaching), as shown by the dashed line in Figure 2.47, the variation of $I_{f,\ total}$ due to velocity fluctuation is only dominated by part of the fluorescent intensity in the detection area. Or in other

words, only the I_f in the region $x \le x_{fb}$ can reflect the variation of velocity. The I_f in the region $x_{fb} \le x \le d_f$ is actually helpless. Therefore, by subtracting the $I_{f,\,total}(0)$ from $I_{f,\,total}(u)$, say $I_{f,\,total,\,net}(u)$, the spatial resolution in this case is actually x_{fb}, not d_f. The actual spatial resolution in the direction of instant velocity could be much smaller than d_f. In practice, because normally $I_{f,\,total}(0)$ is much smaller than $I_{f,\,total}(u)$, $I_{f,total,net}(u) \approx I_{f,total}(u)$. The aforementioned two process can be distinguished by $d_f/(au\tau)$ (a is a coefficient which is determined by the shape of laser focus and the fluorescing and photobleaching processes), and the spatial resolution can be defined as:

$$\begin{cases} l_{sr} = au\tau, & when\ d_f/(au\tau) \ge 1,\ for\ low\ speed\ or\ fast\ photobleaching \\ l_{sr} = d_f, & when\ d_f/(au\tau) < 1,\ for\ high\ speed\ or\ slow\ photobleaching \end{cases} \tag{2.79}$$

For 1st order approximation (i.e. linear relation approximation) of both fluorescing and photobleaching processes (the photobleaching curve is exponential), and also assume uniform laser intensity, a can be selected as 4 for the low speed case. That's because at this position, $\exp(-l_{sr}/u\tau)$ is only 1.8% and the error due to the neglecting part from $l_{sr}/u\tau$ to infinity is less than 1.8%.

From the above discussion, we can find the scale of spatial resolution we normally used, i.e. d_f, is actually the upper limit of LIFPA system. The true spatial resolution is less or equal to d_f.

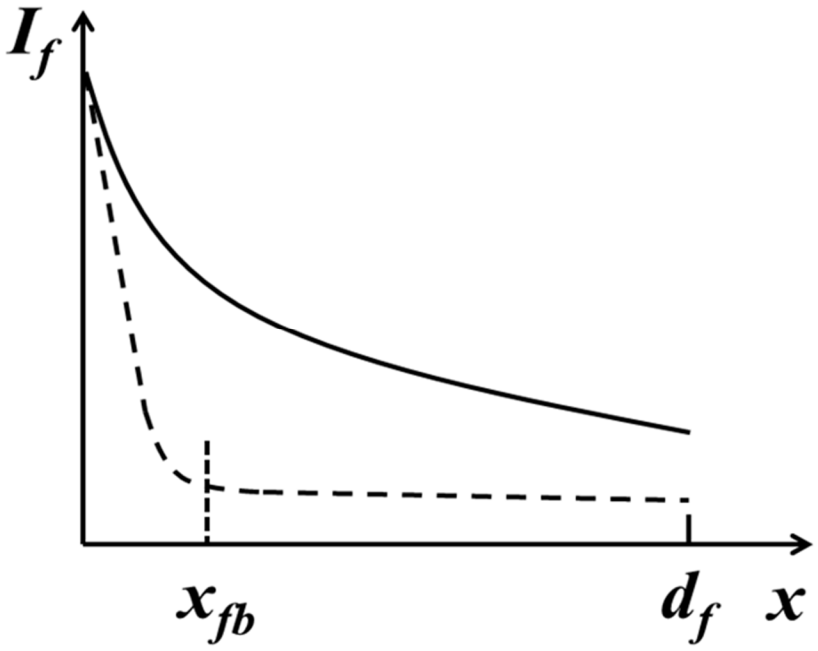

Figure 2.47 Diagram of slow and fast photobleaching process. The solid line indicates a slow photobleaching process or high speed flow. The dashed line indicates a fast photobleaching process or low speed flow

Other problems remained for future investigation

(a) Universal law and scale relation

- **Universal expressions of Ra_e and Gr_e**

In recent investigations, such as introduced in section 2.5.5, we used both the scale based expressions and nominal expressions. However, are these quantities universal is still questionable. Because these parameters are controlled by electric field intensity, conductivity, permittivity, forcing frequency, geometric and flow scales and fluid properties, such as viscosity, diffusivity, density, each of them should be investigated to find the universal expression.

Recently, we have preliminarily found that the small scales of flow structures is inversely proportional to the applied electric field. A Strouhal number is advanced in section 2.6.2. But whether it is a universal expression is also under debating.

- **Universal expressions of both large and small scales**

Similar as the dimensionless quantities, all the large and small scales that advanced in section 2.5.5 should have an universal expressions. In that section, we attempt to give an universal expression on l_K. However, validation is required to confirm our derivation.

- **Their relation with EK subrange and inertial subrange, energy cascade map**

In other turbulence, the inertial subrange and other subranges have been investigated for a long time and quantitative results have been obtained. For instance, in conventional hydrodynamic turbulence, the inertial subrange locates between integral scale and Kolmogorov scale. In RB convection, there exists a Bolgiano scale to separate the buoyancy controlled region and inertial subrange. However, in EK turbulence, whether the scales (l_{ek} and l_K) we suggested in section 2.5.5 can accurately describe the relevant subranges, is still under investigation.

We can only plot the energy cascade map of EK turbulence after the detailed investigations on the above contents.

(b) Physical structure of high intermittency

As introduced in section 2.6.2, abnormally large intermittency factors β can be found. We also found the scaling exponents of p^{th} order moment of velocity structures depart from K41 more than that of conventional hydrodynamic turbulence. This is very interesting. What kind of flow structures can cause this high intermittency should be investigated both experimentally and numerically.

We believe, the abnormal intermittency should be related to the electric-driven small scale velocity fluctuations below inertial subrange.

(c) Optimal mixing enhancement parameters

The purpose of investigating micro EK turbulence in microfluidics flow is helping design high efficiency micro mixer. Our recent mixer is only a conceptual model. By optimally select the parameters, such as conductivity, electric field intensity, forcing frequency, geometry and shape of channel, higher efficiency micro mixers should be available after detailed investigated EK turbulence.

Chapter 3

SUMMARY

3.1 Summarization of the dissertation

In this manuscript, I first introduce my works on mixing enhancement in confined mixing layer—a macroscale phenomenon. The rapid mixing found by Wang (Wang 2003; Wang 2006) is detailed investigated by PIV system. Compared with the traditional free mixing layer, where the initial mixing depends on convective scalar transport by velocity fluctuations, in confined mixing layer, the mixing process can be separated into two stages. The first stage is related to acoustically induced shedding vortex. In the second stage, both the mean and fluctuating vertical velocities work together to enhance the mass transport and the subsequent mixing process. Here, several major conclusions are summarized.

(1) The unforced confined mixing layer has similar universal law of momentum thickness ($\theta_m \sim x^{0.5}$) of mixing layer as in conventional free mixing layer. But at the equivalent Re_θ range, confined mixing layer has larger $d\theta_m/dx$ than in free mixing layer. And the confined mixing layer is more stable (require larger transient Re_θ) than free mixing layer.

(2) The receptivity of 5.3 Hz is the highest in nozzle section, but becomes much weaker in the downstream of mixing chamber. The turbulent energy is "lost". The "lost" turbulent energy is majorly converted to the mean flow energy by the reverse transport

process and relaminarization, which results in the highly wavy U profile, and large V component. And minor dissipated by vortex structures. (3) A “turn-over” point of forcing intensity is found which suggests there should be at least two different mechanisms competed with each other to dominate flow. At low forcing intensity, based on K-H instability, subharmonic mode is the dominant mechanism of mixing enhancement. While forcing at 5.3 Hz with sufficiently large forcing intensity, subharmonic mode is insignificant and the flow is dominated by the forcing frequency, not the intrinsic frequency of flow instability, and acoustically induced shedding vortex becomes important. The short-term effect is also consistent with the existence of acoustically induced shedding vortex. The "turn-over" point can also be considered as a critical point that the flow is transferred from 2-D dominant to 3-D dominant.

(4) From vortex dynamics, the large V component is generated by streamwise vortex structures. Recently, corner vortex mechanism is a reasonable explanation, even though there are still many unsolved questions. Before these problems are solved, we cannot simply ignore other mechanisms arbitrarily, due to the complexity of flow.

(5) Strong V not only enhances the transport of momentum, scalar and energy in vertical direction, but also cause the spanwise vortex to be extremely unstable by high dV/dy. The vortices are stretched and broken down more earlier than other cases which results in faster and more homogeneous mixing.

(6) The optimal frequency, i.e. 5.3 Hz here, is not related to any acoustic resonance or FSI mechanisms.

(7) The important counter-rotation vortex structures is due to the acoustically induced vortex shedding. The requirement of generating CRV is discussed and compared with experiments. Generally say, to achieve CRV, the periodic acoustic boundary layer under external forcing should meet two conditions: (a) The APD should be larger than the sum of the curvature radius of trailing edge and the thickness acoustic boundary layer; (b) The velocity gradient due to acoustic induced flow should be large enough to conquer the gradient of mean flow.

Although the flow dynamics of the fast mixing and many parameters that may related to the optimal frequency are detailed investigated in this section, there are still many unsolved problems. One of the most important is the cause of optimal frequency and the high receptivity. As the flow is strongly nonlinear, linear instability research may not be able to make a sufficient investigation. Recently, only the non-model instability may solve the problem.

Later, the micro EK turbulence and LIFPA velocimeter are investigated in details. The temporal resolution of LIFPA is studied first and then proper correction methods of LIFPA measurement in moderate turbulent intensity flow are introduced. The focus of this part is the existence of turbulence in microfluidics. We first theoretically predicts the presence of turbulence in EK flow in microfluidics, and then experimentally demonstrate the existence of μEK turbulence by LIFPA. Many phenomena which were only found in high Re HD turbulence, such as exponential tail of velocity and scalar structure function, Kolmogorov -5/3 spectrum and O-C spectrum, scaling law of velocity and scalar structure function, exponential decay of scalar variance etc, are also discovered in this μEK turbulence. However, due to the different energy cascade process, there are also many different

characters compared with conventional HD turbulence, such as the abnormal intermittency of dC'/dx. To understand the energy cascade process and its influence on the phenomenology of small-scale velocity structures, a new scaling law and characteristic length scale are derived. Although many efforts have been spend, there are still many unsolved problems, such as the details of physical process of EK turbulence, electric attenuation of flow, kinetic energy evolution and the role of electric body force on different scale ranges.

The researches on EK turbulence is first investigated and achieved in microfluidics. The investigation will not only enhance our understanding on EK turbulent itself, as the similarity of dominant equations between EK turbulence and magnetohydrodynamic (MHD) turbulence, the phenomena discovered in EK turbulence can give us inspiration on MHD investigations, which is very important in astrophysics, such as solar wind.

3.2 Importance of the researches and its influence on future investigations

(1) The cause of optimal frequency

So far, the investigations on confined mixing layer are very limited and not fully understood yet. This causes the misunderstanding of the mixing enhancement mechanism as introduced by Roberts (1985) and MacKinnon and Koochesfahani (1997) who attributed the fast mixing to the second subharmonic mechanism of natural frequency of flow instability. However, through our investigations, all the known instability mechanism have been excluded. We found the optimal frequency is actually not the subharmonic of natural frequency of flow instability, but due to an unknown acoustic mechanism. The optimal

frequency we found is actually a common divider of the frequencies of 1D acoustic resonances in all the piping systems. The reason that Roberts (1985) and MacKinnon and Koochesfahani (1997) attribute the fast mixing to suharmonic mechanism of flow instability is because their studied Re range are too narrow. In the Re range, it's impossible to distinguish the subharmonic mechanism of flow instability from the low frequency and complicated acoustic modes. Although some questions are still remained, the research will be very helpful for future investigations to avoid incorrect understanding on the confined flow.

(2) The nonlinear acoustic shedding vortex

Similar as Wang (Wang 2003; Wang 2006) who attributed the fast mixing process after trailing edge to corner flow instability, people previously believed the fast mixing was because of some unknown absolutely unstable mechanism and fast transition of flow. For this reason, we investigated all the known linear instability mechanisms, such as K-H instability, wake flow instability, Taylor-Görtler instabilities, corner flow instability etc. We also investigated the possible cause of nonlinear instability mechanisms, such as nonmodel stability theories (Schmid 2007). But none of them can clearly explain the fast mixing and the optimal frequency. By focusing on the phenomenon that the intensity of shedding vortex is approximately proportional to the forcing intensity, we found the shedding vortex is actually caused by the pressure wave or acoustics. Relevant generation criterion is suggested too.

(3) LIFPA temporal resolution

As introduced above, LIFPA is a novel velocimeter that can measure velocity fluctuations at high spatial and temporal resolution. The spatial resolution is easily defined and tested. But, the temporal one was hard to be evaluated and can only be estimated from experiments. The lack of theories on evaluating the temporal resolution of LIFPA will severely affect the development and application of LIFPA. Here, we first investigated the temporal resolution of LIFPA and the relevant control parameters. This can help future researchers while building their own LIFPA system for microfluidics measurement.

(4) Correction on the statistics of LIFPA measurement

To solid the foundation of LIFPA measurement and help analyze the error caused by LIFPA, proper correction methods are suggested. The corrections are on mean velocity, velocity fluctuations and first derivative variance of velocity fluctuations. Also, Taylor hypothesis and Local Taylor hypothesis are compared.

(5) Theories on EK turbulence and experimental evidence in micro EK turbulent flow

The theories about generating EK turbulence are advanced. To achieve turbulence, strong EK force are generated to balance the strong viscosity effect. By carefully experiment, turbulence is first and successfully achieved in microfluidics flow. Accompanied with LIFPA method, many statistical quantities, such as mean flow, velocity fluctuations, power spectrum density of velocity fluctuations and concentration

fluctuations, probability density functions of velocity fluctuations and their gradients, are investigated in details. Many feathers, that was believed to be only existed in high Re turbulence, are first time found in a microchannel flow where Re is less than unity.

(6) Scaling law of both velocity and concentration structures in EK turbulence

The scaling behaviors of the second order momentums of velocity and concentration structural functions in EK turbulence are first advanced. Two important microscales are introduced and their possible universal expressions are given. Our theories predict the necessary conditions that EK turbulence can be generated. The EK force in this complex spatial-temporal system is mathematical analyzed. Although the forcing frequency is much higher than the velocity fluctuations, the energy cascading process is believed to be direction cascade. The possible reason is also introduced.

(7) Intermittency structures

The intermittency between the hierarchical structures in EK turbulence is apparently different as in conventional hydrodynamic turbulence. Similarly, strong intermittency can also be found from the scaling exponents of p^{th} order moment of velocity structures. However, in the investigation of the scaling exponents of p^{th} order moment of concentration structures, the intermittency is almost neglectable and much smaller than that of velocity. Possible explanations and models are also introduced.

REFERENCE

Adrian, R. J. (1991). "Particle-imaging techiques for experimental fluid mechanics." Annual Review of Fluid Mechanics **23**: 261-304.

Adrian, R. J. (1997). "Dynamic ranges of velocity and spatial resolution of particle image velocimetry." Measurement Science and Technology **8**: 1393–1398.

Ahn, Y.-C., W. Jung, et al. (2008). "Optical sectioning for microfluidics: secondary flow and mixing in a meandering microchannel." Lab on a Chip **8**(1): 125-133.

Ali, A. M., H. H. S. Yuan, et al. (1981). "Liquid dispersion mechanisms in agitated tanks: Part I. Pitched blade turbine." Chemical Engineering Communications **10**: 205-213.

Alvarez, M. M., J. M. Zalc, et al. (2002). "Mechanisms of mixing and creation of structure in laminar stirred tanks." AIChE Journal **48**(10): 2135-2148.

Armenante, P. M. and Y. T. Huang (1992). "Experimental determination of the minimum agitation speed for complete liquid-liquid dispersion in mechanically agitated vessels." Industrial & Engineering Chemistry Research **31**(5): 1398-1406.

Ascanio, G., M. Brito-Bazán, et al. (2002). "Unconventional Configuration Studies to Improve Mixing Times in Stirred Tanks." The Canadian Journal of Chemical Engineering **80**(4): 558-565.

Balachhandar, S. and M. R. Malik (1995). "Inviscid instability of streamwise corner flow." J. Fluid Mech. **282**: 187-201.

Balasuriya, S. (2010). "Optimal Frequency for Microfluidic Mixing across a Fluid Interface." Physical Review Letters **105**(6): 064501.

Batchelor, G. K. (1959). "Small-scale variation of convected quantities like temperature in a turbulent fluid. I. General discussion and the case of small conductivity." J. Fluid Mech. **5**: 113

Batchelor, G. K. (1959). "Small-scale variation of convected quantities like temperature in turbulent fluid. Part 1. General discussion and the case of small conductivity." Journal of Fluid Mechanics: 113-133.

Batchelor, G. K. (1959). "Small-scale variation of convected quantities like temperature in turbulent fluid. Part 2. The case of large conductivity." Journal of Fluid Mechanics: 134-139.

Baygents, J. C. and F. Baldessari (1998). "Electrohydrodynamic instability in a thin fluid layer with an electrical conductivity gradient." Physics of fluids **10**(1): 301-311.

Benzi, R., L. Biferale, et al. (1996). "Generalized scaling in fully developed turbulence." Physica D **96**: 162-181.

Benzi, R., S. Ciliberto, et al. (1993). "Extended self-similarity in turbulent flows." Physical Review E **48**: R29-R32.

Bernal, L. P. (1981). The coherent structure of turbulent mixing layers. I. Similarity of the primary vortex structure. II. Secondary streamwise vortex structure. Pasadena, Calif. Inst. Technol. **PhD**.

Bernal, L. P. and A. Roshko (1986). "Streamwise vortex structure in plane mixing layers." J. Fluid Mech. **170**: 499-525.Bitsch, L., L. H. Olesen, et al. (2003). Micro PIV on blood flow in a microchannel. 7th lnternational Conference on Miniaturized Chemical and Blochemlcal Analysts Systems. Squaw Valley, Callfornla USA.

Boffetta, G., F. D. Lillo, et al. (2012). "Bolgiano scale in confined Rayleigh-Taylor turbulence." Journal of Fluid Mechanics **690**: 426-440.

Bolgiano, R. (1959). "Turbulent spectra in a stably stratified atmosphere." Journal of Geophysical Research **64**(12): 2226-2229.

Börger, G. (1975). "Optimierung von Windkanaldüsen für den Unterschallbereich." Z Flugwiss **23**: 45-50.

Bown, M. R., J. M. MacInnes, et al. (2006). "Three-dimensional, three-component velocity measurements using stereoscopic micro-PIV and PTV." Measurement Science and Technology **17**: 2175–2185.

Brody, J. P., P. Yager, et al. (1996). "Biotechnology at Low Reynolds Numbers." Biophysical Journal **71**: 3430-3441.

Browand, F. K. and C. M. Ho (1987). Forced, unbounded shear flows. International Conference on Physics of Chaos and Systems Far from Equilibrium. D.-V. M. Amsterdam: North-Holland.

Burghelea, T., E. Segre, et al. (2004). "Chaotic flow and efficient mixing in a microchannel with a polymer solution." Physical Review E **69**(6): 066305.

Campisi, M., D. Accoto, et al. (2009). "A soft-lithographed chaotic electrokinetic micromixer for efficient chemical reactions in lab-on-chips." Journal of Micro-Nano Mechatronics **5**: 69-76.

Cantwell, B. J. (1981). "Organized motion in turbulent flows." Annu. Rev. Fluid Mech. **13**: 457-515.

Capretto, L., W. Cheng, et al. (2011). "Micromixing Within Microfluidic Devices." Topics in Current Chemistry **304**: 27-68.

Catrakis, H. J. and P. E. Dimotakis (1996). "Mixing in turbulent jets: scalar measures and isosurface geometry." Journal of Fluid Mechanics **317**: 369-406.

Chang, C.-C. and R.-J. Yang (2007). "Electrokinetic mixing in microfluidic systems." Microfluidics and Nanofluidics **3**(5): 501-525.

Chang, T. P. K., Y. H. E. Sheu, et al. (1981). "Liquid dispersion mechanisms in agitated tanks: Part II. Straight blade and disc style turbines." Chemical Engineering Communications **10**: 215-222.

Chen, C.-H., H. Lin, et al. (2005). "Convective and absolute electrokinetic instability with conductivity gradients." Journal of Fluid Mechanics **524**: 261-303.

Chen, S., G. Doolen, et al. (1993). "Far-Dissipation Range of Turbulence." Physical Review Letters **70**(20): 3051-3054.

Chevillard, L., B. Castaing, et al. (2005). "On the rapid increase of intermittency in the near-dissipation range of fully developed turbulence." The European Physical Journal B **45**: 561-567.

Chevillard, L., B. Castaing, et al. (2006). "Unified multifractal description of velocity increments statistics in turbulence: Intermittency and skewness." Physica D: Nonlinear Phenomena **218**: 77-82.

Choi, E., B. Kim, et al. (2009). "High-throughput microparticle separation using gradient traveling wave dielectrophoresis." Journal of Micromechanics and Microengineering **19**(125014).

Comte-Bellot, G. and S. Corrsin (1971). "Simple Eulerian time correlation of full- and narrow-band velocity signals in grid-generated, 'isotropic' turbulence." Journal of Fluid Mechanics **48**: 273-337.

Corrsin, S. (1951). "On the Spectrum of Isotropic Temperature Fluctuations in an Isotropic Turbulence." Journal of Applied Physics **22**(4): 469-473.

Corrsin, S. (1964). "The isotropic turbulent mixer: Part II. Arbitrary Schmidt number." AIChE Journal **10**: 870-877.

Cummings, A. (1984). "Acoustic nonlinearities and power losses at orifices." AIAA Journal **22**: 786-792.

Davidson, P. A. (2004). Turbulence- An Introduction for Scientists and Engineers. New York, Oxford Univesity Press.

Davidson, P. A. and P.-Å. Krogstad (2008). "On the deficiency of even-order structure functions as inertial-range diagnostics." Journal of Fluid Mechanics **602**: 287-302.

Deval, J., P. Tabeling, et al. (2002). A dielectrophoretic chaotic mixer. Micro Electro Mechanical Systems, 2002. The Fifteenth IEEE International Conference on Micro Electro Mechanical Systems. Las Vegas, NV, USA**:** 4.

Dhanak, D. R. (1993). "On the instability of flow in a streamwise corner." Proc. R. Soc. Lond. A. Phys. Sci. **441**: 201-209.

Dhanak, M. R. and P. W. Duck (1997). "The Effects of Freestream Pressure Gradient on a Corner Boundary Layer." Proc. R. Soc. Lond. A **453**: 1793-1815.

Dimotakis, P. E. (1986). "Two-dimensional shear-layer entrainment." AIAA J. **24**: 1791-1796.

Dimotakis, P. E. (2005). "Turbulent Mixing." Ann. Rev. Fluid Mech. **37**: 329-356.

Dimotakis, P. E. and G. L. Brown (1976). "The mixing layer at high Reynolds number: large-structure dynamics and entrainment." J. Fluid Mech. **78**: 535-560.

Disselhorst, H. M. and J. Van Wijngaarden (1980). "Flow in the exit of open pipes during acoustic resonance." Journal of Fluid Mechanics **99**: 293-319.

Duck, P. W. and J. Owen (2004). "Non-modal stability and breakdown in corner and three-dimensional boundary layers " Proc. R. Soc. Lond. A **460**: 1335-1357.

Dziomba, B. and H. E. Fiedler (1985). "Effect of initial conditions on two-dimensional free shear layers." J. Fluid Mech. **152**: 419-442.

Erol, M. and D. M. Kalyon (2005). "Assessment of the Degree of Mixedness of Filled Polymers." International Polymer Processing **20**(3): 228-237.

Ewing, D. (2004). "The effect of cross flow on one-dimensional spectra measured using hot wires." Experiments in Fluids **36**: 675-684.

Ewing, D. and W. K. George (2000). "The effect of cross-flow velocity on mean-square derivatives measured using hot wires." Experiments in Fluids **29**: 418-428.

Fiedler, H. E. and P. Mensing (1985). "The plane turbulent shear layer with periodic excitation." J. Fluid Mech. **150**: 281-309.

Fiedler, H. E., C. Nayeri, et al. (1998). "Three-dimensional Mixing Layers and their Relatives." Experimental Thermal and Fluid science **16**: 3-21.

Flamion, B., P. M. Bungay, et al. (1991). "Flow rate measurements in isolated perfused kidney tubules by fluorescence photobleaching recovery." Biophysical Journal **60**(5): 1229-1242.

Fouxon, A. and V. Lebedev (2003). "Spectra of turbulence in dilute polymer solutions." Physics of Fluids (1994-present) **15**(7): 2060-2072.

Frisch, U. (1995). Turbulence—The legacy of A. N. Kolmogorov, Cambridge University Press.

George, W. K. and H. J. Hussein (1991). "Locally axisymmetric turbulence." J. Fluid Mech. **233**: 1-23.

Gessner, F. B. (1973). "The origin of secondary flow in turbulent flow in a corner." Journal of Fluid Mechanics **58**: 1-25.

Gessner, F. B. and J. B. Jones (1965). "On some aspects of fully-developed turbulent flow in rectangular channels." Journal of Fluid Mechanics **23**: 689-713.

Gibson, C. H. and W. H. Schwarz (1963). "The universal equilibrium spectra of turbulent velocity and scalar fields." J. Fluid Mech. **16**: 365-384.

Goldstein, R. J., M. Y. Jabbari, et al. (1992). "The near-corner mass transfer associated with turbulent flow in a square duct." Wärme- und Stoffübertragung **27**: 265-272.

Griffiths, D. J. (2007). Introduction to Electrodynamics. Pearson Education, Dorling Kindersley.

Groisman, A. and V. Steinberg (2000). "Elastic turbulence in a polymer solution flow." Nature **405**(6782): 53-55.

Guilkey, J. E., A. R. Kerstein, et al. (1997). "Mixing mechanisms in turbulent pipe flow." Physics of Fluids **9**: 717-723.

Heidbrink, W. W., J. M. Park, et al. (2009). "Evidence for Fast-Ion Transport by Microturbulence." PHYSICAL REVIEW LETTERS **103**(17): 175001.

Hessel, V., H. Löwe, et al. (2005). "Micromixers—a review on passive and active mixing principles." Chemical Engineering Science(8-9): 2479-2501.

Ho, C. M. and L. S. Huang (1982). "Subharmonics and vortex merging in mixing layer." J. Fluid Mech. **119**: 443-473.

Ho, C. M. and P. Huerre (1984). "Perturbed free shear layers." Annu. Rev. Fluid Mech. **16**: 365-423.

Ho, C. M. and N. S. Nosseir (1981). "Dynamics of an impinging jet. Part 1. The feedback phenomenon." J. Fluid Mech. **105**: 119-142.

Hof, B., J. Westerweel, et al. (2006). "Finite lifetime of turbulence in shear flows." Nature **443**: 59-62.

Hu, H., Z. Jin, et al. (2008). "Fluid Mixing Control Inside a Y-shaped Microchannel by Using Electroknetics Instability." Journal of Fluid Science and Technology **3**(2): 260-273.

Huang, M.-Z., R.-J. Yang, et al. (2006). "Application of electrokinetic instability flow for enhanced micromixing in cross-shaped microchannel." Biomedical microdevices **8**(4): 309-315.

Huerre, P. (1990). "Local and global instabilities in spatially developing flows." Annu. Rev. Fluid Mech. **22**: 473-538.

Ingard, U. and H. Ising (1967). "Acoustic Nonlinearity of an Orifice." Journal of the Acoustical Society of America **42**(1): 6-17.

Ingård, U. and S. Labate (1950). "Acoustic Circulation Effects and the Nonlinear Impedance of Orifices." Journal of the Acoustical Society of America **22**: 211-218.

Jager, C. D. (1954). "High-energy Microturbulence in the Solar Photosphere." Nature **173**(4406): 680-681.

Janasek, D., J. Franzke, et al. (2006). "Scaling and the design of miniaturized chemical-analysis systems." Nature **442**(7101): 374-380.

Joneidi, A. A., G. Domairry, et al. (2010). "Three analytical methods applied to Jeffery-Hamel flow." Commun Nonlinear Sci Numer Simulat **15**: 3423-3434.

Karnovsky, I. A. and O. I. Lebed (2001). Formulas for structural dynamics. Tables, Graphs, and Solutions. New York, McGraw-Hill.

Kerstein, A. R. and P. A. McMurtry (1994). "Low-wave-number statistics of randomly advected passive scalars." PHYSICAL REVIEW E **50**(3): 2057-2063.

Kinoshita, H., S. Kaneda, et al. (2007). "Three-dimensional measurement and visualization of internal flow of a moving droplet using confocal micro-PIV." Lab on a Chip **7**: 338-346.

Kirby, B. (2010). Micro - and Nanoscale Fluid Mechanics: Transport in Microfluidic Devices, Cambridge University Press.

Kirby, B. J. (2010). Micro- and Nanoscale Fluid Mechanics: Transport in Microfluidic Devices New York, Cambridge University Press.

Klein, S. A. and J. D. Posner (2010). "Improvement in two-frame correlations by confocal microscopy for temporally resolved micro particle imaging velocimetry." Measurement Science and Technology **21**(105409).

Kolmogorov, A. N. (1941). "The Local Structure of Turbulence in Incompressible Viscous Fluid for Very Large Reynolds Numbers." Dokl. Akad. Nauk SSSR **30**(4).

Koochesfahani, M. M. and P. E. Dimotakis (1985). "Laser induced fluorescence measurements of mixed fluid concentration in a liquid plane shear layer." AIAA J. **23**(11): 1700-1707.

Koochesfahani, M. M. and P. E. Dimotakis (1986). "Mixing and chemical reactions in a turbulent liquid mixing layer." Journal of Fluid Mechanics **170**: 83-112.

Koochesfahani, M. M. and C. G. Mackinnon (1991). "Influence of forcing on the composition of mixed fluid in a two-stream shear layer." Phys Fluids A **3**: 1135-1142.

Kresta, S. (1998). "Turbulence in stirred tanks: Anisotropic, approximate, and applied." The Canadian Journal of Chemical Engineering **76**(3): 563-576.

Kuang, C. and G. Wang (2010). "A novel far-field nanoscopic velocimetry for nanofluidics." Lab-on-a-Chip **10**: 240-245.

Kuang, C. and G. R. Wang (2009). "Ultrafast Measurement of Transient Electrokinetic Flow in Microfluidics." Ultrafast Measurement of Transient Electrokinetic Flow in Microfluidics **(In preparation)**.

Kuang, C., W. Zhao, et al. (2010). "Far-field optical nanoscopy based on continuous wave laser stimulated emission depletion." Review of Scientific Instruments **81**.

Lee, C.-Y., C.-L. Chang, et al. (2011). "Microfluidic Mixing: A Review." International Journal of Molecular Sciences **12**: 3263-3287.

Lee, Y.-K., J. Deval, et al. (2001). Chaotic mixing in electrokinetically and pressure driven micro flows. MEMS 2001. 14th IEEE International Conference on Micro Electro Mechanical Systems. Interlaken, Switzerland**:** 483-486.

Lesieur, M. (2007). Turbulence in Fluids, Springer.

Li, C.-T., K.-C. Chang, et al. (2009). "PIV measurements of turbulent flow in planar mixing layer." Experimental Thermal and Fluid Science **33**: 527-537.

Lim, C. Y., Y. C. Lam, et al. (2010). "Mixing enhancement in microfluidic channel with a constriction under periodic electro-osmotic flow." Biomicrofluidics **4**(014101).

Lima, R., S. Wada, et al. (2008). "In vitro blood flow in a rectangular PDMS microchannel: experimental observations using a confocal micro-PIV system." Biomedical Microdevices **10**(2): 153-167.

Lohse, D. and K.-Q. Xia (2010). "Small-Scale Properties of Turbulent Rayleigh-Bénard Convection." Annual Review of Fluid Mechanics **42**: 335-364.

Lumley, J. L. (1965). "Interpretation of Time Spectra Measured in HighIntensity Shear Flows." PHYSICS OF FLUIDS **8**(6): 1056-1062.

MacKinnon, C. G. and M. M. Koochesfahani (1997). " Flow structure and mixing in a low Reynolds number forced wake inside a confined channel." Physics of Fluids **9**(10): 3099-3101.

Matta, L. M., C. Zhu, et al. (1996). "Mixing by resonant acoustic driving in a closed chamber." Journal of Propulsion and Power **12**(2): 366-370.

Meinhart, C. D., S. T. Wereley, et al. (1999). "PIV measurements of a microchannel flow." Experiments in Fluids **27**: 414-419.

Meinhart, C. D., S. T. Wereley, et al. (2000). "A PIV algorithm for estimating time-averaged velocity fields." Journal of Fluids Engineering **122**: 285-289.

Meirovitch, L. (1986). Elements of Vibration Analysis, McGraw-Hill.

Miksad, R. W. (1972). "Experiments on the nonlinear stages of free shear layer transition." Journal of Fluid Mechanics **56**: 695-719.

Miksad, R. W. (1973). "Experiments on nonlinear interactions in the transition of a free shear layer." Journal of Fluid Mechanics **59**: 1-21.

Miller, P. and P. Dimotakis (1996). "Measurements of scalar power spectra in high Schmidt number turbulent jets." J. Fluid Mech. **308**: 129-46.

Moinuddin, K. A. M., P. N. Joubert, et al. (2004). "Experimental investigation of turbulence-driven secondary motion over a streamwise external corner." Journal of Fluid Mechanics **511**: 1-23.

Monin, A. S. and A. M. Yaglom (1975). Statistical fluid mechanics. Cambridge, Massachusetts, MIT Press.

Mydlarski, L. and Z. Warhaft (1998). "Passive scalar statistics in high-Peclet-number grid turbulence." J. Fluid Mech. **358**: 135-75.

Natrajan, V. K., E. Yamaguchi, et al. (2007). "Statistical and structural similarities between micro- and macroscale wall turbulence." Microfluidics and Nanofluidics **3**: 89-100.

Ng, W. Y., S. Goh, et al. (2009). "DC-biased AC-electroosmotic and AC-electrothermal flow mixing in microchannels." Lab on a Chip **9**: 802-809.

Nguyen, N. T. (1997). "Micromachined flow sensors--a review." Flow Meas. Instrum. **8**(1): 7-16.

Niemela, J. J., L. Skrbek, et al. (2000). "Turbulent convection at very high Rayleigh numbers." Nature **404**: 837-840.

Nye, J. O. and R. S. Brodkey (1967). "The scalar spectrum in the viscous-convective subrange." Journal of Fluid Mechanics **29**: 151-163.

Nye, J. O. and R. S. Brodkey (1967). "The scalar spectrum in the viscous-convective subrange." J. Fluid Mech. **29**: 151-163.

Obukhov, A. M. (1949). "The structure of the temperature field in a turbulent flow." Izv. Akad. Nauk. SSSR, Ser. Geogr. and Geophys **13**(1): 58-67.

Obukhov, A. M. (1959). "On the influence of Archimedean forces on the structure of the temperature field in a turbulent flow." Dokl. Akad. Nauk. SSR **125**: 1246-1248.

Oddy, M. H., J. G. Santiago, et al. (2001). "Electrokinetic Instability Micromixing." Analytical Chemistry **73**(24): 5822-5832.

Oster, D. and I. Wygnanski (1982). "The forced mixing layer between parallel streams." J. Fluid Mech. **123**: 91-130.

Parikh, P. G. and R. J. Moffat (1982). "Resonant entrainment of a confined pulsed jet." ASME, Transactions, Journal of Fluids Engineering **104**: 482-488.

Park, J., S. Shin, et al. (2005). "Application of electrokinetic instability for enhanced mixing in various micro–T-channel geometries." Physics of Fluids **17**: 118101.1-118101.4.

Park, J. S., C. K. Choi, et al. (2004). "Optically sliced micro-PIV using confocal laser scanning microscopy (CLSM)." Experiments in Fluids **37**: 105-119.

Paul, E. L., V. A. Atiemo-Obeng, et al. (2003). Handbook of industrial mixing : science and practice, John Wiley & Sons, Inc.

Pierrehumbert, R. T. and S. E. Widnall (1982). "The two- and three-dimensional instabilities of a spatialy periodic shear layer." J. Fluid Mech. **114**: 59-82.

Pinton, J.-F. and R. Labbé (1994). "Correction to the Taylor hypothesis in swirling flows." J. Phys. II France **4**: 1461-1468.

Politano, H. and A. Pouquet (1995). "Model of intermittency in magnetohydrodynamic turbulence." Physical Review E **52**: 636-641.

Pope, R. M. and E. S. Fry (1997). "Absorption spectrum (380-700 nm} of pure water. II. Integrating cavity measurements." Applied Optics **36**(33): 8710-8723.

Posner, J. D. and J. G. Santiago (2006). "Convective instability of electrokinetic flows in a cross-shaped microchannel." Journal Of Fluid Mechanics **555**: 1-42.

Raben, J. S., S. A. Klein, et al. (2013). "Improved accuracy of time-resolved micro-Particle Image Velocimetry using phase-correlation and confocal microscopy." Microfluidics and Nanofluidics **14**: 431-444.

Ramos, A. (2011). Electrokinetics and Electrohydrodynamics in Microsystems, Springer.

Ramos, A., H. Morgan, et al. (1998). "Ac electrokinetics: a review of forces in microelectrode structures." Journal of Physics D: Applied Physics **31**: 2338-2353.

Rička, J. (1987). "Photobleaching velocimetry." Experiments in Fluids **5**(6): 381-384.

Rienstra, S. W. and A. Hirschberg (2009). An Introduction to Acoustics. Eindhoven University of Technology.

Roberts, F. A. (1985). Effects of Periodic Disturbance on Structure and Mixing in Turbulent Shear Layers and Wakes. Pasadena, CA, California Institute of Technology. **PhD**.

Rossi, M., R. Segura, et al. (2012). "On the effect of particle image intensity and image preprocessing on the depth of correlation in micro-PIV." Experiments in Fluids **52**: 1063-1075.

Rudolph, L., M. Schäfer, et al. (2007). "Experimental and Numerical Analysis of Power Consumption for Mixing of High Viscosity Fluids with a Co-Axial Mixer." Chemical Engineering Research and Design **85**(5): 568-575.

Ruiz-Chavarria, G., C. Baudet, et al. (1996). "Scaling laws and dissipation scale of a passive scalar in fully developed turbulence." Physica D **99**: 369-380.

Saddoughi, S. G. and S. V. Veeravalli (1994). "Local isotropy in turbulent boundary layers at high Reynolds number." Journal of Fluid Mechanics **268**: 333-372.

Sadr, R., C. Hohenegger, et al. (2007). "Diffusion-induced bias in near-wall velocimetry." Journal of Fluid Mechanics **577**: 443-456.

Sahu, K. C. and R. Govindarajan (2005). "Stability of flow through a slowly diverging pipe." Journal of Fluid Mechanics **531**: 325-334.

Santiago, J. G., S. T. Wereley, et al. (1998). "A particle image velocimetry system for microfluidics." Experiments in Fluids **25**(4): 316-319.

Schmid, P. J. (2007). "Nonmodal Stability Theory." Annual Review of Fluid Mechanics **39**: 129-162.

Sharp, K. V., R. J. Adrian, et al. (2002). Liquid Flows in Microchannels. The Mems Handbook. M. Gad-el-Hak, CRC Press.

She, Z.-S., K. Ren, et al. (2001). "Scalings and structures in turbulent Couette-Taylor flow." Physical Review E **64**: 016308.

She, Z. S. and E. Leveque (1994). "Universal scaling laws in fully developed turbulence." Phys. Rev. Lett. **72**: 336-339.

Shinohara, K., **Y. Sugii**, et al. (2004). "**High-speed micro-PIV measurements of transient flow in microfluidic devices**." Measurement Science and Technology **15**: 1965–1970.

Simonnet, C. and A. Groisman (2005). "Chaotic Mixing in a Steady Flow in a Microchannel." Physical Review Letters **94**(13): 134501.

Sreenivasan, K. R. (1996). "The passive scalar spectrum and the Obukhov-Corrsin constant." Phys. Fluids **8**: 8.

Sreenivasan, K. R. (1997). "The phenomenology of small-scale turbulence." Annual Review of Fluid Mechanics **29**: 435-472.

Stroock, A. D., S. K. W. Dertinger, et al. (2002). "Chaotic Mixer for Microchannels." Science **295**(5555): 647-651.

Sugarman, J. and R. Prud'homme (1987). "Effect of photobleaching on the output of an on-column laser fluorescence detector." Ind Eng Chem Res **26**: 1449-1454.

Sugii, Y., R. Okuda, et al. (2005). "Velocity measurement of both red blood cells and plasma of *in vitro* blood flow using high-speed micro PIV technique." Measurement Science and Technology **16**: 1126–1130.

Suh, J., M. Dawson, et al. (2005). "Real-time multiple-particle tracking: applications to drug and gene delivery." Advanced Drug Delivery Reviews **57**: 63-78.

Tabeling, P. (2010). Introduction to Microfluidics, Oxford University Press, USA.

Tabeling, P., G. Zocchi, et al. (1996). "Probability density functions, skewness, and flatness in large Reynolds number turbulence." Physical Review E **53**: 1613-1621.

Tennekes, H. and J. L. Lumley (1972). A First Course in Turbulence, The MIT press.

Tsouris, C. and L. L. Tavlarides (1994). "Breakage and coalescence models for drops in turbulent dispersions." AIChE Journal **40**(3): 395-406.

Wang, G., F. Yang, et al. (2014). "There can be turbulence in microfluidics at low Reynolds number." Lab on a Chip **14**(8): 1452 - 1458.

Wang, G. R. (1999). Turbulent mixing, instability and secondary flow in a confined configuration, Technische Universität Berlin, Germany.

Wang, G. R. (2000). Turbulent Mixing, Stability and Secondary Flow in a Confined Configuration. Berlin, Verlag Dr. Ko¨ster, ISBN: 3-89574-376-3**,** Bd. 8

Wang, G. R. (2003). "A rapid mixing process in continuous operation under periodic forcing." Chem. Eng. Sci. **58**: 4953-4963.

Wang, G. R. (2005). "Laser induced fluorescence photobleaching anemometer for microfluidic devices." Lab on a Chip **5**(4): 450-456.

Wang, G. R. (2006). "On large scale structures and turbulent mixing in confined mixing layers under strong forcing." AIChE Journal **52**: 111-124.

Wang, G. R. (2013). "Realizing Statistical Features of High Reynolds Number Turbulence at Relatively Low Reynolds Number Flow." Submitted Journal of Fluid Mechanics.

Wang, G. R. and H. E. Fiedler (2000). "On high spatial resolution scalar measurement with LIF. Part 2: The Noise Characteristics." Experiments in Fluids **29**: 265-274.

Wang, G. R., F. Yang, et al. (Submitted). "Direct observation of scalar turbulence in microfluidics at low Reynolds number." Physical Review Letter.

Warhaft, Z. (2000). "Passive scalars in turbulent flows." Annu. Rev. Fluid Mech. **32**: 203-240.

Wędołowski, K., K. Bajer, et al. (2011). Analysis and modelling of the effective reaction rate in a developing mixing layer. 13th European Turbulence Conference (ETC13), Journal of Physics: Conference Series. **318:** 10.

Weisbrot, I. and I. Wygnanski (1988). "On coherent structures in a highly excited mixing layer." J. Fluid Mech. **195**: 137-159.

Wereley, S. T. and C. D. Meinhart (2010). "Recent Advances in Micro-Particle Image Velocimetry." Annual Review of Fluid Mechanics **42**: 557-576.

Westerweel, J., G. E. Elsinga, et al. (2013). "Particle Image Velocimetry for Complex and Turbulent Flows." Annual Review of Fluid Mechanics **45**: 409-436.

Westerweel, J., P. F. Geelhoed, et al. (2004). "Single-pixel resolution ensemble correlation for mPIV applications." Experiments in Fluids **37**: 375-384.

Wiggert, D. C. and A. S. Tijsseling (2001). "Fluid transients and fluid-structure interaction in flexible liquid-filled piping." Applied Mechanics Reviews **54**(5): 455-481.

Williams, B., D. Marteau, et al. (1997). "Mixing of passive scalar in magnetically forced two-dimensional turbulence." Phys. Fluids **9**: 2061-80.

Wiltse, J. M. and A. Glezer (1998). "Direct excitation of small-scale motions in free shear flows." Phys. Fluids **10**(8): 2026-2036.

Wiltse, J. M. and A. Glezer (2004). "Scalar mixing in a forced non-reactive plane shear layer using a thermal analogue to species concentration." J. Fluid Mech. **506**: 369-406.

Wiltse, J. M. and A. Glezer (2011). "The effect of closed-loop feedback control on scalar mixing in a plane shear layer." Experiments in fluids **51**: 1291-1314.

Winant, C. D. and F. K. Browand (1974). "Vortex pairing: the mechanism of turbulent mixing-layer growth at moderate Reynolds number." Journal of Fluid Mechanics **63**: 237-255.

Wygnanski, I. and H. E. Fiedler (1970). "The two-dimensional mixing region." Journal of Fluid Mechanics **41**: 327-361.

Wyngaard, J. C. and S. F. Clifford (1977). "Taylor's hypothesis and high-frequency turbulence spectra." Journal of Atmospheric Sciences **34**: 922-929.

Yan, D., N.-T. Nguyen, et al. (2006). "Visualizing the transient electroosmotic flow and measuring the zeta potential of microchannels with a micro-PIV technique." The Journal of Chemical Physics **124**: 021103.

Zamir, M. (1981). "Similarity and Stability of the Laminar Boundary Layer in a Streamwise Corner." Proc. R. Soc. Lond. A **377**: 269-268.

Zamir, M. and A. D. Young (1970). "Experimental investigation of the boundary layer in a streamwise corner." Aeronaut Q **21**: 313-338.

Zhao, C. and C. Yang (2011). "AC field induced-charge electroosmosis over leaky dielectric blocks embedded in a microchannel." Electrophoresis **32**(5): 629-637.

APPENDIX A: THE RELATION BETWEEN VELOCITY SIGNAL AND LIFPA TIME CONSTANT

Normally in microfluidics, the flow velocity is small. Someone may doubt will the characteristic of LIFPA that the temporal response (i.e. temporal resolution) varies with instant velocity limit LIFPA application and accuracy? Actually, accompanied with the development of laser and fluorescent dye, the time constant of photobleaching can be smaller and smaller which can meet the requirement of practical application.

And if the flow velocity meets some requirement, the accuracy of LIFPA is also reliable. Let's assume a simple case, where a mean velocity U with sinusoidal velocity fluctuations of amplitude u_0:

$$u = U + u_0 \sin(\omega t)$$

where $\omega = 2\pi f$ From equation (10), the theoretical temporal response of LIFPA can be estimated as:

$$\left(\frac{du}{dt}\right)_{LIFPA} = -\frac{U + u_0 \sin(\omega t)}{\tau}$$

While the real one is:

$$\left(\frac{du}{dt}\right)_{flow} = \omega u_0 \cos(\omega t)$$

As for an accurate measurement,

$$\left|\left(\frac{du}{dt}\right)_{LIFPA}\right| \geq \left|\left(\frac{du}{dt}\right)_{flow}\right|$$

which is equivalent to:

$$[\omega u_0 \cos(\omega t)]^2 \leq \left[\frac{U + u_0 \sin(\omega t)}{\tau}\right]^2$$

$$\omega^2 {u_0}^2 [1 - \sin^2(\omega t)] \leq \frac{U^2 + 2U u_0 \sin(\omega t) + u_0^2 \sin^2(\omega t)}{\tau^2}$$

Then,

$$\left(\frac{u_0^2}{\tau^2} + u_0^2\omega^2\right)\sin^2(\omega t) + \frac{2U u_0}{\tau^2}\sin(\omega t) + \left(\frac{U^2}{\tau^2} - u_0^2\omega^2\right) \geq 0$$

This is equivalent to solve the conditions that:

$$f(x) = ax^2 + bx + c \geq 0$$

where $x \in [-1,1]$, $a = \frac{u_0^2}{\tau^2} + u_0^2\omega^2$, $b = \frac{2U u_0}{\tau^2}$, $c = \frac{U^2}{\tau^2} - u_0^2\omega^2$.

There are two possibilities:

$$\begin{cases} f(1) \geq 0 \\ f(1) \geq 0 \\ f\left(-\frac{b}{2a}\right) \geq 0, \quad if -1 \leq -b/(2a) \leq 1 \end{cases} \tag{A1}$$

or

$$\begin{cases} f(1) \geq 0 \\ f(1) \geq 0 \\ -\frac{b}{2a} \leq -1 \; or \; -b/(2a) \geq 1 \end{cases} \tag{A2}$$

From condition (A1), we have:

$$\begin{cases} \dfrac{(u_0 + U)^2}{\tau^2} \geq 0 \\ \dfrac{(u_0 - U)^2}{\tau^2} \geq 0 \\ (U^2 - u_0^2) - u_0^2\omega^2\tau^2 \geq 0, \quad if \; U \leq u_0(1 + \omega^2\tau^2) \end{cases}$$

Then,

$$\begin{cases} \dfrac{(u_0 + U)^2}{\tau^2} \geq 0 \\ \dfrac{(u_0 - U)^2}{\tau^2} \geq 0 \\ \omega\tau \leq \sqrt{\dfrac{U^2}{u_0^2} - 1}, \quad if \; \omega\tau \geq \sqrt{\dfrac{U}{u_0} - 1} \end{cases}$$

And, the velocity signal should satisfy the following conditions:

$$\begin{cases} \frac{(u_0+U)^2}{\tau^2} \geq 0 \\ \frac{(u_0-U)^2}{\tau^2} \geq 0 \\ \frac{1}{2\pi\tau}\sqrt{\frac{U}{u_0} - 1} \leq f \leq \frac{1}{2\pi\tau}\sqrt{\frac{U^2}{u_0^2} - 1} \end{cases} \tag{A3}$$

Hence, $U \geq u_0$ and $U + u_0 sin(\omega t) \ll d_f/\tau$ (for large U/u_0, this can be approximated as $U \ll d_f/\tau$).

For condition (A2), we have:

$$\begin{cases} \dfrac{(u_0+U)^2}{\tau^2} \geq 0 \\ \dfrac{(u_0-U)^2}{\tau^2} \geq 0 \\ U \geq u_0(1+\omega^2\tau^2) \end{cases}$$

where $-b/(2a) \geq 1$ condition doesn't exist in our model and is automatically eliminated. Then,

$$\begin{cases} \dfrac{(u_0+U)^2}{\tau^2} \geq 0 \\ \dfrac{(u_0-U)^2}{\tau^2} \geq 0 \\ \omega\tau \leq \sqrt{\dfrac{U}{u_0}-1} \end{cases}$$

And, the velocity signal should satisfy the following conditions:

$$\begin{cases} \frac{(u_0+U)^2}{\tau^2} \geq 0 \\ \frac{(u_0-U)^2}{\tau^2} \geq 0 \\ f \leq \frac{1}{2\pi\tau}\sqrt{\frac{U}{u_0}-1} \end{cases} \quad \text{(A4)}$$

And also $U \geq u_0$ and $U + u_0 sin(\omega t) \ll d_f/\tau$ (for large U/u_0, this can be approximated as $U \ll d_f/\tau$).

Combine condition (A3) and (A4), we have the only requirement is:

$$f \leq \frac{1}{2\pi\tau}\sqrt{\frac{U^2}{u_0^2}-1} \quad \text{(A5)}$$

with $U \geq u_0$ and $U + u_0 sin(\omega t) \ll d_f/\tau$ (for large U/u_0, this can be approximated as $U \ll d_f/\tau$).

The derivation here means, the frequency of detectable velocity variation is determined by the time constant of LIFPA, mean flow velocity U and velocity fluctuation amplitude u_0 by equation (A5). The larger the U/u_0 (which is equivalent to small turbulent intensity), the higher frequency can be detected. But u_0 cannot be infinitely small and should be larger than the noise level of LIFPA to be distinguished from noise. Normally, for a small u_0, the upper limit of velocity frequency is assume to be no more than $1/\tau$.

APPENDIX B: NOMINAL GRASHOF NUMBER (GRE) AND ELECTRIC RAYLEIGH NUMBER (RAE) FOR DC CASE

In DC case, the Navier-Stokes equation with the presence of electrokinetic (EK) force can be described as:

$$\rho \frac{D\boldsymbol{u}}{Dt} = -\nabla p + \mu \nabla^2 \boldsymbol{u} - \frac{\varepsilon(\nabla\sigma \cdot \boldsymbol{E})}{\sigma}\boldsymbol{E} \tag{B1}$$

$$\boldsymbol{u} = U\hat{\boldsymbol{u}}, \qquad \boldsymbol{t} = \tau\hat{\boldsymbol{t}}, \qquad \boldsymbol{x} = U\tau\hat{\boldsymbol{x}}, \qquad \sigma = \sigma_0\hat{\sigma}, \qquad \boldsymbol{E} = E_0\hat{\boldsymbol{E}}, \qquad p = \rho U^2$$

$$\rho \frac{U}{\tau}\left(\frac{\partial \hat{\boldsymbol{u}}}{\partial \hat{\boldsymbol{t}}} + \hat{\boldsymbol{u}} \cdot \hat{\nabla}\hat{\boldsymbol{u}}\right) = -\rho \frac{U}{\tau}\hat{\nabla}\hat{p} - \frac{\varepsilon \Delta\sigma E_0^2}{\sigma U \tau}\frac{\left(\hat{\nabla}\hat{\sigma} \cdot \hat{\boldsymbol{E}}\right)}{\hat{\sigma}}\hat{\boldsymbol{E}} + \frac{\mu}{U\tau^2}\hat{\nabla}^2\hat{\boldsymbol{u}}$$

Consider the balance between viscosity and EK force terms,

$$\frac{\rho\sigma U^2}{\varepsilon\Delta\sigma E_0^2}\left(\frac{\partial \hat{\boldsymbol{u}}}{\partial \hat{\boldsymbol{t}}} + \hat{\boldsymbol{u}} \cdot \hat{\nabla}\hat{\boldsymbol{u}}\right) = -\frac{\rho\sigma U^2}{\varepsilon\Delta\sigma E_0^2}\hat{\nabla}\hat{p} - \frac{\left(\hat{\nabla}\hat{\sigma} \cdot \hat{\boldsymbol{E}}\right)}{\hat{\sigma}}\hat{\boldsymbol{E}} + \frac{\mu\sigma}{\tau\varepsilon\Delta\sigma E_0^2}\hat{\nabla}^2\hat{\boldsymbol{u}}$$

Consider the balance between the EK force and the convection terms, we have:

$$\frac{\rho\sigma U^2}{\varepsilon\Delta\sigma E_0^2} = 1$$

Which results in a balanced velocity scale:

$$U_e = \sqrt{\varepsilon\Delta\sigma E_0^2/\rho\sigma}$$

Then,

$$\left(\frac{\partial \hat{\boldsymbol{u}}}{\partial \hat{t}} + \hat{\boldsymbol{u}} \cdot \hat{\nabla}\hat{\boldsymbol{u}}\right) = -\hat{\nabla}\hat{p} - \frac{\left(\hat{\nabla}\hat{\sigma}\cdot\hat{\boldsymbol{E}}\right)}{\hat{\sigma}}\hat{\boldsymbol{E}} + \frac{1}{\sqrt{Gr_e}}\hat{\nabla}^2\hat{\boldsymbol{u}} \tag{B2}$$

where Gr_e is:

$$Gr_e = (\tau\varepsilon\Delta\sigma E_0^2/\mu\sigma)^2 \tag{B3}$$

The temporal scale related to the balance between EK force and momentum diffusion is:

$$\tau_{ed} = \frac{\mu\sigma}{\varepsilon\Delta\sigma E_0^2}$$

For a given spatial scale d, the temporal scale evaluated by Ue could be:

$$U_e\tau = d$$

Then, the temporal scale related to forced convection is

$$\tau_{ec} = d/U_e = \sqrt{d^2\rho\sigma/\varepsilon\Delta\sigma E_0^2} \tag{B4}$$

When τ_{ec} is equivalent to the momentum diffusion time $\tau_d = d^2/\nu$, a new spatial scale d_{de} can be expressed as:

$$d_{de} = \sqrt{\nu^2\rho\sigma/\varepsilon E_0^2\Delta\sigma} \tag{B5}$$

Which can also be considered as the smallest scale that the velocity structures can cascade through EK force before smeared by viscosity. By replacing τ with τ_{ec} in equation (B3), we have:

$$Gr_e = \frac{d^2\rho\varepsilon\Delta\sigma E_0^2}{\mu^2\sigma} = \frac{d^2\varepsilon\Delta\sigma E_0^2}{\nu^2\sigma\rho}$$

Because $Ra_e = Gr_e Sc$, where $Sc = \nu / D_e$, D_e is the effective diffusivity and ν is the kinematic viscosity, we have:

$$Ra_e = \frac{d^2 \rho \varepsilon \Delta\sigma E_0^2}{\mu^2 \sigma} = \frac{d^2 \varepsilon \Delta\sigma E_0^2}{\nu \sigma \rho D_e}$$

APPENDIX C: EFFECTIVE DC ELECTRIC FIELD ON THE INTERFACE OF TWO STREAMS WITH DIFFERENT CONDUCTIVITIES

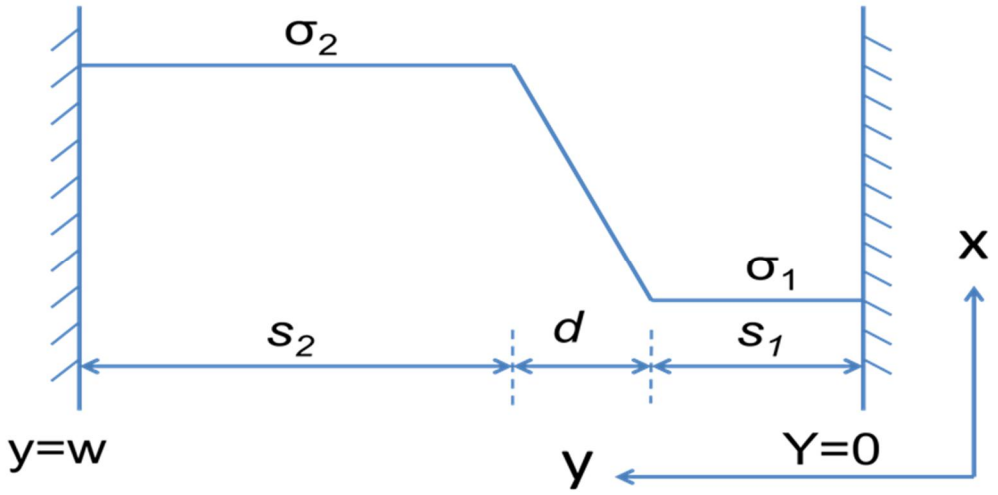

Figure C.1 The profile of conductivity distribution along the spanwise direction of channel. The thickness of interface is d. s_1 and s_2 are the width of stream 1 and 2 respectively.

$E_0=V_0/w$ (V/m) is the nominal intensity of electric field, V_0 is the applied nominal voltage on both poles, w is the width of channel, The thickness of interface is d. s_1 and s_2 are the width of stream 1 and 2 respectively.

$$\sigma(y,t) = \begin{cases} \langle \sigma_1 | s_1 > y \geq 0 \rangle \\ \langle Ay + B | s_1 \leq y \leq s_1 + d \rangle \\ \langle \sigma_2 | s_1 + d < y \leq w \rangle \end{cases} \quad \text{(C1)}$$

where $A = \frac{\sigma_2 - \sigma_1}{d}, B = \sigma_1$. The boundary conditions (B.C.) are:

$$y = -0, \varphi = 0$$

$$y = w, \varphi = V_0$$

where φ is the electric potential, $d = \sqrt{D_e t} = \sqrt{D_e L/U}$ is the diffusion length scale of solutions, U is the convection velocity, L is the distance from trailing edge, D_e is the effective diffusivity.

As the current density J:

$$J = \sigma(y,t)E(y,t) = \frac{E(y,t)}{\rho_R(y,t)} = \frac{V_0}{R_{total}}$$

where $R_{total} = \int_0^w \rho_R(y,t)dy$ and local intensity of electric field,

$$E(y,t) = \frac{d\varphi}{dy}$$

where φ(V) is the electric potential and ρ_R(y, t) is the local resistivity (Ω*m^2).

Then,

$$\frac{\partial \varphi}{\partial y} = \frac{V_0}{R_{total}} \rho_R(y,t)$$

As

$$\rho_R(y,t) = \frac{1}{\sigma(y,t)}$$

Then,

$$\frac{\partial \varphi}{\partial y} = \frac{V_0}{\sigma(y,t) R_{total}}$$

First,

$$R_{total} = \int_0^w \rho_R(y,t)dy = \int_0^{s_1} \frac{1}{\sigma_1} dy + \int_{s_1}^{s_1+d} \frac{1}{Ay+B} dy + \int_{s_1+d}^{w} \frac{1}{\sigma_2} dy$$

$$= \frac{s_1}{\sigma_1} + \frac{w-s_1-d}{\sigma_2} + \frac{d}{\sigma_2-\sigma_1} ln\frac{\sigma_2}{\sigma_1} \quad \text{(C2)}$$

Solve equation (C1) with B.C.:

$$\begin{cases} \varphi(y,t) = \dfrac{V_0 y}{R_{total}(t)\sigma_1}, \quad s_1 > y \geq 0 \\ \varphi(y,t) = \dfrac{V_0}{R_{total}(t)} \left\{ \dfrac{d}{\sigma_2-\sigma_1} ln\left[\dfrac{(\sigma_2-\sigma_1)(y-s_1)+\sigma_1 d}{\sigma_1 d} \right] + \dfrac{s_1}{\sigma_1} \right\}, s_1 \leq y \leq s_1 + d \\ \varphi(y,t) = \left(1 + \dfrac{y-w}{R_{total}(t)\sigma_2}\right) V_0, \quad s_1 + d < y \leq w \end{cases}$$

Hence, the voltage from $y=s_1$ to s_1+d is:

$$V_{int} = \varphi(s_1+d,t) - \varphi(s_1,t) = \frac{V_0}{R_{total}(t)} \frac{d}{\sigma_2-\sigma_1} ln\frac{\sigma_2}{\sigma_1}$$

So:

$$E_{int} = \frac{V_{int}}{d} = \frac{V_0}{R_{total}(\sigma_2-\sigma_1)} ln\frac{\sigma_2}{\sigma_1} \quad \text{(C3)}$$

Because:

$$J = \frac{V_0}{R_{total}} = E_{int}\sigma_{int} = E_0\sigma_{total} \quad \text{(C4)}$$

Then,

$$\sigma_{int} = \frac{d}{R_{int}} = \frac{V_0 d}{V_{int} R_{total}} = \frac{(\sigma_2 - \sigma_1)}{ln\frac{\sigma_2}{\sigma_1}} \tag{C5}$$

$$\sigma_{total} = \frac{w}{R_{total}}$$

where "int" means on interface, and "total" means on the whole channel width.

Introduce a new position, $y_0=s_1+d/2$, as the center of mixing layer and dimensionless the length scale with w, we have $y_0' = y_0/w$ and $d' = d/w$, $d'/2 \le y_0' \le 1 - d'/2$, then:

$$R_{total} = w\left(\frac{y_0' - d'/2}{\sigma_1} + \frac{1 - y_0' - d'/2}{\sigma_2} + \frac{d\prime}{\sigma_2 - \sigma_1} ln\frac{\sigma_2}{\sigma_1}\right) \tag{C6}$$

$$E_{int} = \frac{V_{int}}{d} = \frac{E_0}{\left(\zeta + \frac{1}{\zeta} - 2\right) y_0' + \left[ln\,\zeta - \frac{\zeta}{2} + \frac{1}{2\zeta}\right] d' + 1 - \frac{1}{\zeta}} ln\,\zeta \tag{C7}$$

where $\zeta = \sigma_2/\sigma_1$ and $E_0 = V_0/w$.

So, for DC case, we can define the effective Gr_e and Ra_e as:

$$Gr_e = \frac{d^2 \varepsilon \sigma_{int} E_{int}^2}{\nu^2 \rho \sigma_{total}}$$

$$Ra_e = \frac{d^2 \varepsilon \sigma_{int} E_{int}^2}{\nu \rho D_e \sigma_{total}}$$

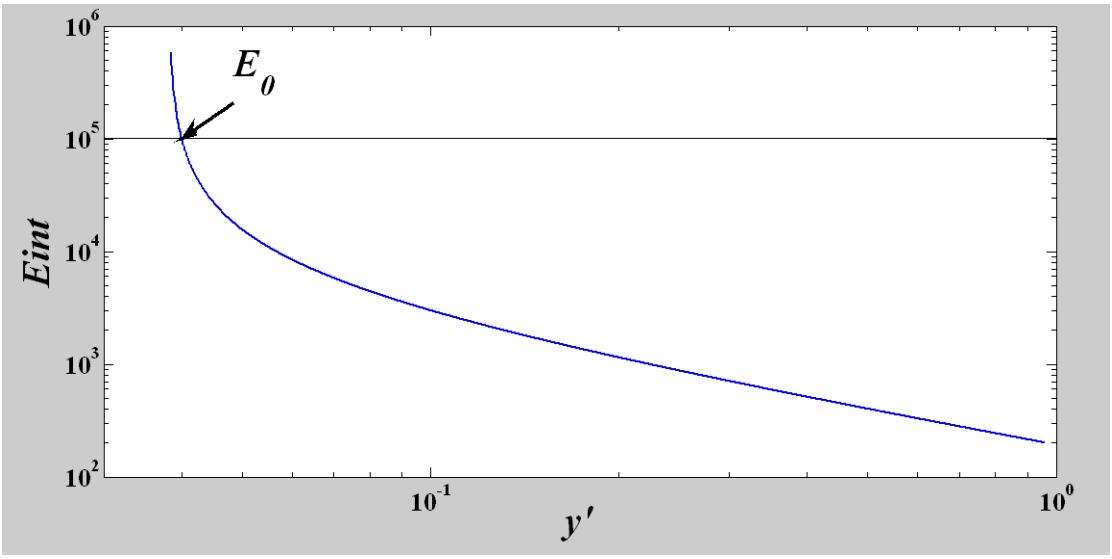

Figure C.2 Effective electric field on the interface varies with the position of interface

APPENDIX D: THE EXPRESSION OF EK FORCE IN AC CASE WITH INITIALLY CONDUCTIVITY GRADIENT:

The control equation of EK flow can be shown below (Ramos 2011):

$$\rho \frac{D\boldsymbol{u}}{Dt} = -\nabla p + F_e + \mu \nabla^2 \boldsymbol{u} \tag{D1}$$

$$F_e = \rho_f \boldsymbol{E} - \frac{1}{2}(\boldsymbol{E} \cdot \boldsymbol{E})\nabla \varepsilon + \frac{1}{2}\nabla \left[\rho \boldsymbol{E} \cdot \boldsymbol{E} \left(\frac{\partial \varepsilon}{\partial \rho}\right)_T\right] \tag{D2}$$

$$\rho_f = \nabla \cdot (\varepsilon \boldsymbol{E}) = \nabla \varepsilon \cdot \boldsymbol{E} + \varepsilon \nabla \cdot \boldsymbol{E} \tag{D3}$$

$$\frac{\partial \rho_f}{\partial t} + \nabla \cdot (\sigma \boldsymbol{E}) + \nabla \cdot \left(\rho_f \boldsymbol{u}\right) = 0 \tag{D4}$$

Assme the flow to be incompressible, $\frac{1}{2}\nabla \left[\rho \boldsymbol{E} \cdot \boldsymbol{E} \left(\frac{\partial \varepsilon}{\partial \rho}\right)_T\right] = 0$. Then, for low speed flow, because the transport of charge by flow convection is much smaller than the transport by electric field, we have $\nabla \cdot \left(\rho_f \boldsymbol{u}\right) = 0$.

In AC electric field where $f_f \ll \sigma/\varepsilon$ (ε/σ is the charge relaxation time), let $\boldsymbol{E} = |\boldsymbol{E}|e^{i\omega t} = \mathrm{Re}(\boldsymbol{E}) + i\mathrm{Im}(\boldsymbol{E}) = \boldsymbol{E_R} + i\boldsymbol{E_I}$, ($\omega = 2\pi f_f$ is the angle frequency), then:

$$F_e = \rho_f \boldsymbol{E_R} - \frac{1}{2}(\boldsymbol{E_R} \cdot \boldsymbol{E_R})\nabla \varepsilon \tag{D5}$$

$$\rho_f = \nabla \cdot (\varepsilon \boldsymbol{E_R}) = \nabla \varepsilon \cdot \boldsymbol{E_R} + \varepsilon \nabla \cdot \boldsymbol{E_R} \tag{D6}$$

where $\varepsilon = \varepsilon_r \varepsilon_0$ is determined by the temperature and medium. Then, for one dimensional case, i.e. $\boldsymbol{E} = E(y,t)\vec{y}$, $E(y,t) = E_m(y,t_l)e^{i\omega t} = E_R(y,t) + iE_I(y,t)$, ($t_l$ is a slow varying time variable. When the characteristic time scale of conductivity fluctuation is much larger than the frequency of AC electric field, the variation of conductivity is assumed to be slow. t_l can be determined by the power spectrum of σ) and $\nabla\varepsilon = \partial\varepsilon/\partial y$, then:

$$F_e = \left(\frac{\partial\varepsilon}{\partial y}E_R + \varepsilon\frac{\partial E_R}{\partial y}\right)E_R - \frac{1}{2}E_R^2\frac{\partial\varepsilon}{\partial y} = \frac{\partial}{\partial y}\left(\frac{1}{2}\varepsilon E_R^2\right) \tag{D7}$$

From equation (D4), and assume low convection velocity,

$$\frac{\partial}{\partial t}\frac{\partial\varepsilon E}{\partial y} + \frac{\partial\sigma E}{\partial y} = 0$$

Taken $E(y,t) = E_m(y,t_l)e^{-i\omega t}$ into account, we have:

$$\frac{\partial}{\partial y}\frac{\partial\varepsilon E}{\partial t} = \frac{\partial}{\partial y}\left[i\omega\varepsilon E + \frac{\partial\varepsilon E_m(y,t_l)}{\partial t}\right] = \frac{\partial}{\partial y}\left[i\omega\varepsilon E + \varepsilon\frac{\partial E_m(y,t_l)}{\partial t_l}\frac{\partial t_l}{\partial t}\right]$$

As $\partial t_l/\partial t \ll 1$, then:

$$\frac{\partial}{\partial y}\frac{\partial\varepsilon E}{\partial t} \approx \frac{\partial}{\partial y}(i\omega\varepsilon E)$$

Then equation (D4) becomes:

$$\frac{\partial i\omega\varepsilon E}{\partial y} + \frac{\partial\sigma E}{\partial y} = 0$$

$$\frac{\partial(\sigma + i\omega\varepsilon)E}{\partial y} = \frac{\partial\sigma^* E}{\partial y} = 0$$

Hence, for 1D case,

$$\sigma^* E = J^*(t) \tag{D8}$$

which is constant for *y*.

For scale *l* conductivity structure, the EK force density is:

$$F_{e,l} = \frac{1}{l}\int_y^{y+l} F_e\, dy = \frac{1}{l}\int_y^{y+l} \frac{\partial}{\partial y}\left(\frac{1}{2}\varepsilon E_R^2\right) dy = \frac{1}{2l}\varepsilon E_R^2\Big|_y^{y+l} \tag{D9}$$

Becasue

$$E_R = \frac{1}{2}\left(E + \tilde{E}\right) \tag{D10}$$

where "~" means complex conjugate.

Plug equation (D8) and (D10) into (D9),

$$F_{e,l} = \frac{\varepsilon}{8l}\left(\frac{J^{*2}}{\sigma^{*2}} + \frac{\widetilde{J^*}^2}{\widetilde{\sigma^*}^2} + 2\frac{|J^*|^2}{|\sigma^*|^2}\right)\Bigg|_y^{y+l}$$

Here,

$$\left.\frac{\boldsymbol{J^{*2}}}{\boldsymbol{\sigma^{*2}}}\right|_{\boldsymbol{y}}^{\boldsymbol{y+l}} = \frac{J^{*2}}{\sigma^{*2}(y+l)} - \frac{J^{*2}}{\sigma^{*2}(y)}$$

$$= J^{*2}\left\{\frac{1}{\left[\langle\sigma^*\rangle_l + \frac{1}{2}\Delta\sigma^*(l)\right]^2} - \frac{1}{\left[\langle\sigma^*\rangle_l - \frac{1}{2}\Delta\sigma^*(l)\right]^2}\right\}$$

$$= -2J^{*2}\frac{1}{\langle\sigma^*\rangle_l^2}\frac{\Delta\sigma^*(l)/\langle\sigma^*\rangle_l}{\left[1-\frac{1}{4}\frac{\Delta\sigma^{*2}(l)}{\langle\sigma^*\rangle_l^2}\right]^2}$$

$$= -2J^{*2}\frac{1}{\langle\sigma^*\rangle_l^2}\frac{\theta_l^*}{\left[1-\frac{1}{4}\theta_l^{*2}\right]^2} \tag{D11a}$$

$$\left.\frac{\widetilde{J}^{*2}}{\widetilde{\sigma}^{*2}}\right|_{\boldsymbol{y}}^{\boldsymbol{y+l}} = -2\widetilde{J}^{*2}\frac{1}{\langle\widetilde{\sigma}^*\rangle_l^2}\frac{\widetilde{\theta}_l^*}{\left[1-\frac{1}{4}\widetilde{\theta}_l^{*2}\right]^2} \tag{D11b}$$

$$\left.\frac{|\boldsymbol{J}^*|^2}{|\boldsymbol{\sigma}^*|^2}\right|_{\boldsymbol{y}}^{\boldsymbol{y+l}} = \frac{|J^*|^2}{\sigma^2(y+l)+\omega^2\varepsilon^2} - \frac{|J^*|^2}{\sigma^2(y)+\omega^2\varepsilon^2}$$

$$= |J^*|^2\left\{\frac{1}{\left[\langle\sigma\rangle_l+\frac{1}{2}\Delta\sigma(l)\right]^2+\omega^2\varepsilon^2} - \frac{1}{\left[\langle\sigma\rangle_l-\frac{1}{2}\Delta\sigma(l)\right]^2+\omega^2\varepsilon^2}\right\}$$

$$= -2\frac{|J^*|^2}{\langle\sigma\rangle_l^2}\frac{\Delta\sigma(l)/\langle\sigma\rangle_l}{\left[1+\frac{1}{4}\frac{\Delta\sigma^2(l)}{\langle\sigma\rangle_l^2}+\frac{\omega^2\varepsilon^2}{\langle\sigma\rangle_l^2}\right]^2-\frac{\Delta\sigma^2(l)}{\langle\sigma\rangle_l^2}}$$

$$= -2\frac{|J^*|^2}{\langle\sigma\rangle_l^2}\frac{\theta_l}{\left[1+\frac{1}{4}\theta_l^2+\beta_l^2\right]^2-\theta_l^2} \tag{D11c}$$

where:

$\langle\sigma\rangle_l = \frac{1}{l}\int_y^{y+l}\sigma\,dy$, $\Delta\sigma(l) = \sigma(y+l)-\sigma(l)$, $\theta_l = \Delta\sigma(l)/\langle\sigma\rangle_l$, $\beta_l = \omega\varepsilon/\langle\sigma\rangle_l \ll 1$, $\theta_l^* = \Delta\sigma^*(l)/\langle\sigma^*\rangle_l = \theta_l\frac{1-i\beta_l}{1-\beta_l^2}$

Because $|\theta_l| \in [0,2], |\theta_l^*| \in [0,2]$, then:

$$\begin{cases} \dfrac{\theta_l^*}{\left[1-\frac{1}{4}\theta_l^{*2}\right]^2} \sim \theta_l - \theta_l\beta_l^2 + \frac{1}{2}\theta_l^3 - i\theta_l\beta_l \\ \dfrac{\widetilde{\theta_l^*}}{\left[1-\frac{1}{4}\widetilde{\theta_l^*}^2\right]^2} \sim \theta_l - \theta_l\beta_l^2 + \frac{1}{2}\theta_l^3 + i\theta_l\beta_l \\ \dfrac{\theta_l}{\left[1+\frac{1}{4}\theta_l^2+\beta_l^2\right]^2-\theta_l^2} = \dfrac{\theta_l}{1-\frac{1}{2}\theta_l^2+2\beta_l^2+\frac{1}{2}\theta_l^2\beta_l^2+\frac{1}{16}\theta_l^4+\beta_l^4} \sim \theta_l\left(1+\frac{1}{2}\theta_l^2-2\beta_l^2\right) \end{cases} \tag{D12}$$

Here, as $\left[1+\frac{1}{4}\theta_l^2+\beta_l^2\right]^2-\theta_l^2 \geq 0$ is always true, $\frac{1}{2}\theta_l^2-2\beta_l^2-\frac{1}{2}\theta_l^2\beta_l^2-\frac{1}{16}\theta_l^4-\beta_l^4$ is definitely smaller than 1. Hence the Taylor expansion can be used. Also higher order terms are ignored.

A new quantity that evaluating the averaging influence of conductivity of scale *l* is introduced as below:

$$\sigma_l^* = 1/\langle 1/\sigma^* \rangle_l \tag{D13}$$

Accompanied with the scale based electric field intensity:

$$E_l = \frac{1}{l}\int_y^{y+l} E\, dy \tag{D14}$$

Which has the relation:

$$\sigma^* E = \sigma_l^* E_l = \sigma_w^* E_w = J^*$$

Then,

$$\begin{cases} \left.\dfrac{J^{*2}}{\sigma^{*2}}\right|_{\boldsymbol{y}}^{\boldsymbol{y+l}} = -2(\sigma_w^* E_w)^2 \frac{\theta_l}{\langle\sigma^*\rangle_l^2}\left(1-\beta_l^2+\frac{1}{2}\theta_l^2-i\beta_l\right) \\ \left.\dfrac{\widetilde{J^*}^2}{\widetilde{\sigma^*}^2}\right|_{\boldsymbol{y}}^{\boldsymbol{y+l}} = -2\left(\widetilde{\sigma_w^*}\widetilde{E_w}\right)^2 \frac{\theta_l}{\langle\widetilde{\sigma^*}\rangle_l^2}\left(1-\beta_l^2+\frac{1}{2}\theta_l^2+i\beta_l\right) \\ \left.\dfrac{|J^*|^2}{|\sigma^*|^2}\right|_{\boldsymbol{y}}^{\boldsymbol{y+l}} = -2\frac{\sigma_w^*\widetilde{\sigma_w^*}E_w\widetilde{E_w}}{\langle\sigma\rangle_l^2}\theta_l\left(1+\frac{1}{2}\theta_l^2-2\beta_l^2\right) \end{cases} \tag{D15}$$

And:

$$F_{e,l} = \frac{\varepsilon}{8l}\Bigg[-2(\sigma_w^* E_w)^2 \frac{\theta_l}{\langle\sigma^*\rangle_l^2}\left(1-\beta_l^2+\frac{1}{2}\theta_l^2-i\beta_l\right) - 2\left(\widetilde{\sigma_w^*}\widetilde{E_w}\right)^2 \frac{\theta_l}{\langle\widetilde{\sigma^*}\rangle_l^2}\left(1-\beta_l^2+\frac{1}{2}\theta_l^2+i\beta_l\right) - 4E_w\widetilde{E_w}\frac{\sigma_w^*\widetilde{\sigma_w^*}}{\langle\sigma\rangle_l^2}\theta_l\left(1+\frac{1}{2}\theta_l^2-2\beta_l^2\right)\Bigg]$$

$$= -\frac{\varepsilon\theta_l}{4l}\left[(\sigma_w^* E_w)^2\frac{\Psi}{\langle\sigma^*\rangle_l^2}+\left(\widetilde{\sigma_w^*}\widetilde{E_w}\right)^2\frac{\widetilde{\Psi}}{\langle\widetilde{\sigma^*}\rangle_l^2}+2E_w\widetilde{E_w}\frac{\sigma_w^*\widetilde{\sigma_w^*}}{\langle\sigma\rangle_l^2}\left(1+\frac{1}{2}\theta_l^2-2\beta_l^2\right)\right]$$

where $\Psi = 1-\beta_l^2+\frac{1}{2}\theta_l^2-i\beta_l$.

Two cases are considered.

Well mixed stage:

Furthermore, considering a low conductivity fluctuation case, i.e.:

$$\theta_l \ll 1, \ \forall l.$$

Then we have following approximations:

$$\begin{cases} \langle\sigma\rangle_l \approx \langle\sigma\rangle_w \approx \sigma_l \approx \sigma_w \\ \langle\sigma^*\rangle_l \approx \langle\sigma^*\rangle_w \approx \sigma_l^* \approx \sigma_w^* \\ \langle\widetilde{\sigma^*}\rangle_l \approx \langle\widetilde{\sigma^*}\rangle_w \approx \widetilde{\sigma_l^*} \approx \widetilde{\sigma_w^*} \\ \beta_l = \beta_w \end{cases} \tag{D16}$$

Because here $\sigma_w^*\widetilde{\sigma_w^*} \approx \langle\sigma\rangle_w^2 + \omega^2\varepsilon^2$, then plug equation (D15) into $F_{e,l}$, we have:

$$F_{e,l} = \frac{\varepsilon}{8l}\Bigg[-2(\sigma_w^* E_w)^2 \frac{\theta_l}{\langle\sigma^*\rangle_l^2}\left(1-\beta_l^2+\frac{1}{2}\theta_l^2-i\beta_l\right)$$

$$-2\left(\widetilde{\sigma_w^*}\widetilde{E_w}\right)^2 \frac{\theta_l}{\langle\widetilde{\sigma^*}\rangle_l^2}\left(1-\beta_l^2+\frac{1}{2}\theta_l^2+i\beta_l\right)$$

$$-4E_w\widetilde{E_w}\frac{\langle\sigma\rangle_w^2+\omega^2\varepsilon^2}{\langle\sigma\rangle_l^2}\theta_l\left(1+\frac{1}{2}\theta_l^2-2\beta_l^2\right)\Bigg]$$

Applying equation (D16), we have:

$$F_{e,l} = \frac{\varepsilon}{8l}\Bigg[-2E_w^2\theta_l\left(1-\beta_l^2+\frac{1}{2}\theta_l^2-i\beta_l\right)-2\widetilde{E_w}^2\theta_l\left(1-\beta_l^2+\frac{1}{2}\theta_l^2+i\beta_l\right)$$

$$-4E_w\widetilde{E_w}\theta_l(1+\beta_l^2)\left(1+\frac{1}{2}\theta_l^2-2\beta_l^2\right)\Bigg]$$

$$\sim -\frac{\varepsilon}{4l}\Big[E_w^2\theta_l\left(1-\beta_l^2+\tfrac{1}{2}\theta_l^2-i\beta_l\right)+\widetilde{E_w}^2\theta_l\left(1-\beta_l^2+\tfrac{1}{2}\theta_l^2+i\beta_l\right)+$$

$$2E_w\widetilde{E_w}\theta_l\left(1+\tfrac{1}{2}\theta_l^2-\beta_l^2\right)\Big] \quad \text{(D17)}$$

Note that:

$$E_w = \frac{V^*}{w} = \frac{V_{amp}e^{i\omega t}}{w} = E_{amp}e^{i\omega t}$$

Then,

$$F_{e,l} = -\frac{\varepsilon E_{amp}^2\theta_l}{2l}\Big[\left(1-\beta_l^2+\tfrac{1}{2}\theta_l^2\right)\cos(2\omega t)+\beta_l\sin(2\omega t)+\left(1+\tfrac{1}{2}\theta_l^2-\beta_l^2\right)\Big] \quad \text{(D18)}$$

If further neglecting $O(\theta_l^3)$, we have:

$$F_{e,l} = -\frac{\varepsilon E_{amp}^2\theta_l}{2l}\left[(1-\beta_l^2)\cos(2\omega t)+\beta_l\sin(2\omega t)+(1-\beta_l^2)\right] \quad \text{(D19)}$$

By taking short-time averaging ($1/f_f \ll T \ll 1/f_\sigma$),

$$\overline{\overline{F_{e,l}}}(T) = \frac{1}{T}\int_t^{t+T} F_{e,l}\, dt = -\frac{\varepsilon E_{amp}^2 \theta_l}{2l}(1-\beta_l^2) \tag{D20}$$

where $\overline{\cdot}$ means short-time averaging.

Initial stage:

Here, an interface of conductivity is present. The initial EBF applied on the interface should be evaluated.

In this case, $\theta_l \ll 1,\ \forall l$ is not satisfied, but $\theta_l \le 2$ on the interface, where *l* is the width of conductivity interface. the situation is more complicated.

$$\begin{cases} \dfrac{\theta_l^*}{\left[1-\frac{1}{4}\theta_l^{*2}\right]^2} \sim \theta_l - \theta_l\beta_l^2 + \frac{1}{2}\theta_l^3 - i\theta_l\beta_l \\ \dfrac{\widetilde{\theta_l^*}}{\left[1-\frac{1}{4}\widetilde{\theta_l^*}^2\right]^2} \sim \theta_l - \theta_l\beta_l^2 + \frac{1}{2}\theta_l^3 + i\theta_l\beta_l \\ \dfrac{\theta_l}{\left[1+\frac{1}{4}\theta_l^2+\beta_l^2\right]^2-\theta_l^2} \sim \theta_l\left(1+\frac{1}{2}\theta_l^2 - 2\beta_l^2 - \frac{1}{2}\theta_l^2\beta_l^2 - \frac{1}{16}\theta_l^4 - \beta_l^4\right) \end{cases} \tag{D21}$$

and

$$\begin{aligned} F_{e,l} = -\frac{\varepsilon}{4l}\Bigg[& (\sigma_w^* E_w)^2 \frac{\theta_l}{\langle\sigma^*\rangle_l^2}\left(1-\beta_l^2+\frac{1}{2}\theta_l^2 - i\beta_l\right) \\ & + \left(\widetilde{\sigma_w^*}\widetilde{E_w}\right)^2 \frac{\theta_l}{\langle\widetilde{\sigma^*}\rangle_l^2}\left(1-\beta_l^2+\frac{1}{2}\theta_l^2 + i\beta_l\right) \\ & + 2E_w\widetilde{E_w}\frac{\sigma_w^*\widetilde{\sigma_w^*}}{\langle\sigma\rangle_l^2}\theta_l\left(1+\frac{1}{2}\theta_l^2 - 2\beta_l^2 - \frac{1}{2}\theta_l^2\beta_l^2 - \frac{1}{16}\theta_l^4 - \beta_l^4\right)\Bigg] \end{aligned}$$

if the conductivity distribution is as following (*l*=*d*):

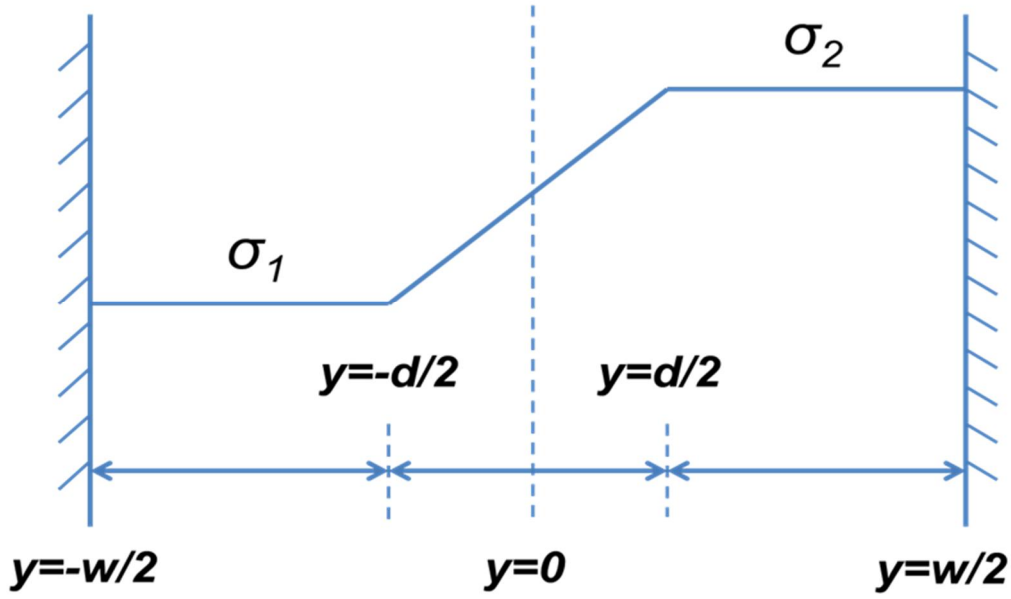

Figure D.1 Conductivity distribution along spanwise direction

$$\sigma_w^* = \frac{w}{\frac{1}{2}(w-d)\left(\frac{1}{\sigma_1^*}+\frac{1}{\sigma_2^*}\right)+\frac{d}{\sigma_2-\sigma_1}\ln\frac{\sigma_2^*}{\sigma_1^*}}$$

Because in our case, the conductivity variation is at a much lower frequency compared to the frequency of AC electric field (100 kHz). During short-time averaging, all the conductivity related variables, such as σ_w^* and $\langle\sigma^*\rangle_l$ etc, could be considered as constant, and:

$$F_{e,d} = -\frac{\varepsilon}{4d}\left[P{E_w}^2 + \tilde{P}\widetilde{E_w}^2 + 2E_w\widetilde{E_w}\frac{\sigma_w^*\widetilde{\sigma_w^*}}{\langle\sigma\rangle_d^2}\theta_d\left(1+\frac{1}{2}\theta_d^2-2\beta_d^2-\frac{1}{2}\theta_d^2\beta_d^2-\frac{1}{16}\theta_d^4-\beta_d^4\right)\right]$$

where $P = {\sigma_w^*}^2\frac{\theta_l}{\langle\sigma^*\rangle_d^2}\left(1-\beta_d^2+\frac{1}{2}\theta_d^2-i\beta_d\right) = A(T)e^{iB}$. Then:

$$PE_w^2 = A(T)e^{i(2\omega t+B)} \text{ and } \overline{{P{E_w}^2 + \tilde{P}\widetilde{E_w}^2}} \approx 0$$

Therefore, the short-time averaged EBF on interface can be evaluated as:

$$\overline{\overline{F_{e,d}}}(T) = F_{e,d} = -\frac{\varepsilon}{2d}\left[\overline{\overline{E_w \widetilde{E_w}}}\frac{\sigma_w^* \widetilde{\sigma_w^*}}{\langle\sigma\rangle_d^2}\theta_d\left(1+\frac{1}{2}\theta_d^2 - 2\beta_d^2 - \frac{1}{2}\theta_d^2\beta_d^2 - \frac{1}{16}\theta_d^4 - \beta_d^4\right)\right]$$

$$\approx -\frac{\varepsilon E_{amp}^2}{2d}\frac{\sigma_w^* \widetilde{\sigma_w^*}}{\langle\sigma\rangle_d^2}\theta_d\left(1+\frac{1}{2}\theta_d^2 - 2\beta_d^2 - \frac{1}{2}\theta_d^2\beta_d^2 - \frac{1}{16}\theta_d^4 - \beta_d^4\right) \quad \text{(D22)}$$

where $\langle\sigma\rangle_d = (\sigma_1+\sigma_2)/2$, $\theta_d = 2(\sigma_2-\sigma_1)/(\sigma_1+\sigma_2)$, $\beta_d = \omega\varepsilon/\langle\sigma\rangle_d$ and $\langle\sigma\rangle_w = \langle\sigma\rangle_d$.

APPENDIX E: DERIVATION OF SCALING EXPONENTS:

$$\langle {u_l}^2 \rangle \sim \langle \left| \overline{\overline{F_{e,l}}} \right| \rangle l/\rho$$

$$\sim \langle \left| -\frac{\varepsilon E_{amp}^2 \theta_l}{2l} (1 - \beta_w^2) \right| \rangle \frac{l}{\rho}$$

$$\sim \frac{\varepsilon E_{amp}^2 (1 - \beta_w^2)}{2\rho} \langle |\theta_l| \rangle$$

$$\sim \frac{\varepsilon E_{amp}^2 (1 - \beta_w^2)}{2\rho} \langle \left| \theta_{l_0} \right| \rangle l^{* \delta_{\sigma,1}}$$

$$\sim \Lambda \, l^{* \delta_{\sigma,1}} / \rho$$

$$\sim l^{* \delta_{\sigma,1}}$$

APPENDIX F: DERIVATION OF SCALING EXPONENTS FROM DIMENSIONS:

The cascading process of kinetic energy is very similar as in RB flow where buoyancy is the driven force of flow. Hence, similar as Bolgiano (1959), Obukhov (1959) and Yakhot (1992), the energy cascade of AC EK flow can be relevantly described by the mean dissipation rate of complex permittivity, nominal electric field intensity and medium density.

$$S_u^2(l) \sim \epsilon_\varepsilon^a E_{amp}^b \rho^c l^d$$

where $\epsilon_\varepsilon = \mathrm{Re}\langle D_\varepsilon(\partial\varepsilon^*/\partial x)^2\rangle \sim \varepsilon^2/s \sim kg^2 \cdot m^2/V^4 \cdot s^5$, $E_{amp} \sim V/m$, $\rho = kg/m^3$, $l \sim m$, $S_u^2(l) \sim m^2/s^2$.

Thus,

$$\begin{cases} 2a + c = 0, & for\ kg \\ 2a - b - 3c + d = 2, & for\ m \\ -5a = -2, & for\ s \\ -4a + b = 0, & for\ V \end{cases}$$

Then, we have:

$$\begin{cases} a = 2/5 \\ b = 8/5 \\ c = -4/5 \\ d = 2/5 \end{cases}$$

Thus,

$$S_u^2(l) \sim \epsilon_\varepsilon^{2/5} E_{amp}^{8/5} \rho^{-4/5} l^{2/5}$$

As the changing of electric permittivity is dominated by the imaginary part of complex permittivity, i.e. σ/ω. The dissipation rate of electric permittivity is intrinsically that of conductivity, as below:

$$\epsilon_\varepsilon = \epsilon_\sigma/\omega^2$$

$$S_u^2(l) \sim \epsilon_\sigma^{2/5} E_{amp}^{8/5} \omega^{-4/5} \rho^{-4/5} l^{2/5}$$

where $\epsilon_\sigma = \langle D_\sigma (\partial\sigma/\partial x)^2 \rangle$ and $D_\varepsilon = D_\sigma$.

Similarly, the scalar transport is also dominated by the dynamical process due to the passive transport. For complex permittivity structure, or the equivalent conductivity structure, we have:

$$S_\varepsilon^2(l) \sim S_\sigma^2(l)/\omega^4 \sim \epsilon_\varepsilon^a E_{amp}^b \rho^c l^d$$

where $S_\varepsilon^2(l) \sim kg^2 \cdot m^2/V^4 \cdot s^4$, $S_\sigma^2(l) \sim kg^2 \cdot m^2/V^4 \cdot s^8$ and $\omega \sim 1/s$. Then, we have:

$$\begin{cases} 2a + c = 2, & for\ kg \\ 2a - b - 3c + d = 2, & for\ m \\ -5a = -4, & for\ s \\ -4a + b = -4, & for\ V \end{cases}$$

The solutions are:

$$\begin{cases} a = 4/5 \\ b = -4/5 \\ c = 2/5 \\ d = 4/5 \end{cases}$$

$$S_\varepsilon^2(l) \sim \epsilon_\varepsilon^{4/5} E_{amp}^{-4/5} \rho^{2/5} l^{4/5}$$

and because $\epsilon_\varepsilon = \epsilon_\sigma/\omega^2$,

$$S_\sigma^2(l) \sim \epsilon_\sigma^{4/5} E_{amp}^{-4/5} \omega^{12/5} \rho^{2/5} l^{4/5}$$

APPENDIX G: DERIVATION OF EXPRESSION OF L_0:

l_0 is a reference scale used to estimate the upper bound of self-similar range of scale. It should be less or equal to the integral length of flow. Because

$$S_u^2(l) \sim \langle|\theta_{l_0}|\rangle \varepsilon E_{amp}^2 (1-\beta_w^2) l_0^{-2/5} l^{2/5}/2\rho \sim \epsilon_\sigma^{2/5} E_{amp}^{8/5} \omega^{-4/5} \rho^{-4/5} l^{2/5}$$

$$l_0^{2/5} \sim \left[\frac{\langle|\theta_{l_0}|\rangle(1-\beta_w^2)}{2}\right] \varepsilon \epsilon_\sigma^{2/5} E_{amp}^{2/5} \omega^{-4/5} \rho^{-1/5}$$

Let $G\left(\langle|\theta_{l_0}|\rangle; \beta_w\right) \sim \left[\langle|\theta_{l_0}|\rangle(1-\beta_w^2)/2\right]^{5/2}$, we have:

$$l_0 \sim G \rho^{-1/2} \varepsilon^{5/2} E_{amp} \epsilon_\sigma^{-1} \omega^2$$

APPENDIX H: DERIVATION OF EXPRESSION OF L_{EK}:

When equation (1) and (21) are balanced, i.e.:

$$S_u^2(l_{ek}) \sim \epsilon_u^{2/3} l_{ek}^{2/3} \sim \epsilon_\sigma^{2/5} E_{amp}^{8/5} \omega^{-4/5} \rho^{-4/5} l_{ek}^{2/5}$$

$$l_{ek}^{4/15} \sim \epsilon_\sigma^{2/5} \epsilon_u^{-2/3} E_{amp}^{8/5} \omega^{-4/5} \rho^{-4/5}$$

$$l_{ek} \sim \epsilon_\sigma^{3/2} \epsilon_u^{-5/2} E_{amp}^{6} \omega^{-3} \rho^{-3}$$

and then:

$$\frac{l_{ek}}{l_0} \sim G^{-1} \omega^{-5} \left(\frac{E_{amp}^2}{\rho \varepsilon} \right)^{5/2} \left(\frac{\epsilon_\sigma}{\epsilon_u} \right)^{5/2} \sim G^{-1} \left(\frac{1}{\omega^2 \varepsilon^2} \frac{\varepsilon E_{amp}^2}{\rho} \right)^{5/2} \left(\frac{\epsilon_\sigma}{\epsilon_u} \right)^{5/2}$$

APPENDIX I: DERIVATION OF EXPRESSION OF L_K:

When the advection has the equivalent time scale with momentum diffusion, we have the relation:

$$l_K/\sqrt{\langle u_l{}^2\rangle} = l_K^2/\nu$$

$$l_K = \nu/\sqrt{\langle u_l{}^2\rangle} \sim \epsilon_\sigma^{-1/5} E_{amp}^{-4/5} \omega^{2/5} \rho^{2/5} l_K^{-1/5} \nu$$

$$l_K \sim \epsilon_\sigma^{-1/6} E_{amp}^{-2/3} \omega^{1/3} \rho^{1/3} \nu^{5/6}$$

By comparing the EK cascading process with RB flow, the scalar cascade has similar process and hence,

$$\epsilon_\sigma \sim D_\sigma \left(\frac{\sigma_2 - \sigma_1}{w}\right)^2 Sh$$

Then,

$$l_K \sim \left[D_\sigma \left(\frac{\sigma_2 - \sigma_1}{w}\right)^2 Sh\right]^{-1/6} E_{amp}^{-2/3} \omega^{1/3} \rho^{1/3} \nu^{5/6}$$

$$\sim D_\sigma^{-1/6} \left(\frac{\sigma_2 - \sigma_1}{w}\right)^{-1/3} Sh^{-1/6} E_{amp}^{-2/3} \omega^{1/3} \rho^{1/3} \nu^{5/6}$$

$$\sim \left[\frac{\varepsilon(\sigma_2 - \sigma_1) w^2 E_{amp}^2}{\rho \nu D_\sigma \langle\sigma\rangle_w}\right]^{-1/3} Sh^{-1/6} \left(\frac{\varepsilon\omega}{\langle\sigma\rangle_w}\right)^{1/3} \left(\frac{\nu}{D_\sigma}\right)^{1/2} w$$

which finally is:

$$l_K \sim Ra_e^{-1/3} Sh^{-1/6} \beta_w^{1/3} Sc^{1/2} w$$

where $Ra_e = \varepsilon(\sigma_2 - \sigma_1) w^2 E_{amp}^2 / \rho \nu D_\sigma \langle \sigma \rangle_w$ is the nominal electric Rayleigh number, $Sh = Kw/D_\sigma$ is the Sherwood number.

APPENDIX J: ENERGY EQUATION OF EK TURBULENCE (FOR THE CASE WHERE FORCING FREQUENCY IS MUCH HIGHER THAN VELOCITY FREQUENCY)

Turbulent energy evolution in EK flow:

$$\rho \frac{D\boldsymbol{u}}{Dt} = -\nabla p + \mu \nabla^2 \boldsymbol{u} + F_e \tag{J1}$$

$$\rho \frac{D\boldsymbol{u}}{Dt} = -\nabla p + \mu \nabla^2 \boldsymbol{u} + (\nabla \varepsilon \cdot \boldsymbol{E})\boldsymbol{E} + \varepsilon(\nabla \cdot \boldsymbol{E})\boldsymbol{E} - \frac{1}{2}(\boldsymbol{E} \cdot \boldsymbol{E})\nabla \varepsilon \tag{J2}$$

Let: $\boldsymbol{u} = \boldsymbol{u}' + \boldsymbol{U},\ \boldsymbol{E} = \boldsymbol{E}' + \bar{\boldsymbol{E}},\ \boldsymbol{E}' = \boldsymbol{E}_{\boldsymbol{h}}' + \boldsymbol{E}_{\boldsymbol{l}}',\ p = p' + P,\ \varepsilon = \varepsilon' + \bar{\varepsilon}$, (where bold font indicates vectors, $\boldsymbol{u}'$, p', ε' and $\boldsymbol{E}_{\boldsymbol{l}}'$ are low-frequency components and E_h' is high-frequency components), and expand equation (J2), we have:

$$\rho\left[\frac{\partial \boldsymbol{u}'}{\partial t} + (\boldsymbol{U} \cdot \nabla)\boldsymbol{U} + (\boldsymbol{U} \cdot \nabla)\boldsymbol{u}' + (\boldsymbol{u}' \cdot \nabla)\boldsymbol{U} + (\boldsymbol{u}' \cdot \nabla)\boldsymbol{u}'\right] = -\nabla(p' + P) +$$

$$\mu \nabla^2(\boldsymbol{u}' + \boldsymbol{U}) + [\nabla(\varepsilon' + \bar{\varepsilon}) \cdot (\boldsymbol{E}' + \bar{\boldsymbol{E}})](\boldsymbol{E}' + \bar{\boldsymbol{E}}) + (\varepsilon' + \bar{\varepsilon})[\nabla \cdot (\boldsymbol{E}' + \bar{\boldsymbol{E}})](\boldsymbol{E}' + \bar{\boldsymbol{E}}) -$$

$$\frac{1}{2}[(\boldsymbol{E}' + \bar{\boldsymbol{E}}) \cdot (\boldsymbol{E}' + \bar{\boldsymbol{E}})]\nabla(\varepsilon' + \bar{\varepsilon}) \tag{J3}$$

Take short-time averaging $\bar{\cdot}$ on equation (J3), and because $\bar{\boldsymbol{E}} = \boldsymbol{0}$ and ε' is low frequency variation:

$$\overline{\overline{[\nabla(\varepsilon'+\bar{\varepsilon})\cdot(\boldsymbol{E'}+\bar{\boldsymbol{E}})](\boldsymbol{E'}+\bar{\boldsymbol{E}})}} = \overline{\overline{\left[\nabla(\varepsilon'+\bar{\varepsilon})\cdot\left(\boldsymbol{E}_{\boldsymbol{h}}'+\boldsymbol{E}_{\boldsymbol{l}}'\right)\right]\left(\boldsymbol{E}_{\boldsymbol{h}}'+\boldsymbol{E}_{\boldsymbol{l}}'\right)}}$$

$$= \overline{\overline{(\nabla\varepsilon'\cdot\boldsymbol{E}_{\boldsymbol{h}}')\boldsymbol{E}_{\boldsymbol{h}}'}} + \overline{\overline{(\nabla\varepsilon'\cdot\boldsymbol{E}_{\boldsymbol{h}}')\boldsymbol{E}_{\boldsymbol{l}}'}} + \overline{\overline{(\nabla\varepsilon'\cdot\boldsymbol{E}_{\boldsymbol{l}}')\boldsymbol{E}_{\boldsymbol{h}}'}} + \overline{\overline{(\nabla\varepsilon'\cdot\boldsymbol{E}_{\boldsymbol{l}}')\boldsymbol{E}_{\boldsymbol{l}}'}}$$

$$+ \overline{\overline{(\nabla\bar{\varepsilon}\cdot\boldsymbol{E}_{\boldsymbol{h}}')\boldsymbol{E}_{\boldsymbol{h}}'}} + \overline{\overline{(\nabla\bar{\varepsilon}\cdot\boldsymbol{E}_{\boldsymbol{h}}')\boldsymbol{E}_{\boldsymbol{l}}'}} + \overline{\overline{(\nabla\bar{\varepsilon}\cdot\boldsymbol{E}_{\boldsymbol{l}}')\boldsymbol{E}_{\boldsymbol{h}}'}} + \overline{\overline{(\nabla\bar{\varepsilon}\cdot\boldsymbol{E}_{\boldsymbol{l}}')\boldsymbol{E}_{\boldsymbol{l}}'}}$$

As, in short time averaging, only the high frequency components are averaged. We have:

$$\overline{\overline{\boldsymbol{E}_{\boldsymbol{h}}'}} = \overline{\overline{(\nabla\varepsilon'\cdot\boldsymbol{E}_{\boldsymbol{h}}')\boldsymbol{E}_{\boldsymbol{l}}'}} = \overline{\overline{(\nabla\varepsilon'\cdot\boldsymbol{E}_{\boldsymbol{l}}')\boldsymbol{E}_{\boldsymbol{h}}'}} = \overline{\overline{(\nabla\bar{\varepsilon}\cdot\boldsymbol{E}_{\boldsymbol{h}}')\boldsymbol{E}_{\boldsymbol{l}}'}} = \overline{\overline{(\nabla\bar{\varepsilon}\cdot\boldsymbol{E}_{\boldsymbol{l}}')\boldsymbol{E}_{\boldsymbol{h}}'}} = 0$$

$$\overline{\overline{\nabla\varepsilon'}} = \nabla\varepsilon', \qquad \overline{\overline{\nabla\bar{\varepsilon}}} = \nabla\bar{\varepsilon}, \qquad \overline{\overline{\boldsymbol{E}_{\boldsymbol{l}}'}} = \boldsymbol{E}_{\boldsymbol{l}}'$$

then,

$$\overline{\overline{[\nabla(\varepsilon'+\bar{\varepsilon})\cdot(\boldsymbol{E'}+\bar{\boldsymbol{E}})](\boldsymbol{E'}+\bar{\boldsymbol{E}})}}$$

$$= \overline{\overline{(\nabla\varepsilon'\cdot\boldsymbol{E}_{\boldsymbol{h}}')\boldsymbol{E}_{\boldsymbol{h}}'}} + \left(\nabla\varepsilon'\cdot\boldsymbol{E}_{\boldsymbol{l}}'\right)\boldsymbol{E}_{\boldsymbol{l}}' + \overline{\overline{(\nabla\bar{\varepsilon}\cdot\boldsymbol{E}_{\boldsymbol{h}}')\boldsymbol{E}_{\boldsymbol{h}}'}} + \left(\nabla\bar{\varepsilon}\cdot\boldsymbol{E}_{\boldsymbol{l}}'\right)\boldsymbol{E}_{\boldsymbol{l}}'$$

$$\overline{\overline{(\varepsilon'+\bar{\varepsilon})[\nabla\cdot(\boldsymbol{E'}+\bar{\boldsymbol{E}})](\boldsymbol{E'}+\bar{\boldsymbol{E}})}}$$

$$= \overline{\overline{\varepsilon'\left(\nabla\cdot\boldsymbol{E}_{\boldsymbol{h}}'\right)\boldsymbol{E}_{\boldsymbol{h}}'}} + \varepsilon'\left(\nabla\cdot\boldsymbol{E}_{\boldsymbol{l}}'\right)\boldsymbol{E}_{\boldsymbol{l}}' + \bar{\varepsilon}\left(\nabla\cdot\boldsymbol{E}_{\boldsymbol{l}}'\right)\boldsymbol{E}_{\boldsymbol{l}}' + \overline{\overline{\bar{\varepsilon}(\nabla\cdot\boldsymbol{E}_{\boldsymbol{h}}')\boldsymbol{E}_{\boldsymbol{h}}'}}$$

$$\overline{\overline{[(\boldsymbol{E'}+\bar{\boldsymbol{E}})\cdot(\boldsymbol{E'}+\bar{\boldsymbol{E}})]\nabla(\varepsilon'+\bar{\varepsilon})}} = \overline{\overline{\boldsymbol{E}_{\boldsymbol{h}}'\cdot\boldsymbol{E}_{\boldsymbol{h}}'}}\nabla\varepsilon' + \boldsymbol{E}_{\boldsymbol{l}}'\cdot\boldsymbol{E}_{\boldsymbol{l}}'\nabla\varepsilon' + \boldsymbol{E}_{\boldsymbol{l}}'\cdot\boldsymbol{E}_{\boldsymbol{l}}'\nabla\bar{\varepsilon} + \overline{\overline{\boldsymbol{E}_{\boldsymbol{h}}'\cdot\boldsymbol{E}_{\boldsymbol{h}}'}}\nabla\bar{\varepsilon}$$

Similarly, as:

$$\overline{\overline{\boldsymbol{u}'}} = \boldsymbol{u}', \qquad \overline{\overline{p'}} = p'$$

Equation (J3) after short-time averaging becomes:

$$\overline{\overline{\rho\left[\frac{\partial\boldsymbol{u}'}{\partial t} + (\boldsymbol{U}\cdot\nabla)\boldsymbol{U} + (\boldsymbol{U}\cdot\nabla)\boldsymbol{u}' + (\boldsymbol{u}'\cdot\nabla)\boldsymbol{U} + (\boldsymbol{u}'\cdot\nabla)\boldsymbol{u}'\right]}} = \overline{\overline{-\nabla(p'+P)}} + \overline{\overline{\mu\nabla^2(\boldsymbol{u}'+\boldsymbol{U})}}$$

$$+\overline{\overline{(\nabla\varepsilon'\cdot\boldsymbol{E}_h')\boldsymbol{E}_h'}}+(\nabla\varepsilon'\cdot\boldsymbol{E}_l')\boldsymbol{E}_l'+\overline{\overline{(\nabla\bar{\varepsilon}\cdot\boldsymbol{E}_h')\boldsymbol{E}_h'}}+(\nabla\bar{\varepsilon}\cdot\boldsymbol{E}_l')\boldsymbol{E}_l'$$

$$+\overline{\overline{\varepsilon'(\nabla\cdot\boldsymbol{E}_h')\boldsymbol{E}_h'}}+\varepsilon'(\nabla\cdot\boldsymbol{E}_l')\boldsymbol{E}_l'+\bar{\varepsilon}(\nabla\cdot\boldsymbol{E}_l')\boldsymbol{E}_l'+\overline{\overline{\bar{\varepsilon}(\nabla\cdot\boldsymbol{E}_h')\boldsymbol{E}_h'}}$$

$$-\frac{1}{2}\left(\overline{\overline{\boldsymbol{E}_h'\cdot\boldsymbol{E}_h'}}\nabla\varepsilon'+\boldsymbol{E}_l'\cdot\boldsymbol{E}_l'\nabla\varepsilon'+\boldsymbol{E}_l'\cdot\boldsymbol{E}_l'\nabla\bar{\varepsilon}+\overline{\overline{\boldsymbol{E}_h'\cdot\boldsymbol{E}_h'}}\nabla\bar{\varepsilon}\right)$$

Or

$$\rho\left[\frac{\partial\boldsymbol{u}'}{\partial t}+(\boldsymbol{U}\cdot\nabla)\boldsymbol{U}+(\boldsymbol{U}\cdot\nabla)\boldsymbol{u}'+(\boldsymbol{u}'\cdot\nabla)\boldsymbol{U}+(\boldsymbol{u}'\cdot\nabla)\boldsymbol{u}'\right]=-\nabla(p'+P)+\mu\nabla^2(\boldsymbol{u}'+\boldsymbol{U})$$

$$+\overline{\overline{(\nabla\varepsilon'\cdot\boldsymbol{E}_h')\boldsymbol{E}_h'}}+(\nabla\varepsilon'\cdot\boldsymbol{E}_l')\boldsymbol{E}_l'+\overline{\overline{(\nabla\bar{\varepsilon}\cdot\boldsymbol{E}_h')\boldsymbol{E}_h'}}+(\nabla\bar{\varepsilon}\cdot\boldsymbol{E}_l')\boldsymbol{E}_l'$$

$$+\varepsilon'\overline{\overline{(\nabla\cdot\boldsymbol{E}_h')\boldsymbol{E}_h'}}+\varepsilon'(\nabla\cdot\boldsymbol{E}_l')\boldsymbol{E}_l'+\bar{\varepsilon}(\nabla\cdot\boldsymbol{E}_l')\boldsymbol{E}_l'+\bar{\varepsilon}\overline{\overline{(\nabla\cdot\boldsymbol{E}_h')\boldsymbol{E}_h'}}$$

$$-\tfrac{1}{2}\left(\overline{\overline{\boldsymbol{E}_h'\cdot\boldsymbol{E}_h'}}\nabla\varepsilon'+\boldsymbol{E}_l'\cdot\boldsymbol{E}_l'\nabla\varepsilon'+\boldsymbol{E}_l'\cdot\boldsymbol{E}_l'\nabla\bar{\varepsilon}+\overline{\overline{\boldsymbol{E}_h'\cdot\boldsymbol{E}_h'}}\nabla\bar{\varepsilon}\right)\qquad\text{(J4)}$$

Then, applying ensemble averaging $\bar{\cdot}$ on equation (J4), we get:

$$\overline{\rho\left[\frac{\partial\boldsymbol{u}'}{\partial t}+(\boldsymbol{U}\cdot\nabla)\boldsymbol{U}+(\boldsymbol{U}\cdot\nabla)\boldsymbol{u}'+(\boldsymbol{u}'\cdot\nabla)\boldsymbol{U}+(\boldsymbol{u}'\cdot\nabla)\boldsymbol{u}'\right]}=\overline{-\nabla(p'+P)}+\overline{\mu\nabla^2(\boldsymbol{u}'+\boldsymbol{U})}$$

$$+\overline{\left[\overline{(\nabla\varepsilon'\cdot\boldsymbol{E}_h')\boldsymbol{E}_h'}\right]}+\overline{(\nabla\varepsilon'\cdot\boldsymbol{E}_l')\boldsymbol{E}_l'}+\overline{\left[\overline{(\nabla\bar{\varepsilon}\cdot\boldsymbol{E}_h')\boldsymbol{E}_h'}\right]}+\overline{(\nabla\bar{\varepsilon}\cdot\boldsymbol{E}_l')\boldsymbol{E}_l'}$$

$$+\overline{\left[\varepsilon'\overline{(\nabla\cdot\boldsymbol{E}_h')\boldsymbol{E}_h'}\right]}+\overline{\varepsilon'(\nabla\cdot\boldsymbol{E}_l')\boldsymbol{E}_l'}+\overline{\bar{\varepsilon}(\nabla\cdot\boldsymbol{E}_l')\boldsymbol{E}_l'}+\overline{\left[\bar{\varepsilon}\overline{(\nabla\cdot\boldsymbol{E}_h')\boldsymbol{E}_h'}\right]}$$

$$-\frac{1}{2}\left[\overline{\left(\overline{\boldsymbol{E}_h'\cdot\boldsymbol{E}_h'}\nabla\varepsilon'\right)}+\overline{\boldsymbol{E}_l'\cdot\boldsymbol{E}_l'\nabla\varepsilon'}+\overline{\boldsymbol{E}_l'\cdot\boldsymbol{E}_l'\nabla\bar{\varepsilon}}+\overline{\left(\overline{\boldsymbol{E}_h'\cdot\boldsymbol{E}_h'}\nabla\bar{\varepsilon}\right)}\right]$$

which is:

$$\rho\left[(\boldsymbol{U}\cdot\nabla)\boldsymbol{U}+\overline{(\boldsymbol{u}'\cdot\nabla)\boldsymbol{u}'}\right]=-\nabla P+\mu\nabla^2\boldsymbol{U}$$

$$+\overline{(\nabla\varepsilon'\cdot\boldsymbol{E}_l')\boldsymbol{E}_l'}+\overline{\overline{(\nabla\bar{\varepsilon}\cdot\boldsymbol{E}_h')\boldsymbol{E}_h'}}+\overline{(\nabla\bar{\varepsilon}\cdot\boldsymbol{E}_l')\boldsymbol{E}_l'}$$

$$+\overline{\varepsilon'(\nabla\cdot\boldsymbol{E}_l')\boldsymbol{E}_l'}+\bar{\varepsilon}\overline{(\nabla\cdot\boldsymbol{E}_l')\boldsymbol{E}_l'}+\bar{\varepsilon}\overline{\overline{(\nabla\cdot\boldsymbol{E}_h')\boldsymbol{E}_h'}}$$

$$-\frac{1}{2}\left[\overline{\boldsymbol{E}_l'\cdot\boldsymbol{E}_l'\nabla\varepsilon'}+\overline{\boldsymbol{E}_l'\cdot\boldsymbol{E}_l'}\nabla\bar{\varepsilon}+\left(\overline{\overline{\boldsymbol{E}_h'\cdot\boldsymbol{E}_h'}}\nabla\bar{\varepsilon}\right)\right] \tag{J5}$$

where any components of tensor $\overline{\overline{\boldsymbol{E}_h'\boldsymbol{E}_h'}}=\overline{\overline{\boldsymbol{E}_h'\boldsymbol{E}_h'}}(\boldsymbol{x},\boldsymbol{y},\boldsymbol{z})$, and:

$$\overline{\left[\overline{(\nabla\varepsilon'\cdot\boldsymbol{E}_h')\boldsymbol{E}_h'}\right]}=\overline{\left[\varepsilon'(\nabla\cdot\boldsymbol{E}_h')\boldsymbol{E}_h'\right]}=\overline{\left(\overline{\boldsymbol{E}_h'\cdot\boldsymbol{E}_h'}\nabla\varepsilon'\right)}=0,\qquad\overline{\left[\overline{(\nabla\bar{\varepsilon}\cdot\boldsymbol{E}_h')\boldsymbol{E}_h'}\right]}=\overline{\overline{(\nabla\bar{\varepsilon}\cdot\boldsymbol{E}_h')\boldsymbol{E}_h'}},$$

$$\overline{\left[\bar{\varepsilon}\overline{(\nabla\cdot\boldsymbol{E}_h')\boldsymbol{E}_h'}\right]}=\overline{\bar{\varepsilon}\overline{(\nabla\cdot\boldsymbol{E}_h')\boldsymbol{E}_h'}},$$

$$\overline{\left(\overline{\boldsymbol{E}_h'\cdot\boldsymbol{E}_h'}\nabla\bar{\varepsilon}\right)}=\overline{\overline{\boldsymbol{E}_h'\cdot\boldsymbol{E}_h'}}\nabla\bar{\varepsilon},\qquad\overline{\boldsymbol{E}_h'\cdot\boldsymbol{E}_l'}=\boldsymbol{0},\qquad\overline{\overline{\boldsymbol{E}_h'\cdot\boldsymbol{E}_h'}}=\overline{\boldsymbol{E}_h'\cdot\boldsymbol{E}_h'}$$

Use equation (J4)-(J5), we have:

$$\rho\left[\frac{\partial\boldsymbol{u}'}{\partial t}+(\boldsymbol{U}\cdot\nabla)\boldsymbol{u}'+(\boldsymbol{u}'\cdot\nabla)\boldsymbol{U}+(\boldsymbol{u}'\cdot\nabla)\boldsymbol{u}'-\overline{(\boldsymbol{u}'\cdot\nabla)\boldsymbol{u}'}\right]=-\nabla p'+\mu\nabla^2\boldsymbol{u}'$$

$$+\overline{\overline{(\nabla\varepsilon'\cdot\boldsymbol{E}_h')\boldsymbol{E}_h'}}+(\nabla\varepsilon'\cdot\boldsymbol{E}_l')\boldsymbol{E}_l'+(\nabla\bar{\varepsilon}\cdot\boldsymbol{E}_l')\boldsymbol{E}_l'-\overline{(\nabla\varepsilon'\cdot\boldsymbol{E}_l')\boldsymbol{E}_l'}-\overline{(\nabla\bar{\varepsilon}\cdot\boldsymbol{E}_l')\boldsymbol{E}_l'}$$

$$+\varepsilon'\overline{\overline{(\nabla\cdot\boldsymbol{E}_h')\boldsymbol{E}_h'}}+\varepsilon'(\nabla\cdot\boldsymbol{E}_l')\boldsymbol{E}_l'+\bar{\varepsilon}(\nabla\cdot\boldsymbol{E}_l')\boldsymbol{E}_l'-\overline{\varepsilon'(\nabla\cdot\boldsymbol{E}_l')\boldsymbol{E}_l'}-\bar{\varepsilon}\overline{(\nabla\cdot\boldsymbol{E}_l')\boldsymbol{E}_l'}$$

$$-\frac{1}{2}\left(\overline{\overline{\boldsymbol{E}_h'\cdot\boldsymbol{E}_h'}}\nabla\varepsilon'+\boldsymbol{E}_l'\cdot\boldsymbol{E}_l'\nabla\varepsilon'+\boldsymbol{E}_l'\cdot\boldsymbol{E}_l'\nabla\bar{\varepsilon}-\overline{\boldsymbol{E}_l'\cdot\boldsymbol{E}_l'\nabla\varepsilon'}-\overline{\boldsymbol{E}_l'\cdot\boldsymbol{E}_l'}\nabla\bar{\varepsilon}\right) \tag{J6}$$

Use $\boldsymbol{u}'$·(J6), we have:

$$\rho\left[\frac{\partial k}{\partial t}+(\boldsymbol{U}\cdot\nabla)k+(\boldsymbol{u'}\cdot\nabla)k+\boldsymbol{u}'\cdot(\boldsymbol{u'}\cdot\nabla)\boldsymbol{U}\right]=-\boldsymbol{u}'\cdot\nabla p'+\mu\nabla^2 k-2\mu\Omega+\boldsymbol{u}'\cdot$$

$$\left[\overline{\overline{(\nabla\varepsilon'\cdot\boldsymbol{E}_h')\boldsymbol{E}_h'}}+(\nabla\varepsilon'\cdot\boldsymbol{E}_l')\boldsymbol{E}_l'+(\nabla\bar{\varepsilon}\cdot\boldsymbol{E}_l')\boldsymbol{E}_l'-\overline{(\nabla\varepsilon'\cdot\boldsymbol{E}_l')\boldsymbol{E}_l'}-\overline{(\nabla\bar{\varepsilon}\cdot\boldsymbol{E}_l')\boldsymbol{E}_l'}\right]+\boldsymbol{u}'\cdot$$

$$\left[\varepsilon'\overline{\overline{(\nabla\cdot\boldsymbol{E}_h')\boldsymbol{E}_h'}}+\varepsilon'(\nabla\cdot\boldsymbol{E}_l')\boldsymbol{E}_l'+\bar{\varepsilon}(\nabla\cdot\boldsymbol{E}_l')\boldsymbol{E}_l'-\overline{\varepsilon'(\nabla\cdot\boldsymbol{E}_l')\boldsymbol{E}_l'}-\bar{\varepsilon}\overline{(\nabla\cdot\boldsymbol{E}_l')\boldsymbol{E}_l'}\right]-\frac{\boldsymbol{u}'}{\boldsymbol{2}}\cdot$$

$$\left[\overline{\overline{\boldsymbol{E}_h'\cdot\boldsymbol{E}_h'}}\nabla\varepsilon'+\boldsymbol{E}_l'\cdot\boldsymbol{E}_l'\nabla\varepsilon'+\boldsymbol{E}_l'\cdot\boldsymbol{E}_l'\nabla\bar{\varepsilon}-\overline{\boldsymbol{E}_l'\cdot\boldsymbol{E}_l'\nabla\varepsilon'}-\overline{\boldsymbol{E}_l'\cdot\boldsymbol{E}_l'}\nabla\bar{\varepsilon}\right] \quad \text{(J7)}$$

where $k=\boldsymbol{u'}\cdot\boldsymbol{u}'/2$ and $\Omega=\frac{1}{2}\boldsymbol{\omega}\cdot\boldsymbol{\omega}$, $\omega=\nabla\times\boldsymbol{u}'$,

Taking ensemble averaging again, we have:

$$\rho\left[\frac{\partial\bar{k}}{\partial t}+\overline{(\boldsymbol{U}\cdot\nabla)k}+\overline{(\boldsymbol{u'}\cdot\nabla)k}+\overline{\boldsymbol{u}'\cdot(\boldsymbol{u'}\cdot\nabla)\boldsymbol{U}}\right]=\overline{-\boldsymbol{u}'\cdot\nabla p'}+\mu\nabla^2\bar{k}-2\mu\bar{\Omega}+$$

$$\overline{\boldsymbol{u}'\cdot\left[\overline{\overline{(\nabla\varepsilon'\cdot\boldsymbol{E}_h')\boldsymbol{E}_h'}}+(\nabla\varepsilon'\cdot\boldsymbol{E}_l')\boldsymbol{E}_l'+(\nabla\bar{\varepsilon}\cdot\boldsymbol{E}_l')\boldsymbol{E}_l'-\overline{(\nabla\varepsilon'\cdot\boldsymbol{E}_l')\boldsymbol{E}_l'}-\overline{(\nabla\bar{\varepsilon}\cdot\boldsymbol{E}_l')\boldsymbol{E}_l'}\right]}+$$

$$\overline{\boldsymbol{u}'\cdot\left[\varepsilon'\overline{\overline{(\nabla\cdot\boldsymbol{E}_h')\boldsymbol{E}_h'}}+\varepsilon'(\nabla\cdot\boldsymbol{E}_l')\boldsymbol{E}_l'+\bar{\varepsilon}(\nabla\cdot\boldsymbol{E}_l')\boldsymbol{E}_l'-\overline{\varepsilon'(\nabla\cdot\boldsymbol{E}_l')\boldsymbol{E}_l'}-\bar{\varepsilon}\overline{(\nabla\cdot\boldsymbol{E}_l')\boldsymbol{E}_l'}\right]}-$$

$$\overline{\frac{\boldsymbol{u}'}{\boldsymbol{2}}\cdot\left[\overline{\overline{\boldsymbol{E}_h'\cdot\boldsymbol{E}_h'}}\nabla\varepsilon'+\boldsymbol{E}_l'\cdot\boldsymbol{E}_l'\nabla\varepsilon'+\boldsymbol{E}_l'\cdot\boldsymbol{E}_l'\nabla\bar{\varepsilon}-\overline{\boldsymbol{E}_l'\cdot\boldsymbol{E}_l'\nabla\varepsilon'}-\overline{\boldsymbol{E}_l'\cdot\boldsymbol{E}_l'}\nabla\bar{\varepsilon}\right]} \quad \text{(J8)}$$

Because:

$$\overline{\boldsymbol{u}'\cdot\overline{(\nabla\varepsilon'\cdot\boldsymbol{E}_l')\boldsymbol{E}_l'}}=\overline{\boldsymbol{u}'\cdot\overline{(\nabla\bar{\varepsilon}\cdot\boldsymbol{E}_l')\boldsymbol{E}_l'}}=\overline{\boldsymbol{u}'\cdot\overline{\varepsilon'(\nabla\cdot\boldsymbol{E}_l')\boldsymbol{E}_l'}}=\overline{\boldsymbol{u}'\cdot\bar{\varepsilon}\overline{(\nabla\cdot\boldsymbol{E}_l')\boldsymbol{E}_l'}}=\overline{\boldsymbol{u}'\cdot\overline{\boldsymbol{E}_l'\cdot\boldsymbol{E}_l'\nabla\varepsilon'}}$$

$$=\overline{\boldsymbol{u}'\cdot\overline{\boldsymbol{E}_l'\cdot\boldsymbol{E}_l'}\nabla\bar{\varepsilon}}=0$$

Then,

$$\rho\left[\frac{\partial\bar{k}}{\partial t}+\overline{(\boldsymbol{U}\cdot\nabla)k}+\overline{(\boldsymbol{u'}\cdot\nabla)k}+\overline{\boldsymbol{u}'\cdot(\boldsymbol{u'}\cdot\nabla)\boldsymbol{U}}\right]=\overline{-\boldsymbol{u}'\cdot\nabla p'}+\mu\nabla^2\bar{k}-2\mu\bar{\Omega}+$$

$$\overline{\boldsymbol{u}'\cdot\overline{\overline{(\nabla\varepsilon'\cdot\boldsymbol{E}_h')\boldsymbol{E}_h'}}}+\overline{\boldsymbol{u}'\cdot(\nabla\varepsilon'\cdot\boldsymbol{E}_l')\boldsymbol{E}_l'}+\overline{\boldsymbol{u}'\cdot(\nabla\bar{\varepsilon}\cdot\boldsymbol{E}_l')\boldsymbol{E}_l'}+\overline{\varepsilon'\boldsymbol{u}'}\cdot\overline{(\nabla\cdot\boldsymbol{E}_h')\boldsymbol{E}_h'}+$$

$$\overline{\varepsilon'\boldsymbol{u}'\cdot\left(\nabla\cdot\boldsymbol{E}_{\boldsymbol{l}}'\right)\boldsymbol{E}_{\boldsymbol{l}}'}+\bar{\varepsilon}\overline{\boldsymbol{u}'\cdot\left(\nabla\cdot\boldsymbol{E}_{\boldsymbol{l}}'\right)\boldsymbol{E}_{\boldsymbol{l}}'}-\frac{1}{2}\Big[\overline{\boldsymbol{u}'\cdot\left(\overline{\overline{\boldsymbol{E}_{\boldsymbol{h}}'\cdot\boldsymbol{E}_{\boldsymbol{h}}'}}\right)\nabla\varepsilon'}+\overline{\boldsymbol{u}'\cdot\left(\boldsymbol{E}_{\boldsymbol{l}}'\cdot\boldsymbol{E}_{\boldsymbol{l}}'\right)\nabla\varepsilon'}+$$

$$\overline{\boldsymbol{u}'\cdot\left(\boldsymbol{E}_{\boldsymbol{l}}'\cdot\boldsymbol{E}_{\boldsymbol{l}}'\right)\nabla\bar{\varepsilon}}\Big] \tag{J9}$$

(1) If I **only consider the initial state of flow** (the interface just enter the channel), where significant changing of conductivity distribution due to velocity fluctuations under electrokinetic force is still small, and the temperature effect is not neglectable, I have:

$$\boldsymbol{E}_{\boldsymbol{l}}'\ll\boldsymbol{E}_{\boldsymbol{h}}'\quad\text{and}\quad\nabla\bar{\varepsilon}\ll\nabla\varepsilon'$$

Then, equation (J9) becomes:

$$\rho\left[\frac{\partial\bar{k}}{\partial t}+\overline{(\boldsymbol{U}\cdot\nabla)k}+\overline{(\boldsymbol{u}'\cdot\nabla)k}+\overline{\boldsymbol{u}'\cdot(\boldsymbol{u}'\cdot\nabla)\boldsymbol{U}}\right]=\overline{-\boldsymbol{u}'\cdot\nabla p'}+\mu\nabla^2\bar{k}-2\mu\bar{\Omega}$$

$$+\overline{\boldsymbol{u}'\cdot\overline{\overline{(\nabla\varepsilon'\cdot\boldsymbol{E}_{\boldsymbol{h}}')\boldsymbol{E}_{\boldsymbol{h}}'}}}+\overline{\varepsilon'\boldsymbol{u}'}\cdot\overline{\overline{(\nabla\cdot\boldsymbol{E}_{\boldsymbol{h}}')\boldsymbol{E}_{\boldsymbol{h}}'}}-\frac{1}{2}\overline{\boldsymbol{u}'\cdot\left(\overline{\overline{\boldsymbol{E}_{\boldsymbol{h}}'\cdot\boldsymbol{E}_{\boldsymbol{h}}'}}\right)\nabla\varepsilon'}$$

As

$$\overline{\boldsymbol{u}'\cdot\left(\overline{\overline{\boldsymbol{E}_{\boldsymbol{h}}'\cdot\boldsymbol{E}_{\boldsymbol{h}}'}}\right)\nabla\varepsilon'}=\overline{2\boldsymbol{u}'\cdot\nabla\Pi'}-\overline{\boldsymbol{u}'\varepsilon'}\cdot\nabla\overline{\left(\boldsymbol{E}_{\boldsymbol{h}}'\cdot\boldsymbol{E}_{\boldsymbol{h}}'\right)}$$

where *Π* is the fluctuating energy density of electric field (Griffiths 2007) on the time scale of ε', i.e. low frequency. It has the expression:

$$\Pi'=\frac{1}{2}\varepsilon'\overline{\overline{\boldsymbol{E}\cdot\boldsymbol{E}}}\approx\frac{1}{2}\varepsilon'\overline{\overline{\boldsymbol{E}_{\boldsymbol{h}}'\cdot\boldsymbol{E}_{\boldsymbol{h}}'}}$$

then,

$$\rho\left[\frac{\partial \bar{k}}{\partial t}+\overline{(\boldsymbol{U}\cdot\nabla)k}+\overline{(\boldsymbol{u}'\cdot\nabla)k}+\overline{\boldsymbol{u}'\cdot(\boldsymbol{u}'\cdot\nabla)\boldsymbol{U}}\right]=\overline{-\boldsymbol{u}'\cdot\nabla p'}+\mu\nabla^2\bar{k}-2\mu\bar{\Omega}-$$

$$\overline{\boldsymbol{u}'\cdot\nabla\Pi'}+\overline{\boldsymbol{u}'\cdot\overline{\overline{(\nabla\varepsilon'\cdot\boldsymbol{E}_h')\boldsymbol{E}_h'}}}+\overline{\varepsilon'\boldsymbol{u}'}\cdot\overline{\overline{(\nabla\cdot\boldsymbol{E}_h')\boldsymbol{E}_h'}}+\frac{1}{2}\overline{\boldsymbol{u}'\varepsilon'}\cdot\nabla\overline{(\boldsymbol{E}_h'\cdot\boldsymbol{E}_h')} \qquad \text{(J10)}$$

If there exists steady state, equation (J10) can also be written as:

$$\rho\left[\overline{(\boldsymbol{U}\cdot\nabla)k}+\overline{(\boldsymbol{u}'\cdot\nabla)k}+\overline{\boldsymbol{u}'\cdot(\boldsymbol{u}'\cdot\nabla)\boldsymbol{U}}\right]=\overline{-\boldsymbol{u}'\cdot\nabla p'}+\mu\nabla^2\bar{k}-2\mu\bar{\Omega}-\overline{\boldsymbol{u}'\cdot\nabla\Pi'}+$$

$$\overline{\boldsymbol{u}'\cdot\overline{\overline{(\nabla\varepsilon'\cdot\boldsymbol{E}_h')\boldsymbol{E}_h'}}}+\overline{\varepsilon'\boldsymbol{u}'}\cdot\overline{\overline{(\nabla\cdot\boldsymbol{E}_h')\boldsymbol{E}_h'}}+\frac{1}{2}\overline{\boldsymbol{u}'\varepsilon'}\cdot\nabla\overline{(\boldsymbol{E}_h'\cdot\boldsymbol{E}_h')} \qquad \text{(J11)}$$

(2) If the **temperature effect is neglected**, equation (J9) becomes:

$$\rho\left[\frac{\partial \bar{k}}{\partial t}+\overline{(\boldsymbol{U}\cdot\nabla)k}+\overline{(\boldsymbol{u}'\cdot\nabla)k}+\overline{\boldsymbol{u}'\cdot(\boldsymbol{u}'\cdot\nabla)\boldsymbol{U}}\right]=\overline{-\boldsymbol{u}'\cdot\nabla p'}+\mu\nabla^2\bar{k}-2\mu\bar{\Omega}+\overline{\varepsilon'\boldsymbol{u}'}\cdot$$

$$\overline{\overline{(\nabla\cdot\boldsymbol{E}_h')\boldsymbol{E}_h'}}+\overline{\varepsilon'\boldsymbol{u}'\cdot(\nabla\cdot\boldsymbol{E}_l')\boldsymbol{E}_l'}+\bar{\varepsilon}\overline{\boldsymbol{u}'\cdot(\nabla\cdot\boldsymbol{E}_l')\boldsymbol{E}_l'} \qquad \text{(J12)}$$

For steady state,

$$\rho\left[\overline{(\boldsymbol{U}\cdot\nabla)k}+\overline{(\boldsymbol{u}'\cdot\nabla)k}+\overline{\boldsymbol{u}'\cdot(\boldsymbol{u}'\cdot\nabla)\boldsymbol{U}}\right]=\overline{-\boldsymbol{u}'\cdot\nabla p'}+\mu\nabla^2\bar{k}-2\mu\bar{\Omega}+\overline{\varepsilon'\boldsymbol{u}'}\cdot$$

$$\overline{\overline{(\nabla\cdot\boldsymbol{E}_h')\boldsymbol{E}_h'}}+\overline{\varepsilon'\boldsymbol{u}'\cdot(\nabla\cdot\boldsymbol{E}_l')\boldsymbol{E}_l'}+\bar{\varepsilon}\overline{\boldsymbol{u}'\cdot(\nabla\cdot\boldsymbol{E}_l')\boldsymbol{E}_l'} \qquad \text{(J13)}$$

This equation means, the energy production due to electrokinetic force should be controlled by three factors: (1) the electrokinetic force is majorly dominated by electrostatic force; (2) the coupling between permittivity fluctuations (due to temperature fluctuations) and velocity fluctuations at low frequency; (3) the contribution of high frequency electric fields by $\overline{\overline{(\nabla\cdot\boldsymbol{E}_h')\boldsymbol{E}_h'}}$ on low frequency components.

(3) If the flow is forced at low frequency, i.e. within the frequency range of velocity fluctuations, the equation of kinetic energy can be modified by letting $\boldsymbol{E_h'} = \mathbf{0}$ on equation (J9), as:

$$\rho\left[\frac{\partial \bar{k}}{\partial t} + \overline{(\boldsymbol{U}\cdot\nabla)k} + \overline{(\boldsymbol{u'}\cdot\nabla)k} + \overline{\boldsymbol{u}'\cdot(\boldsymbol{u'}\cdot\nabla)\boldsymbol{U}}\right]$$

$$= \overline{-\boldsymbol{u}'\cdot\nabla p'} + \mu\nabla^2\bar{k} - 2\mu\bar{\Omega} + \overline{\boldsymbol{u}'\cdot(\nabla\varepsilon'\cdot\boldsymbol{E_l'})\boldsymbol{E_l'}} + \overline{\boldsymbol{u}'\cdot(\nabla\bar{\varepsilon}\cdot\boldsymbol{E_l'})\boldsymbol{E_l'}}$$

$$+ \overline{\varepsilon'\boldsymbol{u}'\cdot(\nabla\cdot\boldsymbol{E_l'})\boldsymbol{E_l'}} + \bar{\varepsilon}\overline{\boldsymbol{u}'\cdot(\nabla\cdot\boldsymbol{E_l'})\boldsymbol{E_l'}}$$

$$-\frac{1}{2}\left[\overline{\boldsymbol{u}'\cdot(\boldsymbol{E_l'}\cdot\boldsymbol{E_l'})\nabla\varepsilon'} + \overline{\boldsymbol{u}'\cdot(\boldsymbol{E_l'}\cdot\boldsymbol{E_l'})}\nabla\bar{\varepsilon}\right]$$

$$= \overline{-\boldsymbol{u}'\cdot\nabla p'} + \mu\nabla^2\bar{k} - 2\mu\bar{\Omega} + \overline{\boldsymbol{u}'\cdot(\nabla\varepsilon\cdot\boldsymbol{E_l'})\boldsymbol{E_l'}} + \overline{\varepsilon\boldsymbol{u}'\cdot(\nabla\cdot\boldsymbol{E_l'})\boldsymbol{E_l'}} - \frac{1}{2}\overline{\boldsymbol{u}'\cdot(\boldsymbol{E_l'}\cdot\boldsymbol{E_l'})\nabla\varepsilon}$$

APPENDIX K: LIFPA TEMPORAL RESOLUTION FOR SMALL DETECTION AREA

Normally, in LIFPA measurement, the diameter of laser focus (d_f) is less or equal to the size of the detection area of detector (d_{da}). The temporal resolution of LIFPA can be estimated by section 2.2.1. However, in some special cases, when the $d_{da} < d_f$, the theories introduced in section 2.2.1 cannot explicitly describe the physical process.

For the case where $d_{da} < d_f$, the total fluorescent intensity in the detection area can be calculated by:

$$I_{f,total}(u) = \int_{(d_f-d_{da})/2}^{(d_f+d_{da})/2} \int_{(d_f-d_{da})/2}^{(d_f+d_{da})/2} I_f(u;x,y)dx\,dy + I_{f,end,da}$$

$$= \int_{(d_f-d_{da})/2}^{(d_f+d_{da})/2} \int_{(d_f-d_{da})/2}^{(d_f+d_{da})/2} I_{f0}\psi(u;x,y)e^{-x/(u\tau)}dx\,dy + I_{f,end,da}$$

$$= I_{f0}\psi_{s,da}(u)d_{da} \int_{(d_f-d_{da})/2}^{(d_f+d_{da})/2} e^{-x/(u\tau)}dx + I_{f,end,da}$$

$$= I_{f0}\psi_{s,da}(u)u\tau d_{da}\left[e^{\frac{d_f}{2u\tau}(R-1)} - e^{\frac{d_f}{2u\tau}(-R-1)}\right] + I_{f,end,da} \qquad \text{(K1)}$$

where $R = d_{da}/d_f < 1$. By applying Taylor expansion on $e^{\frac{d_f}{2u\tau}(R-1)}$ and $e^{\frac{d_f}{2u\tau}(-R-1)}$, we have:

$$e^{\frac{d_f}{2u\tau}(R-1)} = e^{-\frac{d_f}{2u\tau}}\left[1 + \frac{d_f}{2u\tau}R + \left(\frac{d_f}{2u\tau}\right)^2\frac{R^2}{2!} + \left(\frac{d_f}{2u\tau}\right)^3\frac{R^3}{3!} + O(R^4)\right]$$

$$e^{\frac{d_f}{2u\tau}(-R-1)} = e^{-\frac{d_f}{2u\tau}}\left[1 - \frac{d_f}{2u\tau}R + \left(\frac{d_f}{2u\tau}\right)^2\frac{R^2}{2!} - \left(\frac{d_f}{2u\tau}\right)^3\frac{R^3}{3!} + O(R^4)\right]$$

Then,

$$I_{f,total}(u) = I_{f0}\psi_{s,da}(u)u\tau d_{da}\left[\frac{d_{da}}{u\tau}e^{-\frac{d_f}{2u\tau}} + \frac{1}{24}\left(\frac{d_{da}}{u\tau}\right)^3 e^{-\frac{d_f}{2u\tau}}\right] + I_{f,end,da}$$

$$= I_{f0}\psi_{s,da}(u)d_{da}^2 e^{-\frac{d_f}{2u\tau}}\left[1 + \frac{1}{24}\left(\frac{d_{da}}{u\tau}\right)^2\right] + I_{f,end,da} \quad \text{(K2)}$$

Similar as has been done in section 2.2.1, by equivalent $I_{f,total}(u)$ with the fluorescent intensity in quiescent flow, i.e. $I_{f,total,quie}(u)$, we have:

$$I_{f0}\psi_{s,da}(u)d_{da}^2 e^{-\frac{d_f}{2u\tau}}\left[1 + \frac{1}{24}\left(\frac{d_{da}}{u\tau}\right)^2\right] + I_{f,end,da} = I_{f0}\psi_{s,da}(0)d_{da}^2 e^{-\frac{t_{quie}}{\tau}} + I_{f,end,da}$$

Then,

$$\psi_{s,da}(u)e^{-\frac{d_f}{2u\tau}}\left[1 + \frac{1}{24}\left(\frac{d_{da}}{u\tau}\right)^2\right] = \psi_{s,da}(0)e^{-\frac{t_{quie}}{\tau}} \quad \text{(K3)}$$

By taking derivative on t_{quie}, the two sides of equation become:

$$\frac{du}{dt_{quie}}\left\{\frac{d\psi_{s,da}}{du}e^{-\frac{d_f}{2u\tau}}\left[1 + \frac{1}{24}\left(\frac{d_{da}}{u\tau}\right)^2\right] + \psi_{s,da}(u)e^{-\frac{d_f}{2u\tau}}\frac{d_f}{2u^2\tau}\left[1 + \frac{1}{24}\left(\frac{d_{da}}{u\tau}\right)^2\right] -$$

$$\psi_{s,da}(u)e^{-\frac{d_f}{2u\tau}}\frac{1}{12u}\left(\frac{d_{da}}{u\tau}\right)^2\right\} = -\frac{1}{\tau}\psi_{s,da}(0)e^{-\frac{t_{quie}}{\tau}} = -\frac{1}{\tau}\psi_{s,da}(u)e^{-\frac{d_f}{2u\tau}}\left[1 + \frac{1}{24}\left(\frac{d_{da}}{u\tau}\right)^2\right]$$

(K4)

Similar as that has been introduced in section 2.2.1, $d\psi_{s,da}/du \sim 0$, then equation (K4) becomes:

$$\frac{du}{dt_{quie}}\left\{\frac{d_f}{2u^2\tau}\left[1+\frac{1}{24}\left(\frac{d_{da}}{u\tau}\right)^2\right]-\frac{1}{12u}\left(\frac{d_{da}}{u\tau}\right)^2\right\}=-\frac{1}{\tau}\left[1+\frac{1}{24}\left(\frac{d_{da}}{u\tau}\right)^2\right]$$

Then, the upper bound of velocity changing that LIFPA can respond is:

$$\frac{du}{dt_{quie}}=-\frac{u}{\tau}\frac{1+\frac{1}{24}\left(\frac{d_{da}}{u\tau}\right)^2}{\frac{d_f}{2u\tau}\left[1+\frac{1}{24}\left(\frac{d_{da}}{u\tau}\right)^2\right]-\frac{1}{12}\left(\frac{d_{da}}{u\tau}\right)^2} \quad \text{(K5)}$$

Compared to equation (2.10) and (2.11), the result shown in equation (K5) is more complicated. But, as we only approximate the Taylor expansion to 3rd order of *R*, when *R* approaches 1, the approximation is still not accurate and more orders should be kept in Taylor expansion. This rough approximation will cause some misleading when $d_{da}=d_f$.

Hence, equation (K5) is more proper for $R \ll 1$. This should be noted while using this equation.

APPENDIX L: TEMPERATURE VARIATION IN OUR MICROCHANNEL AND ITS INFLUENCE ON LIFPA MEASUREMENT

In EK flow, there are two sources of heating that could cause the variation of temperature. One is from the laser, and another is from Joule heating. Both influences on solution temperature are roughly estimated. The temperature influence on the mean velocity by LIFPA measurement is also investigated.

(1) Laser heating effect

The laser induced heating can be estimated below:

$$\rho C_p \left(\frac{\partial T}{\partial t} + \vec{u} \cdot \nabla T \right) = \lambda \Delta T + \alpha P_d$$

where α (is no more than 0.01 1/m for UV light around 405 nm (Pope and Fry 1997)) is the light absorption coefficient in water, P_d (W/m^2) is the power density of laser, $\rho = 10^6$ (g/m^3) is the density of water and $C_p = 4.1813$ (J/g·K) is the specific heat capacity of water (25 °C). $\lambda = 0.6$ (W/m·K) is the thermal conductivity and $\boldsymbol{K} = \lambda/\rho C_p = 1.435 \times 10^{-7}$ (m^2/s) is the thermal diffusivity.

Assume 1D steady state and constant P_d and α, we have:

$$\boldsymbol{K}\frac{d^2T}{dx^2} - U\frac{dT}{dx} + I = 0$$

where $I = \alpha P_d/\rho C_p$ (K/s) is the temperature source term due to laser heating. By solving this equation with boundary conditions:

$$\begin{cases} x = 0, & T = T_0 \\ x = d_f, & \dfrac{dT}{dx} = 0 \end{cases}$$

where T_0=298 K and $d_f = 2.03 \times 10^{-7}$ (m), we have:

$$T = \frac{I}{U}x + \frac{I\boldsymbol{K}}{U^2}e^{\frac{-d_f U}{\boldsymbol{K}}}\left(1 - e^{\frac{U}{\boldsymbol{K}}x}\right) + T_0\,, \quad x \in [0, d_f]$$

Here, assume the laser power is 50 mW, then $P_d = 0.05/\left(\frac{\pi}{4}d_f^2\right) = 1.545 \times 10^{12}$ W/m^2 and $I = \alpha P_d/\rho C_p = 3.69 \times 10^3$ (K/s). Also assume U = 2 mm/s, then:

$$x = d_f, \qquad T = 25.0005\ ℃$$

Hence, the maximum temperature increasing due to laser heating is only 0.0005 ℃. Furthermore, "50 mW" is the initial output power of laser. After the complicated optical system, the actual laser power on focus is only 25% of the initial value. Therefore, the laser heating effect on local temperature is negligible.

In fact, the laser heating effect can also be estimated by the PSD of unforced flow in Figure 2.18. In the case, laser heating effect is present. However, there is no velocity fluctuations above 10 Hz. The PSD below 10 Hz could be due to pump, vibration of channel or laser heating. It is slightly larger than the noise level. But compared to the signal level

of forced flow, it is negligible. This clearly indicates the influence of laser heating won't affect our LIPFA measurement.

(2) <u>Joule heating effect:</u>

The temperature of solution affected by Joule heating can be expressed by:

$$\rho C_p\left(\frac{\partial T}{\partial t}+\vec{u}\cdot\nabla T\right)=\lambda\Delta T+\sigma\vec{E}(t)\cdot\vec{E}(t)$$

where: λ is thermal conductivity of solution; ρ: density of solution; σ: conductivity of solution and C_p: the specific heat capacity of solution. As the slope of side wall is very small and assuming the side walls are adiabatic, 1D model is proper for a rough estimation on the streamwise variation of temperature. If ignoring the nonlinear terms, the temperature equation can be simplified as:

$$\frac{\partial T'}{\partial t}+U\frac{\partial \bar{T}}{\partial x}+U\frac{\partial T'}{\partial x}+\overrightarrow{u'}\cdot\nabla\bar{T}=\boldsymbol{K}(\Delta\bar{T}+\Delta T')+\frac{\sigma E(t)^2}{\rho C_p}$$

where $\boldsymbol{K}=\frac{\lambda}{\rho C_p}$ is the thermal diffusivity, $\vec{E}(t)=E(t)\vec{j}=|E_{max}|[sin(2\pi ft)-sin(2\pi ft+\pi)]\vec{j}$, $T=\bar{T}+T'$and $\vec{u}=U\vec{\imath}+\vec{u}'$. The bar indicates temporal averaging and prime means fluctuations. U is the mean velocity in streamwise direction. The electric field is applied by two channels of function generator. Both of them can generate electric field intensity with amplitude of $|E_{max}|$. By taking temporal averaging on the equation above, the mean temperature along streamwise can be expressed as:

$$\frac{\partial^2 \bar{T}}{\partial x^2} - \frac{U}{\boldsymbol{K}} \frac{\partial \bar{T}}{\partial x} + \frac{\sigma \overline{E(t)^2}}{\boldsymbol{K} \rho C_p} = 0$$

with boundary conditions: x=0, $\bar{T} = T_0 = 25$ ℃; x=L, $\partial \bar{T}/\partial x = 0$, ($L$ is the length of channel), 1D solution of temperature along streamwise direction is:

$$\bar{T}(x) = -\frac{B}{A^2} e^{A(L-x)} - \frac{B}{A} x + T_0 + \frac{B}{A^2} e^{AL}$$

where $\bar{T}_0$ is initial temperature, $A = -U/\boldsymbol{K}$, $B = \sigma \overline{E(t)^2}/\boldsymbol{K} \rho C_p = 2\sigma |E_{max}|^2/\lambda$. Assume λ=0.6 W/(m*K), ρ=10^6 g/m^3, C_p=4.1813 J/(g*K), σ=0.25 S/m (which is the spatial averaged value in experiments), $|E_{max}| = 7.69 \times 10^4$ V/m, $U = 2 \times 10^{-3}$ m/s, $L = 5 \times 10^{-3}$ m, T_0=25°, the temperature of solution at x = 200 μm downstream of the entrance will be at most 83 ºC. As the channel is not adiabatic (gold side wall) and electric field intensity decreases along x-direction, the real temperature should be much smaller than the estimation here.

The temperate increasing due to Joule heating may cause three results: (1) the changing of fluorescent efficiency; (2) stronger Brownian motion; (3) additional thermal flow. The first one determines fluorescent intensity. The second one will enhance the fluorescence molecule transport along the edge of laser beam and may slightly enhance the fluorescent intensity. The third one will introduce unknown thermal flow in the field and cause unexpected signal. Hence, their influence on LIFPA measurement should be estimated.

The first influence can be evaluated by Figure L.. Here, the fluorescence intensity at different temperature is investigated. In the test, σ = 0.5 S/m is supplied for both injected

fluid. The flow rate was kept 10 μl/min for each syringe. In order to investigate influence of temperature, photobleaching should be reduced to negligible level. To avoid photobleaching, a low laser power of 2 mW is applied. Therefore, the fluorescent signal (or efficiency) is only characterized by the temperature without the influence of velocity or others. In the test, the solution is heated upstream and an IR thermometer was used to measure the temperature.

It can be seen, the mean fluorescence intensity $I_{f,total}$ decreases with the temperature which indicates the fluorescent efficiency decreases with T. However, this variation is very small and about 4.5% from 22 to 80 ºC, which is negligible for LIFPA measurement. Hence, the temperature variation will not apparently affect the fluorescent efficiency and so does LIFPA measurement.

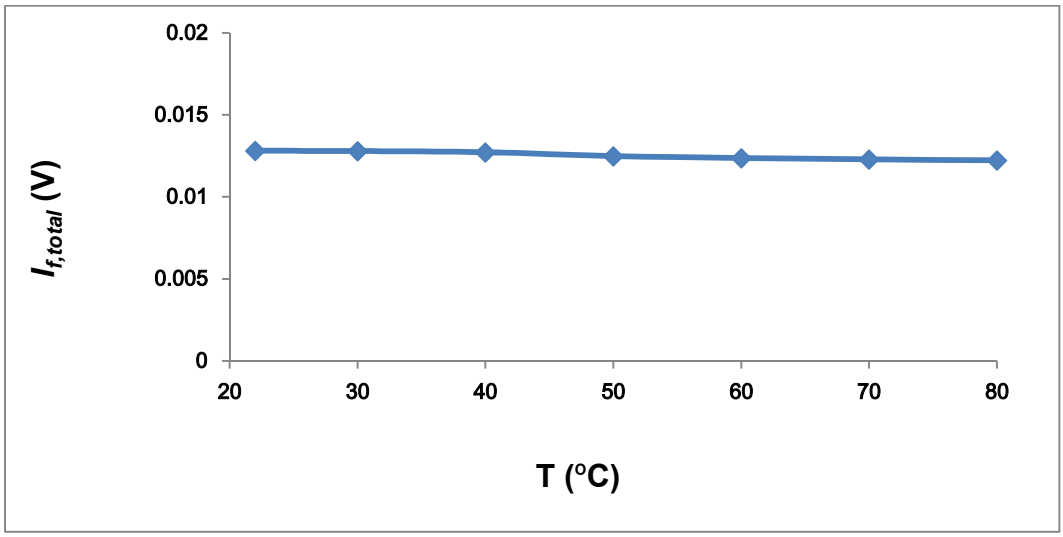

Figure L.1 Fluorescence intensity vs temperature. $\sigma = 0.5$ S/m. flow rate is 10 μl/min for each stream. Laser power is 2 mW.

The influence of second factor, i.e. Brownian motion, is not fully investigated yet. Recently, we can only say the Brownian motion won't significantly affect the measurement of velocity fluctuations. There are two reasons. First is that Brownian motions only affect the background noise level but won't affect the valid velocity signals. Second, from the PSD of forced flow, the noise level beyond the cutoff of high frequency signal doesn't significantly changes with streamwise positions and voltages. But, we should also see, the noise level actually increases with applied voltages. The increasing of noise level is majorly caused by the increasing of velocity signals which generates higher shot noise. Thus, we say the Brownian motion has neglectable influence on velocity measurement.

APPENDIX M: LIABILITY OF LIFPA IN ELECTRIC FIELD AND CHEMICAL ENVIRONMENT

(1) Influence of electric field intensity on LIFPA measurement

The potential influence of electric field intensity on LIFPA measurement was also investigated. σ=0.5 S/m for both injected solutions was used to avoid fluorescence intensity variation due to unsteady electrically driven flow. Laser power was 2 mw. And the flow rate was kept 10 μl/min for each stream. The fluorescent signal at different electric field intensity is plotted in Figure M., which shows, the $I_{f,total}$ doesn't exhibit apparent change in a wide range of electric field intensity. Hence, LIFPA measurement in this electric-driven flow is not affected by external electric field.

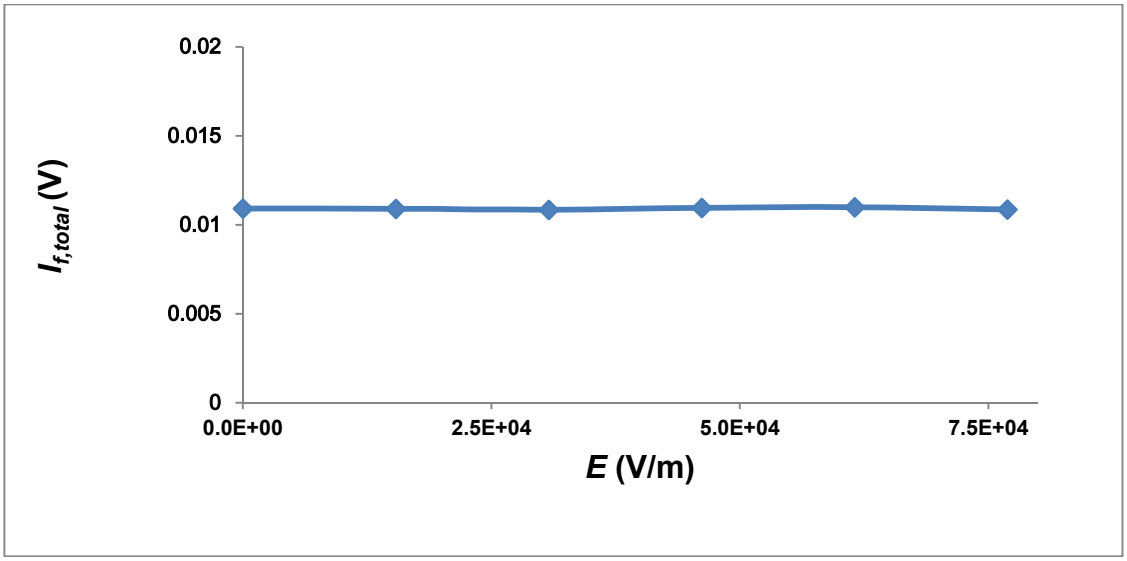

Figure M.1 Fluorescence intensity vs electric field intensity

(2) Influence of solution conductivity

As the PH value is kept about 7.3 in all our experiments, its influence on $I_{f,total}$ is ignored. The relation of fluorescence intensity with solution conductivity is investigated in a large conductivity range (from 0.0001 to 1.32 S/m) as shown in Figure M.. To simulate the real LIFPA measurement, laser power is 50 mW accompanied with proper electric amplifier setting. As shown, using different conductivity solution won't make apparent influence on the fluorescence signal. In the conductivity range of 0.0001 – 0.5 S/m, where our experiments are pursued, the LIFPA measurement is reliable.

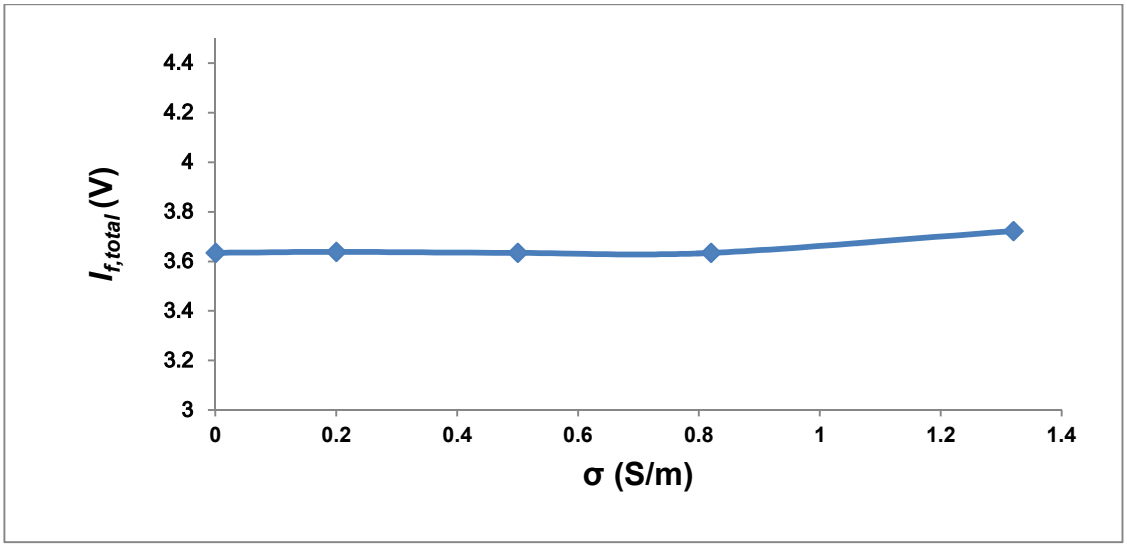

Figure M.2 Fluorescence intensity vs solution conductivity

APPENDIX N: SOME USEFUL SUMMARY ABOUT THE UNCERTAINTY OF MICROPIV

(**Shinohara** et al. 2004): They measured the mean velocity profile in a microchannel with different fluid at the existence of interface. They analyzed the error due to Brownian motions, which is about 4.3%, and claims the error on measuring mean velocity is not due to Brownian motion. However, from the profile, the errors in center is at least 0.1 mm/s and 0.4 mm/s near the interface. 1 μm particles. 2000 continuous images using CMOS camera and CW laser. 60x NA 0.9 water immersion lens.
(Sugii et al. 2005): They measured the mean velocity profile with the existence of RBC. The Uavg is 3.5 mm/s with rms of velocity from 0.5 mm/s to 1 mm/s. High speed camera, mercury lamp with proper filters, 2048 images, 100 μm inner diameter channel, 1 μm particle (427nm/468nm).
(Lima et al. 2008): The measured the mean velocity in vitro blood flow in a 300 μm by 45 μm channel. The Re is 0.02 with maximum Uavg of about 0.45 mm/s. The error is estimated to be 0.04 mm/s. High speed camera, laser (should be CW, DPSS), confocal microscope, 20x NA 0.75 lens, 100 velocity fields for averaging, 1μm red particle, exposure time 4.995 ms, time interval 5 ms.

(Yan et al. 2006): They measured the EOF flow in a 300μm by 300μm square channel. The maximum Uavg is about 0.9 mm/s with an error of about 0.2 mm/s. CCD camera, double-pulsed laser, 20x NA 0.45 lens, 0.9μm red particle, time interval 0.5ms to 2ms. Brownian motion cause error between 30 to 46μm/s.
(Westerweel et al. 2013): They summarized all the new development of μPIV techniques and give a theoretical estimation on the error of mean velocity measurement. As they said:"high spatial resolution only with the penalty of reduced relative measurement accuracy, and vice versa (Adrian, 1997)". The error of μPIV comes from the following factors: uncertainty of position (in-plane and depth-of-correlation); uncertainty cross-correlation peak and the error while calculating peak position due to the irregular shape of particles and their images, low signal-noise ratio, interrogation window size; Brownian motion; optical distortion; acceleration lag; dielectrophoresis effect and other possible electric effect while electric field is applied; out-of-plane effect and so on.
(Adrian 1997): Dynamic velocity range (DVR) is estimated to be 143 for best and theoretically. This cannot be achieved in practice.
(Rossi et al. 2012): They estimated the influence of depth of correlation (DOC) and found the effect DOC is much larger than the theoretical one, especially for the high magnification and large NA lens. This will cause much larger error.(For example, in a channel with 240μm depth, and using 63x/0.75 lens and 1μm particle, the DOC is about 36.9μm. Even at the center of channel, it can result in a 15% error due to fake z position. And this will more signification while far from centerline.). They believe:" the experimental analysis carried out in this work suggests that completely removing the

bias error due to DOC in practical μPIV applications is very difficult or not possible at all". And the effective NA is smaller than the nominal NA.

(Wereley and Meinhart 2010): summarize the development of μPIV, such as Confocal μPIV, 3D, Stereo, Holography and so on.

(Bown et al. 2006): 3D distribution of all three velocity components, paraxial assumption, z-direction position estimation and so on.

Michal M. Mielnik, Lars R. Saetran, Micro Particle Image Velocimetry – an overview, Turbulence, 2004, 10, 83: The SNR of μPIV is pretty low, as:

SNR of the in-focus particle-image field for various particle concentrations and test – section depth.

Test-section depth (μm)	Particle concentration (by volume)			
	0.01%	0.02%	0.04%	0.08%
25	2.2	2.1	2.0	1.9
50	1.9	1.7	1.4	1.2
125	1.5	1.4	1.2	1.1
170	1.3	1.2	1.1	1.0

(Bitsch et al. 2003): Blood flow.

(Park et al. 2004): Confocal μPIV and conventional μPIV. Hagen-Poiseuille flow. Uavg is 55 μm/s, while by conventional μPIV, it is 40μm/s.

(Klein and Posner 2010): Confocal microscope, high speed camera 2500 Hz max, Nipkow disk, unsteady flow, continuous 532 laser, channel 100μm(width) *

24μm(height) * 15mm(length). Solution has PH =4 to reduce electrophoretic effect. Particle (500 nm polystyrene) concentration from 0.05% to 1%. μPIV spatial resolution: 4.9μm by 4.9μm. Interrogation window size: 64*64 to 16*16.
(Natrajan et al. 2007): conventional μPIV, microchannel high Re turbulence, bulk flow velocity 8.4 m/s, inner diameter 536μm, 15 Hz pulse laser, 10x NA 0.3 lens, 2000*2000 CCD camera, 1μm particle, 32*32 interrogation window, 11.6μm*11.6μm resolution.